Novel quantum behaviors induced by random disorder in highly frustrated magnets

Suvam Bhattacharya

université PARIS-SACLAY

Novel quantum behaviors induced by random disorder in highly frustrated magnets

Nouveaux effets quantiques induits par désordre aléatoire dans les composés magnétiques frustrés

Thèse de doctorat de l'université Paris-Saclay

École doctorale n° 564, physique en Île-de-France (PIF)
Spécialité de doctorat : Physique
Graduate School : Physique. Référent : Faculté des sciences d'Orsay

Thèse préparée au **Laboratoire de Physique des Solides** (Université Paris-Saclay, CNRS), sous la direction de **Philippe MENDELS**, Professeur des universités, et le co-encadrement d'**Edwin KERMARREC**, Maître de conférence

Thèse soutenue à Paris-Saclay, le 07 Janvier 2022, par

Suvam BHATTACHARYA

Composition du jury

Françoise DAMAY Directrice de recherche, Laboratoire Léon Brillouin	Présidente
Pierre DALMAS DE RÉOTIER Directeur de recherche, Commissariat à l'Energie Atomique Grenoble (CEA)	Rapporteur & Examinateur
Virginie SIMONET Directrice de recherche, Institut Néel	Rapporteure & Examinatrice
Ludovic JAUBERT Chargé de recherche, Laboratoire Ondes et Matière d'Aquitaine (LOMA)	Examinateur
Philippe MENDELS Professeur des universités, Université Paris-Saclay	Directeur de thèse

THESE DE DOCTORAT
NNT : 2022UPASP005

université PARIS-SACLAY | ÉCOLE DOCTORALE Physique en Île-de-France (PIF)

Titre : Nouveaux effets quantiques induits par désordre aléatoire dans les composés magnétiques frustrés

Mots clés : diffusion inélastique de neutrons, désordre quantique, frustration, pyrochlore, liquide de spin, triangulaire

Résumé : Cette thèse est dédiée à l'étude expérimentale de nouveaux matériaux quantiques frustrés à base de terre rare de spin effectif S=1/2, par mesures d'aimantation et de susceptibilité magnétique, ainsi que par spectrocopies de neutrons et de muons. Le dénominateur commun de l'ensemble de ce travail expérimental est la compréhension de l'effet d'un désordre aléatoire sur les états quantiques exotiques présents dans ces composés frustrés à base de terre rare. Motivés par la récente découverte du nouveau composé triangulaire $YbMgGaO_4$ – qui montrent des signatures expérimentales d'un état de liquide de spin quantique en présence d'un désordre chimique important -, nous étudions d'abord le composé iso-structural $ErMgGaO_4$ afin de mettre à jour les effets du désordre sur les propriétés magnétiques dans cette famille de composés. Nous confirmons l'anisotropie de l'ion magnétique Er^{3+} (1) rapportée par des mesures précédentes sur monocristal et mettons en évidence l'existence d'un ordre de spin modulé de type « stripe » en dessous de T = 2.5 K d'après les mesures de diffusion élastique de neutrons. De plus, les spectroscopies de neutrons et de muons démontrent l'existence de fluctuations de spins qui persistent jusqu'à 25 mK, d'après la présence d'un continuum (intensité quasi-élastique) en diffusion de neutrons et d'un taux de relaxation constant en spectroscopie de muons. Ce comportement de liquide de spin est peut-être dû à la superposition de tous les états dégénérés des ordres modulés de spin, séparés par une faible barrière d'énergie qui peut alors être franchie grâce aux fluctuations thermiques ou bien par effet tunnel. Cette hypothèse pourrait permettre de mieux comprendre les fluctuations de spins quasi-omniprésentes dans les composés frustrés à base de terre-rare en présence d'un désordre important. Dans une approche alternative, nous avons également étudié de nouveaux composés quantiques triangulaires à base d'ytterbium, qui présentent un réseau triangulaire régulier et sans la présence de désordre détectée, afin de rechercher de nouveaux candidats expérimentaux à l'état de liquide de spin quantique. Enfin, nous avons sondé les propriétés d'une nouvelle famille de pyrochlore, $Yb_2(Ti_{(1-x)}Zr_x)_2O_7$, dans laquelle la substitution du Zr sur le site du Ti induit une pression chimique qui déstabilise l'ordre magnétique observé dans le composé parent x=0 et avons suivi l'évolution de la dynamique de spin par diffusion inélastique de neutrons pour différentes valeurs x, en champ magnétique nul et appliqué. La compréhension fine de nos résultats expérimentaux de spectroscopie neutronique pourrait permettre de mieux comprendre le mécanisme responsable de la transition d'un état ordonné ferromagnétique (x=0) vers un état de type liquide de spin, par exemple à cause de la diffusion des magnons causée par un désordre aléatoire. Nos résultats fournissent une base solide pour de futurs modèles théoriques dédiés à la compréhension de l'origine d'un continuum d'excitations dans les composés frustrés désordonnés à base de terre rare.

Title : Novel quantum behaviors induced by random disorder in highly frustrated magnets
Keywords : inelastic neutron scattering, quantum disorder, frustration, pyrochlore, spin liquid, triangular

Abstract : This thesis is dedicated to the experimental study of new effective spin S=1/2 rare-earth based frustrated quantum magnets using magnetization measurements, neutron and muon spectroscopies. The common thread of this body of experimental work is to understand the effect of random disorder on the exotic quantum states of these highly frustrated rare earth based magnets. Motivated by the recent discovery of the new quantum triangular magnet $YbMgGaO_4$ –which shows controversial experimental signatures of spin liquid behavior in the presence of strong chemical disorder –, we first investigate the sister compound $ErMgGaO_4$ of the same structural family in order to shed new light on the effect of disorder on their magnetic properties. We confirmed the single-ion anisotropy already reported on single-crystal and further detected the signature of a striped-order state at T = 2.5K from elastic neutron scattering. Furthermore, neutron and muon spectroscopies both showed the existence of persistent dynamics in the form of a quasi-elastic continuum and a constant muon spin relaxation rate down to 25 mK. Its spin liquid behavior may originate from the superposition of all the possible degenerate stripe-ordered phases, separated by a small energy barrier, which can be overcome by thermal fluctuations or quantum tunneling. Our results pave the way to the understanding of the ubiquitous spin fluctuations in the context of rare-earth frustrated magnets with strong disorder. Alternatively, we focus on new Yb-based quantum triangular magnets, with a perfect triangular lattice and without any detectable disorder, to search for other quantum spin liquid candidates. Finally, we investigate the new pyrochlore series $Yb_2(Ti_{(1-x)}Zr_x)_2O_7$, where the substitution of Zr on the Ti site is used as chemical pressure to destabilize the magnetic order observed for the pure, x=0, parent compound, and explored the evolution of the spin dynamics in the vicinity of this peculiar x=0 phase in zero and in applied magnetic fields. A detailed modelling of our inelastic neutron scattering results on the x=0 and Zr-substituted samples may hold the key for understanding the mechanism that turns the splayed ferromagnetic order into a fluctuating spin liquid regime, perhaps because of a strong scattering of magnons caused by random disorder. It provides a strong constrain to any theoretical model trying to address the origin of the continuum of scattering in disordered rare-earth frustrated systems.

Bhaskar Banerjee

Without whom this adventure would not have been possible

Acknowledgements

First of all, I would like to thank Edwin Kermarrec for your guidance and support. During these last three years, I am grateful for your guidance and help which allowed me to progress while gaining my independence little by little. Thank you also for your enthusiasm, your kindness, and your patience which allowed me to stay motivated even when the results were not there yet. I shall keep your teachings in mind preciously, I'm sure they will help me in the future. I also thank Philippe Mendels for the knowledge that you brought me on the experimental points, for the discussions, and for your insights and corrections. I take this opportunity to thank Mr. Fabrice Bert who helped me clarify my doubts and rectify my mistakes.

A big thank you also to the members of the jury for the time and energy you have given to this manuscript and for the highly stimulating questions that you asked me during the defense. Thanks to Pierre Dalmas de Réotier and Virginie Simonet for accepting to be reporters and to evaluate my thesis work. Thanks to Ludovic Jaubert and Françoise Damay who agreed to examine this thesis.

Next, I want to thank all the past and present group members of the Spectroscopie des Matériaux Quantiques (SQM) at LPS. Thank you H. Alloul, V. Brouet, I. Mukhamedshin, B. Le Pennec, H. Lohani, D. Chatterjee, P. Foulquier, Q. Barthélemy, R. Sharma, G. Simutis and A. Louat.

I am also grateful to the human resource and administration team of LPS, Orsay. I am indebted to V. Thieulart, S. Hoarau, S. Tourlet, and P. Foury.

During the 3 years of my doctoral studies, I also had the chance to get guided by my mentors in the lab, I would like to thank G. Tresset, M. Monteverde, and M. Gabay.

During the experimental trips and conferences, I had the opportunity to meet a large number of scientists and engineers. I am thankful to all of these inspiring people. I would especially like to thank B. Gaulin, N. Butch, S. Petit, M. Gingras, C. Decourse, J-M. Zanotti and all our collaborators and instrument scientists.

Lastly, I want to thank all my friends and family outside of the laboratory with special thanks to my parents B. Banerjee and M. Bhattacharya.

Résumé

Les nombreuses découvertes en matière condensée qui ont ponctuées tout le XXe siècle soulignent certes la singularité de ce domaine en physique, mais peut-être plus important encore, ont montré que la matière condensée est un fantastique terrain de jeu pour l'émergence de nouvelles idées et de nouveaux concepts. Le concept de l'état isolant de Mott en est un exemple. Dans cet état, les fortes interactions entre les électrons sont responsables du comportement isolant observé dans un état supposé métallique, comme le prédit la théorie des bandes. Dans le domaine du magnétisme quantique, l'effet des corrélations fortes a été intensément étudié dans les composés de faible dimension présentant des interactions antiferromagnétiques, comme la chaîne de spin antiferromagnétique de Heisenberg $S = 1/2$. Grâce à l'Ansatz de Bethe, ce modèle est exactement soluble, avec une énergie de l'état fondamental qui est inférieure à l'énergie de l'état antiferromagnétique de Néel. La nature de cet état fondamental purement quantique est bien connue : il s'agit d'un état résonant, formé par la superposition quantique de deux configurations de singulets. Il s'agit peut-être de l'exemple le plus simple d'une phase topologique du magnétisme, le liquide de spin quantique, qui se caractérise à la fois par l'absence de toute symétrie brisée et par des spins intriqués jusqu'à $T = 0$ K. Il est alors naturel de se demander si de tels états quantiques exotiques sont possibles dans des dimensions supérieures ($d = 2$ et 3). Cette possibilité a été envisagée par P. W. Anderson qui a introduit le concept d'un état quantique RVB (*Resonating Valence Bond*) sur un réseau antiferromagnétique triangulaire bidimensionnel. Cependant, en dimension $d = 2$, on constate expérimentalement que la plupart des systèmes semblent préférer l'ordre à basse température. On s'est rendu compte par la suite qu'une approche nécessaire était d'utiliser des interactions anisotropes ou entre second plus proche voisins pour le réseau triangulaire, ou encore des réseaux plus frustrés à faible connectivité constitués de triangles partageant leurs sommets (kagomé) ou de tétraèdres (pyrochlore). C'est la voie suivie au cours de cette thèse, où nous avons étudié de nouveaux composés triangulaires à base de terres rares avec échange anisotrope ainsi que des composés pyrochlore pour rechercher des candidats liquides de spin quantique en utilisant des techniques de diffusion inélastique de neutrons et de relaxation de spin de muons.

L'autre fil conducteur de notre travail expérimental est de comprendre l'effet du désordre aléatoire sur les propriétés à basse température de ces aimants à base de terres rares hautement frustrés. Il s'agit d'un domaine de recherche très vaste qui englobe en fait des problèmes très fondamentaux en physique, comme l'a récemment

souligné le prix Nobel de physique 2021, attribué "pour des contributions révolutionnaires à notre compréhension des systèmes physiques complexes", et notamment à G. Parisi pour "la découverte de l'interaction du désordre et des fluctuations dans les systèmes physiques, de l'échelle atomique à l'échelle planétaire". La physique de la matière condensée est également un exemple de système complexe, où la frustration est générée par le désordre conduisant à la phase de verre de spin et souligne ainsi le potentiel de frustration magnétique dans la physique moderne de la matière condensée.

Ici, nous nous intéressons plus particulièrement à l'effet du désordre chimique dans les aimants quantiques frustrés à base de terres rares. Ce sujet de recherche a été largement motivé par l'observation récente en 2015 d'un état magnétique fluctuant dans le composé triangulaire à base de terre rare $YbMgGaO_4$, qui a relancé l'intérêt pour la recherche d'un état liquide de spin quantique sur le réseau triangulaire, mais a également remis en question l'authenticité d'un comportement liquide de spin quantique en présence de désordre chimique. À la lumière de cette découverte, nous adoptons deux approches différentes pour étudier les aimants triangulaires à base de terres rares. Premièrement, nous avons étudié les propriétés magnétiques du composé isostructural $ErMgGaO_4$ (chapitre 4), qui possède le même désordre chimique que dans $YbMgGaO_4$, mais avec une possible différence d'anisotropie de spin et/ou d'interactions d'échanges, et qui dont l'étude comparative devrait donc permettre de tirer des conclusions sur l'effet de ce désordre. Notre deuxième approche consiste à étudier de nouveaux composés triangulaires parfaits sans désordre qui ont été identifiés par nos collaborateurs : $K_3YbV_2O_8$ et $K_2CsYbP_2O_8$ (chapitre 5), et $Ba_6Yb_2Ti_4O_{17}$ (chapitre 6).

Au cours de cette thèse, nous avons également étudié la nouvelle famille de pyrochlore à base d'ytterbium, $Yb_2(Ti_{1-x}Zr_x)_2O_7$. Initialement, le composé parent de cette série, $Yb_2Ti_2O_7$ (x=0), était reconnu comme un candidat potentiel pour une phase de liquide de spin quantique. Cependant, après plus d'une décennie d'intenses efforts de recherche, il s'avère que son état fondamental est extrêmement dépendant de l'échantillon, et qu'il est plus proche d'une phase ordonnée ferromagnétique, mais qu'il présente étonnamment une forte dynamique de spin (chapitre 7). Ces propriétés inhabituelles peuvent être conciliées si l'on considère que $Yb_2Ti_2O_7$ se trouve près d'une transition de phase dans le diagramme de phase, comme cela a été récemment découvert par des études de diffusion inélastique de neutrons et modélisé théoriquement. Le grand nombre d'expériences réalisées sur $Yb_2Ti_2O_7$ a révélé la grande sensibilité de l'état fondamental à la contrainte chimique, et nous exploitons cette sensibilité inhérente en introduisant un désordre chimique artificiel dans le but de sélectionner sa phase magnétique en remplaçant Ti dans $Yb_2Ti_2O_7$ par Zr avec différents niveaux de dopage (chapitre 8).

Nous résumons ci-dessous les principaux résultats obtenus dans les différents chapitres.

Les composés $S_{\text{eff}} = 1/2$ antiferromagnétiques anisotropes triangulaires

Dans le chapitre 3, nous passons en revue les principaux résultats obtenus sur le candidat liquide de spin quantique $YbMgGaO_4$ et le désordre chimique inhérent à cette famille dû au mélange intersite de Mg et Ga. Le chapitre 4 présente notre étude expérimentale du nouveau composé isostructural $ErMgGaO_4$. Er^{3+}, en tant qu'ion de terre rare, implique une différence significative de l'anisotropie des moments par rapport aux moments des ions Yb^{3+} ; c'était le principal objectif expérimental, pour étudier les séparer les effets du désordre de l'anisotropie magnétique. Ce travail s'est concentré sur un échantillon de poudre récemment synthétisé et de grande pureté, obtenu auprès de nos collaborateurs de l'Université McMaster. A partir de mesures d'aimantation, nous avons confirmé l'anisotropie $g_\perp/g_\parallel$ = 1.0(1) déjà rapportée sur un monocristal et avons en outre détecté une signature d'ordre magnétique à $T = 2.5$ K avec une division zfc-fc dans la susceptibilité magnétique. Cet ordre statique est caractérisé par une forme de raie asymétrique de l'intensité de la diffusion élastique des neutrons près du point M de la zone de Brillouin, en accord avec la fonction de Warren attendue pour un ordre bidimensionnel mais avec une distribution des longueurs de corrélation. Notre analyse indique que ces corrélations peuvent avoir un étalement spatial jusqu'à 70 Å. Cette diffusion élastique apparaît clairement en dessous de $T = 2.5$ K et est cohérente avec nos mesures de susceptibilité. La position de cette intensité élastique (point M) est en accord avec un ordre magnétique de rangées antiferromagnétiquement alternées, comme prédit pour le composé $YbMgGaO_4$ par les calculs DMRG. De plus, les spectroscopies neutroniques et muoniques ont toutes deux montré l'existence d'une dynamique persistante sous la forme respectivement d'un continuum quasi-élastique et d'un taux de relaxation de spin du muon constant jusqu'à 25mK. L'émergence d'un état ordonné en présence d'une dynamique de spin est un thème récurrent dans les systèmes frustrés de terres rares, et peut être interprété ici comme un état fondamental constitué d'une superposition de tous les domaines possibles de l'ordre magnétique en rangées alternées, séparés par une petite barrière énergétique qui peut être surmontée par des fluctuations thermiques ou par un effet tunnel quantique. Bien que ce ne soit pas la définition d'un liquide de spin quantique, cela donne peut-être un scénario plus générique pour comprendre les fluctuations de spin omniprésentes dans le contexte des aimants frustrés à base de terres rares en présence d'un fort désordre. Enfin, nous notons que ce continuum inélastique observé pour $ErMgGaO_4$ est très similaire à la situation rencontrée dans $YbMgGaO_4$. Cependant, notre très récente expérience de diffusion inélastique de neutrons (non présentée ici) sur $YbMgGaO_4$ ne montre aucune corrélation statique émergeant dans le régime basse température, en accord avec les résultats de la littérature. Si ce continuum d'excitation est principalement dû à des ondes de spin élargies provenant d'une phase ordonnée, pourquoi un tel ordre est-il absent dans $YbMgGaO_4$? La différence des paramètres hamiltoniens entre les deux composés pourrait donc être, après tout, la clé pour comprendre leurs différents états fondamentaux. De futures expériences avec un monocristal d'$ErMgGaO_4$ de haute qualité devraient permettre de clarifier cette situation.

$K_3YbV_2O_8$ and $K_2CsYbP_2O_8$ (chapitre 5): Dans cette nouvelle famille de composés triangulaires sans désordre,

nous avons rapporté à partir des mesures de $M(H)$ et de susceptibilité magnétique que les interactions inter-ioniques entre les ions Yb^{3+} sont antiferromagnétiques pour les deux composés mais plutôt faibles, d'un ordre de grandeur inférieur par rapport aux membres de la famille *Re*$MgGaO_4$. L'interaction magnétique dans $K_2CsYbP_2O_8$ est encore plus faible, probablement en raison des orbitales phosphates sur le chemin d'échange, et nous nous sommes donc concentrés sur $K_3YbV_2O_8$. D'après notre ajustement de la susceptibilité magnétique, nous avons estimé que l'interaction antiferromagnétique était de l'ordre de 0,5 K dans $K_3YbV_2O_8$. D'après notre analyse CEF des mesures INS dans les deux composés, nous n'avons pas noté de signes d'élargissement des niveaux CEF dû aux effets du désordre comme cela a été observé dans $YbMgGaO_4$ et avons validé le modèle de spin effectif S_{eff} = 1/2 de Yb^{3+} à basse température, avec un caractère anisotrope des moments selon $g_\perp/g_\parallel$ = 0.6(1). Les fluctuations des spins sont confirmées par la spectroscopie μSR pour $K_3YbV_2O_8$ jusqu'à 60mK, avec une augmentation du taux de relaxation du spin du muon qui suggère que les spins entrent dans un régime corrélé à basse température ($\leq 1K$). Il est intéressant de noter que les expériences INS ont permis d'observer une intensité faible, dépendant de la température, dans le spectre inélastique en dessous de 800mK. D'après notre analyse, l'explication la plus probable du signal inélastique sont les excitations paramagnétiques qui apparaissent dans un régime corrélé au-dessus d'une température de transition, T_c qui est probablement inférieure à 100mK. Les expériences futures visant à rechercher la faible T_c sur de tels composés seront très intéressantes.

$Ba_6Yb_2Ti_4O_{17}$ (chapitre 6): La deuxième famille sans désordre que nous avons étudiée est la famille $Ba_6Re_2Ti_4O_{17}$, avec Re = Yb. Ici, nos mesures d'aimantation ont également mis en évidence une interaction d'échange extrêmement faible (0,05K), probablement due aux distances inter-ioniques encore plus grandes. Les mesures d'aimantation et INS ont toutes deux montré que $Ba_6Yb_2Ti_4O_{17}$ satisfaisait au modèle S_{eff} = 1/2. Les études spectroscopiques INS et muoniques ont mis en évidence une phase paramagnétique jusqu'à 100mK dans $Ba_6Yb_2Ti_4O_{17}$. Un régime corrélé en dessous de cette température est tout à fait possible, mais serait très difficile à sonder expérimentalement.

Famille de composés pyrochlore quantique - $Yb_2(Ti_{1-x}Zr_x)_2O_7$ (chapitre 7 et 8)

Dans cette partie , nous avons rapporté nos mesures sur la nouvelle série d'échantillons polycristallins $Yb_2(Ti_{1-x}Zr_x)_2O_7$, et sur deux monocristaux avec un niveau de substitution $x = 0$ et $x = 0.025$, qui permettent une analyse comparative entre le composé parent ($x = 0$) et les homologues substitués en Zr. Nos résultats reproduisent quantitativement les résultats précédents obtenus sur la phase stchiométrique $x = 0$, $Yb_2Ti_2O_7$, et confirment l'extrême sensibilité de l'ordre ferromagnétique, qui n'existe que pour le composé parent $x = 0$. A partir de mesures d'aimantation et de susceptibilité, nous constatons que la température de Curie-Weiss peut éventuellement être modifiée d'une valeur ferromagnétique à une valeur antiferromagnétique par l'effet de ces substitutions. Nous avons ensuite observé la présence d'un continuum d'excitation dans le spectre de l'INS pour tous les niveaux de substitution et avons en outre révélé un changement non-trivial dans la distribution spectrale en champ nul lorsque le niveau de substitution augmente de $x = 0$ à $x = 0.2$. En effet, pour $x = 0,025$, nous avons trouvé des preuves d'un changement de com-

portement dans le spectre inélastique, avec une réduction notable du poids spectral à des valeurs Q élevées et à de faibles énergies. Sous l'effet d'un champ externe appliqué, le continuum devient plus net et se déplace linéairement avec l'amplitude du champ, ressemblant à des ondes de spin polarisées, larges et amorties. À des énergies encore plus élevées, on observe un deuxième type d'excitations larges qui a été interprété comme une bande d'excitations à deux magnons pour la phase $x = 0$ dans la littérature. Alors que nos mesures ont reproduit ce comportement pour l'échantillon $x = 0$, cette explication ne tient pas pour la phase $x = 0.025$ qui montre un déplacement linéaire de la bande avec une amplitude différente de celle de la bande d'excitation du premier magnon, accompagné d'un élargissement significatif. Une modélisation détaillée de notre diffusion de neutrons polarisés sur les deux échantillons monocristallins $x = 0$ et $x = 0.025$ pourrait être la clé pour comprendre le mécanisme qui transforme l'ordre ferromagnétique étalé en un régime de liquide de spin fluctuant, peut-être à cause d'une forte diffusion des magnons par un désordre induit aléatoire. À la lumière de ces résultats, de futures expériences visant à caractériser magnétiquement les cristaux $x = 0,025$ sous pression externe peuvent être très intéressantes si nous pouvons reproduire des observations similaires à celles du cas stchiométrique $x = 0$, ce qui nous permettra de quantifier les effets du désordre par dopage. Les travaux de recherche actuels fournissent de multiples cas de composés à base de terres rares présentant à la fois un ordre magnétique avec des fluctuations. Les résultats obtenus ici imposent une contrainte forte pour tout modèle théorique essayant d'aborder l'origine du continuum de diffusion dans les systèmes désordonnés à base de terres rares.

Collaborations

Ce travail de thèse a bénéficié de collaborations avec plusieurs chercheurs/enseignant-chercheurs et d'institutions, dont notamment:

- **Sylvain Petit, Françoise Damay** Laboratoire Léon Brillouin, CNRS CEA Saclay
- **Claudia Decorse** Institut de Chimie Moléculaire et des Matériaux dOrsay, Université Paris Saclay
- **Z. Cronkwright, S. Huang, E.M. Smith, B. D. Gaulin** McMaster University, Ontario, Canada
- **Jean-Marc Zanotti, Quentin Berrod, C. Colin, Lucile Mangin-Tanhro, Andrew Wildes** Institut Laue Langevin
- **David Voneshen, Helen Walker, James Lord, Pabitra Biswas** ISIS STFC, UK
- **N.P. Butch, W. Chen, Y. Qiu, Y. Vekhov** NCNR NIST, USA
- **Elsa Lhotel** Institut Néel, CNRS
- **U. K. Voma, B. Koteswararao** Department of Physics, Indian Institute of Technology Tirupati, India
- **J. Khatua, P. Khuntia** Department of Physics, Indian Institute of Technology Madras, India

Publications

Une partie des résultats des travaux de recherche présentés dans ce manuscript, ainsi que d'autres études, ont été publiés, soumis ou bien sont en préparation pour être soumis dans différents journaux scientifiques:

- **Electronic structure and magnetic properties of the effective spin Jeff = 1/2 two-dimensional triangular lattice $K_3Yb(VO_4)_2$**
  U. K. Voma , S. Bhattacharya , E. Kermarrec, J. Alam, Y. M. Jana, B. Sana , P. Khuntia, S. K. Panda and B. Koteswararao
  Phys. Rev. B 104, 144411 (2021)
- **Quantum spin-liquid candidate in a rare-earth hyperkagome lattice** *J. Khatua, S. Bhattacharya, Q. P. Ding, S. Vrtnik, N. P. Butch, H. Luetkens, E. Kermarrec, M. S. Ramachandra Rao, A. Zorko, Y. Furukawa and P. Khuntia*
  Submitted to Communication Physics
- **The case for a $U(1)_\pi$ Quantum Spin Liquid Ground State in the Dipole-Octupole Pyrochlore $Ce_2Zr_2O_7$**
  E. M. Smith, O. Benton, D. R. Yahne, B. Placke, J. Gaudet, J. Dudemaine, A. Fitterman, J. Beare, A. R. Wildes, S. Bhattacharya, T. DeLazzer, C. R. C. Buhariwalla, N. P. Butch, R. Movshovich, J. D. Garrett, C. A.

Marjerrison, J. P. Clancy, E. Kermarrec, G. M. Luke, A. D. Bianchi, K. A. Ross and B. D. Gaulin

arXiv 2108.01217 (2021)

- **Disordered-induced spin liquids in anisotropic triangular antiferromagnets : $ErMgGaO_4$ versus $YbMgGaO_4$**

  S. Bhattacharya et al.,

  In preparation

Introduction

The numerous discoveries in condensed matter that punctuated the whole XXth century certainly highlight the singularity of this field in physics and, perhaps more importantly, have shown that condensed matter is a fantastic playground for the emergence of new ideas and concepts. The concept of a Mott insulator state is such an example. There, the strong interactions between electrons are responsible for the insulating behavior observed in a supposedly metallic state, as would be predicted by the band theory.

In quantum magnetism, the effect of strong correlations has been heavily investigated in low-dimensional compounds with antiferromagnetic interactions, such as the S=1/2 Heisenberg antiferromagnetic spin chain. Thanks to the Bethe Ansatz, this model is exactly solvable, with a ground state energy which is lower than the energy of the antiferromagnetic Néel state. The nature of this purely quantum ground state is well known: this is a resonating state, formed by the quantum superposition of two singlets configurations. This is perhaps the simplest example of a topological phase in magnetism, the quantum spin liquid phase, which is characterized by both the absence of any broken symmetry and entangled spins till T=0 K. It is natural to then wonder if such exotic quantum states are possible in higher dimensions (d = 2 and 3). This possibility was considered by P. W. Anderson who introduced the concept of a Resonating Valence Bond (RVB) quantum state on a two-dimensional triangular antiferromagnetic lattice. However, in dimension d = 2, it is experimentally found that most systems seem to prefer order at low temperatures. It was later realized that a necessary approach was to use anisotropic or second nearest-neighbor interactions for the triangular lattice, or even more frustrated lattices with low connectivity made of corner-sharing triangles (kagomé) or tetrahedra (pyrochlore). This is the path followed during this PhD, where we investigated new rare-earth triangular magnets with anisotropic exchange along with pyrochlore compounds to look for quantum spin liquid candidates using inelastic neutron scattering and muon spin relaxation techniques.

The other common thread of our experimental work is to understand the effect of random disorder on the low temperature properties of these highly frustrated rare-earth based magnets. This is a very broad field of research that actually embraces very fundamental problems in physics, as pointed out recently by the Physics Nobel prize 2021, awarded “for groundbreaking contributions to our understanding of complex physical systems”, and notably to G. Parisi for “the discovery of the interplay of disorder and fluctuations in physical systems from atomic to planetary scales”. Condensed matter physics is also an example of a complex system, where frustration is generated by

disorder leading to the spin-glass phase and thus underlines the potential for magnetic frustration in modern condensed matter physics. Here, we focus more specifically on the effect of chemical disorder in frustrated rare-earth quantum magnets. This research topic was largely triggered by the recent observation in 2015 of a fluctuating magnetic state in the quantum triangular rare-earth magnet $YbMgGaO_4$, which revived the interest in the search for a quantum spin liquid state on the triangular lattice but also questioned the genuineness of a quantum spin liquid behavior in the presence of chemical disorder. In the light of this discovery, we take two different approaches to study triangular rare-earth magnets. First, we investigate the magnetic properties of the sister compound $ErMgGaO_4$ (chapter 4), which hosts the same chemical disorder as in $YbMgGaO_4$ but with an expected different spin anisotropy and/or anisotropic interactions, and thus should permit a proper comparison of their low temperature properties. Our second approach is to investigate new, disorder-free perfect triangular compounds that were identified by our collaborators: $K_3YbV_2O_8$ and $K_2CsYbP_2O_8$ (chapter 5), and $Ba_6Yb_2Ti_4O_{17}$ (chapter 6).

During this PhD we have also investigated the new Yb-based pyrochlore family $Yb_2(Ti_{1-x}Zr_x)_2O_7$. Initially, the end member of this series, $Yb_2Ti_2O_7$ (x=0), was acknowledged as potential quantum spin liquid candidate. However, after more than a decade of intense research efforts, it turns out that its ground state is extremely sample-to-sample dependent, is closer to a ferromagnetic ordered phase, but surprisingly displays strong spin dynamics (chapter 7). These unusual properties may be reconciled when considering that $Yb_2Ti_2O_7$ sits near a critical phase boundary in the phase diagram, as recently found by inelastic neutron scattering studies and modelled theoretically. The large set of experiments performed on $Yb_2Ti_2O_7$ has revealed the high sensitivity of the ground state on chemical stress, and we exploit this inherent sensitivity by introducing artificial chemical disorder to tune its magnetic phase by substituting Ti in $Yb_2Ti_2O_7$ by Zr with different doping levels (chapter 8).

This manuscript is organized as follows.

The first part (I) is devoted to a brief theoretical introduction on magnetic frustration and on the quantum spin liquids (Chapter 1), followed by a description of the two main experimental techniques used in this work, inelastic neutron scattering and muon spin relaxation (Chapter 2).

The second part (II) is dedicated to the new family of rare-earth triangular compounds $ReMgGaO_4$, with Re = Yb and Er. In Chapter 3 we review the main results obtained on the quantum spin liquid candidate $YbMgGaO_4$ and the chemical disorder inherent to this family due to the intersite mixing of Mg and Ga. Chapter 4 presents our experimental investigation of the new, sister compound $ErMgGaO_4$.

The third part (III) is about the experimental characterization of new, disorder-free perfect triangular compounds that were identified by our collaborators: $K_3YbV_2O_8$ and $K_2CsYbP_2O_8$ (chapter 5), and $Ba_6Yb_2Ti_4O_{17}$ (chapter 6).

The last part (IV) presents our study of the series $Yb_2(Ti_{1-x}Zr_x)_2O_7$, where we controlled the level of chemical disorder through the partial substitution of Zr on the Ti site in order to induce a negative chemical pressure. We

first review the important results obtained on the pure, x=0, phase (chapter 7) before presenting our experimental investigations of the new Zr-substituted family (chapter 8).

Collaborations

This PhD work notably benefited from the collaboration with different researchers and institutions, including but not limited to:

- **Sylvain Petit, Françoise Damay** Laboratoire Léon Brillouin, CNRS – CEA Saclay
- **Claudia Decorse** Institut de Chimie Moléculaire et des Matériaux d'Orsay, Université Paris Saclay
- **Z. Cronkwright, S. Huang, E.M. Smith, B. D. Gaulin** McMaster University, Ontario, Canada
- **Jean-Marc Zanotti, Quentin Berrod, C. Colin, Lucile Mangin-Tanhro, Andrew Wildes** Institut Laue Langevin
- **David Voneshen, Helen Walker, James Lord, Pabitra Biswas** ISIS STFC, UK
- **N.P. Butch, W. Chen, Y. Qiu, Y. Vekhov** NCNR NIST, USA
- **Elsa Lhotel** Institut Néel, CNRS
- **U. K. Voma, B. Koteswararao** Department of Physics, Indian Institute of Technology Tirupati, India
- **J. Khatua, P. Khuntia** Department of Physics, Indian Institute of Technology Madras, India

Publications

Part of the results of the research work described in this manuscript, along with other studies, have been published, submitted, or are in preparation for the submission, in different journals:

- **Electronic structure and magnetic properties of the effective spin Jeff = 1/2 two-dimensional triangular lattice $K_3Yb(VO_4)_2$**
  U. K. Voma , S. Bhattacharya , E. Kermarrec, J. Alam, Y. M. Jana, B. Sana , P. Khuntia, S. K. Panda and B. Koteswararao
  Phys. Rev. B 104, 144411 (2021)
- **Quantum spin-liquid candidate in a rare-earth hyperkagome lattice** *J. Khatua, S. Bhattacharya, Q. P. Ding, S. Vrtnik, N. P. Butch, H. Luetkens, E. Kermarrec, M. S. Ramachandra Rao, A. Zorko, Y. Furukawa and P. Khuntia*
  Submitted to Communication Physics
- **The case for a $U(1)_\pi$ Quantum Spin Liquid Ground State in the Dipole-Octupole Pyrochlore $Ce_2Zr_2O_7$**
  E. M. Smith, O. Benton, D. R. Yahne, B. Placke, J. Gaudet, J. Dudemaine, A. Fitterman, J. Beare, A. R. Wildes, S. Bhattacharya, T. DeLazzer, C. R. C. Buhariwalla, N. P. Butch, R. Movshovich, J. D. Garrett, C. A.

Marjerrison, J. P. Clancy, E. Kermarrec, G. M. Luke, A. D. Bianchi, K. A. Ross and B. D. Gaulin

arXiv 2108.01217 (2021)

- **Disordered-induced spin liquids in anisotropic triangular antiferromagnets : $ErMgGaO_4$ versus $YbMgGaO_4$**

  S. Bhattacharya et al.,

  In preparation

Contents

Part I

A survey of experimental techniques and theory

Chapter 1

Frustration and exotic quantum magnets

At the dawn of the 20^{th} century, Max Planck [1] reformulated the third law of entropy in the context of materials and stated, "As the temperature diminishes indefinitely, the entropy of a chemically homogeneous body of finite density approaches indefinitely near to the value of zero". However, in 1936, Giauque and Stout [2] measured the heat capacity of ice at low temperatures and realized that the interpolated entropy in the limit T$\rightarrow$ 0K is non-zero and amounts to 3.4J/mol.K, in contradiction to Planck's statement of thermodynamics. This posed a fundamental problem to the well-established thermodynamic principles and needed a deeper investigation. Only after the structure of ice was considered by Linus Pauling [3] was it understood that the reason for the residual entropy at 0K is due to configurational disorder intrinsic to the hydrogen ions or protons positions.

Oxygen atoms in ice are surrounded by four other oxygen atoms through hydrogen bonds. Each H_2O molecule is oriented in such a way as to direct its two hydrogen atoms toward two of the four neighbors; this particular geometrical organization allows multiple configurations of equal energy in a perfect lattice and is a pattern of frustration that has also been observed in magnetic systems. A magnetically analogous [4] situation to the degeneracy in ice was experimentally confirmed in the so-called spin ice pyrochlore compound $Ho_2Ti_2O_7$ which opened the possibility of exploring frustrated magnetism in this family of compounds. The concept of frustration has since then seen enormous success as it is found to explain a wide variety of complex systems, for example, in the protein folding problem [5], to understand superconducting junctions [6] and to study nuclear matter [7] to name a few. In the context of this thesis, we focus on frustration in magnetic systems in two and three dimensions.

1.1 Magnetic frustration

Frustration is thus used to describe a system's inability to simultaneously minimize the competing interaction energy between its components [8, 9]. The degree of magnetic frustration can be quantified by using a frustration parameter, defined as f = $\frac{\Theta_{CW}}{T_c}$, where Θ_{CW} is the Curie Weiss temperature (see Sec.2.4) and T_c is the ordering

temperature of an antiferromagnet. In frustrated magnetic systems, a high value of f can be interpreted as $T_c \rightarrow 0$ and is thus a mechanism by which magnetic order can be suppressed. Magnetic frustration is not only limited to the pyrochlore family; a straightforward example is the triangular Ising antiferromagnet [8] with nearest-neighbor interactions (Fig.1.2), where the Hamiltonian is written as:

$$H = -J \sum_{i,j} S_i \cdot S_j \tag{1.1}$$

As the spins are either $|\pm 1/2\rangle$ in the Ising case, for a negative J corresponding to an antiferromagnetic exchange, no configuration simultaneously minimizes the competing interactions, and the ground state is six-fold degenerate in energy for a single triangular cell. If we consider the entire triangular lattice, then the GS of the lattice would be highly degenerate. The amount of frustration is also affected by a multitude of factors; in the context of this work, we explore frustration in the presence of factors such as the anisotropy [10] of the spins: XY, Ising or Heisenberg, the anisotropy of the exchange interactions (see Sec.1.3.2) and finally chemical disorder.

1.2 The Anderson-Fazekas Resonating Valence Bond (RVB) state

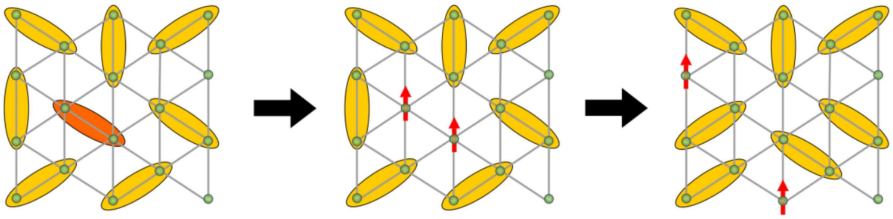

Figure 1.1: Spinon excitation in a RVB phase: An excitation to the system breaks a singlet into a non-local triplet; This triplet pair is then delocalized through out the lattice. Extracted from Li, Gegenwart, and Tsirlin [11]

Anderson and Fazekas [9] considered competing correlations as a way to stabilize a correlated and degenerate ground state with the most straightforward situation of pair-wise entanglement between Heisenberg spins of a triangular lattice. The lower energy of the proposed RVB state prevents long-range ordering (Neel order in the antiferromagnetic case) or symmetry breaking. They showed that, in the low-temperature range, if the exchange is antiferromagnetic, the spins gain additional energy by forming non-local pairs or quantum-mechanical singlets. Since the different configurations of the singlets are all degenerate in energy, the singlet configurations can resonate and hence the name, resonating valence bond liquid (RVB). Such a liquid-like phase that is quantum in nature offers the possibility to explore fractional excitation that is not otherwise present in most classical magnets. Excitation from the ground state with correlated singlet states would bring the singlet into a triplet state (Fig.1.2). The excited triplets are non-local with spin S=1. Because the ground state has all possible combinations of singlets, the emergent excitation can break down or fractionalize into two spin 1/2 excitations that can propagate freely within

the crystal, revealing the highly non-trivial, entangled nature of the RVB state. The ground state of such a system is then a correlated liquid-like system with persistent spin fluctuation or dynamics till the lowest temperatures known as a Quantum Spin Liquid (QSL) phase (see review by [12, 13] for a detailed description).

However, in certain situations, the singlet bonds do not resonate, break the lattice symmetry and are then characterized as a valence bond solid [3]. The moments are strongly correlated in this singlet phase that do not show on-site magnetism. The essential ingredient of a QSL phase is thus not the lack of order but the presence of a high degree of entanglement and fractionalized excitation. This makes it hard to identify QSL experimentally as there is no simple experimental probe for quantum entanglement [14]. Because of this one has to use complementary experimental techniques (see Sec.2) like Inelastic Neutron Scattering (INS), Muon Spin Relaxation (muSR) (see sec) and Nuclear Magnetic Resonance (NMR) [15, 16], to probe the dynamic nature of the spins.

1.3 The quantum triangular antiferromagnet models

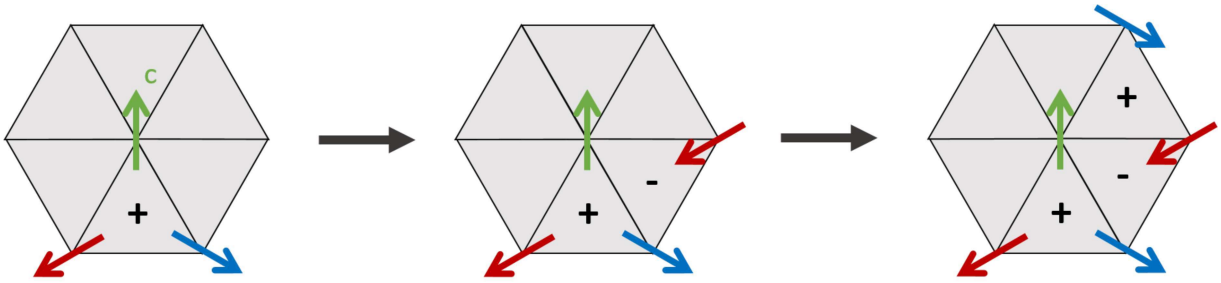

Figure 1.2: Degeneracy of the Heisenberg antiferromagnet model on the triangular lattice. a, b and c denote the spin direction for each sublattice. The spins are oriented at 120° from each other. When the spin configuration of a given triangle is fixed (left), the configurations of the neighbouring triangles are constrained (middle and right). The remaining double degeneracy is due to the choice of the chirality ($+$ or $-$) for the first triangle, defined to be positive when the rotation of the spin is clockwise on a triangle and negative otherwise.

It is natural under the promise of RVB theory to consider the triangular antiferromagnet model as a basis to look for quantum spin liquids. In this section, we discussed specifically the frustration effect inherent to the Heisenberg antiferromagnetic model on the triangular lattice.

1.3.1 The Heisenberg triangular antiferromagnet

Interestingly, the case of Heisenberg spins, allowed to point in every direction in three dimensions, turned out to be very different than the Ising case. If one considers a single triangle with Heisenberg spins coupled by an antiferromagnetic interaction, the minimization of the energy of one triangle occurs for the coplanar configuration where the spins directions are at 120° from each other. Indeed, for classical spins the Hamiltonian (1.1) can be written as:

$$H = -\frac{J}{2}\sum_{\Delta}\left|\vec{S_a}+\vec{S_b}+\vec{S_c}\right| + \frac{J}{2}\sum_{i}\vec{S_i}^2 \tag{1.2}$$

where a, b and c label the corner position on the triangle and a particular orientation for a given spin, and the sum of the first term runs over all different triangles. If the spins are oriented at 120° from each other, $\vec{S_a}+\vec{S_b}+\vec{S_c}=\vec{0}$, and the energy is thus minimized leaving only a constant energy term in the Hamiltonian. Furthermore, once the configuration on one triangle is chosen, the spin configurations of the neighbouring triangles are also fixed by this first choice, and so on for the rest of the lattice (see Fig.1.2). The degeneracy of the ground state is thus no longer infinite and reduced to only two, i.e. the chirality of the first triangle, provided one do not consider the global rotation of all spins. This is a direct consequence of the topology of the triangular lattice, made of edge-sharing triangles. It is not true anymore when the lattice is made of corner-sharing triangles: the ground state of this so-called *kagome* lattice remains with a macroscopic degeneracy and its quantum version is currently one of the primary option for the observation of a quantum spin liquid in two dimensions [12, 17, 18].

This calculation gives a simple, although incomplete, reason as to why the Heisenberg triangular antiferromagnet model possesses a long range order at $T = 0$. A more rigourous approach is to compute numerically the ground state energy of such ordered state and directly compare with the energy of the RVB-type quantum spin liquid proposed by P. W. Anderson. This was undertaken by D. A. Huse and V. Elster who used a variational approach combined with Monte-Carlo numerical technique to estimate the ground state energy of the wavefunction of the $S = 1/2$ Heisenberg triangular antiferromagnet model [19]. They found an upper bound of $E \simeq -0.1789$, which compared favourably to the typical energy of RVB-type wavefunctions of $E = -0.158 \pm 0.005$ [19]. The Heisenberg triangular antiferromagnet model thus shows a long range order at $T = 0$ and one needs an other ingredient to stabilize a quantum spin liquid on this lattice.

1.3.2 Anisotropic spin Hamiltonian of triangular antiferromagnets

The S=1/2 next nearest neighbor XXZ Heisenberg model with anisotropic exchanges on a triangular lattice is considered as a potential model to describe triangular antiferromagnets [11]. We do not focus here on effects like ring exchange [21] and multiple spin interaction exchange mechanism [22] that are less important in the case of rare-earth oxides. The J_1-J_2 Hamiltonian consists of the anisotropic exchanges along with the XXZ term and is expressed as,

$$H^{J_1-J_2} = \sum_{n=1}^{2} H_n^{XXZ} + H_n^{\pm\pm} + H_n^{z\pm} \tag{1.3}$$

the first term is the XXZ Hamiltonian, the second is the pseudo-dipolar term, and the third represents the off-diagonal components. In this model, the XXZ term consists of the exchange interaction between the spins in the x, y, and z

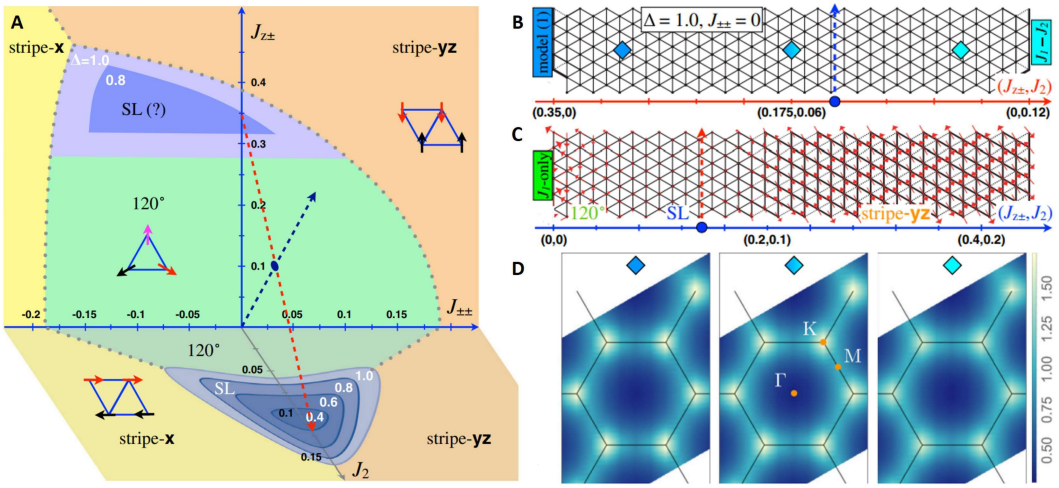

Figure 1.3: **A.** Classical phase diagram of a 2D triangular antiferromagnet with only nearest neighbor interactions (back panel), and of the J_1-J_2-$J_n^{\pm\pm}$ XXZ model (lower panel). **B,C.** DMRG scans with Δ=1 along the blue and the red dotted lines of **A.**. The crossing point of the scans are shown by dotted arrows. The S(Q,ω) is calculated at three different points marked by diamonds and is found to be of the same topological nature and is shown in **D**. Extracted from Zhu et al. [20]

directions, and owing to the 2D lattice, the anisotropy is in the z-direction and is quantitatively denoted by Δ. The H_n^{XXZ} is expressed as:

$$H_n^{XXZ} = \sum_{i,j} J_n (S_i^x S_j^x + S_i^y S_j^y + \Delta S_i^z S_j^z) \tag{1.4}$$

Where J_1 and J_2 are the nearest and the next-nearest neighbor interactions. Here, $\Delta \leq 1$ corresponds to an easy plane anisotropy. Δ = 1 corresponds to the isotropic interactions and, $\Delta \geq 1$, corresponds to the easy axis Hamiltonian where the exchange couples mainly to the z-component of the spins. The pseudo-dipolar term $H^{\pm\pm}$ transforms similarly as H^{XXZ} under symmetry operations and is sometimes essential when the spin-orbit interaction is strong, as for rare-earth elements (see Sec.2.3). This effect causes an anisotropic interaction that is bond dependent and is given by:

$$H_n^{\pm\pm} = 2J_n^{\pm\pm} \sum_{i,j} \left\{ (S_i^x S_j^x - S_i^y S_j^y) \cos(\phi_\alpha) - (S_i^x S_j^y + S_i^y S_j^x) \right\} \tag{1.5}$$

and the off-diagonal component is given by:

$$H_n^{z\pm} = J_n^{z\pm} \sum_{i,j} \left\{ (S_i^y S_j^z + S_i^z S_j^y) \cos(\phi_\alpha) - (S_i^x S_j^z + S_i^z S_j^x) \sin(\phi_\alpha) \right\} \tag{1.6}$$

Where ϕ_α are bond-dependent phases, and α correspond to the different bond directions on the triangular lattice. If one considers only nearest-neighbor bond overlap then ϕ_α can take value 0, $\pm$ 2π/3. The corresponding phase

diagram (Fig.1.3) of this Hamiltonian shows the ground state can be a 120° order or a striped order state. Further DMRG and spin-wave simulation [20] predicts regions of the phase diagram where a spin liquid phase can be stabilized under the presence of anisotropic exchange interactions. With this theoretical framework in place, we examine multiple triangular QSL candidates to explore the phase diagram of the frustrated triangular antiferromagnet.

Chapter 2

Experimental techniques and physical modelling

We describe two spectroscopic techniques utilized in this work in this chapter: muon spin relaxation and inelastic neutron scattering. A more extensive introduction is available in [23, 24]. Additionally, we discuss the peculiarities of rare-earth magnetism, emphasizing the estimation of CEF levels and our physical models for analyzing magnetization observations.

2.1 Muon spin relaxation

C.D. Anderson discovered [25] highly penetrating particles in 1934 while examining cosmic radiation. These particles curled differently in a magnetic gas chamber than electrons and other known particles at the time. Anderson and Seth Neddermeyer identified this as a new type of subatomic particle eventually named muon. Even today, the characteristics of this particle are of prime importance due to a mismatch between the calculated magnetic moment and the experimentally determined value; this is the famous g-2 muon experiment [26].

Muons also have a wide range of applications in various scientific fields, most notably condensed matter research. This section discusses the muon's usage as an ultrasensitive probe of local magnetism and its applications to quantum magnetism in condensed materials [27].

2.1.1 The muon: a spin-polarized particle

The muon is an elementary particle of the lepton family; it is similar to an electron in that it has a negative electric charge of -e and a spin of 1/2, but it is 207 times heavier (105.66 MeV/c^2) and has a gyromagnetic ratio of γ_μ= 851.616 Mrad/s/T. The muon has an antiparticle with the same mass and spin but the opposite charge (+e), termed

the antimuon or positive muon μ^+. In this thesis and more broadly in condensed matter physics, antimuons are referred to as muons.

Large-scale cyclotron and synchrotron facilities generate muons for application in condensed matter physics. When high-energy protons are accelerated in a cyclotron and smashed into the nuclei of a production target, positive pions (π^+) are produced by the relation,

$$\begin{aligned} p + p &\rightarrow p + n + \pi^+ \\ p + n &\rightarrow n + n + \pi^+ \end{aligned} \tag{2.1}$$

The pions of interest for our experiments are at rest in the laboratory frame of reference and decay into muons and neutrinos (ν_μ).

$$\pi^+ \rightarrow \nu_\mu + \mu^+ \tag{2.2}$$

The muons and neutrinos produced in this process have equal and opposite momentum and spin in the laboratory frame. Because neutrinos have negative helicity, the momentum vector is antiparallel to the spin direction. This implies that the muon spins are similarly related to its momentum vector. So the muons produced by this process are 100$\%$ spin polarised in the antiparallel direction to their momentum. The muons then pass through a series of beam filters, focusing quadrupoles, bending magnets, collimators, and the cryostat to finally arrive at the surface of the sample with the energy of the order of 4MeV. For such incident energies, the average surface density of samples needs to be 200 mg.cm^{-2}.

Once entering the sample, the muons thermalize in regions of high electron density, where they quickly get implanted. It is found that muons stop at interstitial positions that minimize their electrostatic energy; in rare-earth oxides (the samples we study) muons get implanted near oxygen ions. A small fraction of these muons, usually less than 30$\%$ might get implanted in the silver sample holder or the cryostat tail and provide a small but fixed background signal. The muon has a magnetic moment 3.14μ_p (μ_p is the moment of the proton), making it extremely sensitive to small magnetic fields such as the ones created by nuclear spins.

Muon implantation is a short process compared to the average lifetime of the muon (1 ns vs. 2.2 μs), and the muon spins all have the same polarization before they start precessing around the local magnetic fields B$_{loc}$. Once implanted, the muon spins are mostly coupled to the immediate environment by dipolar interactions. The muon's spin start precessing around the local field direction with an angular frequency ω = γ_μB$_{local}$, where B$_{local}$ = B$_{applied}$ + B$_{sample}$. The accessible magnetic fields and widths of field distributions range from about 10 μT to several Teslas. Additionally, μSR is sensitive to magnetic fluctuations with nuclear and electronic origins on a timescale of 10^{-12}-10^{-13} seconds. These characteristics make the muon a fascinating experimental tool for exploring small-moment magnetism (up to 10^{-3} μ_B/ion) and fluctuating phases of magnetism (e.g., spin liquids).

Muon decay is a radioactive process that follows the standard exponential law for the chance of survival over time t and has a mean lifespan of 2.2μs. The muon decays according to the rule,

$$\mu^+ \rightarrow e^+ + \nu_e + \overline{\nu} \tag{2.3}$$

This process is governed by the weak interaction or weak nuclear force. Parity violation in the weak interaction causes an anisotropic distribution of the positron emission direction with respect to the spin direction of the muons. This positron emission probability is given by

$$P(\theta)d\theta \propto (1 + a\cos(\theta))d(\theta) \tag{2.4}$$

where θ is the angle between the positron trajectory and the muon spin and a is the intrinsic asymmetry parameter of the weak interaction mechanism. P(θ) takes the maximum value when θ = 0, thus correlating the positron momentum strongly with the muon spin direction at the time of its decay.

2.1.2 Principle of μSR measurements

Pulsed sources

There are currently five sources of muons in the world: Paul Scherrer Institut (PSI, Switzerland), Tri-University Meson Facility (TRIUMF, Canada), High Energy Accelerator Research Organization (KEK, Japan), MuSiC muon center (Osaka, Japan), and Rutherford Appleton Laboratory (ISIS, England).

In the framework of this thesis, we conducted experiments primarily using the MuSR instrument at ISIS, which features a pulsed muon source. The muon beam is temporally structured in these sources, and muons come in "packets" without any flux restrictions. A muon packet arriving in the sample starts the clock, so each packet also resets the clock upon arrival. Thus, positron detection events are measured by assuming simultaneous implantation of all muons and the pulse width (80ns) limits the time resolution. The advantage of using a pulsed source is that a large number of muons implanted can probe weak relaxations by minimizing the statistical error. However, the detection rate is limited by the detector desaturation time (10 ns); hence it is critical to use a significant number of detectors to achieve a high signal-to-noise ratio (the MuSR apparatus at ISIS has 64 detectors). Furthermore, the relaxation can be studied over a much more extended period (around 20μs) than a quasi-continuous beam.

These characteristics of pulsed source muon instruments make it attractive to study spin fluctuation and dynamics in rare-earth oxides, for example, as one has to detect weak changes of the relaxations to characterize these materials properly. In the following sections, we will go through the essential points relevant to pulsed sources.

Experimental Setup

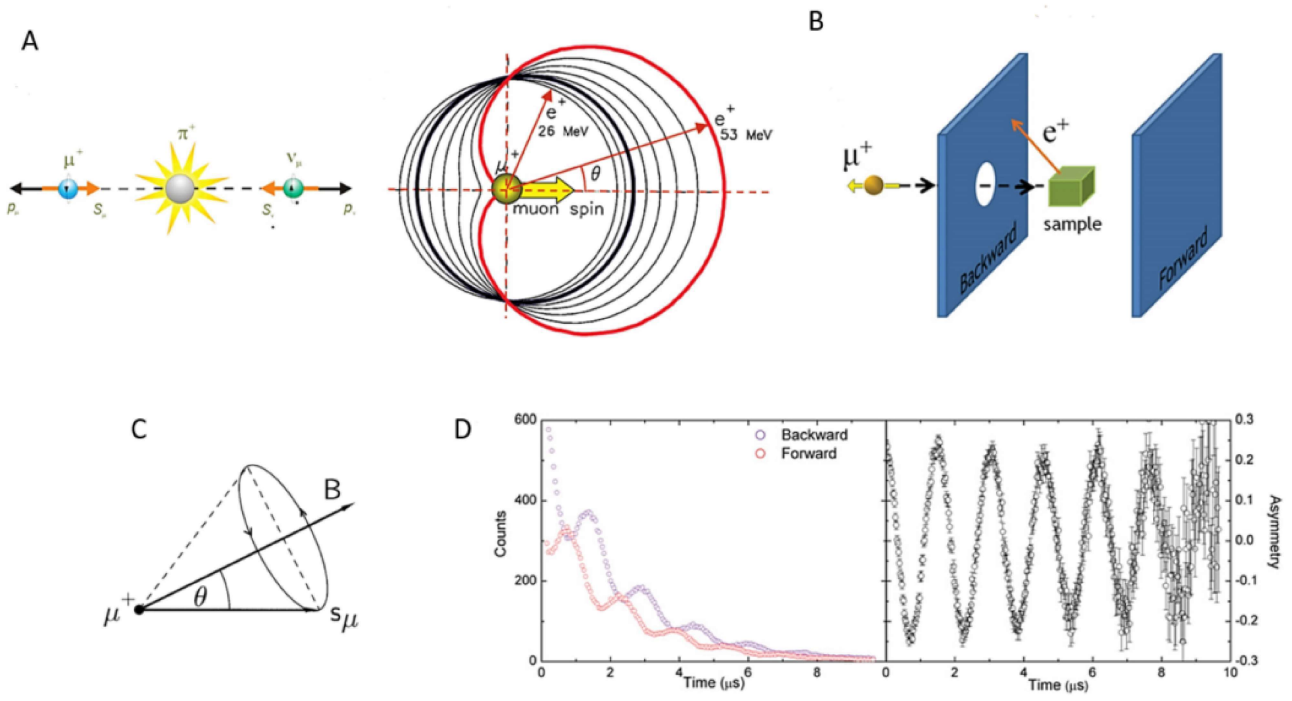

Figure 2.1: **A**The pion decay process gives a muon which in turn decays into a positron. The positron decay is asymmetric, as shown in the right. **B.** Geometrical arrangement of the instrument with respect to the incident beam and the two detectors. **C.** Larmor precession under the influence of an applied field or the sample's own field leads to an oscillatory signal that decays with time. The normalized difference of the detection rates between the detectors gives the polarisation of the muon spin as a function of time.**D.**. extracted from [28]

The simplified experimental setup of a μSR experiment is shown in Fig.2.1B. The incident muons pass through the cryostat walls and through Kapton foil windows to hit the sample. The Kaplan films are transparent to the muons and only slightly reduce their kinetic energy. Two groups of detectors surround the sample. These detector groups cover a large solid angle and are called forward and backward detectors in relation to the incident muon direction. The positrons emitted by the decayed muons are detected by scintillation, and the rate of detection is measured. The number of detected events can be expressed using the decay asymmetry and the probability of a muon decay at a time t:

$$N_\alpha(t) = N_0 \exp\{-t/\tau_\mu\}(1 + \alpha A \cos \omega t) \tag{2.5}$$

where, $N_{B,F}$ is the positron count rate of the backward or the forward detector. The final momentum of the emitted positron (see Eqn.2.4) is correlated to the muon spin direction, and the difference of the rate of detected events between the two groups of detectors is correlated to the longitudinal component of the muon spin. The initial direction of the muon spin can be traced back to an excellent approximation by recording the time histogram of

the number of decayed positrons in each of the detectors. By calculating the normalized difference between the forward and the backward detector, one obtains the principal physical quantity of interest, called the asymmetry of the emission of positrons, A(t):

$$A(t) = \frac{N_B - \alpha N_F}{N_B + \alpha N_F} \tag{2.6}$$

Here, α is an instrument parameter that is used to correct for the geometry and the detector efficiency. The observable A(t) then probes the muon polarization and its evolution indirectly with time.

Modes of measurement: Longitudinal and Transverse

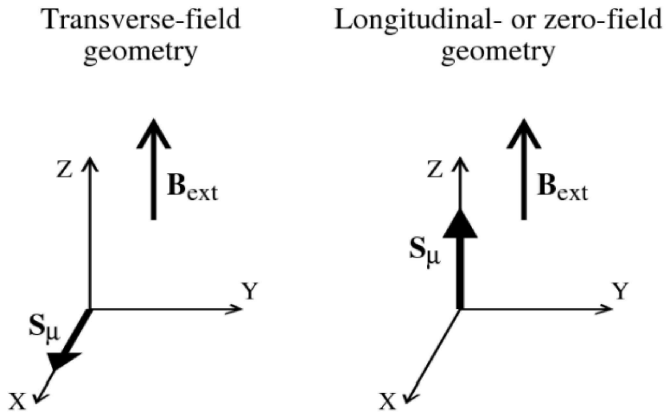

Figure 2.2: The two modes of measurement. Extracted from [23]

The instrument geometry discussed previously allows two different modes of measurement called the transverse mode and the longitudinal mode (see Fig.2.2). In the transverse field mode (TF), an external magnetic field is applied along the z direction of the muon polarization. In the presence of a perpendicular field, the muon spin starts to precess, resulting in an oscillating A(t) as a function of time. The TF measurement can be used to estimate α under the condition that no internal field develops in the sample. This is done by applying a very small field of around 20G and centering A(t) at A=0, by fitting the asymmetry to a damped oscillating function,

$$A(t) = G(t)\cos(\omega t + \phi) + B \tag{2.7}$$

where G(t) is usually a slowly decaying function, ω is the precession frequency, and B is the background. When a high external field is applied, a weak variation of α occurs, which should be considered during the analysis.

In the longitudinal field (LF) mode of measurement, the magnetic field is applied along the z component of the muon polarization axis; thus the LF does not cause the muon to precess as it is aligned with its spin. A sufficient

amount of LF will decouple the muon from the local microscopic field.

Additionally, since the muon is fully polarized, it is possible to do a zero external field study. In this mode, the muon is sensitive enough to interact with nuclear moments even if there is no magnetic order. This is an essential difference with an NMR experiment where a large magnetic field is necessary.

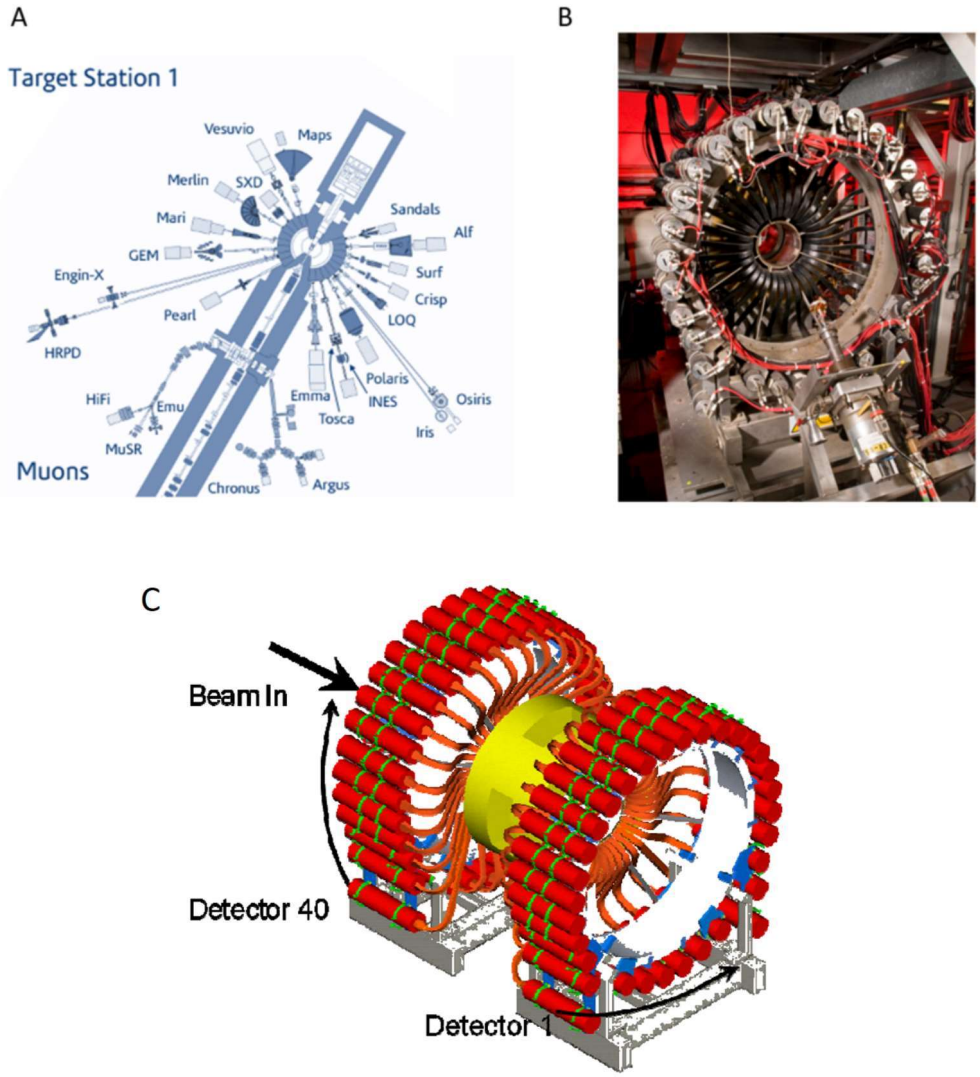

Figure 2.3: **A** Muon target station at ISIS, STFC (UK). Multiple instruments use the muons produced by the target station. **B.** The MUSR instrument **C.** Schematic representation of the detector banks and the incoming muon beam of the MUSR instruement at ISIS. Extracted from STFC website (MUSR manual).

Muon Interaction with local magnetic field

Muon spin relaxation is a highly sensitive experimental technique, as the muon particle is responsive to the local magnetic environment. The implanted muon with a moment, μ, and gyromagnetic ratio, γ_μ, interacts primarily by dipolar interaction with an electron with moment μ_e, orbital moment L, gyromagnetic ratio γ_e and at a position vector $\vec{r}$. The first-order magnetic interaction Hamiltonian [23] between the muon spin and the electron spin is then given

by:

$$H = \hbar\gamma_\mu \left[\frac{3(\vec{\mu}\cdot\vec{r})(\vec{\mu_e}\cdot\vec{r}) - (\vec{\mu}\cdot\vec{\mu_e})r^2}{r^5} \right] \tag{2.8}$$

The dipole-dipole interaction is the most significant term in our experiments. Under this approximation, the muon, once implanted in the sample, will experience the local field. In theory, the surrounding moments produce a discrete quantum field operator; however, we present here the more intuitive semiclassical approach in which the quantum field can be approximated by a classical continuous field vector . The time evolution of the muon spin $S_\mu(t)$, with the muon moment m_μ and under a field B_{loc} can then be expressed by the Larmor equation:

$$\frac{d\hbar S_\mu(t)}{dt} = m_\mu \times B_{loc}(t) \tag{2.9}$$

and the solution of this equation for the z component of S_μ(t) in the longitudinal direction is given by:

$$S^z_\mu(t) = S_\mu(\cos^2(\theta) + \sin^2(\theta)\cos(\omega_\mu t)) \tag{2.10}$$

This is the characteristic precession motion of the muon moments that is measured through A(t).

2.1.3 Static local magnetic field

First, we consider the situation where the material of interest has static moments distributed with no long-range order. Consider for example, the spin glass phase where the spins are frozen below a freezing temperature T_g. If the local dipolar field is distributed following a distribution $D_v(B_{loc})$, then the probability distribution of the z component of the muon polarization is given by:

$$P_z(t) = \langle S^z_\mu(t)\rangle = \int S^z_\mu(t) D_v(B_{loc}) d^3 B_{loc} \tag{2.11}$$

For isotropic Gaussian distributed static fields of magnitude B_{loc} and distribution width Δ, P_z(t) takes the form of the so-called Kubo-Toyabe function [29].

$$P_{KT}(t) = \frac{1}{3} + \frac{2}{3}(1 - \gamma^2_\mu \Delta^2_G t^2)\exp\big(-\frac{\gamma^2_\mu \Delta^2_G t^2}{2}\big) \tag{2.12}$$

When t is large the 2^{nd} term becomes negligible and we recover the 1/3 of the total asymmetry, which is referred to as the 1/3rd tail.

This relaxation is often observed in measurements in zero field mode, particularly in materials exhibiting a paramagnetic state at high temperatures. Indeed the spins are fluctuating; however, the probed nuclear spins always appear as static in the time window of the muon lifetime and are generally responsible for the observation of

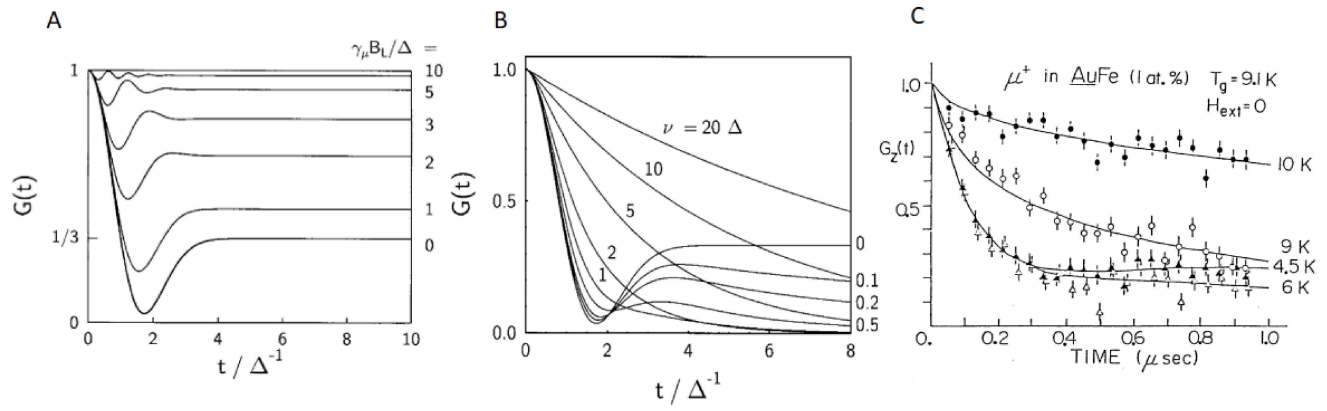

Figure 2.4: **A.** The decoupling from a static random internal field by an applied external field is explained well by the static Kubo-Toyabe model. We observe that as the external field is increased the 1/3rd tail starts to disappear and the initial characteristic dip flattens out into an oscillation.**B.** Evolution of the dynamic Kubo Toyabe function as the fluctuation is increased. In the limiting case when ν = 0, it corresponds to the static Kubo Toyabe function. In the fast fluctuation limit it takes the form of an exponential decay. The distinctive feature of this relaxation function is the 1/3rd tail first starts decreasing till the relaxation becomes exponential and increases beyond this point.**C.** Experimental example with AuFe where the spin relaxation and the dynamics are studied with temperature. Data and figure extracted from [29]

the Kubo-Toyabe relaxation, with very weak field distributions of the order of 1 G.

2.1.4 Probing spin dynamics

When the muon is implanted in the sample with a time-dependent internal field, it starts to couple with the corresponding frequency spectrum of this time dependency. If z is the quantized direction fixed by the instrument geometry, then the S_μ=1/2 spin of the muon will result in a 2-state system, where the polarization of the muon is either in +z or -z direction and is affected only by the torque exerted by the field transverse to this direction. By using the Fermi-Golden rule to calculate the transition rate, $\Gamma_{i\to f}$ between these two muon spin levels induced by the time-dependent local fields, one gets:

$$\Gamma_{i\to f} = \frac{1}{\hbar^2}\int_{-\infty}^{\infty} \langle f|\, H(0)\,|i\rangle\,\langle i|\, H(t)\,|f\rangle\, e^{-i\omega_0 t} dt \tag{2.13}$$

Where H is the magnetic Hamiltonian and $|i\rangle$ and $|f\rangle$ are the initial and the final state and $\omega_0 = (E_f - E_i)/\hbar$. In the context of this thesis, we will deal with fluctuations of the local field due to the electronic moments. It is practical to recast Eqn.2.13 in a form depicting the spin-spin correlation in time:

$$\lambda = 2\Gamma = \gamma^2 A^2 \int_{-\infty}^{\infty} \langle S^+(t) S^-(0)\rangle e^{-i\omega_0 t} dt \tag{2.14}$$

Intuitively, this means that λ measures the spin-spin autocorrelation function in time or the probability at time t of finding a spin in the flipped state given that it was observed at t=0 in a non-flipped state. By using the fluctuation dissipation theorem, one can then obtain

$$\lambda = \frac{\gamma^2}{\mu_B^2} \sum_q A^2 \frac{\chi_\perp''(q,\omega_0)}{\omega_0} \tag{2.15}$$

For muons, the energy difference between the two quantized states does not differ much in energy because ω_0 is very weak, of the order of a few μeV.

Dynamical Kubo Toyabe

In cases where the local field B_{loc} fluctuates with time, the situation can be described with a stochastic time variable B_{loc} instead of a static Gaussian distribution as in the static Kubo-Toyabe function. To study fluctuations of the local field at the muon site, one can use the strong collision approximation. This model assumes that the fluctuating field is not correlated in time and thus describes a Markovian process. Mathematically this situation is precisely analogous to the scenario where the muon, instead of stopping definitively, keeps on hopping from one site to another through a diffusive process and thus experiencing a different field after each hopping action. Thus the field B_{loc}(t) changes direction after a time δt, with a probability ν, where ν corresponds to the frequency of fluctuation of the system.

$$P_{DKT} = e^{-\nu t} P_{KT} + \nu e^{-\nu t} \int_0^t P_{KT}(t_1) P_{KT}(t - t_1) dt_1 + \nu^2 e^{-\nu t} \int_0^t \int_0^{t_2} P_{KT}(t_1) P_{KT}(t_2 - t_1) P_{KT}(t - t_2) dt_1 dt_2 + .. \tag{2.16}$$

In the zero fluctuation limit, that is the static case, we can verify that P_{DKT} has indeed the same expression as P_{KT}. As ν is increased, the 1/3rd tail starts to disappear as the relaxation becomes close to an exponential (see Fig.2.4)B. Then when ν = $\gamma_\mu \Delta$, the overall shape becomes similar to an exponential decay relaxation. In at the fast hopping/ fluctuation regime, the dynamical Kubo-Toyabe takes the exact form of an exponential decay. For a detailed discussion on dynamic Kubo Toyabe [30].

Stretched exponentials

When there are many relaxation sites in the sample, such as in spin glasses or disordered systems in general [31], the analysis is considerably simplified by using the phenomenological stretched exponential model. Consider the distribution,

$$A(t) = \int p(\lambda) \exp(-\lambda t) d\lambda$$

where, $p(\lambda)$ is the probability distribution for the random variable λ, then we can recast this into:

$$A(t) \approx A \exp(-\lambda t)^{\beta} \tag{2.17}$$

this is referred to as a stretched exponential and can be used to model the muon relaxation with time. However, it is hard to determine the number of different relaxation sites purely based on the value of β, as it is also correlated with λ when one models the measurements. More accurate estimation can be done by determining the muon stopping sites by density functional theory (DFT) simulations, however, these numerical simulations are complex computational problems, and we did not perform such simulations in our work.

Redfield Equation:

Using the LF mode, we can study the dependence of λ under an external field. To understand the field dependence, we first consider the correlation of the internal fluctuating field B_{loc} with time. We can estimate the internal field B's fluctuation by calculating the correlation in time as follows:

$$\langle \delta\vec{B}(0)\delta\vec{B}(t)\rangle \approx \frac{\Delta^2}{\gamma_\mu^2}\exp(-\nu t) \tag{2.18}$$

where, $\Delta^2 \approx \gamma_\mu \sqrt{\langle B_{loc}^2 \rangle}$, with B_{loc} being the local field.

The LF decouples the static moments, but it also influences the spin relaxation process in the presence of dynamics. In paramagnetic salts, for example, because there is a fluctuating random field, the autocorrelation function (Eqn.2.18) falls off exponentially with time. Then one can evaluate the Eqn.2.14 with the inclusion of an applied field to obtain the simplified Redfield equation:

$$\lambda = \frac{2\gamma_\mu^2 \Delta^2 \nu}{\nu^2 + \gamma_\mu^2 H_{LF}} \tag{2.19}$$

where, H_{LF} is the longitudinal field. The LF dependence has two critical applications in the context of this work. First, it will help us decouple the static contributions. Second, it indicates the nature of the internal response when an external field is applied. Studying the field dependence of λ will help us quantify the fluctuation rates and estimate the local field distribution.

Phonon-induced relaxation

In addition to relaxation induced by exchange interactions, spin relaxations can also be caused by lattice vibrations. CEF levels at energies much higher than the thermal energy can induce an additional relaxation that involves a coupling between phonons and a high-energy CEF level called the Orbach process [32, 23]. The Orbach equation

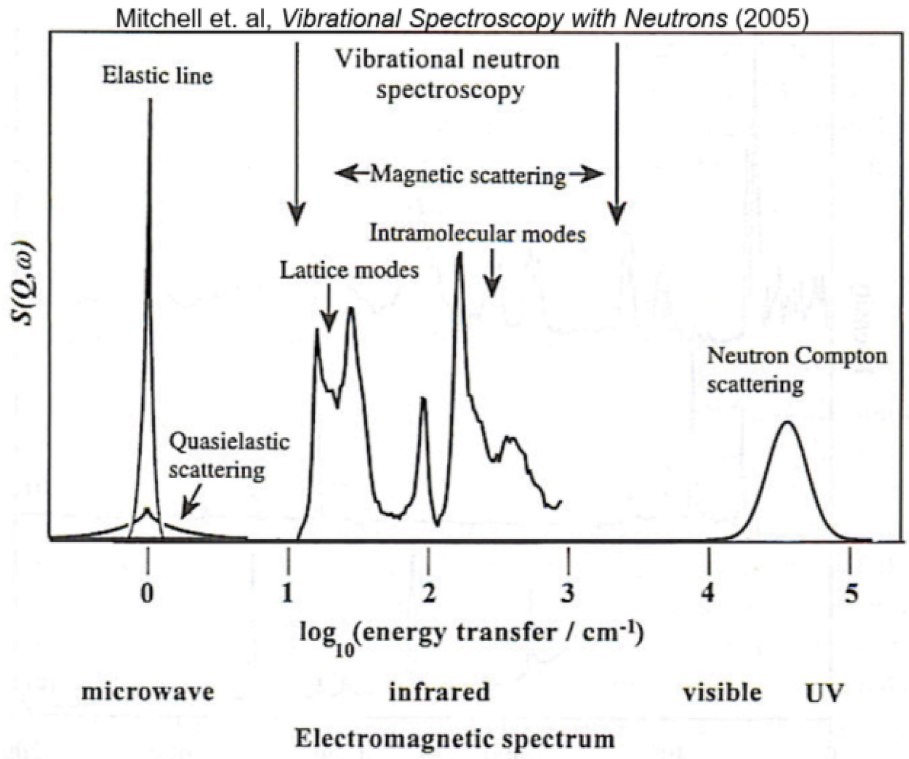

Figure 2.5: Energy transfer of INS and corresponding excitations. In the current work we focus on quasielastic scattering, lattice modes and magnetic scattering.

is given by:

$$\lambda = \frac{1}{A \exp^{-\frac{\Delta}{k_B T}} + B} \tag{2.20}$$

Where Δ is the energy of the CEF level, A a constant magneto-elastic coupling and B is the low T value of $1/\lambda$ and it reflects the characteristic spin-spin correlation time. The muon is sensitive to this abrupt change in spin fluctuation with a rise in temperature, and one can estimate the lowest-lying CEF levels using this process.

When the sample is at sufficiently high temperature, the S_{eff}=1/2 model is not valid as several CEF levels can be occupied. However, as the temperature is lowered below the first excited CEF level, the Orbach process leads to a decrease of fluctuations, increasing λ over a temperature range until the system is essentially a 2-state system.

2.2 Neutron Spectroscopy

The neutron is a neutral subatomic particle of mass m = 1.625×10^{-27} kg, spin s=1/2 and a long lifetime of 15 mins outside the nucleus. In 1932, James Chadwick discovered the neutron, preceeding slightly the discovery of nuclear fission and sparkling off an era of discoveries in science and technology. More recently, neutron science has allowed research on the SARS-CoV-2 virus [33]. Being uncharged, the neutron can avoid interacting with electrons, and they

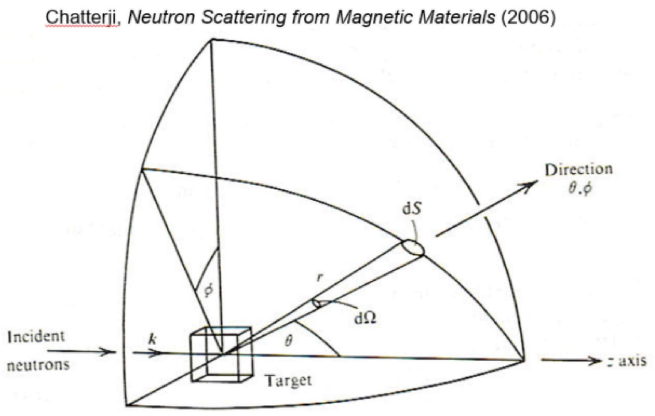

Figure 2.6: Schematic representation of neutron cross section

penetrate deeply into the bulk of the sample, unlike x-rays. Additionally, the neutron spin s=1/2 makes it scatter from magnetic structures or magnetic field gradients. This property of the neutron is intensively used to investigate the nature of the magnetic order and magnetic excitations. Modern day neutrons are made in large-scale facilities that are either nuclear reactors (fission source) or spallation sources.

In this chapter we discuss the basic principles of a thermal neutron scattering experiment and why it is useful in the context of studies in quantum magnetism.

2.2.1 Neutron: an invaluable probe of magnetism

Thermal neutrons have a wavelength similar to inter-atomic distances, around 0.5Å to 30Å and an energy typically less than 200meV. Using thermal neutrons, we can extract information on the atomic structure and the microscopic properties of solids by measuring atomic positions and crystal symmetry, and dispersion relations (energy-wavelength dependence) of excitations. Furthermore, it is often possible to compare the theoretical predictions directly to the experimental neutron scattering intensity, making this an invaluable probe to test different physical models in condensed matter physics.

Neutron cross section

In a neutron scattering experiment, one typically measures the rate of scattered neutrons per second into a solid angle $\delta\Omega$ with energy transfer between E and E$\pm\delta$E. This is defined by the partial differential neutron cross section ($\frac{\delta^2\sigma}{\delta\Omega\delta E}$) and is given by the expression :

$$\left(\frac{\delta^2\sigma}{\delta\omega\delta E}\right)_{k_i\to k_f} = \frac{1}{N}\frac{k_f}{k_i}\left(\frac{m}{2\pi\hbar^2}\right)^2 \sum p_i p_f \sum |\langle k_f| V |k_i\rangle|^2 \delta(E + E_i - E_f) \tag{2.21}$$

Where σ is the total cross-section, $k_{i/f}$ are the initial and final momentum wavevectors, $p_{i/f}$ are the probability that the neutron is in the state i or f and V is the interaction term. This equation defines the dynamical structure factor S(Q,ω), a principal quantity of interest in inelastic neutron scattering. The Eqn.2.21, can be recasted in terms of S(Q,ω) and the scattering length b:

$$\left(\frac{\delta^2\sigma}{\delta\omega\delta E}\right)_{k_i\to k_f} = N\frac{k_f}{k_i}b^2 S(Q,\omega) \tag{2.22}$$

2.2.2 Magnetic neutron scattering

In the case of magnetic scattering by magnetic moment of the electrons, the interaction $\hat{V}$ relates to the neutron's interaction with the electron's spin and orbital magnetic moment. From theory, the Fourier transform of the magnetization density $\vec{m}_Q$ of an individual atom can be written as the sum of orbital and spin components:

$$\vec{m}(Q) = \vec{m}_s(Q) + \vec{m}_l(Q) \tag{2.23}$$

where both the spin (m_s) and the orbital (m_l) contributions from the individual electrons in the atom are taken into account. Considering the crystal, one has to sum up these moments to obtain the total magnetization $\vec{M}(\vec{Q})$ where $\vec{Q}$ is the reciprocal lattice vector:

$$\vec{M}_Q = \int e^{-i\vec{Q}\cdot r}\sum_j \vec{m}_j(\vec{r}+\vec{R}_j)d^3\vec{r} \tag{2.24}$$

where j is the j^{th} position in the lattice and $\vec{M}_Q$ is also refereed to as the magnetic form factor.

Adding the magnetic contributions from all atoms in the crystal and averaging over the neutron spin polarization (in case of unpolarised neutron scattering), Eqn.2.21 can be recast as:

$$\left(\frac{\delta^2\sigma}{\delta\omega\delta E}\right)_{k_i\to k_f} = N\frac{k_f}{k_i}r_m^2\sum_{\alpha,\beta}\left(\delta_{\alpha\beta}-\frac{Q_\alpha Q_\beta}{Q^2}\right)\frac{1}{2\mu_B^2}S^{\alpha,\beta}(Q,\omega) \tag{2.25}$$

Where, α,β = x, y, z components and r_m = -2$\mu_B\mu_n$(2$m_n/\hbar^2$) = 5.391$\times10^{-13}$cm is the magnetic characteristic length of neutrons. S(Q,ω) is the magnetic dynamical structure factor given by:

$$S^{\alpha,\beta}(Q,\omega) = \frac{1}{2\pi\hbar}\int_{-\infty}^{\infty} e^{-i\omega t}\langle M_Q^\alpha M_{-Q}^\beta(t)\rangle dt \tag{2.26}$$

In the case of unpolarized neutron scattering, the average of the $S^{\alpha,\beta}$(Q,ω) components, S(Q,ω), is experimentally measured and probes the time and space-dependent correlations of the magnetic moments in the sample.

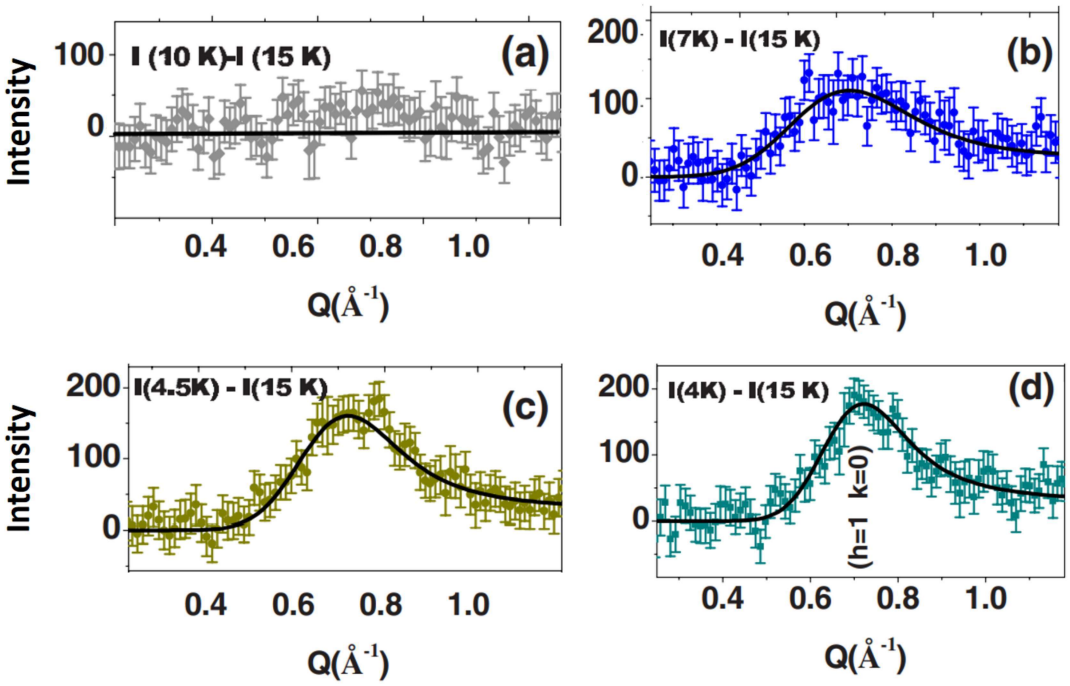

Figure 2.7: The evolution of an asymmetric peak in temperature that is modeled with a Warren lineshape for $Zn_2VO(PO4)_2$. Extracted from Yusuf et al. [34]

2D correlations

B. Warren [35] discovered that heat-treated carbon blacks are made up of discrete graphite layers that are stacked parallel to one another at about the typical graphite spacing, but that translation parallel to the layer and rotation about the normal are random. There are two types of reflections in the powder pattern of such material: crystalline type reflections and diffuse two-dimensional lattice reflections. Warren formulated the general equations for two-dimensional reflection-induced x-ray powder patterns, now known as Warren lineshapes.

For example, 2D magnetic correlations are observed in $Zn_2VO(PO_4)_2$, a 2D square lattice system with a layered structure, where the effective inter-plane magnetic exchange coupling along the vertical axis is very weak compared to intra-plane interaction. Magnetic correlations are viewed as asymmetric lineshapes in the elastic spectrum of neutron scattering experiment, and can be well explained using Warren lineshapes. These lineshapes are given by the equation,

$$W_{hk}(2\theta) = C\sqrt{\frac{\xi_{2D}}{\lambda\sqrt{\pi}}} j_{hk}|F_{hk}|^2 \frac{1+\cos^2(\theta)}{2\sqrt{\sin(\theta)}} F(a) \tag{2.27}$$

where, C is a scale factor, ξ_{2D} is the 2D spin-spin correlation length within the 2D layer, λ is the wavelength of the incident neutrons, j_{hk} is the multiplicity of the 2D reflection with 2D magnetic structure factor F_{hk}, and 2θ is the scattering angle. F(a) is given by,

$$F(a) = \int_0^\infty \exp\left(-(x^2 - a)^2\right) dx \tag{2.28}$$

here, a = $2\xi_{2D}\sqrt{\pi}/\lambda(\sin(\theta) - \sin(\theta_{2DB}))$, where θ_{2DB} is the Bragg's angle for the 2D reflection considered. In the present work we shall use the notation $W(Q; C, \xi_{2D})$ to indicate a Warren lineshape, with Q being the reciprocal wave-vector.

With the theoretical framework in place, we differentiate the key types of neutron scattering based on the physical phenomena that they measure:

- **Elastic scattering:** Elastic scattering describes a process in which the total kinetic energy of the system (neutron + sample) is conserved. In this process, k_f = k_i and so ω=0 in S(q,ω). S(q,0) is thus the Fourier transform of the pair correlation function, that describes the probability of finding a particle at a position $\vec{r}$ at a given time, taken at zero energy. The elastic part of the spectrum, therefore, reveals the crystal structure. If the sample has static magnetism, the magnetic form factor is a time-independent constant. Then the signature of static magnetism is observed in the form of magnetic Bragg peaks in the elastic spectrum of the neutron scattering.

- **Inelastic Scattering:** This is the case where the incoming neutron can lose energy by exciting the sample and in general $k_f \neq k_i$. The S(Q,ω) then is the Fourier transform of the two particle pair correlation function both in space and time. This mode of measurement allows the neutron to be sensitive to non-magnetic excitations such as phonons. If the scattering is due to the magnetic interactions of the neutron and electronic moments, the fluctuating magnetic state can be written as a time-dependent variation around a static equilibrium (which the elastic line will measure). In such cases, inelastic neutron scattering is an excellent probe to investigate magnetic excitations such as magnons and spin waves, spinons and other exotic excitations, and crystal field excitations.

- **Quasielastic scattering:** This is the limiting case of the inelastic scattering, where the S(Q,ω) is centered at $\omega = 0$. The quasielastic spectrum probes the fluctuations around the static equilibrium position corresponding to the elastic line, resulting in the apparent broadening of the elastic line and is essential to describe the spin dynamics.

2.2.3 Time of flight neutron spectroscopy

In 1935, only three years after the discovery of the neutron, the neutron time-of-flight (TOF) technique was developed. This technique has the advantage of directly probing the neutron scattering spectrum's inelastic, quasielastic, and elastic components at the same time. With recent developments in TOF instrumentation, it is possible to probe

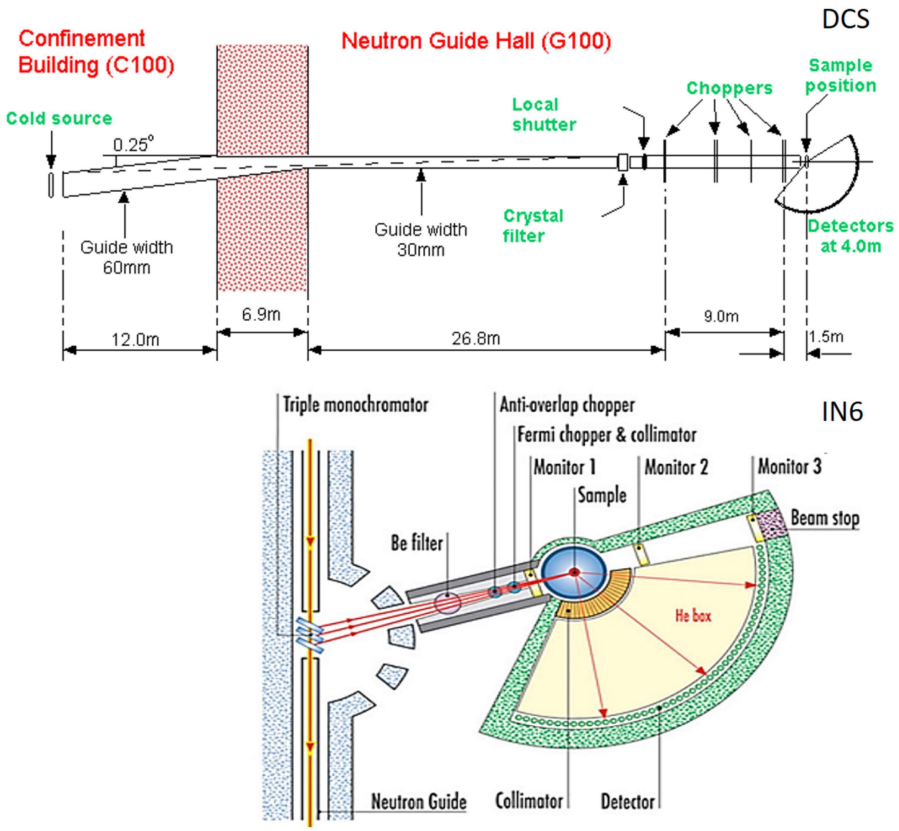

Figure 2.8: Schematic representation of the instrument geometry of the DCS and the IN6 TOF instruments.

a large region in the (Q, ω) space with a single measurement. Moreover, it is even possible to probe using multiple incident energies without compromising on the incident flux in some setups (for example, MERLIN at ISIS, STFC).

A TOF neutron spectrometer has four main components: a neutron source, a setup that filters the neutrons by energy E_i and momentum $\vec{k}_i$, the sample environment and detector banks to measure the final energy E_f and momentum $\vec{k}_f$. In the following section, we describe two different ways neutrons can be produced, and later we discuss how a TOF instrument geometry allows us to measure the scattering cross-section.

2.2.4 Neutron Production

Principle of TOF spectroscopy:

The physical quantity measured in a TOF experiment is the intensities I(ϕ,t), where ϕ is the scattering angle and t is the time, with detectors located at the different scattering angles having time channels centered at times t_j = 1,2,. .n, relative to an appropriate start time t_0. It can be shown that the measured time-resolved intensity function I(ϕ, t) can be recast to the partial differential cross section $(\frac{\delta^2\sigma}{\delta\omega\delta E})_{k_i \to k_f}$ by transforming it from the time domain to the energy/frequency domain.

To measure this intensity, let's consider t_{CD}, the total time a neutron of a given $\vec{k}_i$ takes starting from a chopper

C at time t_0 to arrive at the detector D at scattering angle ϕ:

$$t_{CD} = t_{CS} + t_{SD} = \frac{L_{CS}}{v_i} + \frac{L_{CD}}{v_f} \tag{2.29}$$

Where, t_{CS} is the time the neutron takes to travel with a speed $|\vec{v}_i|$ between the chopper and the sample and t_{SD} is the time it takes between the sample and the detector with speed $|\vec{v}_f|$. Thus from the experimental setup, if E_i, k_i, ϕ, and t_0 is known so the final scattering vector $\vec{k}_f$ and the final neutron energy E_f can be calculated.

In this setup, neutrons from the reactor either strike a monochromator (IN6) which is oriented at angle θ_M to the initial beam direction and which, by the principle of Bragg's reflection the monochromator filters the neutrons of energy E_i and k_i into the guide, or they pass through a monochromator chopper (DCS). In order to create a pulsed incident beam that gives a well-resolved intensity spectrum in the time domain, there are in general, four types of choppers used according to the role that they play (see Fig.2.8A.):

- Monochromator: This chopper can replace a monochromatic crystal and filter neutrons of a given energy. Usually, these are made of counter-rotating pair of disks (for example on the DCS instrument) where the relative phase only permits neutrons of a given velocity or kinetic energy to pass through.
- Pulse chopper: This chopper breaks down the continuous flux into well defined pulses.
- Order remover : The neutrons while traveling between the choppers can have a time of travel that is an integer number of chopper periods longer or shorter than the desired time of travel. To prevent this from happening, order removal choppers are used.
- Frame overlap: If the scattered pulses are very close in time, then the resulting scattered pulses arriving at the detectors can get overlapped in time, for example, a high velocity scattered neutron from a later pulse arrives at the same time as a slow scattered neutron from an earlier pulse. To prevent this, a frame overlap chopper is used that spreads out the pulse to prevent overlaps.

Detector Geometry

In time-of-flight experiments, the detector trajectory or the (Q, ω) region explored, as a function of the energy transfer and value of Q is a key quantity to evaluate beforehand as it determines the range of energy transfer and Q-space to be probed. The detector trajectory is a consequence of the principle of energy and momentum conservation for the neutrons. This kinematic constraint can be tuned depending on the instrument and the experiment by changing the incident energy E_i and the chopper frequencies or their relative phases. In these experiments it is important to keep in mind the relation, imposed by energy and momentum conservation:

$$\frac{\hbar^2 Q^2}{2m_n} = 2E_i - E - 2\sqrt{E_i E}\cos(\phi) \tag{2.30}$$

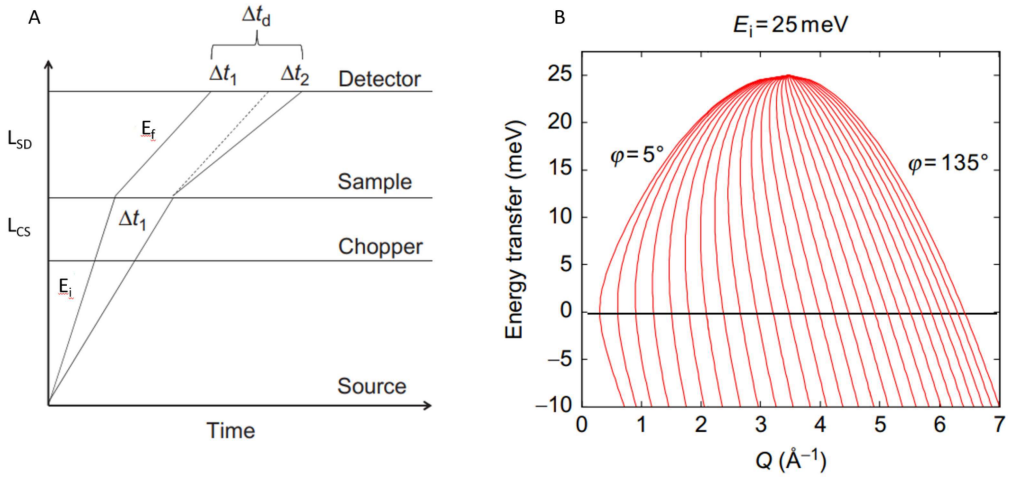

Figure 2.9: **A.**Neutron world lines in space time diagram of the experimental setup. Δt_d is the time resolution of the instrument. **B.** Example of the detector trajectory projected in energy-transfer and Q space where the scattering angle probes is between ϕ = 5° and 135° due to the kinematic constraint. Extracted from Arai [36]

where, E_i is the incident energy, E is the energy transfer, and ϕ is the angle between the initial and the final momentum of the neutron. On plotting the locus obtained by Eqn.2.30, we obtain the schematic slice as shown in Fig.2.9B.

In the case of single crystal experiments, the crystal is aligned in the plane of interest. Depending on instrument geometry, it can then be rotated around an axis to probe the reciprocal space.

In this work, we have also used polarised neutron diffraction to study diffuse scattering close to zero-energy transfer. A large part of the basic scattering principles remain the same, and additional details can be found in the book by Squires [24].

2.3 Rare-earth magnetism and crystal field effects

In rare-earth magnets [37] the single-ion physics strongly dominates over the two-ion interactions. This implies a clear hierarchy of energy scales, with spin-orbit coupling dominating over Coulomb interactions, which itself dominates over the effects of the crystalline environment. Thus we have to carefully consider the 3 different terms of the Hamiltonian that can be written as:

$$H = H_{spin} + H_{SO} + H_{CEF} \tag{2.31}$$

Where, H is the total Hamiltonian. H_{SO} is the spin orbit coupling term and H_{CEF} is the crystal field Hamiltonian, both of which we discuss in this Chapter. In terms of energy scales, H_{CEF} is in the order of 100K depending on the material, H_{spin} = 1K and H_{SO} = 10^3K.

2.3.1 Magnetism of rare-earth atoms

The microscopic aspects of magnetism for rare earth elements are not as straightforward as lighter elements of the periodic table. There are essential higher-order terms that come into play, giving a richer physics to realize exotic states of matter.

The electrons of an atom, in their frame of reference experience a magnetic field as it rotates around the nucleus. In the reference frame of the electron, the electrostatic field of the nucleus is transformed into an electromagnetic field. In rare-earth elements where Z, the atomic number is large, this relativistic correction that scales linearly with Z^4, has to be considered as a first-order perturbation correction and is referred to as the intrinsic spin-orbit coupling. In rare-earth ions, the presence of a strong spin-orbit effect implies that the spin $\hat{S}$ of the electron couples to the orbital angular momentum $\hat{L}$ and the interaction term is given by $H_{SO} = \lambda\vec{L}\cdot\vec{S}$, where λ is the coupling strength. In quantum mechanical terms, L and S are not separately conserved, but the total angular momentum $\hat{J}$ is conserved and is a good quantum number. Thus, states with $\hat{L}$ and $\hat{S}$, split $\hat{J}$ and remove the degeneracy in energy, resulting in a number of levels known as the fine structure with a difference in energy given by

$$E(J) - E(J-1) = \lambda J \tag{2.32}$$

From this spectrum, one can then directly estimate the spin-orbit coupling strength.

If one wants to estimate the magnetic moment operator, then the electronic states have to be projected into the J-manifold to get the good magnetic quantum numbers that commute with the Hamiltonian.

$$\mu\hat{J} = \mu_B(\hat{L} + \hat{S}) \equiv g_J\mu_B\hat{J} \tag{2.33}$$

where, g_J is the lande-g factor in the J manifold. Using the relationship between $\hat{L}$, $\hat{S}$ and $\hat{J}$, g_J can be expressed as:

$$g_J = \frac{3}{2} + \frac{S(S+1) - L(L+1)}{2J(J+1)} \tag{2.34}$$

2.3.2 Crystal electrical field and Steven's Operator Equivalent formalism

In order to understand the effects of the local charge environment due to the surrounding atoms, their electrostatic effects and spatial positions with respect to the rare-earth ion have to be considered. However, this takes a rather complicated form on a Cartesian basis. To rewrite the electrostatic potential as an operator acting on the electronic states, Steven [38] developed the operator equivalent formalism. To do this, let us observe that the electrostatic potential at a position $\vec{r}$ can be written as a sum over the surrounding charges :

$$V(r,\theta,\phi) = \sum_i \frac{q_i}{|\vec{r} - \vec{R_i}|} \tag{2.35}$$

Where the sum runs over all the neighboring ions at position $\vec{R_i}$ with charge q_i. After some algebra this expression can be recast into a workable form by using tesseral harmonics Z as the basis of the multinomial expansion of $\frac{1}{|\vec{r}-\vec{R_i}|}$ term. This takes the following form :

$$V(r,\theta,\phi) = \sum_i q_i \sum_n \frac{r^n}{R_i^{n+1}} \frac{4\pi}{2n+1} \sum_{m=-n}^{n} Z_{n,m}(\theta,\phi) Z_{n,m}(\Theta,\Phi) \tag{2.36}$$

where, Θ, Φ are the angular coordinates of the R_i^{th} ion. Recasting the equation in this way has the advantage of separating into products the source terms or the local charge distribution from the rare-earth ion coordinates. The grouped coefficients arising from the distribution of charges at R_i can then be written in terms of a parameter A_n^m and the equation takes the simplified form:

$$V(r,\theta,\phi) = \sum_{n=0}^{\infty} \sum_{m=-n}^{n} A_m^n r_i^n Z_{n,m}(\theta,\phi) \tag{2.37}$$

This largely simplifies for f orbitals where n$\leq$6, due to specific properties of the tesseral harmonics. Furthermore, the point group symmetry of the rare earth ion puts a constraint allowing only a specific number of nonzero coefficients A_n^m. Knowing the symmetry of the environment of the rare-earth ion, we can calculate individual expressions of V, the potential, in Cartesian coordinates. The Hamiltonian of the crystal field interaction can therefore be represented:

$$H_{CEF} = -e \sum_i V(x,y,z) = -e \sum A_n^m V_n^m(x_i,y_i,z_i) \tag{2.38}$$

However, this Hamiltonian is in a Cartesian basis, by using Wigner's theory, the basis vectors in Cartesian coordinate can be represented by a transformation into the J-manifold and it can be shown that the Hamiltonian takes the following form :

$$H_{CEF} = \sum_{m,n} A_n^m \Theta_n(J) < r^n > A_n^m \hat{O}_n^m(J, J_z, J_\pm) = \sum_{m,n} B_n^m \hat{O}_n^m(J, J_z, J_\pm) \tag{2.39}$$

Where, Θ is a prefactor proportional to $\hat{J}$ that arises due to the Wigner transformation, $< r^n >$ are the average values of the nth power distance between the nucleus position and the f shell (for rare-earth ions), B_n^m are Steven's operator coefficients and $\hat{O}_n^m$ are Steven's operators in the J-manifold. We recall here that most of Steven's operator coefficients will be 0 due to symmetry considerations. In the context of this thesis, we investigate compounds in which the rare earth ion sits in a D_{3d} environment. In such a situation, the corresponding Hamiltonian with the non-zero coefficients is given by:

$$H_{CEF} = B_2^0 O_2^0 + B_4^0 O_4^0 + B_6^0 O_6^0 + B_6^3 O_6^3 + B_4^3 O_4^3 + B_6^6 O_6^6 \tag{2.40}$$

where the relevant O_n^m operators projected in the $|m_J\rangle$ basis are written as follows:

$$\begin{aligned}
O_2^0 &= 3J_z^2 - J(J+1) \\
O_4^0 &= 35J_z^4 - 30J(J+1)J_z^2 + 25J_z^2 - 6J(J+1) + 3J^2(J+1)^2 \\
O_6^0 &= 231J_z^6 - 315J(J+1)J_z^4 + 735J_z^4 + 105J^2(J+1)^2 J_z^2 - 525J(J+1)J_z^2 \\
&\quad + 294J_z^2 - 5J^3(J+1)^3 + 40J^2(J+1)^2 - 60J(J+1) \\
O_6^3 &= \frac{1}{4}(11J_z^3 - 3J(J+1)J_z - 59J_z)(J_+^3 + J_-^3) \\
&\quad + (J_+^3 + J_-^3)(11J_z^3 - 3J(J+1)J_z - 59J_z) \\
O_4^3 &= \frac{1}{4}(J_z(J_+^3 + J_-^3) + (J_+^3 + J_-^3)J_z) \\
O_6^6 &= \frac{1}{2}(J_+^6 + J_-^6)
\end{aligned} \tag{2.41}$$

The effect of the CEF is to split the (2J+1) levels. Additionally, the CEF Hamiltonian has a time-reversal symmetry, and its eigenvectors follow Kramer's rule. That is, every eigenstate has a corresponding time-reversed degenerate eigenstate resulting in doubly degenerate energy levels in the case of rare-earth ions with a half-filled electronic shell.. Furthermore, at sufficiently low temperatures, typically below 50K, only the CEF ground state doublet will be occupied; this is the $S_{eff} = 1/2$ picture as the quantum state space is now a 2-state system.

The combination of eigenstates leads to a g-tensor that can be characterized by its perpendicular and parallel components when it is represented in the diagonal form. Hence the single ion anisotropy can be determined, which in extreme cases will either have an easy axis (Ising) or an easy plane (XY). In the intermediate situation when the parallel and perpendicular components are equivalent one obtains an isotropic (Heisenberg) nature of the moments. The single-ion anisotropy is of crucial importance as it determines the symmetry of the exchange Hamiltonian, H_{spin}, and the CEF analysis is one of the most direct experimental ways to estimate the g-tensor of the S_{eff} = 1/2 model.

2.3.3 Determination of CEF parameters from inelastic neutron scattering measurements

The parameters of the CEF Hamiltonian can be directly estimated from the partial differential cross-section obtained from INS measurements. The function S(Q,ω) gives the positions and the relative intensity of the transition between CEF levels. At constant temperature T and wave vector $|Q|$, the scattered intensity due to transitions between different CEF levels can be written as :

$$S(|Q|,\omega) = \sum_{i,i'} \frac{\sum_\alpha |\langle i| J_\alpha |i'\rangle|^2 e^{-\beta E_i}}{\sum_j e^{-\beta E_j}} L(\Delta E + \hbar\omega) \tag{2.42}$$

Where, α=x, y, z, ΔE is the difference between two CEF levels, $L(\Delta E+\hbar\omega) = L(E_i - E_{i'} + \hbar\omega)$ is a peak function, normally represented by a Lorentzian or a Gaussian. To fit the CEF peaks first, accurate identification of the CEF levels is needed. This is achieved by fitting the magnetic form factor $F(|Q|)$ with an E-integrated Q-cut centered around a CEF peak. Once the CEF peaks are identified, we fit them with a Gaussian function of constant width to estimate the energy and their relative intensities.

$$S(|Q|,\omega) = \sum_i G_i(\omega, \sigma_i) + B \tag{2.43}$$

Where i corresponds to the i^{th} peak position, G(ω, σ) is the corresponding Gaussian fitting function with σ as the width and B is a linear background.

To determine Steven's operator coefficients, we start with an initial guess of the parameters. By using Eqn:2.40, in the $|J, m_J\rangle$ basis, from this initial parameter set, we calculate the matrix elements to estimate the Hamiltonian H_{CEF} that is then represented as a matrix. H_{CEF} is then diagonalized to obtain the eigenvalues, which are the CEF energies, and the eigenvectors, which are the CEF wavefunctions. We then use the calculated wavefunctions to estimate S(Q,ω) at a particular temperature T to obtain the relative intensities of the CEF excitations. The calculated energies and their relative intensities can then be directly compared to the experimental values as obtained from the INS. For comparing the calculated values with the observed values, we define a convex error function as follow:

$$err(B_n^m) = \alpha \frac{\sum_i (E_i^{obs} - E_i^{calc})^2}{\sum (E_i^{obs})^2} + \beta \frac{\sum_i (I_i^{obs} - I_i^{calc})^2}{\sum (I_i^{obs})^2} + \gamma \frac{(m^{obs} - m^{calc})^2}{(m^{obs})^2} \tag{2.44}$$

where, E_i^{obs} is the experimental position in the energy of the i^{th} CEF with relative intensity I_i^{obs}. E_i^{calc} is the calculated CEF energy of the i^{th} peak with the calculated relative intensity I_i^{calc}. m_i^{obs} is the measured magnetic saturation value, and m_i^{calc} is estimated from the GS wave vector.

As the error in intensity, energy and magnetization are physically distinct measured quantities, they are normalized, but furthermore, the sensitivity of the error function can be dominated by any one of them. To equalize this sensitivity, I use an additional set of 3 constant parameters α, β, and γ that allow one to experiment with the error weights in the case when the fit algorithm does not converge.

For optimizing the convergence of this fit, one needs to use a two-phase method [39] that combines a global stepping algorithm with local minimization to prevent converging into a local minimum corresponding to an unrealistic physical scenario. This can be done best by using the Basin Hopping algorithm with the Powell minimization [40] algorithm.

From the error minimized GS doublet, one can then estimate the corresponding g-tensor numerically. Using the

following relationships, where $|\pm\rangle$ are the GS Kramer's doublets.

$$\begin{aligned} g_{\parallel} &= 2g_J \langle + | J_z | + \rangle \\ g_{\perp} &= g_J \langle + | J_+ | - \rangle \\ g_{avg} &= \sqrt{\frac{2}{3}g_{\perp}^2 + \frac{1}{3}g_{\parallel}^2} \\ m_{avg} &= 2g_{avg} \end{aligned} \tag{2.45}$$

The anisotropy of the S_{eff} = 1/2 spin is then determined by the ratio $g_{\perp}/g_{\parallel}$.

2.4 Magnetic Measurements

To characterize the magnetic behavior of a rare-earth magnet over a large temperature range, we perform magnetization and susceptibility measurements. In this section, we discuss the typical analysis that is applied several times in the following chapters.

For magnetic characterizations [30] a superconducting quantum interference device (SQUID) is used. This is a very sensitive magnetometer used to measure extremely tiny magnetic fields based on superconducting loops containing Josephson junctions. SQUID magnetometers can characterize all kinds of magnetic materials and allow us to determine quantitatively the magnetic phases and even impurity phases in some cases.

The SQUID magnetometer consists of superconducting circuits with a Josephson junction that can detect a change in flux if a magnet passes through. In the case of a DC SQUID, the change in voltage ΔV is directly proportional to the change in flux $\Delta\Phi$. This allows us to detect the volume magnetization in a sample that is moved through the coils of a SQUID. It is also possible to apply a static external field in a DC measurement. As the static field does not change the flux rate, it does not interfere with the magnetization measurements and only magnetizes the sample. In the DC mode, one can investigate the dependence of the magnetization on an external field or temperature from which one can extract the magnetic susceptibility.

To check for the emergence of order or sign of any transition in the sample, we use the zero-field cooled field cooled (ZFC-FC) protocol. In this method, the sample is cooled in the absence of an external field, and the susceptibility is measured when it is heated up under a small external magnetic field. Then it is cooled again, but this time under the external field, and the same measurement process is carried out. In the presence of a ferromagnetic component, a spin-glass phase, the ZFC-FC curve bifurcates at the ordering temperature. In this thesis, however, we mainly focused on paramagnetic behavior in the measured temperatures and fields. For paramagnetic compounds, the susceptibility measurement provides information on g_J (Single ion Lande-g factor), C, the Curie constant, θ_{CW} the Curie Weiss temperature.

Curie Weiss behavior

In the paramagnetic regime of an insulator, the Curie Weiss law is the appropriate model to describe the response of the sample to an external magnetic field. It assumes a mean field that is due to the interaction between the moments in the material and has a characteristic temperature θ_{CW} below which it should undergo a phase transition. $\theta_{CW} <$ 0 implies that the exchange is antiferromagnetic in nature and gives the law:

$$\chi_T = \frac{C}{T - \theta_{CW}} \tag{2.46}$$

For a crystal with N magnetic moments, with $\hat{J} = \hat{L} + \hat{S}$, the susceptibility takes the following form:

$$\chi_0 = \frac{N\mu_0\mu_B^2 g_J^2}{3k_B T} J(J+1) = \frac{N\mu_0\mu_{eff}^2}{3k_B T} \tag{2.47}$$

where g_J is the lande-g factor of the free ion in the low temperature regime and μ_{eff} is the effective moment.

Van-Vleck paramagnetism

The Curie Weiss approximation described a simplified first-order model, however in the case of rare earth magnets with S_{eff} = 1/2, higher-order effects need to be considered. This is because at very low temperatures compound is essentially a two state system with the GS doublet well separated from the higher energy CEF levels, but with the increase of temperature, the higher levels start to get populated, and to estimate the susceptibility correctly, it is found that we need to consider the second-order effects.

The energy difference can be calculated using 2^{nd} order perturbation theory and is given by:

$$\Delta E = \sum_n \frac{|\langle 0|\, \hat{J} \cdot \vec{B}\, |n\rangle|^2}{E_0 - E_n} \tag{2.48}$$

Where J = 1/2, in the low-temperature regime, and the sum is taken over all the excited levels. Thus from this we obtain the Van-Vleck susceptibility as:

$$\chi_V = 2\mu_B^2 \frac{N}{V} \sum_n \frac{|\langle 0|\, \hat{J}\, |n\rangle|^2}{E_n - E_0} \tag{2.49}$$

The Van-Vleck susceptibility turns out to be always positive as $E_n \geq E_0$ by definition.

However, the total temperature-independent susceptibility χ_0, has another component due to intrinsic diamagnetism. This is because an external field will induce an opposite polarisation on the electronic orbitals. The diamagnetic susceptibility, χ_D, is usually small and temperature-independent and can be roughly estimated for a compound by summing up the individual diamagnetic susceptibilities of its constituent ions. The diamagnetic term is quantita-

tively given as:

$$\chi_D = -\frac{Ne^2\mu_0}{6Vm_e}\sum_i^Z < r_i^2 > \tag{2.50}$$

Where $< r_i^2 >$ is the mean square radius of the ith electron in the constituent atom. The total temperature independent magnetic susceptibility, χ_0 is given by:

$$\chi_0 = \chi_D + \chi_V \tag{2.51}$$

The Brillouin function

The magnetization [30] can be expressed as the sum of the average magnetization density $\langle m_J \rangle$ per atom. This average magnetization density is calculable from the ensemble average using the partition function Z over (2J+1) states, and the relationship is given by:

$$< m_J >= \frac{\sum_{-J}^{J} m_J e^{m_J x}}{\sum_{-J}^{J} e^{m_J x}} = \frac{1}{Z}\frac{\delta Z}{\delta x} \tag{2.52}$$

with $x = \frac{g_J\mu_B B}{k_B T}$. This mean-field approach gives the net magnetization of the sample:

$$M = M_s B_J\left(\frac{g_J\mu_B JB}{k_B T}\right) = ng_J\mu_B JB_J\left(\frac{g_J\mu_B JB}{k_B T}\right) \tag{2.53}$$

Where M_s is the saturation value of magnetization and B_J is the Brillouin function:

$$B_J(y) = \frac{2J+1}{2J}\coth\frac{2J+1}{2J}y - \frac{1}{2J}\coth\frac{y}{2J} \tag{2.54}$$

For J=1/2 the Brillouin function simplifies to $B_J(y) = \tanh(y)$. Secondly, to take into account the interaction, we can replace T with (T-θ). Finally, for powder samples, we reformulate the magnetization as a function of ϕ, the angle the local z-direction of the crystal makes with the applied field. In this notation, $g_{\parallel}$ is the component of the g-tensor parallel c-axis, and $g_{\perp}$ is the perpendicular component. The polarisation P is given by $P^2 = g_{\perp}^2\sin^2(\phi) + g_{\parallel}^2\cos^2(\phi)$, and the Brillouin function with interaction θ for J=1/2 can be written as :

$$M(H,\phi) = \frac{1}{2}P\mu_B\tanh\frac{\Delta(H)}{2k_B(T-\theta)} \tag{2.55}$$

where, $\Delta(H) = \mu_B HP$. To estimate the powder average of M(H,θ), and to consider the temperature-independent susceptibility χ_0, we can rewrite the magnetization as:

$$M(H,\theta) = \frac{1}{2}\int_0^{\pi} M(H,\phi)\sin(\phi)d\phi + \chi_0 H \tag{2.56}$$

For modeling the experimental data with this function, one can use the g-tensors, interaction strength, and temperature-independent susceptibility as the fit parameters. However, to get an accurate estimation, a series of M(H) measurements in temperature need to be performed. We note here that from the powder averaged measurement we can obtain two sets of $g_{\perp}$ and $g_{\parallel}$ for a given value of m_{sat}. Thus, one needs to perform complementary experiments like INS to determine the CEF levels to accurately predict the anisotropy of the g-tensor.

Part II

$Re\mathbf{MgGaO}_4$: $\mathbf{S}_{eff} = 1/2$ anisotropic triangular antiferromagnets with chemical disorder

Chapter 3

$YbMgGaO_4$: a 2D quantum spin liquid candidate

In this section, we review the literature on the highly investigated S_{eff} = 1/2 triangular anisotropic Heisenberg antiferromagnet (THAF) $YbMgGaO_4$. $YbMgGaO_4$ has been known for decades [41] but was thought of as a simple paramagnet. Recently, its low-temperature magnetic properties were investigated, revealing the rich physics of this family of compounds. It has attracted much attention because unlike the majority of the QSL candidates, it was thought to be free from spin vacancies, and antisymmetric Dzyaloshinsky-Moriya anisotropy [42]. $YbMgGaO_4$ was proposed as the first structurally perfect rare-earth triangular antiferromagnet that crystallizes in the symmetric space group [41, 43] of $R\bar{3}m$ (see Fig.3.1). XRD measurements [41] have evaluated the Yb-Yb inter-ionic distance, a = b = 3.4 Å and the interlayer separation 8.4 Å with c = 25 Å. No direct exchange mechanism for interaction between the 2D layers are considered as a relatively large distance separates them and so the Yb-Yb planes form an isolated true 2D triangular plane with an excellent approximation. The rare-earth ion Yb^{3+} sits on the corner of the 2D triangular lattice and is surrounded by six O^{-2} anions, forming a YbO_6 octahedron with D_{3d} site symmetry. The non-magnetic Mg^{2+} and Ga^{3+} ions occupy the centers of the triangular bipyramids between the 2D triangular layers. However, these transition metal ions occupy the same crystallographic position giving rise to the possibility of exchange between Mg^{2+} and Ga^{3+} ions, a natural source of disorder.

3.1 Low temperature magnetic properties

Magnetic characterization reveals $YbMgGaO_4$ to be a simple paramagnet as the Curie-Weiss model explains its paramagnetic behavior to low temperatures (1.9K). Recent characterizations show neither noticeable splitting [42] between the ZFC-FC curves (see Sec.2.4), nor anomaly in the susceptibility down to 40 mK, indicating the absence

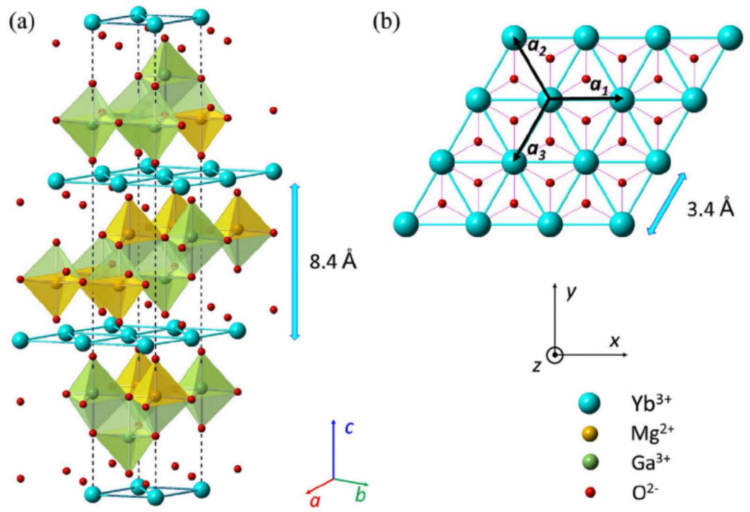

Figure 3.1: **(a)** Crystal structure of $YbMgGaO_4$ with the 8.4Å interlayer separation. **(b)** 2D triangular planes of Yb^{3+} ions [44].

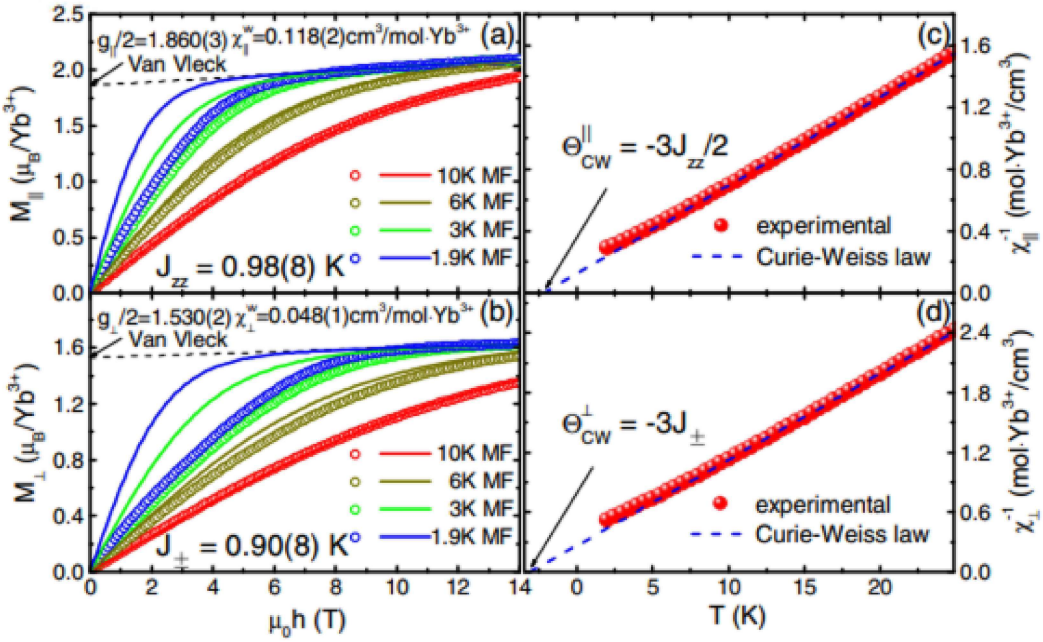

Figure 3.2: Magnetic characterization of $YbMgGaO_4$ single crystal [43]. **(a)** The magnetization of the $YbMgGaO_4$ single crystals measured at 10, 6, 3, and 1.9 K. The dashed lines are linear fits of the experimental results for fields above 12 T at 1.9 K to estimate the magnetic saturation value parallel or perpendicular to the sample. The solid curves are molecular field fits. (c),(d) The inverse susceptibilities fitted by the Curie-Weiss law between 1.9K and 25K, with $\theta_{CW}^{\parallel}$= -1.4(1)K and $\theta_{CW}^{\perp}$ = -2.7(2)K.

of long-range order. Susceptibility measurements [43] also estimate a negative Curie Weiss temperature ($\theta_{CW}^{\parallel}$= -1.4(1)K and $\theta_{CW}^{\perp}$ = -2.7(2)K) that corresponds to an antiferromagnetic interaction (see Fig.3.2). However, rare earth magnetism [45] is characterized by exchange interactions measuring up to a few Kelvins. In such a situation, the exchange interaction has a dominating effect only in the low-temperature regime. Interestingly, muon spin relaxation experiments [44, 46] confirms the lack of long range magnetic order to 22mK. Additionally, the Yb^{3+} ions have spin-

orbit interaction that is an order of magnitude larger than the CEF energy scale, and the local environment is thus crucial in selecting the ground state (see Sec.2.3.1). In $YbMgGaO_4$, CEF excitations are found [44] at 40meV, 61meV and 97meV (see Fig.3.3). The lowest-lying energy level at 40meV (460K) has a significant separation from the ground state doublet, which means that at low temperatures ($k_BT << \Delta$), only the ground state doublet is occupied, and, Yb^{3+} spins form a two-state system which is degenerate in the absence of an external field. The g-tensor anisotropy ($g_\perp/g_\parallel$) of the CEF ground state moments are estimated from M(H) measurements [42] to nearly isotropic with $g_\perp$ = 3.0(1) , $g_\parallel$ = 3.7(1), and CEF experiments [44] (see Sec.2.3.3) confirm such Heisenberg character of the Yb^{3+} moments at low temperatures.

3.2 Is $YbMgGaO_4$ a spin liquid or a spin glass?

Due to the weak nature of exchange interactions in rare-earth magnets, it has been found that structural disorders [44, 47] are often crucial to understand the low-temperature properties. XRD analysis [42] reveals that the Yb^{3+} ion is displaced from the mean position, along the c direction by about 0.1Å. The disorder effect is primarily due to the intrinsic Mg-Ga site mixing as Mg^{2+} and Ga^{3+} occupy the same crystallographic positions but have different charges. The intrinsic Mg-Ga site mixing thus causes a distortion of the local electrostatic field that causes the displacement of Yb^{3+} ions from the plane. This displacement from the ideal position of the Yb^{3+} moments then causes bond randomness. Indeed, INS experiments by Li et al. [44] found an anomalous broadening of CEF excitation, ascribed to such disorder. Numerical simulations taking into account the modified electrostatic neighborhood of the Yb^{3+} ions can reproduce the observed CEF broadening. The inter-site disorder effect also imposes randomness on the g-tensor of Yb^{3+} moments; however, the CEF energy scale remains with the same magnitude.

Another effect of disorder, in the case of $YbMgGaO_4$, is that the additional randomness can prevent a long-range ordered ground state. Such a situation can be due to a spin glass [50], where magnetic moments freeze into random orientations without long-range order and prevent significant fluctuations to any of the other degenerate spin configurations. To check for the emergence of any glassy behavior, Ma et al. [49] performed AC susceptibility measurement. At a frequency of 100 Hz, the real part of the susceptibility χ' shows a broad peak at T_f = 0.099(6) K (see Fig.3.5). The decrease of the peak height and the shift of the peak position to higher temperatures as the ac frequency is increased is consistent with a broad distribution of the spin relaxation times around the freezing temperature T_f, and is typical of a spin glass or slow spin relaxation [51]. However, the spin-glass phase is not consistent with the muon spin relaxation measurements [48] (see Fig.3.4) at low temperature, where no signature of freezing was observed till 48mK. A recent muon relaxation experiment by Ding et al. [46] confirms persistent spin dynamics till 22mK. The conflict is resolved if the ac susceptibility peaks are a consequence of the fluctuating spins in the QSL phase [52].

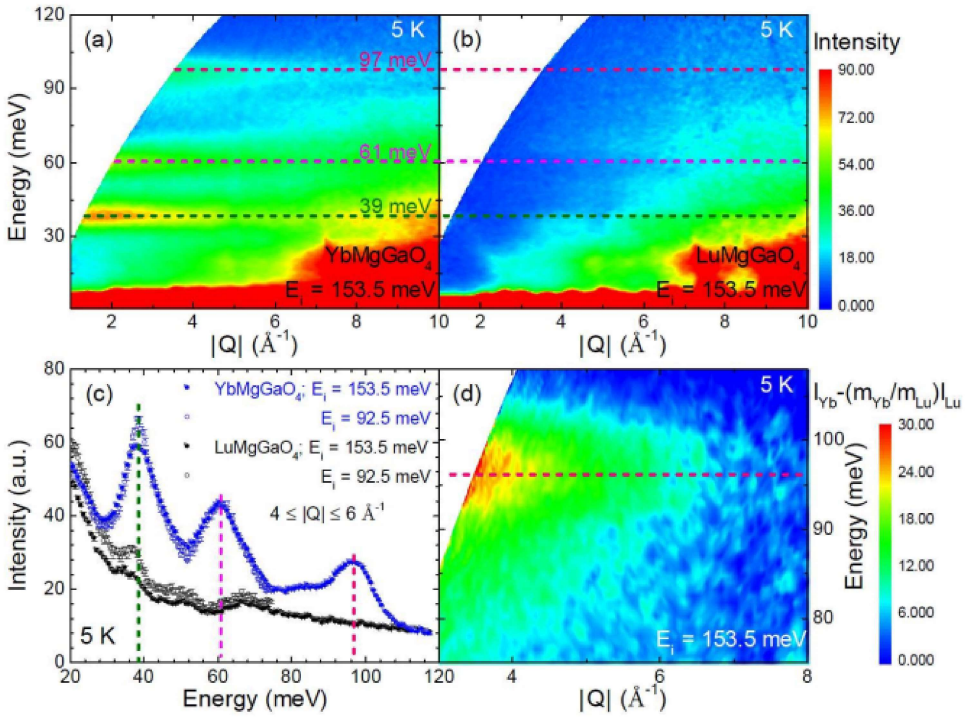

Figure 3.3: a) S(Q,ω) intensity plots for $YbMgGaO_4$ showing the CEF positions, b) Comparison with the non magnetic analog compound $LuMgGaO_4$. c) Q-integrated E cuts of $YbMgGaO_4$ and $LuMgGaO_4$. d) Zoomed S(Q,ω) at 90meV. Extracted from [44]

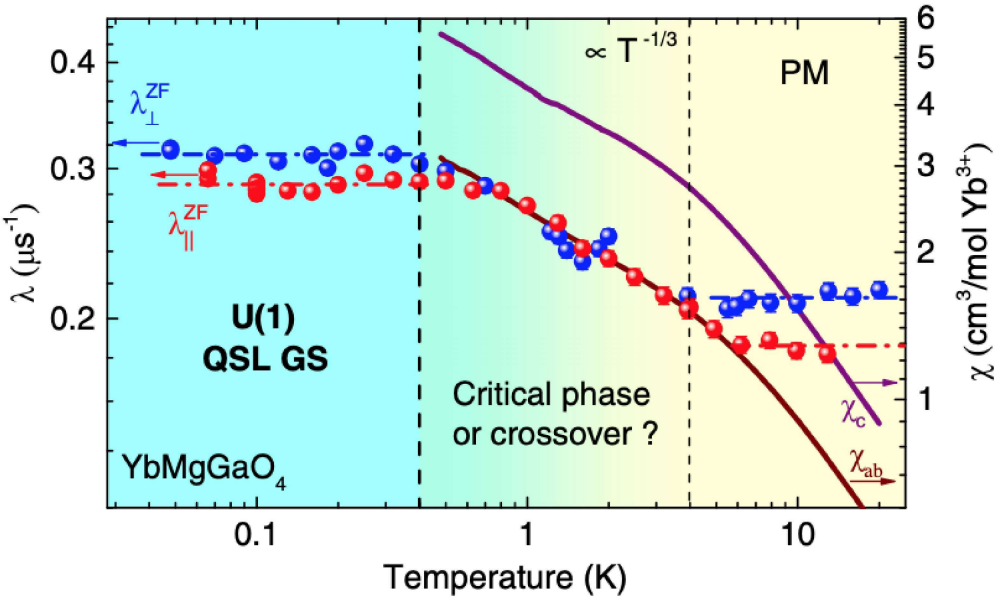

Figure 3.4: Temperature dependence of the muon spin relaxation rates from the zero field measurements represented by red and blue circles. The bulk static susceptibilities measured in the applied field of 0.01 T is represented by solid lines. PM represents the paramagnetic phase. The μsr and the susceptibility measurements are both performed in directions parallel and perpendicular to the c-axis. Extracted from [48]

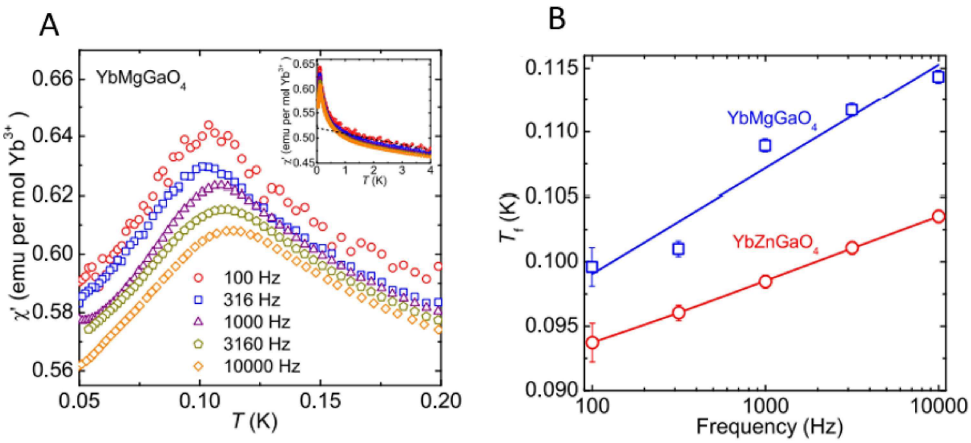

Figure 3.5: **A.** AC susceptibility measurement of $YbMgGaO_4$ **B.** Comparison of frequency dependence of the freezing temperature for both $YbZnGaO_4$ and $YbMgGaO_4$, extracted from Ma et al.[49]

3.3 Experimental detection of the dynamic phase

This section focuses on the INS experimental literature to identify the critical properties of the dynamical ground state and the microscopic cause of its origin. INS experiment on single-crystal $YbMgGaO_4$ reveals a continuum of excitation that persists till the lowest measured temperature of 60mK in the S(Q,ω) intensity maps (see Fig.3.6B). The excitation continuum has a bandwidth of 1.3meV and is gapless within the experimental energy resolution of approximately 0.1meV. Similar neutron scattering experiments [53] report a broad spin excitation covering a wide region of the Brillouin zone.

A continuation of this investigation was performed by Shen et al. [52], where in-field INS experiments were used to probe the nature of the broad excitations. The authors observe that at low fields($\leq 2.5T$), the field dependence of the inelastic scattering intensity shows no clear shift of the overall continuum; instead, a redistribution of the spectral weight is observed. However, at higher fields ($\geq$ 9T), sharper spin-wave excitations with a 1.2 meV gap are observed in a nearly polarized state. The field-dependent evolution is inconsistent with magnon-only behavior, and the high-field spectrum shows a distinct dispersion compared to the low-field regime. Their analysis concluded that the transfer of spectral weight from M and K points in the Brillouin zone to Γ point as the field is increased which is consistent with spinon excitations [54]. However, the calculated spin Hamiltonian fails to reproduce the weak and broad scattering intensity at the Γ point of the Brillouin zone.

Another possible microscopic explanation of the zero-field scattering continuum is the intrinsic chemical disorder in $YbMgGaO_4$. Zhu et al. [47] propose that randomness in the pseudodipolar term($J_{\pm\pm}$), which originates due to chemical disorder, mimics the signatures of a QSL phase and locally stabilize a striped order phase. Randomizing $J_{\pm\pm}$ in DMRG simulations with the parameters [55] Δ = 0.58 and J_2/J_1 = 0.22, the authors report that **A.** If $|J_{\pm\pm}|$ is large $\geq 0.2J_1$, then the lattice will stabilize a mixed order striped phase. **B.** If $|J_{\pm\pm}|$ is small, the spins fluctuate

between two striped ordered states and lead to a stripe superposition. It is possible then that the Z_3 symmetry that is not compatible with the striped phase is restored by the superposition of striped states, which can then account for the continuum of excitation and reproduce the spectral weights in the M and M' points of the Brillouin zone as is observed in INS experiments.

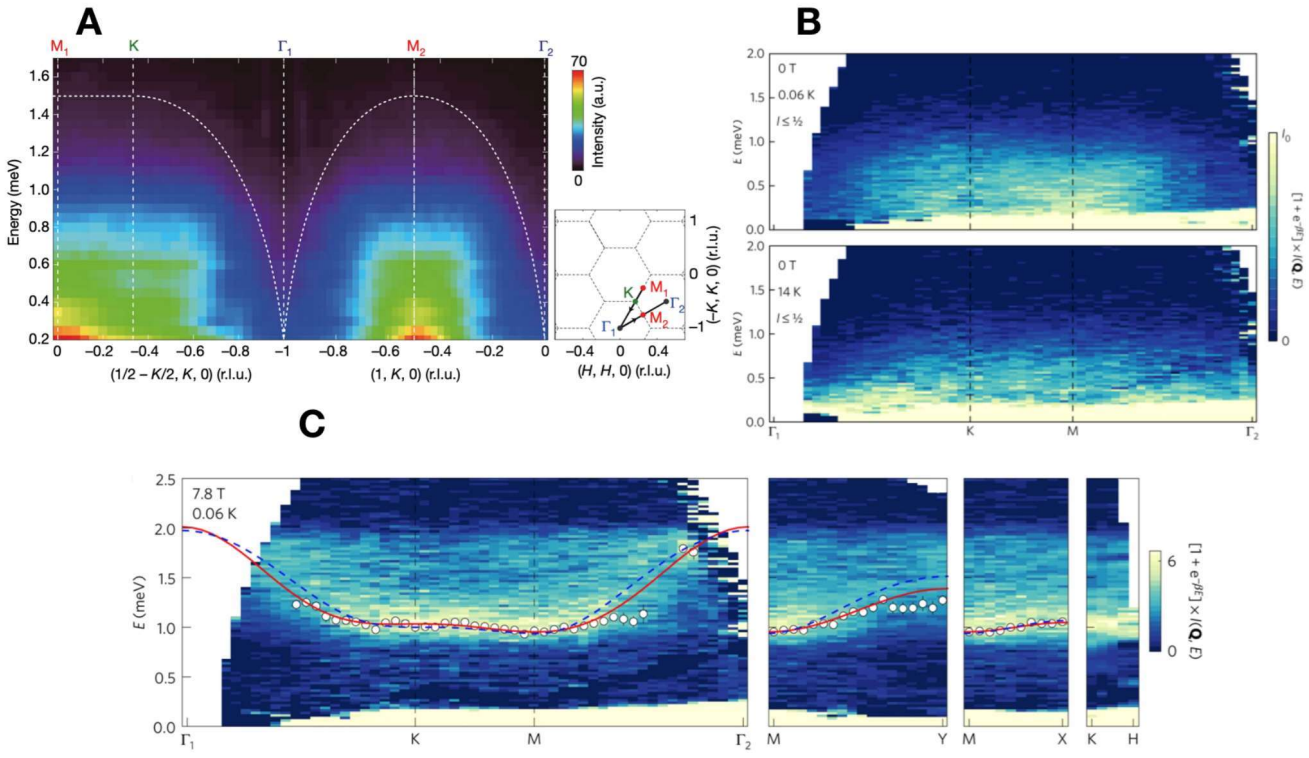

Figure 3.6: **A.**INS intensity plots [55] on $YbMgGaO_4$. The plot shows a broad continuum of the intensity along the M–K–Γ–M–Γ directions. The contour direction is shown by the black lines in the subplot. **B** In the INS experiment [55] on $YbMgGaO_4$, at T = 60mK and 14K, a continuum of scattering intensity is observed along the high symmetry direction in reciprocal space. The red and blue lines show a fit to the spin-wave dispersion relation. **C.**The continuum of excitation persists at 60mK in the presence of an applied field of 7.8T.

Alternatively, a formation of valence bonds [56] in $YbMgGaO_4$ also justifies the observed continuum. INS experiment down to low energy, 0.07meV, and in zero fields, revealed that the continuum has a distinct character in the low energy region compared to the high energy region. The authors offer an explanation where the rearrangement of valence bonds primarily causes the low energy continuum, and at high energies ($\geq$ 0.2meV), the continuum results from the breaking of nearest-neighbor valence bonds.

In the sister compound [49] $YbZnGaO_4$, a spin glass behavior is observed around 100mK. In this glassy phase, the authors report a continuum of excitation in the zero field spectrum of the INS experiment. More importantly, comparing $YbZnGaO_4$ with $YbMgGaO_4$ reveals a similar scattering continuum in INS experiments, leading the authors to conclude to a spin-glass phase also in $YbMgGaO_4$ (driven by disorder effects). However, Li et al. [56]

argues that the fraction of spins that become static in $YbMgGaO_4$ in the low-temperature regime is insignificant.

In conclusion, the dynamical nature of the ground state in $YbMgGaO_4$ continues to be puzzling, and more precisely, the exact role of disorder is yet to be clarified.

3.4 Summary

To summarize the main results in $YbMgGaO_4$, the lowest CEF levels are at 40meV/460K, thus sufficiently separated from the GS doublet. The magnetization along with the CEF measurements both estimate Yb^{3+} spins to be nearly isotropic (Heisenberg) with $g_\perp/g_\parallel$ = 0.9(1). Additionally, The CEF analysis and magnetization measurements establish $YbMgGaO_4$ as a S_{eff} = 1/2 anisotropic THAF (see Sec.1.3.2).

Further investigation of the nature of the collective spin ground state of $YbMgGaO_4$ by INS experiments reveals a scattering continuum in the inelastic channel that persists till 60mK. Multiple complementary experiments show that the continuum becomes gapped under an external field while remaining anomalously broad. The broad-spectrum has been attributed primarily to the disorder effects due to the Mg-Ga site mixing [47, 44, 43]. Numerous scenarios [52, 54, 57] have been proposed to explain the origin of the ZF continuum observed in the INS experiment including spinon excitation in a U(1) QSL phase and, more recently, valence bond formation [56]. Additionally, the low temperature ($\leq$ 100mK) ac susceptibility measurements point out the possibility of glassy behavior [49] which directly contradict μSR measurements [48, 46].

Thus we discovered in this chapter, the physics of $YbMgGaO_4$ which is extremely rich and complicated and, it is not clear if the QSL phase features are genuine or if structural disorder leads to a disorder-induced mimicry of such QSL phase. In the spirit of these findings, it is then essential to explore the underlying phase diagram by studying related compounds, which is the purpose of the work detailed in the following chapters of this thesis.

Chapter 4

$\mathbf{ErMgGaO_4}$: a new $\mathbf{S_{eff} = 1/2}$ triangular antiferromagnet

The series of the triangular compounds ReMgGaO$_4$, where Re^{3+} is a rare earth ion, was first synthesized and structurally characterized by Kimizuka and Takayama [41] in 1982. In this family, YbMgGaO$_4$ has drawn attention in recent years as a potential quantum spin liquid candidate (see Sec.1.3.2). However, the cumulative evidence of a strong impact of the chemical disorder [47] on the magnetic properties of YbMgGaO$_4$ calls for additional measurements to make a definitive conclusion of the nature of its ground state. Alternatively, the investigation of other members of this chemical family could help to gain further insights on the nature of the effects of the disorder and to explore the phase diagram of the S_{eff} = 1/2 triangular anisotropic antiferromagnet (THAF) model (see Sec.1.3). With this in mind, we choose to investigate its sister compound, ErMgGaO$_4$, where Yb^{3+} is replaced by Er^{3+}.

We present in this chapter our experimental findings on ErMgGaO$_4$. Our collaborators at McMaster University (Z. Cronkwright, S.Huang, E. smith, G.M.Luke and B. Gaulin) provided the polycrystalline sample, where a highly pure phase ($> 99\%$) of ErMgGaO$_4$ was synthesized. We magnetically characterize this sample using M(H) and susceptibility measurements, and report the detailed investigation of its low-temperature magnetic properties from INS experiment.

4.1 A literature survey on ErMgGaO$_4$

4.1.1 Structure and sample synthesis

X-ray characterization on ErMgGaO$_4$ reveals that it crystallizes in the space group R$\bar{3}$m, forming 2D triangular layers of Er^{3+} ions separated by non-magnetic Ga^{3+} and Mg^{2+} ions (see Fig.4.1). In ErMgGaO$_4$, Er^{3+} is surrounded by six O^{2-} anions that form an octahedron, resulting in D_{3d} local point group symmetry, At 300K the lattice parameters

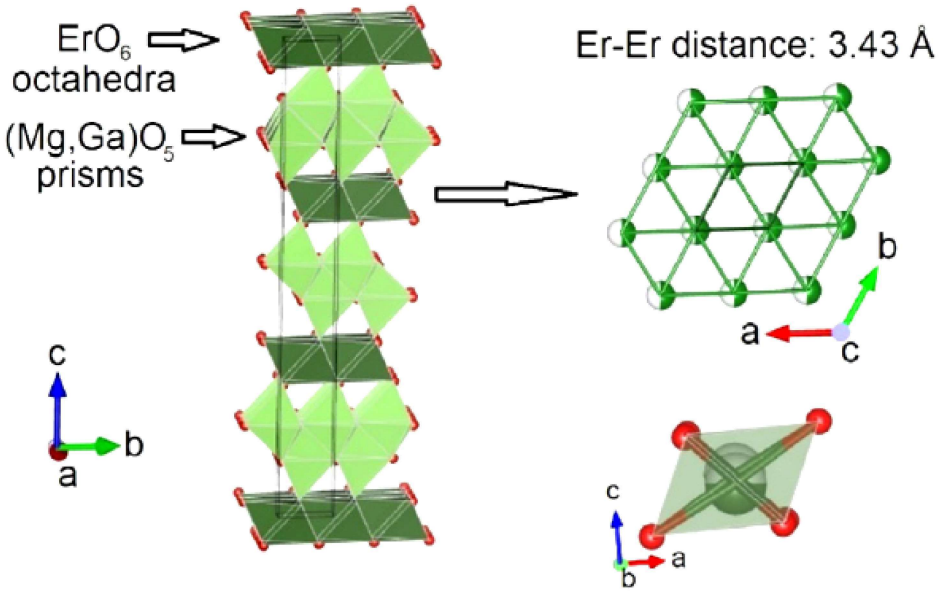

Figure 4.1: 2D triangular planes of magnetic Er^{3+} separated by non-magnetic ions Mg and Ga. Extracted from [58]

are estimated by X-ray diffraction [41], and were later confirmed [58] to be a = 3.4317(1)Å and c = 25.104(1)Å, similar to that of $YbMgGaO_4$ (a = 3.39(3)Å and c= 25.13(3)Å) at 300K (see Sec.3). We also note that the common solid-state synthesis route often leads to the nondesirable presence of a magnetic impurity phase, $Er_3Ga_5O_{12}$, that is known to give signs of magnetic order [59] at 0.8K, which will contribute to the bulk measurements.

A detailed analysis [58] showed that the Er^{3+} ions are, like Yb^{3+} in $YbMgGaO_4$, affected by the intersite disorder. Investigation of a single crystal [58] of $ErMgGaO_4$ with refined thermal parameters reveals an anomalously broad electron distribution along the z-axis at the position of the Er^{3+} moments. The refined positional displacement of the Er^{3+} ion from its ideal positions in the 2D triangular plane in the c direction is found to be significant (0.1 Å) and confirms the presence of positional disorder of Er^{3+}.

Research Group	Sample Type	Impurity phase % by weight
Kimizuka and Takayama	Powder	Not specified
Cevallos *et al.* [58]	Single crystal	Not specified
Cai et al. [59]	Small crystals with common c-axis and powder	5%
B. Gaulin *et al.*[1]	Powder	1%

Table 4.1: List of $ErMgGaO_4$ samples that have been experimentally characterized and reported till now.

[0]Our Sample (unpublished)

4.1.2 A S_{eff} = 1/2 anisotropic triangular Hamiltonian

The Er^{3+} ion has an electronic configuration [Xe]$4f^{11}$, with S=3/2, L=6 and J = 15/2. Additionally, by Kramer's theorem, each state is at least doubly degenerate for half-integer total spin. This implies that with J = 15/2, the crystal field interaction (see Sec.2.3.2) will lift the degeneracy of the J manifold, and there will be seven excited doublets and a ground state doublet. Because of the intrinsic Mg-Ga site disorder, INS may prove to be difficult to analyze as one expects significant broadening combined with additional CEF levels [44, 53, 55], and as an alternative, point charge calculations have been first carried out [59]. The energy of these excitation levels and the ground state anisotropy of Er^{3+} ions can be estimated using a point charge model in the Steven's operator formalism (see Sec.2.3.2), for Er^{3+} ion. This point charge calculation takes into account the six nearest O^{2-} anions and ignores any distortion of the octahedron formed by these oxygen anions. Table.4.2 shows the energy levels calculated by the point charge model by Cai et al. [59]. The first CEF level is at 19meV (221K), which implies that only the doubly degenerated Kramer's ground state is populated at low temperatures. This is the situation for Yb^{3+} ion in $YbMgGaO_4$ as well, where the energy gap is 39.4meV [44], and it justifies here that an S_{eff} = 1/2 model is appropriate for Er^{3+}. Additionally, the g-tensor for Er^{3+} can be deduced from the ground state wavefunction (see Sec.2.3.3) and is compared to experimental results in Table.4.3. Magnetization provides another way to estimate the g-tensor; from the saturation value of magnetization parallel and perpendicular to the z-axis of the crystal, the study [58] reports, $M_{sat}^{\perp,\parallel} = g_{sat}^{\perp,\parallel}\mu_S$. where μ_S is the effective S=1/2 moment. Fig.4.2.C shows M(H) measurement performed on a single crystal of $ErMgGaO_4$ by Cevallos, Stolze, and Cava [58], in a direction parallel and perpendicular to c axis. The anisotropy of the g-tensor is visually apparent from the two curves, where we observe the difference in the magnetic saturation value from the inset plot, depicting M(H) at T = 2K and the authors concludes to a nearly Heisenberg type anisotropy, with $g^{\perp} = 7$ and $g^{\parallel} = 6.8$ (see Table.4.3).

Lastly, we note the negative or antiferromagnetic Curie-Weiss temperatures [58, 59] θ_{CW} from the magnetic susceptibility ($\chi(T)$) measurements at low temperature (see Sec.2.4) . To summarize, initial characterization experiments shows that $ErMgGaO_4$ fits the S_{eff}=1/2 anisotropic triangular antiferromagnet (THAF) description, much like $YbMgGaO_4$.

CEF level	1^{st}	2^{nd}	3^{rd}	4^{th}	5^{th}	6^{th}	7^{th}
E in meV	19.06	36.99	48.63	52.91	61.71	62.69	64.37

Table 4.2: Point charge estimation of crystal field excitation levels for $ErMgGaO_4$ [59]

Study	μ_{eff} in μ_{B} (150-300)K	θ_{CW} in K (150-300)K	θ_{CW} Low Temp	$g_{\perp}$	$g_{\parallel}$	$g_{\perp}/g_{\parallel}$
Cevallos et al.(2018)[1] [H = 1k G]	9.2	-30.4	-5.9K[2]	7	6.8	1.02[3]
Cai et al.(2020) [H = 100G]	9.59	-33	-3.9K[4]	0	17.91[5]	0

Table 4.3: Comparison of reported magnetic characterization measurements on $ErMgGaO_4$. Data taken from [58, 59]

4.1.3 A dynamical ground state ?

In this section, we report the characterization measurements performed to determine the nature of the ground state in $ErMgGaO_4$. Previous work concluded to the absence of order, with the presence of fluctuations down to 25mK. We briefly review the ZFC-FC susceptibility measurements and specific heat data (see Sec.2.4) to identify any phase transition or the development of long-range order.

Zero field cooled and field cooled measurements

ZFC-FC susceptibility measurements have been reported for $ErMgGaO_4$ crystal and powder samples to check for signs of magnetic ordering or freezing. For the single crystal, no bifurcation appears till 1.8K [58]. Moreover, experiments performed on a 95% pure powder sample of $ErMgGaO_4$ down to 0.5K [59] also give the same conclusion. Below this temperature, around 0.5K, the ZFC-FC curves slightly bifurcate, as indicated by the red and black dots in the inset of Fig.4.2.D. Additionally, we observe that the susceptibility curve does not follow a power-law or Curie Weiss behavior, and we note a weak inflection between 1.2K and 0.8K, followed by saturation.

Specific Heat

The specific heat measurement in the temperature range (0.1, 4)K has been performed on a powder sample of $ErMgGaO_4$ [59] to determine the presence or absence of a $\lambda-$type anomaly or a phase transition and to determine the low-temperature magnetic excitation (Fig.4.2.B). As the temperature is reduced, the specific heat C_p, as shown in Fig.4.2B., shows a bump at 1.5K. At lower temperatures below 1.5K, a minimum is reached at 0.2K, and then C_p increases till the lowest measured temperature of 0.1K. The rise below 0.2K may be explained by ^{167}Er nuclear Schottky anomaly[6]. A similar bump in specific heat was observed in $YbMgGaO_4$ at 2.4K and interpreted as a crossover to a QSL regime [42].

[1] Weighted average of parallel and perpendicular measurements
[2] T = (2,10)K
[3] g-values are estimated at low temperature
[4] T = (2,5)K
[5] Estimated from point charge calculation
[6] That we analyze in the following section.

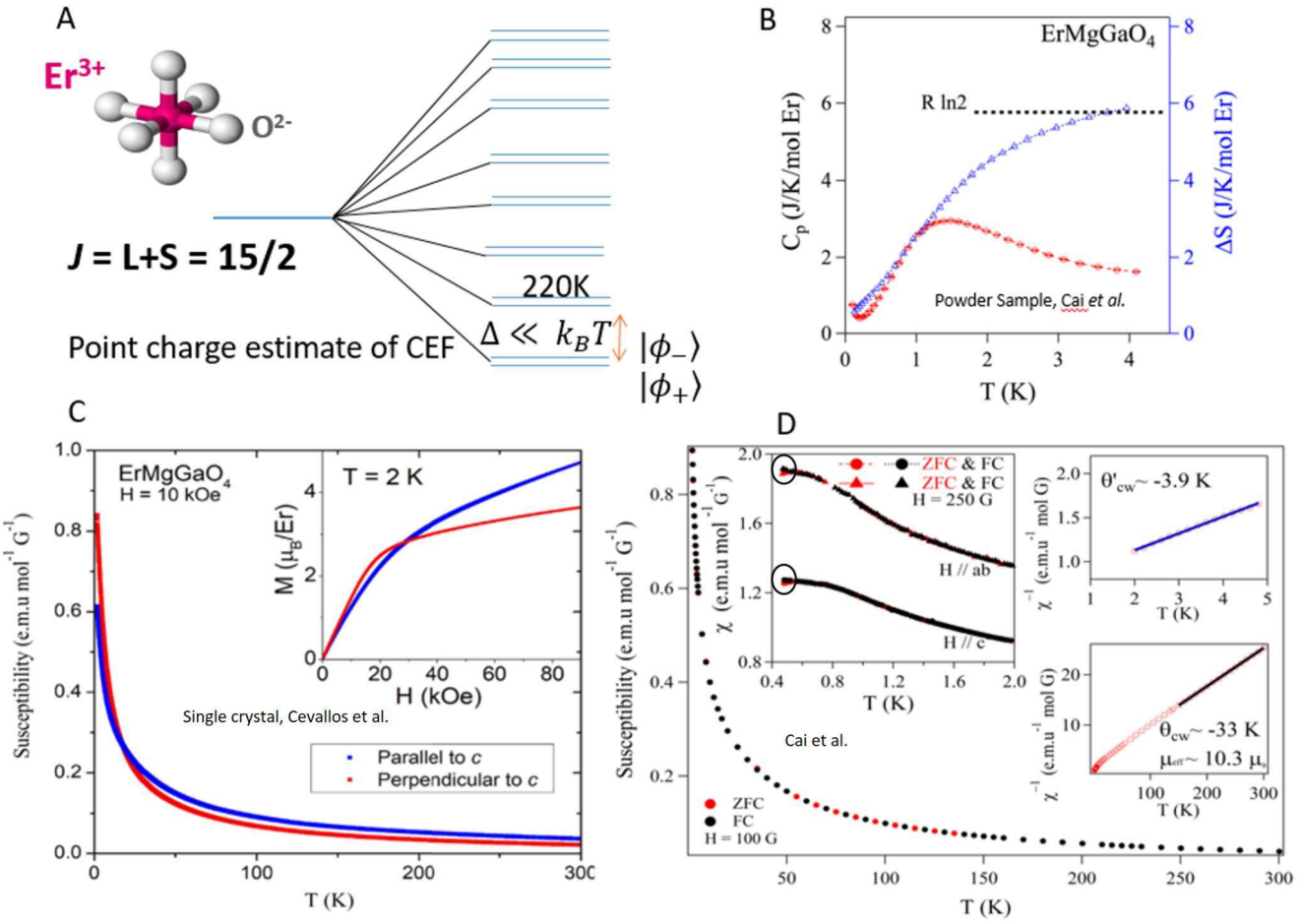

Figure 4.2: **A.** CEF scheme estimated from point charge calculation; **B.** Specific heat measurement [59] performed in zero applied field. The full entropy of a S_{eff}=1/2 is recovered by 4K. **C.** Susceptibility and M(H) measurement (inset) of a single crystal of $ErMgGaO_4$ [58]. **D.** ZFC-FC and M(H) measurement [59] on crystal sample of $ErMgGaO_4$ down to 0.5K. Round circles on the left inset highlight the bifurcation of the ZFC-FC at 0.5K.

It is found from these experiments that the residual entropy C_p/T, also shown in Fig.4.2, saturates at Rln(2) by 4K. In comparison, for $YbMgGaO_4$, the residual entropy similarly tends towards a zero value as is estimated from the low temperatures (60mK) measurements [42].

Muon Spin Resonance

Muon spin relaxation measurements have been recently performed on $ErMgGaO_4$ by Cai et al. [59], down to 25mK. At this low temperature, the asymmetry of the muon spin relaxation shows an exponential decrease in the ZF mode (Fig.4.3) and remains almost unchanged for large values of applied fields up to 1T. Furthermore, the relaxation does not follow a static Kubo-Toyabe dependence (see Sec.2.1.3) and does not show a $1/3^{rd}$ tail at higher times. All these point to the presence of a fluctuating ground state down to 25mK.

The temperature dependence of the muon spin relaxation rate λ is extracted from the temperature evolution of the ZF relaxation using a stretched exponential model (see Sec.2.1.4), $\mathrm{Ae}^{-(\lambda \mathrm{t})^{\beta}} + \mathrm{B}$, where A is the sample

asymmetry, β is the stretch coefficient and B is the background. In Fig.4.3.C, as the temperature is lowered in zero applied field, there is an increase of the spin relaxation rate from 100K to 10K. This is due to the crystal field levels being populated in this high-temperature region. As the temperature is lowered further below 10K, a plateau is observed and it continues till the base temperature of 25mK. A similar situation is encountered in $YbMgGaO_4$, where the large gap between the CEF ground state and the first excited state generate a plateau of relaxation above 10K due to exchange interaction in the paramagnetic regime [48]. Below 4K, a rise in the spin relaxation rate is followed by a second plateau at low T, i.e, below 0.4K, which is interpreted as a signature of persistent dynamics dye to a U(1) quantum spin liquid phase [48]. These low temperature-independent plateaus have been observed for other QSL candidates in the literature, and ascribed to the presence of persistent dynamics.

From Fig.4.3.C, we also observe the dependence of β, the stretch coefficient. β decreases as the temperature is lowered and plateau around 2K with a value of 0.4. A value of β much lower than 1 indicates a distribution of relaxation rates.

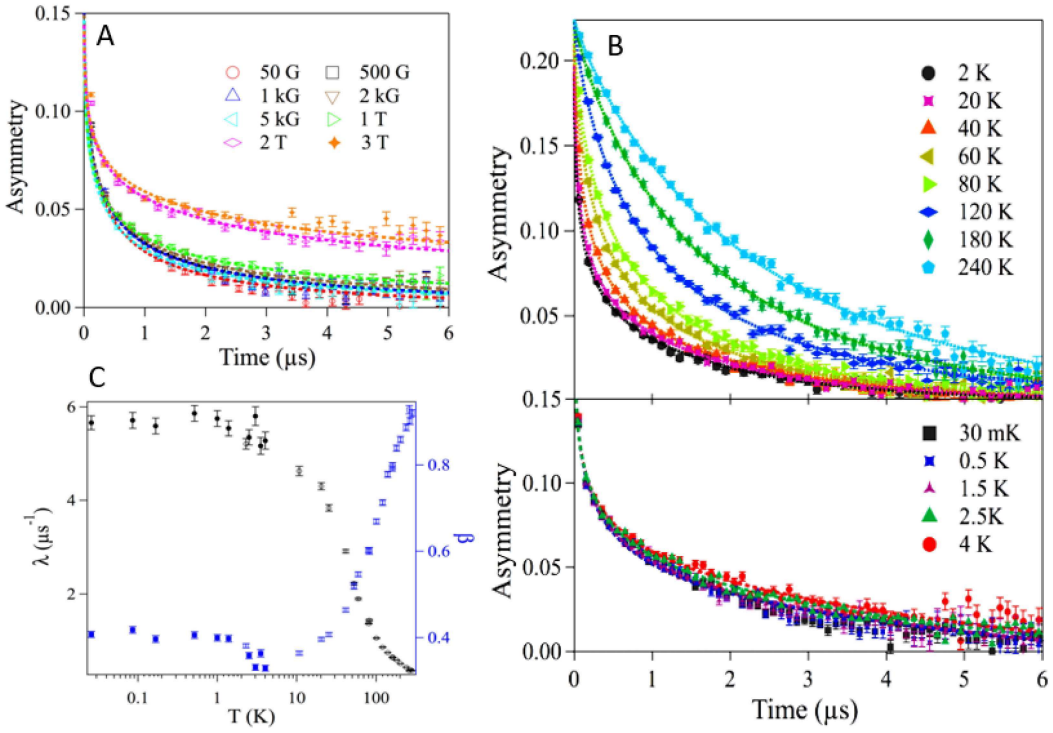

Figure 4.3: Muon relaxation experimental results on powder sample of $ErMgGaO_4$. **A.** Longitudinal field (LF) dependence of the muon spin relaxation, extracted from Cai et al. [59]. **B.** Temperature evolution of muon asymmetry in the zero field. **C.** Temperature dependence of the spin-lattice relaxation rate λ (circles) and of the stretch coefficient, β (square), determined from a fit of the muon asymmetry.

4.1.4 Summary

The structural characterization previously performed by Cevallos, Stolze, and Cava [58], Cai et al. [59], confirms the triangular layered structure of $ErMgGaO_4$, where Er^{3+} occupies the vertices of the triangles. However intrinsic structural disorder is also present in $ErMgGaO_4$ as found by detailed characterization measurements. Magnetic characterizations, point charge calculations, and specific heat capacity measurements show that $ErMgGaO_4$ has a Kramer's GS doublet well separated from the first CEF excitation level. Additionally, the fits of the susceptibility curves shows that $ErMgGaO_4$ is expected to host antiferromagnetic interactions. Muon spin relaxation experiment conclude spin dynamics down to 25mK. Thus, $ErMgGaO_4$ fits the initial requirements for a QSL candidate according to previous work. In the light of these results and knowing that the same intrinsic chemical disorder is present in both $ErMgGaO_4$ and $YbMgGaO_4$, there is an opportunity for a comparative analysis between these two compounds. In the following sections, we investigate a $ErMgGaO_4$ powder sample of high purity using magnetic measurements and INS spectroscopy.

4.2 Sample characterization

4.2.1 Magnetic and susceptibility measurements

	M(H)	$\chi^{-1}(T)$	$\chi^{-1}(T)$	Cevallos et *al* [58]	Cai et al. [59]
	(6-20)K	(6-20)K	(150-300)K	(2-10)K	(2-5)K
		100G	5T		
C		4.3(3)	10.52(7)		
μ_{eff} (μ_B)		0.8(1)	10.5(8)	9.2 (150K-300K)	10.3(1) (150K-300K)
θ_{CW} (K)	-0.6(1)	-4.2(1)	-13.8(8)	-5.9	-3.9
χ_0 (cm^3/mol)	0.122	0.122(1)	0.0022(1)		
$g_{\parallel}$	6.5(3)			6.8	17.91
$g_{\perp}$	6.7(3)			7	0
$\frac{g_{\perp}}{g_{\parallel}}$	1.0(1)			1.02	0

Table 4.4: Comparison of reported magnetic characterization measurements on $ErMgGaO_4$

For characterization (see Sec.2.3.1) and comparison with previous studies [59, 58] we perform M(H) and susceptibility measurements on our ultrapure sample[7] of $ErMgGaO_4$. The ZFC-FC measurement, shows (Fig.4.4) a

[7] From B. Gaulin *et al*, see Table.4.1

clear splitting occurring between the ZFC and FC curves at 2.5K. The temperature at which the splitting occurs is much higher than the reported [59, 58] value of 0.6K.

To model the paramagnetic region above this temperature, we use a Curie-Weiss model between 6K to 20K, and we obtain an antiferromagnetic Curie-Weiss temperature, θ_{CW} = -4.2(1)K, which is in agreement with the reported values in the literature. We performed several M(H) measurements between 1.8K and 15K to extract the saturation value and obtain the g-tensor anisotropy. In Fig.4.4, we observe for low temperatures ($\leq$ 5K) and high fields ($\geq$ 4T) a linear dependence of M(H), which is due to a contribution from the temperature-independent susceptibility, χ_0. It is possible to extract the saturated moment by linear extrapolation from this region (H $\geq$ 6T) of the M(H) curve, assuming a full saturation of the Er^{3+} moments. For the higher temperatures, the temperature-independent susceptibility (see Sec.2.4) does not produce such a dominating effect, and we continue to observe a contribution from the temperature-dependent susceptibility to the highest applied field of 7T.

We fit these M(H) isotherms with a phenomenological model based on a Brillouin function (see Sec.2.4) with interaction. We find that the fit quality is inadequate at 5K and below, and it becomes evident that the magnetization curve deviates from a Curie Weiss behavior. The $g_{\|}, g_{\perp}$ and, the saturation value of magnetization (Table.4.4) are estimated from the Brillouin function fits between 6K and 20K. As it is not possible to determine the anisotropy from a powder sample (see Sec.2.4), we use the temperature-independent susceptibility extracted from the measurements of Cevallos, Stolze, and Cava [58], χ_0 = 0.122 cm^3/mol. Under this constraint we estimate the $g_{\|}$ and $g_{\perp}$ to be 6.7(3) and 6.5(3), respectively. We find the anisotropy of $ErMgGaO_4$ to be, $g_{\perp}/g_{\|}$ = 1.0(1) , which implies an isotropic nature of the spins. In this temperature range the fits give an antiferromagnetic θ_{CW} = -0.6K.

Using a Curie-Weiss model we fit (see Fig.4.4) the low-temperature inverse-susceptibility, $\chi^{-1}(T)$, measurement by similarly constraining the temperature independent susceptibility, χ_0. The estimated effective moment is 6(1) μ_{B}, much smaller than the free ion value 9.59 μ_B. We also report a stronger antiferromagnetic θ_{CW} = -4.2(1)K.

From the high temperature (150K to 300K) fit of χ^{-1}(T), we estimate the effective moment μ_{eff} = 10.5(8)μ_{B} which is much closer to the single ion moment of Er^{3+}. The qualitative difference between the low temperature and the high-temperature effective Er^{3+} moments arise primarily due to CEF effects.

These experimental results offer a better approximation than the point charge calculation and are in reasonable agreement with the estimate of Cevallos, Stolze, and Cava [58]. Thus, the different experiments converge to an isotropic nature of the spins similar to $YbMgGaO_4$ for which ($g_{\perp}$ / $g_{\|}$) = 1.0(1)) and additionally confirms that $ErMgGaO_4$ is an S_{eff} = 1/2 antiferromagnet that is in a paramagnetic regime above 5K.

4.2.2 Analysis of the specific heat

We could not perform advanced specific heat measurements down to very low temperatures on our sample. Instead, we present here an analysis of the published data [59], shown in Fig4.5.

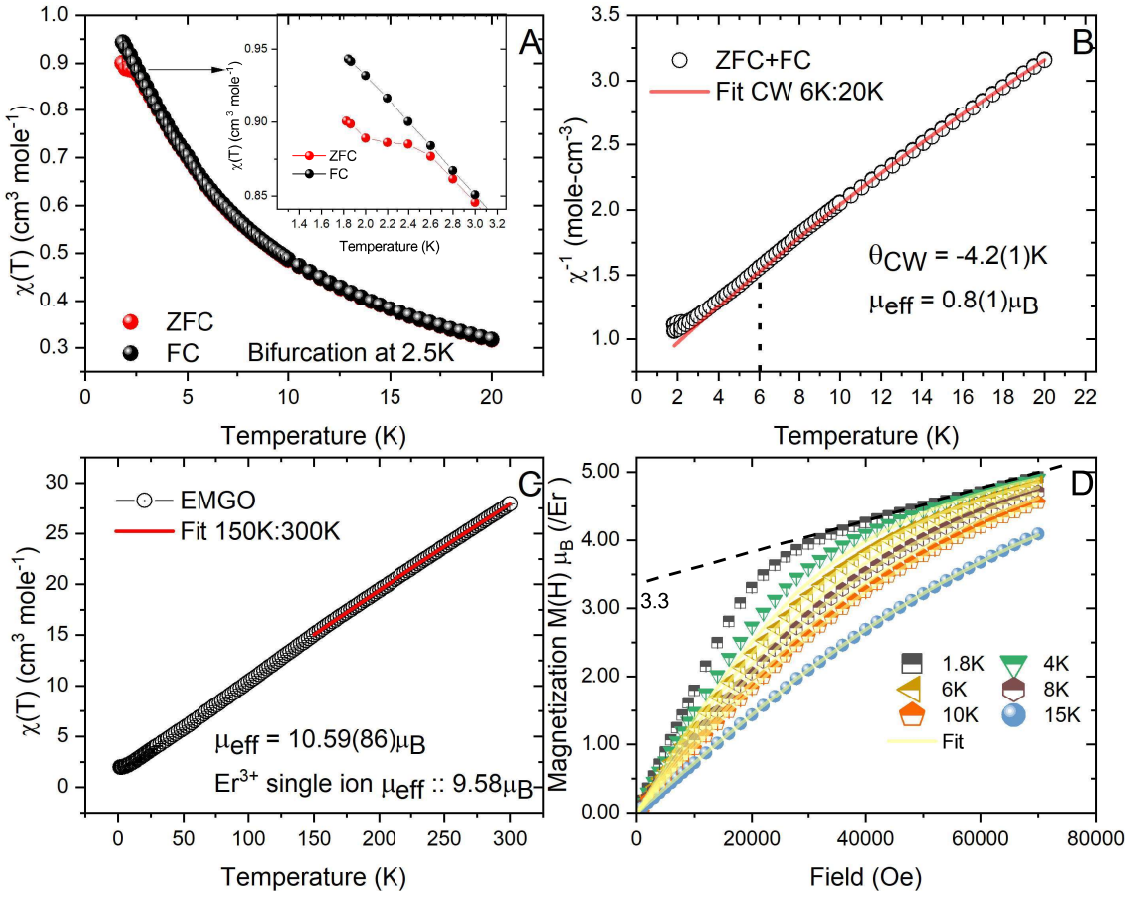

Figure 4.4: A. ZFC FC curves and bifurcation. B. Low temperature inverse susceptibility [1.8,20]K with fit between [6,20]K at an applied field of 100G. C. Inverse susceptibility measurement with Curie-Weiss fit at high temperature [150,300]K under 1T external field, D. M(H) measurement [1.8,15]K and corresponding fits [5,15]K

In the context of the 2D THAF model with ring exchanges [21], the specific heat capacity C_p for a QSL ground state is expected to vary as $T^{2/3}$ in the QSL regime, where T is the temperature. It is thus interesting to compare the specific heat of $ErMgGaO_4$[8] and $YbMgGaO_4$ [42] and fit with a power law (see Fig.4.5). For $ErMgGaO_4$, we use a model of the form $C_p = AT^{-2} + BT^{\gamma}$, where T is the temperature. The term, AT^{-2} is due to the contribution from the nuclear Schottky anomaly; the second term is the power-law dependence of the specific heat with γ as the exponential coefficient. From the fit we obtain A = 60(7)$\times$ 10^{-4} J-K/mol and B = 2.50(7), γ=1.32(4). In contrast, $YbMgGaO_4$ is fitted with a simple power law, $T^{2/3}$ and the factor 2/3 was reported [42] to be a signature of the QSL phase. For $ErMgGaO_4$, the situation appears to be quite different. From the inverse-square increase of C_p(T) below 0.2K it is likely due to a nuclear Schottky anomaly. This can arise from hyperfine interactions with the static local field at the nucleus positions. Moreover, this observation is consistent with the evidence of static order found in the

[8]Specific heat on powder sample as measured by Cai et al. [59]

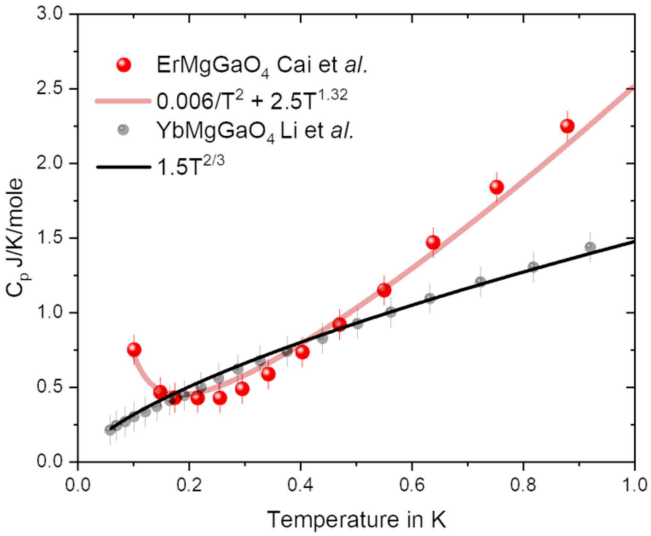

Figure 4.5: Specific heat comparison of $ErMgGaO_4$ [59] and $YbMgGaO_4$ [42] and fits with power law.

susceptibility measurements.

4.3 Neutron scattering measurement

In this section, we discuss the results obtained for $ErMgGaO_4$ powder sample with the time-of-flight neutron scattering experiment (see Sec.2.2.3) on the IN6 instrument at ILL, France.

4.3.1 Elastic Scattering

Elastic scattering measurements are a way to probe the static correlations in magnetic materials (see Sec.2.2.2). We use the elastic signal (Fig.4.6) from our TOF neutron scattering experiment by taking a Q-cut integrated over the energy resolution, Δ E = 0.08meV, centered at 0. At T=125mK, we report the emergence of an asymmetric peak, with a maximum at Q=1.08Å^{-1}, close to the M point (Q = 1.05Å^{-1}) of the reciprocal lattice. We further observe that both the asymmetry and the intensity of the peak gradually decreases with rising temperature (see Fig.4.6B). Moreover, it resembles a Warren lineshape (see Sec.2.2.2) which is strongly suggestive of the presence of 2D correlations. A closer inspection of the peak shape, particularly the shoulder around 1.3Å^{-1} points out that a single component Warren lineshape is not sufficient to model the experimental data (Fig.4.6). It is then likely that in $ErMgGaO_4$, the Er^{3+} moments have not one but a distribution of such correlation lengths.

Thus an accurate distribution would consist of multiple Warren lineshapes, each corresponding to a specific correlation length. However, for simplicity, we choose a model with only two Warren lineshape components, centered at the same Bragg's position (θ_{2DB}) but with different correlation lengths and intensity, and a background:

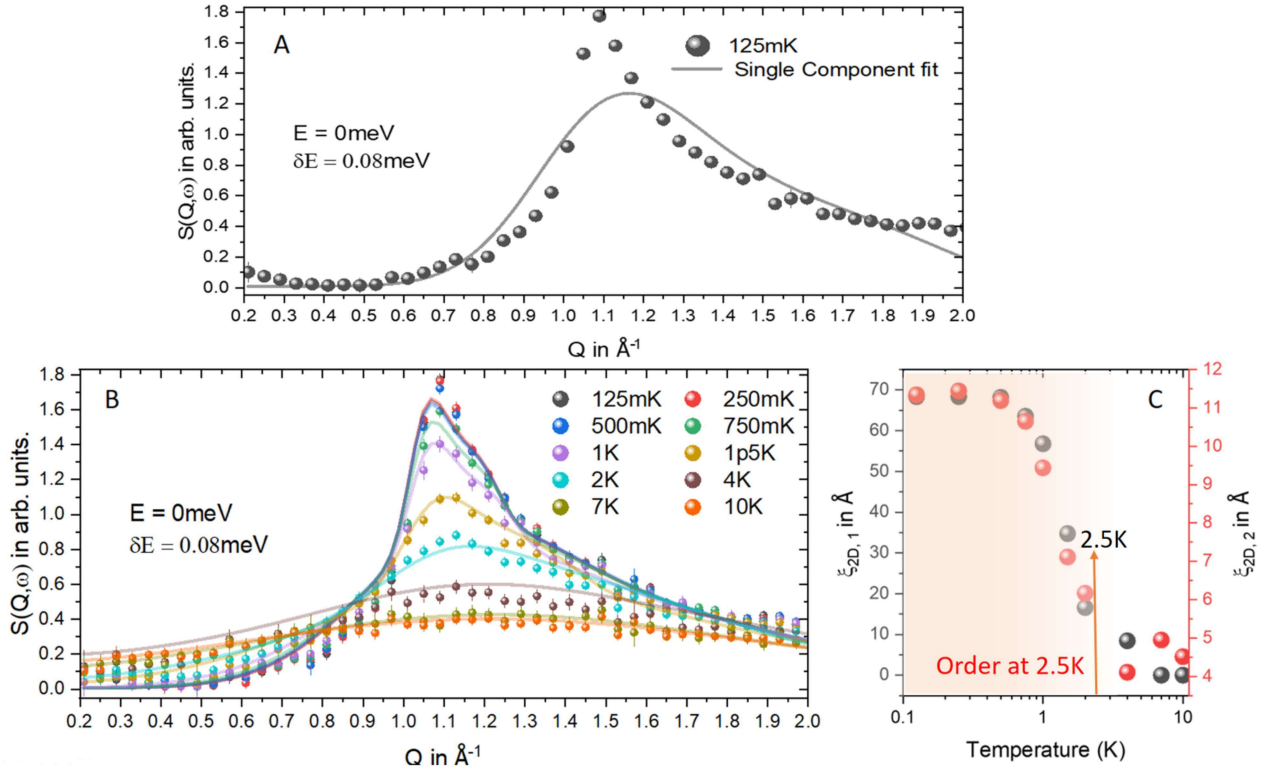

Figure 4.6: E integrated Q cut of the elastic channel and the fit with an asymmetric Warren lineshape **A.** Single component fit of 125mK data with a Warren lineshape model. **B.** 2-component Warren lineshape **C.** 2D correlation length as a function of temperature from 2-component Warren lineshape.

$$I(Q) = W_1(Q; C_1, \xi_{2D,1}) + W_1(Q; C_2, \xi_{2D,2}) + I_0 \tag{4.1}$$

where $W_{1,2}$ is the Warren lineshape function (see Sec.2.2.2), $\theta_{2DB} = 2.7$rad ($|Q_{2DB}| = 1.03\text{Å}^{-1}$) while the other parameters are not constrained. The fits of this model are shown in Fig.4.6B. The two correlation lengths $\xi_{2D,1}$ and $\xi_{2D,2}$, have a similar variation with temperature but differ in magnitude. Furthermore, they indicate that the correlations gradually increasing with temperature (Fig.4.6C.) below 2.5K in good agreement with the transition temperature (T_N = 2.5K) found in susceptibility measurements. We also note that the peak position, $\theta_{2DB} = 1.03\text{Å}^{-1}$ is close to the M point of the Brillouin zone of the 2D triangular lattice of Er^{3+} ($Q_M = 1.05\text{Å}^{-1}$). In the light of this analysis, we remark that our model captures the temperature dependence of the intensity. A plausible scenario could be that a broad signal located at all M points of the Brillouin zone would give a contribution at the K points also. This would be the case for a superposition of different striped orders, as discussed in [47] and in more details later. The distribution of correlation lengths at the M-point could originate from the intrinsic chemical disorder in $ErMgGaO_4$. So, in conclusion, we establish the presence of a 2D static correlated regime; however, the exact nature of this correlation remains to be identified and we speculate the possibilities in the conclusion.

4.3.2 Inelastic Neutron Scattering

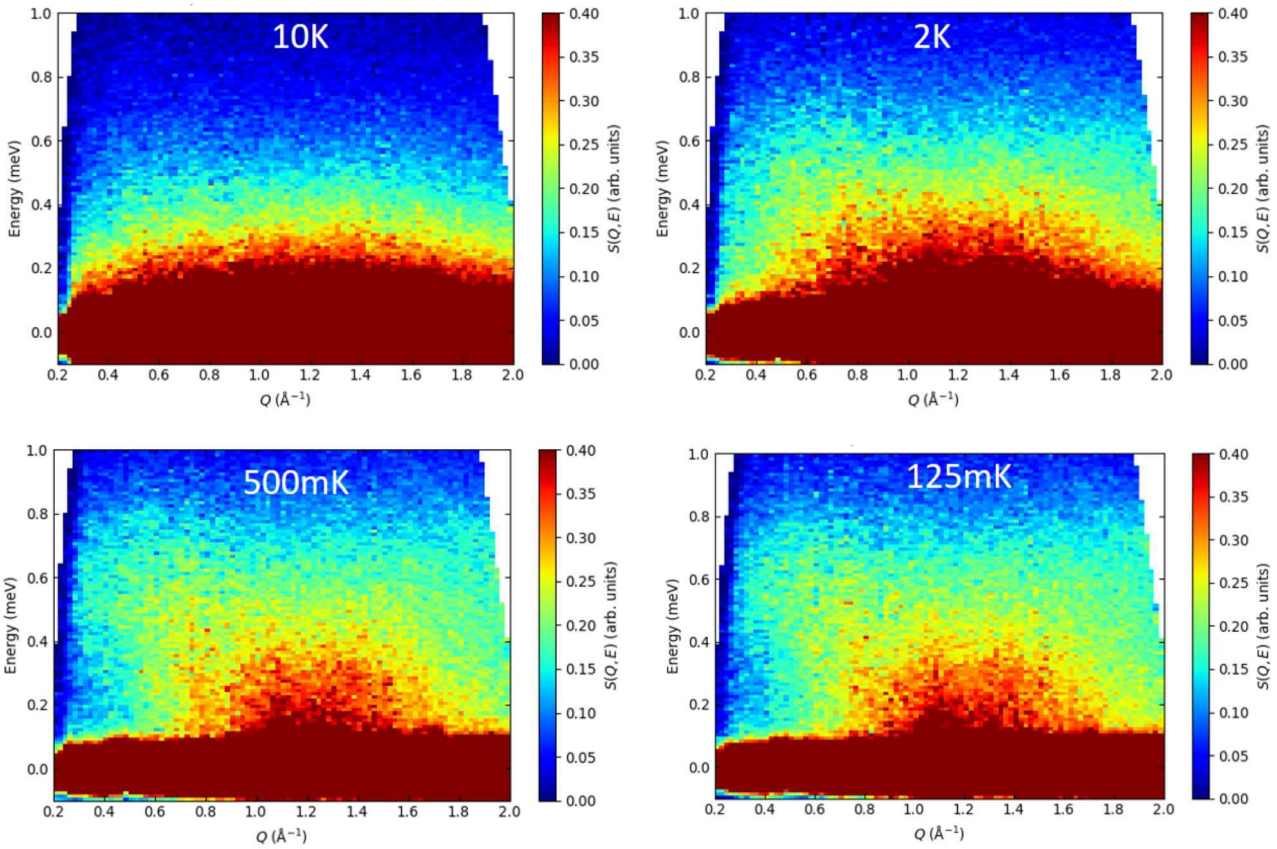

Figure 4.7: INS dataset for powder sample of $ErMgGaO_4$ with E_i = 3.2meV. The figures show the evolution of the dynamical structure factor, S($|Q|, \omega$), with temperature for 125mK, 500mK, 2K and 10K, with the same intensity scale

We performed INS experiment at ILL, Grenoble, France, using the IN6 instrument to probe the magnetic excitations (see Sec.2.2.2) in $ErMgGaO_4$ between 125mK and 100K. In Fig.4.7, we show the dynamic structure factor S(Q,ω) for selected temperatures. We observe the presence of diffusive scattering and its gradual evolution with decreasing temperature from 10K down to 125mK. At 10K, the diffuse scattering intensity is relatively flat over Q and has a bandwidth of 0.4meV, consistent with a paramagnetic phase with the exchange J around 5K. As the temperature is lowered, we remark a redistribution of spectral intensity and, below 1K, high intensities are observed between 1Å^{-1} to 1.4Å^{-1} and below 0.4meV. Further away from this region in both Q and E, the scattering intensity reduces, giving evidence of a broad dispersive excitation in the inelastic channel. In order to get further insights into the low energy excitations, we analyze the E-cuts of S(Q,ω) in Fig.4.8. The intensity plots for Q = 0.62Å^{-1} show an inelastic signal that increases with decreasing temperature and peaks around 0.5meV below 1K. The rise of intensity (Fig.4.8A.) with the lowering of temperature indicates the magnetic character of these excitations. For the E-cuts at Q= 0.88Å^{-1}, 1.12Å^{-1}, 1.38Å^{-1}, the situation is less clear with the presence of a scattering continuum extending from 1meV down to the instrument energy resolution of 0.08meV.

To account for the detailed balance in the dynamical structure factor, S(Q,ω) is scaled by the Bose factor $(1 - e^{-E/k_BT})^{-1}$ to obtain the dynamical susceptibility, $\chi''(Q,\omega)$ in Fig.4.9. A comparison of χ"(Q,ω) at E = 0.1,0.2,0.3,0.4 meV for different temperatures confirms the temperature dependence. Additionally, we observe such temperature dependence for the lowest energy E = 0.1meV. This observation further justifies the presence of a quasielastic component.

We thus model the INS spectrum by taking into account an elastic, quasielastic and an inelastic component and the fit function is depicted below,

$$S(E) = A_1 \exp\left(-\left[\frac{E}{\sqrt{2}w_1}\right]^2\right) + \left(\frac{2A_2}{\pi} E \frac{w_2^2}{4E^2 + w_2^2} + A_3 \exp\left(-\left[\frac{E - E_c}{\sqrt{2}w_3}\right]^2\right)\right) \Big/ \left(1 - \exp\left(-\frac{E}{k_B T}\right)\right) \tag{4.2}$$

where, A_1 is the intensity of the Gaussian peak, with a width w_1, centered at 0 meV, corresponding to the elastic peak. A_2 is the intensity of the Lorentz peak, centered at 0, which models the quasielastic component. w_2 represents the width of the quasielastic contribution and is kept fixed to 0.1 meV for this analysis. A_3 is the intensity of the 3^{rd} component, a Gaussian peak function that models the magnetic excitation centered at E_c with width w_3. We use this model to fit the Q-integrated E-cut of the 125mK measurement at different Q positions.

Fig.4.10A. shows the experimental data along with fits to eqn.4.2. The Q and E dependence of S(Q, ω) is satisfactorily modelled by Eqn.4.2. This is particularly evident for Q-integrated energy cuts at low Q, for Q=0.3 and 0.5 Å, where a single inelastic component cannot account for the spectral weight observed for E $<$0.3meV. Alternative models assuming a second inelastic component at lower energies did not give a satisfactory fit. The quasielastic component suggests a gapless continuum of excitations down to 125mK, similar to INS experimental observations in $YbMgGaO_4$ [55]. In Fig.4.10B, we plot the dispersion of the inelastic magnetic excitation, and interestingly, the Q-dispersion suggests that the excitation continuum is due to damped and broad spin-wave modes, which is likely due to the disorder effects.

Zhu et al. [47] propose that the origin of the zero-field continuum in the INS experiment of $YbMgGaO_4$ (see Fig.3.6) can be a superposition of striped ordered phase where the orders co-exist and correspond to the M and M' symmetry points. For the powdered averaged S(Q,ω), these two points would have the same Bragg's angle θ_{DB}, and this is observed for $ErMgGaO_4$ (see Fig.4.6). Owing to the similarities between both compounds, this is a possibility for the ground state to explore further.

4.4 Summary

To summarise the results obtained here and the previous findings, we can categorize the results into two cate-

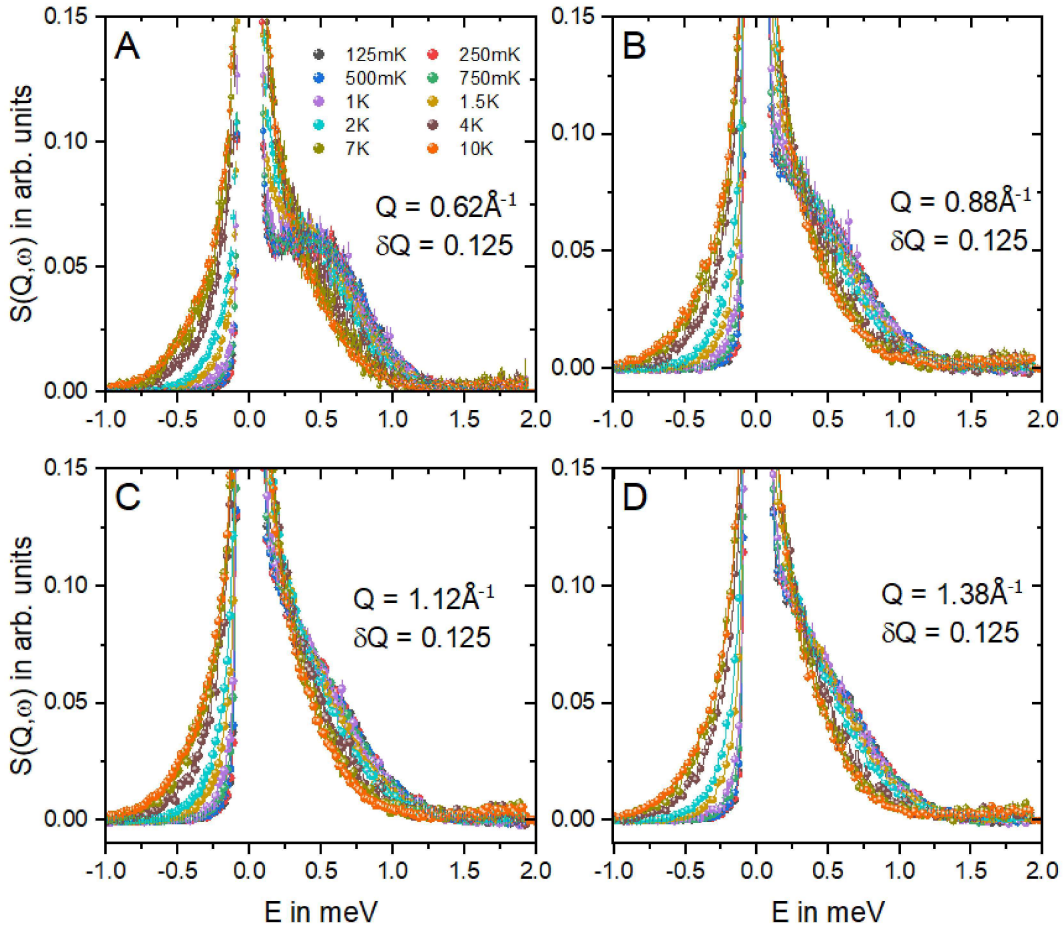

Figure 4.8: Q integrated E-cuts of the dynamical structure factor, S(Q,ω), of $ErMgGaO_4$ for E_i = 3.2meV. Figures A,B,C,D compare the integrated S(Q,ω) at different Q points integrated between Q-δQ and Q+δQ for temperature $\leq$ 10K.

gories, **A)** Evidence for order **B)** Evidence for dynamics and fluctuations.

A) From the ZFC-FC measurements we observe that at T $\leq$ 2.5K, $ErMgGaO_4$ deviates from the Curie Weiss behavior. The Warren peaks that appears in the low temperature measurement in the inelastic channel of $ErMgGaO_4$ (Fig.4.6) indicates a crossover to an ordered phase with correlations in two dimension and a distribution of correlation lengths. This ordered phase is possibly a striped phase as the Warren peak position ($Q = 1.03\text{Å}^{-1}$) coincides with the M point of the Brillouin zone of the triangular lattice, i.e $Q = 1.05\text{Å}^{-1}$. Additionally, the Q dispersion relation of the excitation peak resembles damped and powder averaged spin waves that can originate from the magnons of the ordered striped phase.

B) The zero field temperature dependence of the muon spin relaxation(Fig.4.3) with the relaxation plateauing down to 0.06K indicate persistent dynamics down till 25mK. We also observe the presence of a quasielastic component in $ErMgGaO_4$, which could be due to liquid like correlations down to 125mK.

In addition, it is interesting that our results are compatible with the phase diagram of the THAF model calculated from DMRG numerical calculations on $YbMgGaO_4$ [47] which speculates the emergence of a striped phase at low

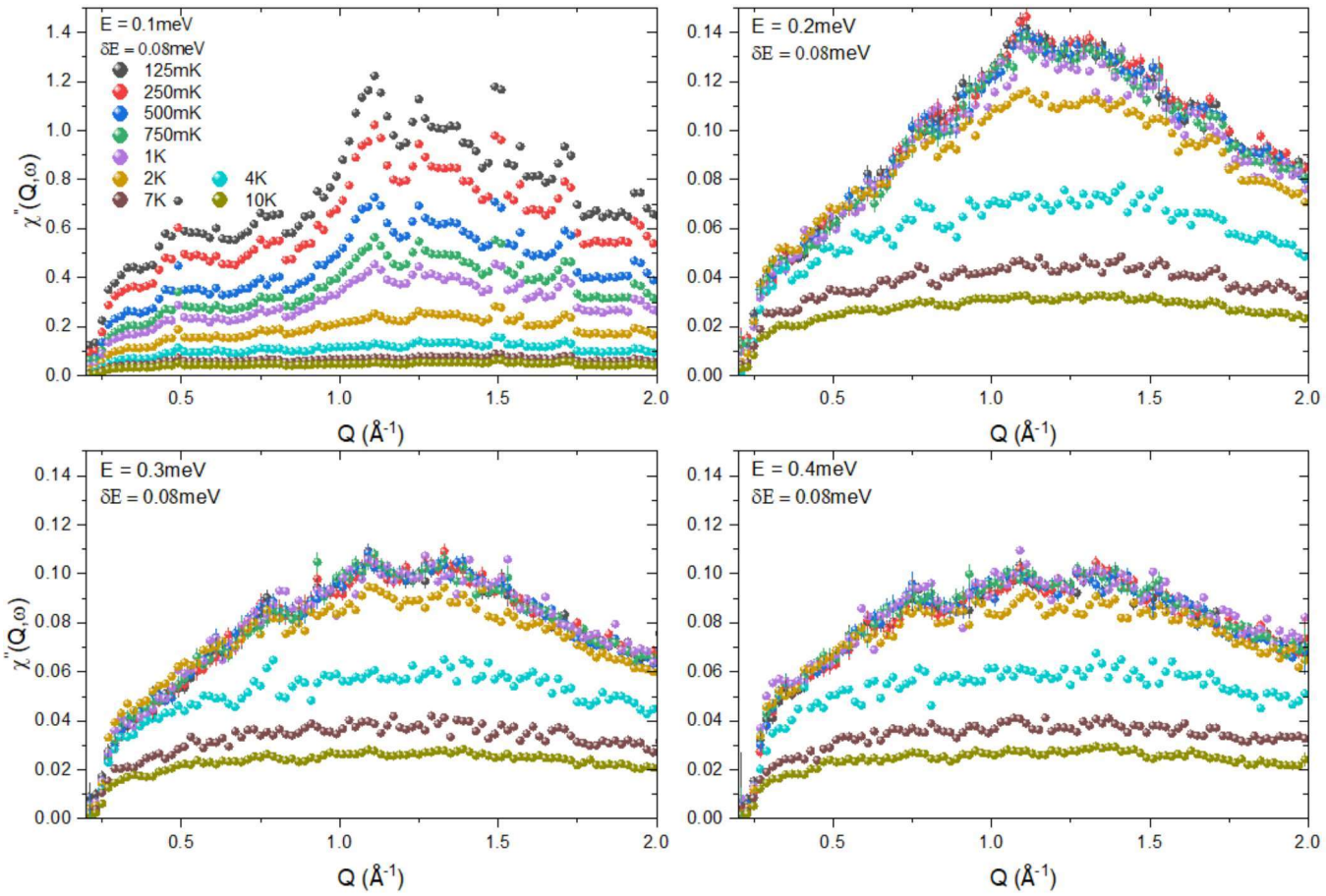

Figure 4.9: E integrated Q-cuts of the dynamic susceptibility χ''(Q,ω) for E_i = 3.2meV. The cuts are taken with an integration window of 0.08meV for E = 0.1,0.2,0.3,0.4 meV.

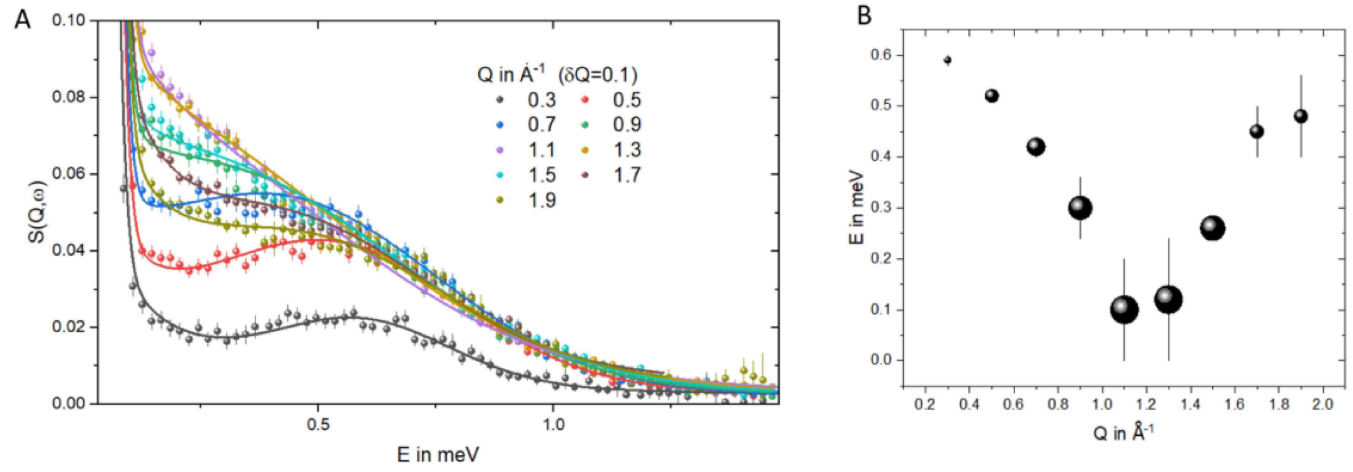

Figure 4.10: **A.** Q integrated E cuts at different Q values for 125mK and the corresponding fits (solid lines). **B.** Center position E_c of the inelastic contribution to the spectrum showing a pronounced dispersion. Size of symbols is proportional to the peak amplitude.

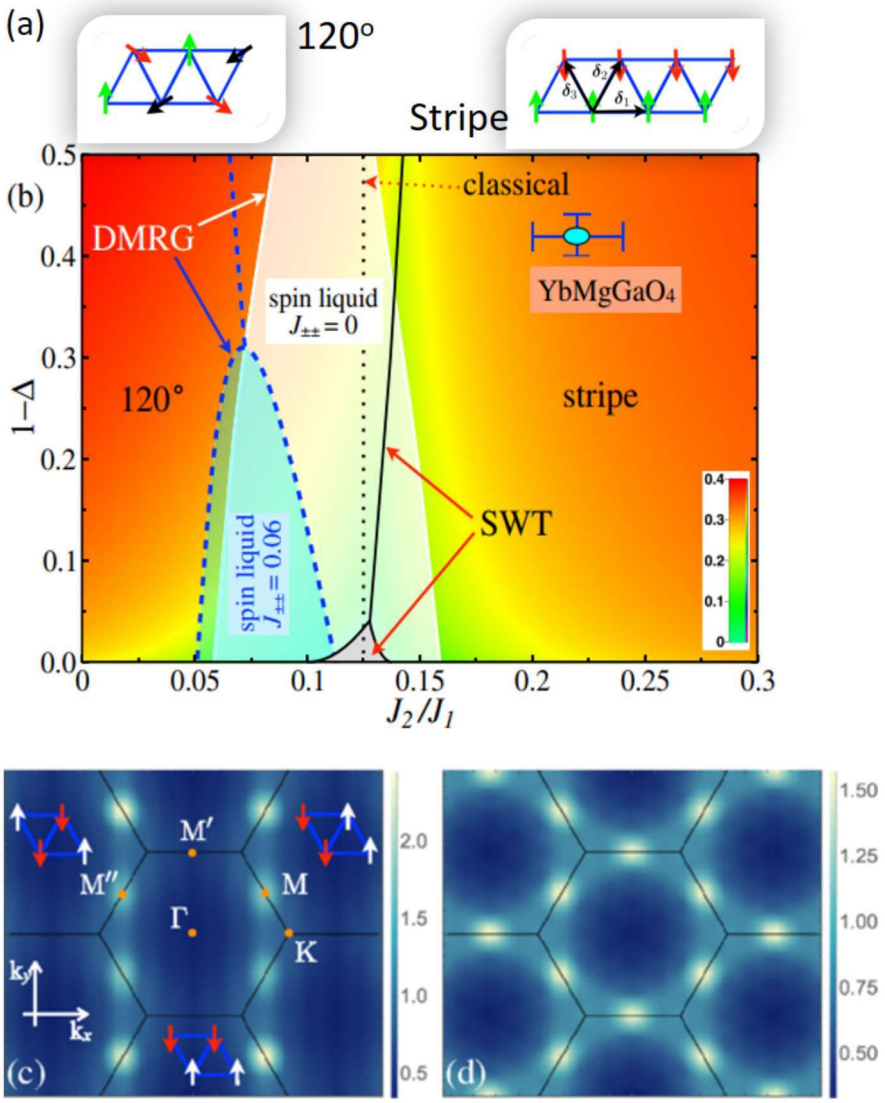

Figure 4.11: Phase diagram of a 2D THAF as estimated by Zhu et al.[47]. The top panel (a), shows the 2 ordered phases of the triangular lattice, the striped and the the 120° ordered phase. In (b) Δ is the anisotropy($\Delta = 2J_{zz}/(J_{xx} + J_{yy})$) and J_1, J_2 are the parameters of the XXZ component of the spin Hamiltonian indicating the first and second nearest neighbor exchanges, (c) is the DMRG simulated structure factor with $\Delta = 0.56$, and (d) is the symmetry averaged structure factor replicating the INS spectrum of $YbMgGaO_4$

temperatures (see Fig.4.11). However, it remains unclear as to why Er^{3+} orders more favourably with respect to Yb^{3+} in $YbMgGaO_4$.

4.5 Conclusion and outlook

In conclusion, the signatures of striped phase from the INS spectrum coupled with persistent dynamics till 25mK gives a convincing argument to consider the ground state as a superposition of striped orders. Indeed, if we assume

that the exchange parameters of the DMRG simulation for $YbMgGaO_4$ are close to $ErMgGaO_4$[9] we can expect a superposition of striped order that involves fluctuations. Thus in the light of this result, it is interesting to perform single-crystal INS measurements of $ErMgGaO_4$ to fit the corresponding DMRG calculation and then to model the inelastic diffused scattering with spin waves. From fitting the spin waves, one can estimate the parameters of the spin Hamiltonian [47].

In contrast to $ErMgGaO_4$, $YbMgGaO_4$ does not display any order[10] down to 60mK but shows a similar bump in the specific heat around 2.5K. Below this bump, the dependence of C_p follows a $T^{4/3}$ power-law dependence. In $YbMgGaO_4$, however, the temperature dependence of C_p is different from $ErMgGaO_4$ and follows a $T^{2/3}$ dependence that is speculated to be compatible with U(1) spin liquid model.

In the future it will be interesting to perform INS measurement of $YbMgGaO_4$ and compare the elastic scattering to investigate if the stripe phase exists. Neutron experiments on a high-quality single crystal of $ErMgGaO_4$ will allow quantifying the spin Hamiltonian's exchange parameters, and supporting numerical simulations [47] will help us locate the compound in the 2D THAF phase space (Fig.4.11). Another intriguing future possibility is performing a polarised neutron scattering experiment on $ErMgGaO_4$ single crystal to pinpoint the magnetic nature of the ground state on the Brillouin zone.

These additional experiments and simulations will give us a new perspective on $YbMgGaO_4$ and, more generally, 2D THAF models (see 4.11). The comparative analysis and future experimentation will then shed light on the ground state of this family of compounds and may indicate future measures on how to stabilize a quantum spin liquid state in the presence of chemical disorder.

[9] The anisotropy Δ, $\frac{J_1}{J_2}$ and $J_{\pm\pm}$

[10] Recent experiment with IN6-Sharp, ILL, France in collaboration with B.Gaulin, S.Huang and E. Smith, McMaster University.

Part III

Magnetic properties of new disorder-free $S_{eff} = 1/2$ triangular antiferromagnets

Chapter 5

$K_3YbV_2O_8$ and $K_2CsYbP_2O_8$

In this chapter we investigate two members of a new family of Yb-based triangular compounds with the chemical formula $K_3YbV_2O_8$ and $K_2CsYbP_2O_8$. Compared to the well-studied $ReMgGaO_4$ family, the interplane disorder introduced via chemical substitution between Mg and Ga is absent because of the different crystal structures. As a result, these new Yb-based triangular antiferromagnet compounds should provide a new perspective on the physics of rare-earth-based triangular quantum magnets. In Sec.5.1 we first summarize the crystal structure as found by our collaborators and then present our sample characterization using magnetization measurements (Sec.5.2). Sec.5.3 is devoted to the analysis of the anisotropy of the effective spin S_{eff} = 1/2 using inelastic neutron scattering. Finally, Sec.5.3 and Sec.5.5 deal respectively with the spin fluctuations probed by μsr and the low energy excitations probed by INS.

The relevance of this novel family of triangular antiferromagnets in the context of the search for spin liquid candidates is essential as it provides plausible disorder-free systems. The investigation of the magnetic ground state could shed light on the unexplored regions of the 2D THAF phase diagram (see Sec.1.3.2) and will help us deepen our understanding of the role of disorder in ground state selection.

5.1 Structure and synthesis

Our collaborators[1] synthesized the powder samples using the usual solid-state synthesis approach. For $K_3YbV_2O_8$, the rare-earth oxide Yb_2O_3 was fired at 1000°C for 6 hours to remove the moisture and absorbed CO_2, and then mixed with K_2CO_3, V_2O_5 in stoichiometric proportion and ground thoroughly. The pressed pellets are placed in an alumina crucible and fired at 750°C for 48 hours with several intermediate grindings. X-ray diffraction confirmed the presence of a single phase.

Both compounds crystallize in $P\bar{3}m1$ space group and feature triangular planes of magnetic Yb^{3+} ions, forming

[1] U.K. Voma, B. Koteswararao Department of Physics, Indian Institute of Technology Tirupati, India

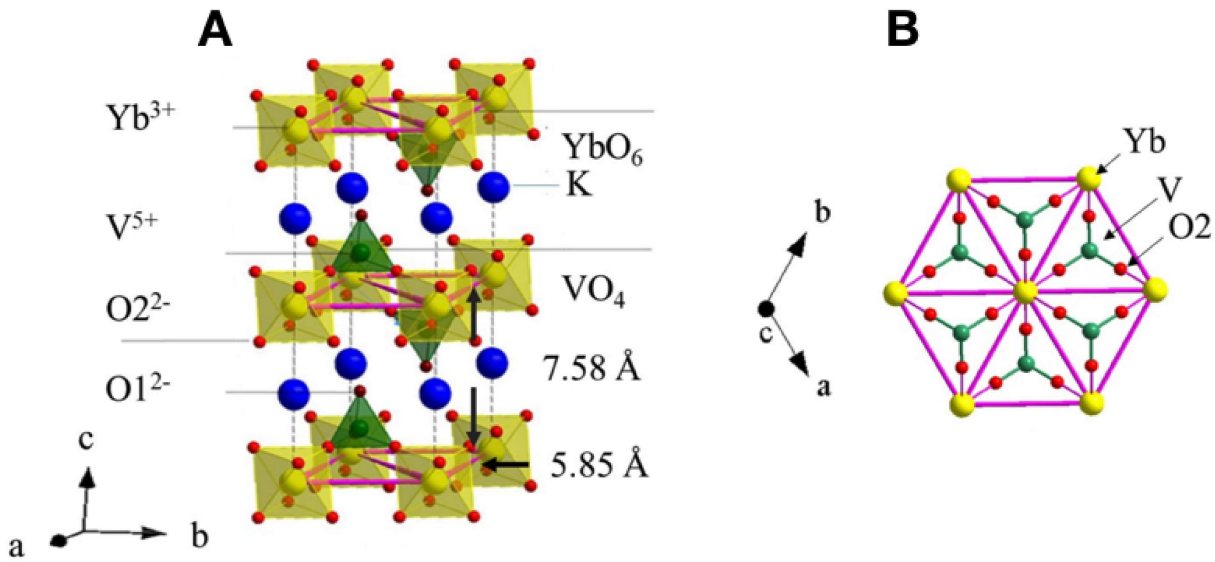

Figure 5.1: **A.** Triangular layers of Yb^{3+} in $K_3YbV_2O_8$ separated by K^{1+} ions. Yb^{3+} is at the center of an octahedra made of 6 neighboring O^{2-} anions and the associated oxygen atoms are denoted by O2.**B.** Yb^{3+} in triangular layers connected to V through O2. For more details see [60]

.

a two-dimensional magnetic system. The lattice parameters are given in Table5.1. The interlayer separation 7.58Å is larger than the nearest neighbor distance of Yb-Yb. The ratio between the interlayer and intralayer distance (d_{inter}/d_{intra}) is only 1.29[60]. This ratio for the $K_3Yb(VO_4)_2$ is smaller than the values of 1.7 for $NaYbO_2$ and 2.4 for $YbMgGaO_4$. The local point group symmetry of Yb^{3+} for both compounds is D_{3d} as found in $ReMgGaO_4$. For $K_3YbV_2O_8$, the x-ray characterization reveals that the 2D triangular layers are separated by K atomic layers, as shown in Fig.5.1.

In comparison to $YbMgGaO_4$, however, this compound's magnetic exchange path is Yb-O-V-O-Yb, whereas it is through O atoms only in $YbMgGaO_4$. The bond angles in this path are Yb-O2-V = 164.4°, O2-V-O2 = 108.7°. We anticipate that by altering the magnetic exchange paths, the spin Hamiltonian's parameters will differ from those of $YbMgGaO_4$. The form of the spin Hamiltonian, as discussed in Chapter 1, remains the same here due to the symmetry of the triangular lattice. Additionally, intersite disorder should be absent in $K_3YbV_2O_8$ and $K_2CsYbP_2O_8$, as the very different local environments of K^+ and A (V^{5+} or P^{5+}, forming $[(AO_4)_2]^{6-}$ group) prevent inter-ion exchange.

The following set of studies intends to determine whether these novel two-dimensional compounds are QSL candidates and to further examine the two-dimensional THAF phase diagram without intrinsic chemical disorder (see Sec.2.4).

Lengths in Å	$K_3YbV_2O_8$	$K_2CsYbP_2O_8$	$YbMgGaO_4$ (see Sec.3)
a = b	5.84	5.62	3.4
c	7.58	7.99	25
d_{inter}/d_{intra}	1.29	1.42	2.4

Table 5.1: Lattice parameters of $K_3YbV_2O_8$ and $K_2CsYbP_2O_8$ extracted using Rietveld refinement of XRD data.

5.2 Magnetism

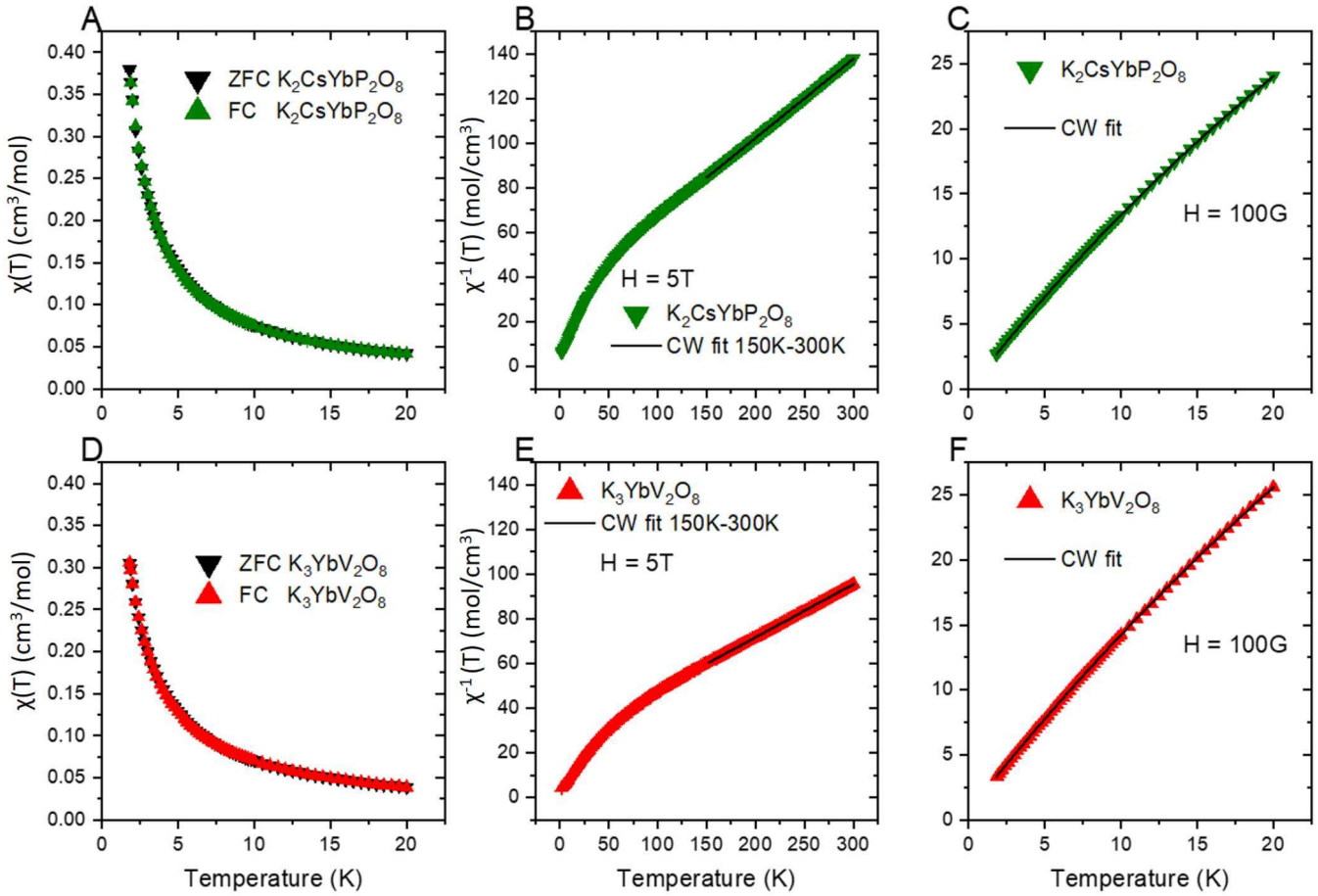

Figure 5.2: **A.**,**D.** ZFC-FC for $K_2CsYbP_2O_8$ and $K_3YbV_2O_8$ at 100G. **B.**,**E.** $\chi^{-1}(T)$ as a function of temperature under 5T external field, solid lines depicts the Curie-Weiss fits between 150K to 300K. **C.**,**F.** $\chi^{-1}(T)$ as a function of temperature in the range 1.8K to 20K under an external field of 100G with the corresponding Curie Weiss fits.

We perform a ZFC-FC measurement on powder samples of both K2CsYbP2O8 and K3YbV2O8 to determine whether order or spin freezing emerges at low temperatures. As shown in Fig.5.2, we observe that the ZFC and FC curves do not separate above 1.8K.

In Fig.5.2.B,C,E,F. the inverse susceptibility, $\chi^{-1}(T)$ as a function of temperature for both compounds are presented. In the low-temperature part (1.8K to 20K), we fit the inverse susceptibility with a Curie Weiss model (see Sec.2.4) for both compounds under a 100G applied field to avoid saturation effects.

For $K_2CsYbP_2O_8$ the effective moment, μ_{eff} = 2.0(1) μ_B, is relatively reduced from the high T (5T) value as the spins only populate the ground state Kramer's doublet in this temperature range. We estimate from the low temperature fit of the measurement (Fig.5.2C.) the total temperature independent susceptibility χ_0 = 8.45(2)$\times$ 10^{-3} cm^3/mol. Using the total diamagnetic susceptibility[61] estimated for $K_2CsYbP_2O_8$, $\chi_{D,KCYPO}$ = -1.8$\times 10^{-4} cm^3/mol$, and using the relation $\chi_0 = \chi_V + \chi_D$, we deduce the Van-Vleck susceptibility $\chi_{V,KCYPO}$ = 8.63(2)$\times 10^{-3} cm^3/mol$.

For $K_3YbV_2O_8$, the situation is similar in this low temperature regime and we use the same model. It is found that the effective moment, μ_{eff} = 2.0(1) μ_B, is similar to that of $K_2CsYbP_2O_8$. The total temperature independent susceptibility χ_0 = 6.59(7)$\times$ 10^{-3} cm^3/mol is also in close proximity to $K_2CsYbP_2O_8$. Subtracting the diamagnetic contribution to the total temperature independent susceptibility of $K_3YbV_2O_8$, χ_D = -1.6$\times 10^{-4}$ cm^3/mol, we report a Van-Vleck susceptibility $\chi_{V,KYVO}$ = 6.75(7)$\times$ 10^{-3} cm^3/mol.

To analyze the high-temperature region, in Fig.5.2B,E. we report the inverse susceptibility for the temperature range 1.8K to 300K under an applied field of 5T. As the temperature is increased from 1.8K onwards, the behavior of $\chi^{-1}(T)$ deviates from linearity with the appearance of a kink in the susceptibility in both $K_3YbV_2O_8$ and $K_2CsYbP_2O_8$ around 50K. In both compounds, as the temperature increases, the CEF levels get populated, resulting in a change in the susceptibility which explains the kink observed in the χ_0 curve for both compounds around 50K. We fit the inverse susceptibility in the higher temperature range of 150K to 300K with a Curie Weiss model for both compounds to have a qualitative idea of the effective moment. For $K_2CsYbP_2O_8$ we report the effective moment, μ_{eff} = 4.2(1) μ_B, where the free ion Yb^{3+} moment is 4.5μ_B, with J = 7/2, and θ = -87.9(3)K. For $K_3YbV_2O_8$, we perform the same analysis and estimate μ_{eff} = 5.1(1) μ_B. The Tab.5.3 and Tab.5.2, compares the extracted values from the susceptibility plots for $K_3YbV_2O_8$ and $K_2CsYbP_2O_8$. At H=5T the susceptibility cannot be defined with M/H because the linearity regime is not satisfied which explains the large value of θ for both compounds.

We perform M(H) measurements at multiple temperatures from 1.8K to 20K (see Fig.5.3) and report the magnetization isotherms as a function of the external field till 7T (Fig.5.3). As is typical in paramagnets, a linear dependence with the external field is observed for low field values. As the field is increased at the lower temperatures, the moments start to saturate with a temperature-independent linear slope and is observed for both compounds below 3K. At higher temperatures, the dependence of the magnetization of Yb^{3+} is linear for both compounds up to 7T. This is because the moments need a stronger field to overcome the fluctuations induced by the increased temperatures. Overall, this behavior corresponds to a paramagnetic phase with no order, which we model with a Brillouin function with interaction (see Sec.2.4). The Curie-Weiss fits satisfactorily explain the experimental data, and we summarize the resulting physical quantities in Table.5.2 and Table.5.3.

We estimate g_{avg} = 2.75(5) for $K_2CsYbP_2O_8$ from the M(H) isotherms, where $g_{\parallel}$ = 3.5(1) and $g_{\perp}$ = 2.3(2) (see Chapter 2). The significant contribution from both the perpendicular and the parallel component of the g-tensor indicates an intermediate character between Heisenberg and Ising type anisotropy, $g_{\perp}/g_{\parallel}$ = 0.6(1). We note that the interaction θ_{CW} is very weak for $K_2CsYbP_2O_8$ and agrees with the fit of the M(H) isotherms.

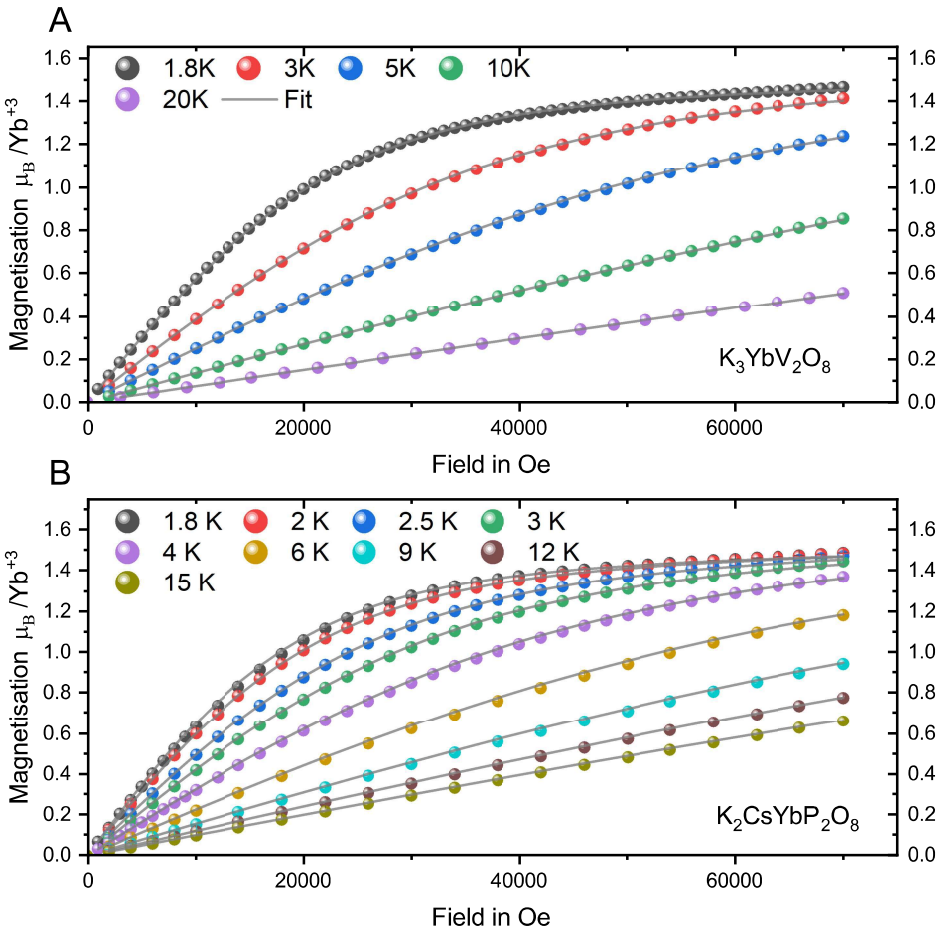

Figure 5.3: M(H) measurement for $K_3YbV_2O_8$ and $K_2CsYbP_2O_8$ at different temperatures below 20K. **A**) is $K_2CsYbP_2O_8$ **B** is $K_3YbV_2O_8$ powder samples. The solid lines depicts the powdered average fits to the experimental data.

$K_2CsYbP_2O_8$	(150,300)K 5T	(1.8,20)K 100G	M(H)	CEF (from INS see next section)
C_{CW} (mol-cm^{-3}K^{-1}) :	2.816(3)	0.662(1)		
μ_{eff} (in μ_B)	4.2(1)	2.0(1)		
θ (K)	87.9(3)	-0.01(1)	-0.08(2)	
χ_T (cm^3/mol)		8.45(2)$\times 10^{-3}$	8.9(1)$\times 10^{-3}$	
g_{avg}		2.4(1)	2.75(5)	2.7(2)
$g_\perp$			2.3(2)	2.1(1)
$g_\parallel$			3.5(1)	3.7(1)
$g_\perp/g_\parallel$			0.6(1)	0.6(1)

Table 5.2: Summary of the estimated physical quantities from the characterization measurements for $K_2CsYbP_2O_8$

$K_3YbV_2O_8$	(150,300)K 5T	(1.8,20)K 100G	M(H)	CEF (from INS see next section)
C_{CW} (mol-cm^{-3}K^{-1}) :	4.210(3)	0.665(1)		
μ_{eff} (in μ_B)	5.1(1)	2.0(1)		
$\theta(K)$	102.0(3)	-0.45(1)	-0.35(2)	
χ_T (cm^3/mol)		6.59(7)$\times 10^{-3}$	6.75(5)$\times 10^{-3}$	
g_{avg}		2.4(1)	2.77(5)	2.7(2)
$g_\perp$			2.3(2)	2.2(1)
$g_\parallel$			3.5(1)	3.5(1)
$g_\perp/g_\parallel$			0.6(1)	0.6(1)

Table 5.3: Summary of the estimated physical quantities from the characterization measurements for $K_3YbV_2O_8$

For $K_3YbV_2O_8$ the situation is similar, with g_{avg} = 2.77(5), where $g_\parallel$ = 3.5(1) and $g_\perp$ = 2.3(2), which again suggests an intermediate character between Heisenberg and Ising type anisotropy of the Yb^{3+} spins. Secondly, the antiferromagnetic interaction between Yb^{3+} ions is relatively larger than what we report for $K_2CsYbP_2O_8$, with $\theta_{CW,KYVO}$ = -0.35K, however in comparison to $YbMgGaO_4$ ($\theta_{CW,YMGO}$=-4K) it is relatively weak. Even though $K_3YbV_2O_8$ and $K_2CsYbP_2O_8$ have similar lattice parameters, the interaction strength varies in a nontrivial way because it is likely mediated by the $(VO_4)^{3-}$ or the $(PO_4)^{3-}$ group. The magnetic characterizations thus reveal that both $K_3YbV_2O_8$ and $K_2CsYbP_2O_8$ have anisotropic spins with antiferromagnetic exchanges that are very weak. In order to probe the interesting magnetic behavior, we need to explore the properties at very low temperatures, in the order of the Curie-Weiss temperature, where the interaction exchanges dominate over thermal interactions. We study the single ion physics in the following section as it imposes the spin anisotropy and determines the ground state wave function of the moments in the low-temperature regime more directly using INS.

5.3 S_{eff} = 1/2 model and single ion anisotropy

This section reports the inelastic neutron scattering experiment to obtain the CEF Hamiltonian using Steven's operator formalism for $K_2CsYbP_2O_8$ and $K_3YbV_2O_8$. The experiment is performed on powder samples of $K_2CsYbP_2O_8$ and $K_3YbV_2O_8$ at the MERLIN instrument at ISIS, STFC (UK).

5.3.1 $K_2CsYbP_2O_8$

Fig.5.4, shows the experimental S(Q,ω) for $K_2CsYbP_2O_8$ as measured using incident energies, E_i = 70meV and 170meV at 7K. Magnetic scattering intensity is distinguishable from phonon modes from the Q-dispersion. First, we introduce our analysis by identifying the phonon modes from the S(Q,ω) intensity plots. We note the presence of diffused scattering in the high Q and low E spectrum for both measurements due to phonon modes. Moreover, for the 170meV measurement, we observe further scattering at higher energies, near 70meV and 120meV, increasing

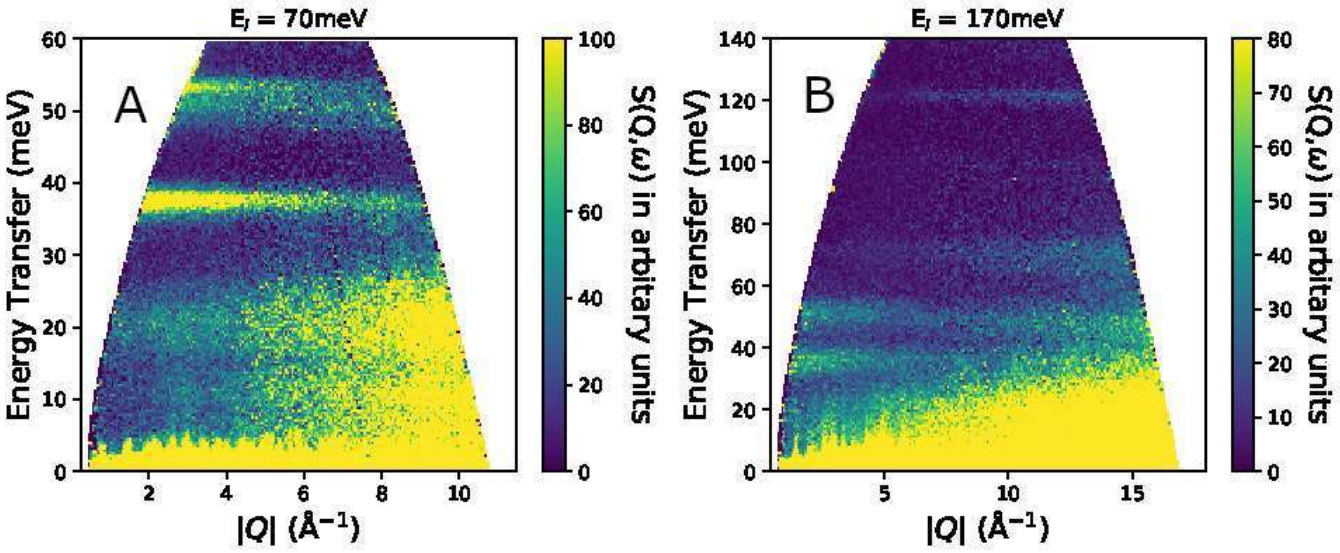

Figure 5.4: S(Q,ω) measured with an incident energy E_i = 70meV and 170meV at 7K for $K_2CsYbP_2O_8$.

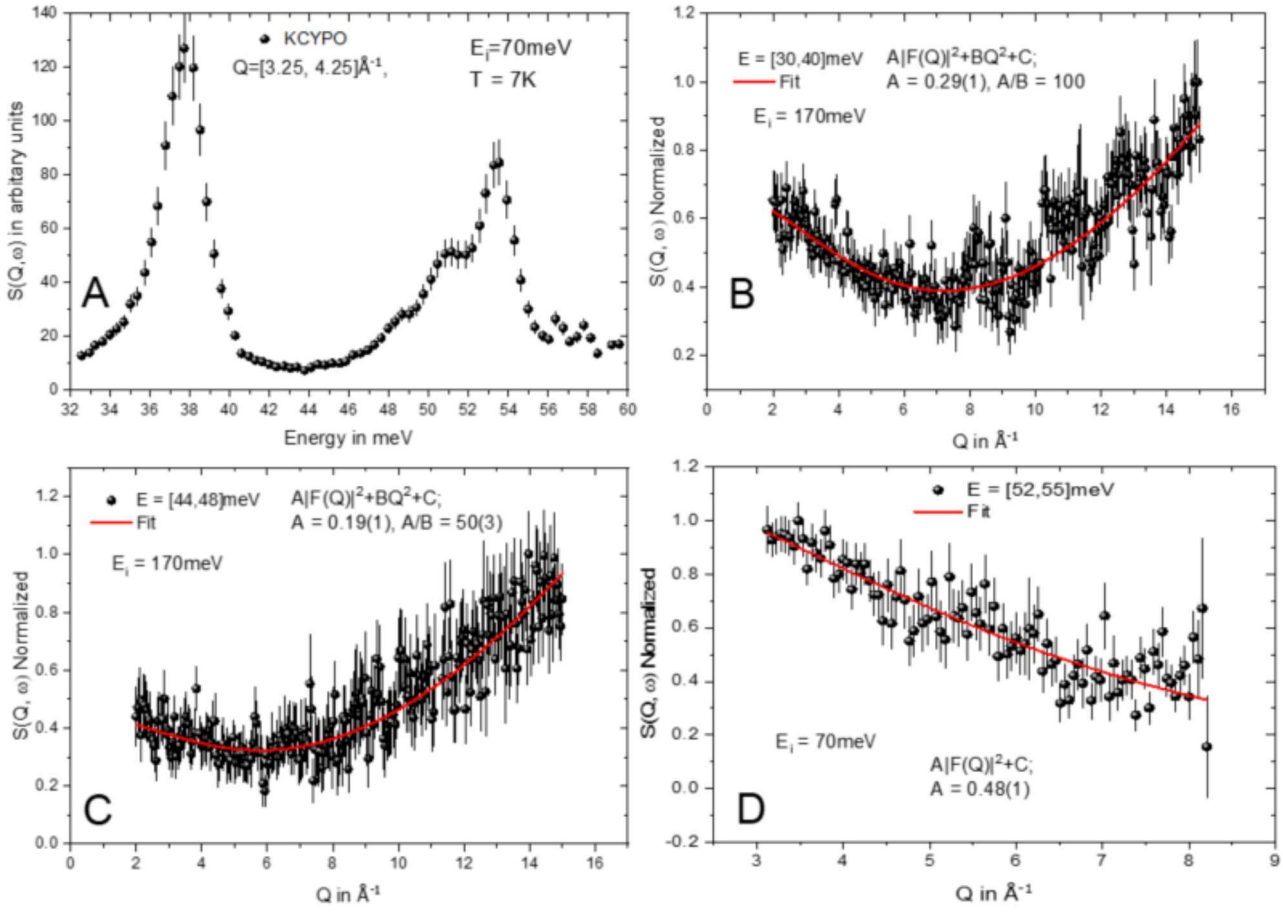

Figure 5.5: **A.** Q-integrated E-cut of KCYPO taken at 7K. **B-D**. S(Q,ω) Q-cuts at the peak positions. Solid lines depict fits with Eqn.5.1.

intensity at larger Q-values and thus due to phonons.

In contrast to the phonon excitations, we observe that excitations in the energy ranges (35,40)meV and (50, 55)meV in Fig.5.4A,B. have a distinct Q-dependence, and the intensity decrease with increasing Q. For clarity, we show (Fig.5.5A.) the Q-integrated E-cuts between 3.25Å^{-1} and 4.25Å^{-1}, where we observe the presence of multiple peaks between 32meV and 60meV.

Now, these magnetic excitation peaks may be contaminated with phonons. In order to decouple the phonon modes, we first consider the Q-dispersion of these excitation peaks (Fig.5.5B-D.). Fig.5.5B,C. shows the Q-dispersion of the peaks between [30meV, 40meV] and [44meV, 48meV] respectively, and we observe a rise in intensity at large Q values. We also observe that the peak between [52,55] meV (Fig.5.5D.) does not show phonon contributions but could be measured up to 8Å^{-1} only.

Thus, to model the Q-dependence of this intensity I(Q), one has to consider both the magnetic and lattice contribution, and so we fit the intensity with an empirical formula (Eqn.5.1) accounting for the Yb^{3+} form factor, F(Q) [2], a constant background, C, and a phonon contribution.

$$I(Q) = AF(Q) + BQ^2 + C \tag{5.1}$$

where A is the scaling factor for Yb^{3+} form factor, and B the scaling factor for phonon contribution.

	B_0^2	B_0^4	B_0^6	B_6^6	B_3^4	B_3^6
Inital Guess :	1.5	0.02	0.02	0.003	0.5	-0.004
$K_2CsYbP_2O_8$:	0.189	-0.0192	0.00003	-0.0043	0.359	0.0292
$K_3YbV_2O_8$:	-0.0827	-0.00117	0.00062	-0.00214	-0.265	0.01316

Table 5.4: Comparison of estimated Steven's operator coefficients (in meV) for $K_2CsYbP_2O_8$ and $K_3YbV_2O_8$ from CEF simulation

Thus, we have to consider the energy of the phonon modes when fitting the experimental data to determine the CEF energy levels accurately. It is also crucial to accurately estimate the relative intensity of the CEF peaks, and there is a risk of inaccuracy if the phonon energy and intensity are not correctly determined. In Fig.5.6A. the 1st peak at 38meV is skewed with a left asymmetry extending till 32meV. As CEF peaks are symmetric about their peak positions, the asymmetry can be present only if there is more than one peak in the range of (32,42)meV. Secondly, we observe two left shoulders for the peak at 54meV, suggesting that there are in total at least three peaks in the range (44,56)meV. Finally, if we take all the evidence of phonons into account from fits of Fig5.5B-D, the measurement is fit to a good approximation with CEF peaks at 38, 51, and 54meV (see Fig.5.6) and intermediate broad phonon modes at 37meV and 49meV. This physical scenario is consistent with the three excitations expected from the J = 7/2 state of Yb^{3+} ion (4 doublets).

[2]For the analytical expression of the form factor, consult www.ill.eu/sites/ccsl/ffacts

Using this model, we estimate Steven's operator coefficients by the fitting procedure discussed in Sec.2.3.3. We use the estimated peak positions along with their relative intensities and constrain the problem using g_{avg} = 2.7 (in agreement with the M(H) fits in the previous section). The estimated Hamiltonian obtained from the best fit of Steven's operator parameter set is listed in Table.5.5. From the Table.5.5 we note the nature of ground state Kramer's doublet of Yb^{3+},

$$|\pm\rangle = \pm 0.63\,|\pm 7/2\rangle \pm 0.15\,|\mp 5/2\rangle - 0.76\,|\pm 1/2\rangle \tag{5.2}$$

The ground state doublet is then composed primarily of $|\pm 1/2\rangle$ and $|\pm 7/2\rangle$. For this particular ground state doublet, we obtain $g_{\perp}$ = 2.1(2) and $g_{\parallel}$ = 3.8(2), with g_{avg} = 2.7(1). The anisotropy, $g_{\perp}$ / $g_{\parallel}$ = 0.6(1) indicates an intermediate character between Heisenberg and Ising-like nature of the spins for the GS Kramer's doublet. The estimated values for the g-tensor are in good agreement with the M(H) results in the previous section.

5.3.2 $K_3YbV_2O_8$

The crystal field levels for $K_3YbV_2O_8$ are determined in the same way as in $K_2CsYbP_2O_8$. Still, we briefly summarize the analysis protocol for future reproduction if needed. First, we note the presence of the phonon modes at low energy and high Q regions. These excitations disappear when we subtract the 310K measurement from the 7K measurement (Fig.5.7C.). Secondly, we identify the excitations between 35meV and 60meV as distinct from the phonon modes. To confirm these as magnetic excitations and to decouple them from the phonon modes, we take various Q-cuts (Fig.5.8) to see if the Yb^{3+} form factor models the Q-dependence. By this approach, we pinpoint three different excitations as we show in Fig.5.6A. We also identify a broad phonon mode present in this energy range, and the detailed identification is not shown for clarity.

Finally, we fit the Q-integrated E-cuts (Q = [3.25,4.25]) with four Gaussian peaks. Three of these four Gaussian corresponds to magnetic excitations, whereas one corresponds to the broad phonon mode. The Gaussians modeling the magnetic excitations are constrained to have a fixed width (FWHM), and the best fit is shown in Fig.5.6A.

From the analysis, we find the CEF peaks at E = 38.2meV, 50.7meV, and 55.2meV. Using Steven's operator formalism, we fit the peak positions and their relative intensity to obtain the CEF Hamiltonian for $K_3YbV_2O_8$, shown in Table.5.5. The corresponding Steven's operator coefficients are listed in Table.5.4. For this set of coefficients, the ground state wavefunction is,

$$|\pm\rangle = \mp 0.8\,|\pm 7/2\rangle \pm 0.54\,|\pm 5/2\rangle + 0.28\,|\pm 1/2\rangle \tag{5.3}$$

This doublet has $g_{\perp}$ = 2.2(1) and $g_{\parallel}$ = 3.5(1), with g_{avg} = 2.7(1). The anisotropy, $g_{\perp}/g_{\parallel}$ = 0.6(1) indicates an intermediate character between Heisenberg and Ising character of the spins for the GS Kramer's doublet.

The CEF peak positions are comparable for both the compounds as expected from the identical crystal structure and local oxygen environment of Yb^{3+} and the significant separation between the ground state doublet and the first excitation justifies the S_{eff}=1/2 model. The g-tensor for $K_3YbV_2O_8$ is similar to $K_2CsYbP_2O_8$ and the two compounds therefore have a similar anisotropy. However, the key difference between these two compounds is the Curie-Weiss temperature, θ_{CW}. Because of the extremely weak value of θ_{CW} for $K_2CsYbP_2O_8$, we decided to perform advanced measurements (INS and μSR) on only $K_3YbV_2O_8$ only. The following sections present our results on $K_3YbV_2O_8$ which has a larger antiferromagnetic interaction θ_{CW} = -0.35(2)K.

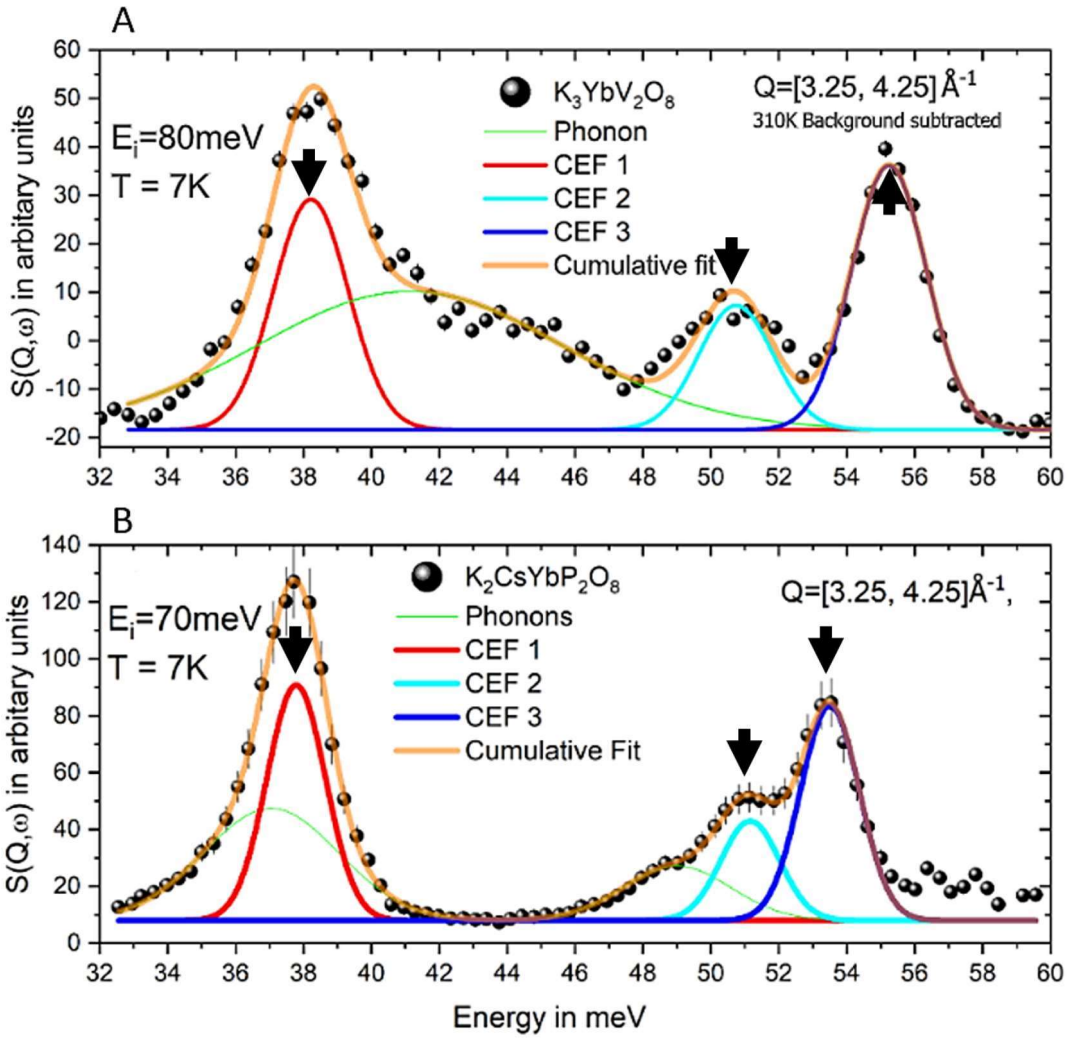

Figure 5.6: S(Q,ω) E-cuts depicting the CEF peak positions (black arrows). Thick solid lines indicate the CEF contribution with Gaussian peak functions with the same width (FWHM) while the green lines indicate the broader phonon peaks. **A.** shows the 7K measurement at E_i = 70meV for $K_2CsYbP_2O_8$ while **B.** shows the 7K measurement for $K_3YbV_2O_8$ subtracted from the 310K dataset.

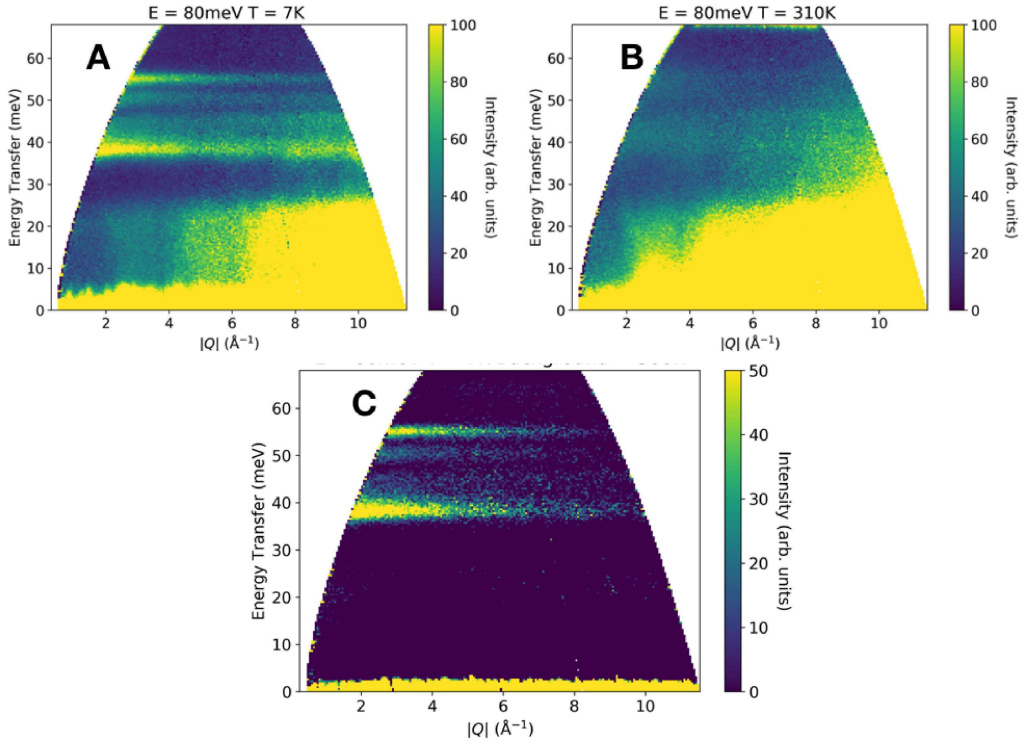

Figure 5.7: S(Q,ω) at 7K and 300K with E_i = 80meV for $K_3YbV_2O_8$. **C**. shows the subtracted 7K data using 310K scan as the background.

Energy (meV)	$\|-7/2\rangle$	$\|-5/2\rangle$	$\|-3/2\rangle$	$\|-1/2\rangle$	$\|1/2\rangle$	$\|3/2\rangle$	$\|5/2\rangle$	$\|7/2\rangle$
$K_2CsYbP_2O_8$								
0	-0.63	0	0	-0.76	0	0	-0.153	0
0	0	0.15	0	0	-0.76	0	0	0.63
37.7	0	0	-0.96	0	0	0.28	0	0
37.7	0	0	0.28	0	0	0.96	0	0
51.2	0.56	0.21	0	-0.32	-0.09	0	-0.71	-0.17
51.2	0.17	-0.71	0	-0.09	0.32	0	-0.21	0.56
53.5	-0.03	0.65	0	0.04	0.55	0	-0.04	0.51
53.5	0.51	0.04	0	-0.55	0.04	0	0.65	0.03
$K_3YbV_2O_8$								
0	0.80	0	0	0.28	0	0	0.54	0
0	0	-0.54	0	0	0.28	0	0	-0.80
38.2	-0.04	0.70	0	-0.11	0.64	0	0.12	-0.26
38.2	0.26	0.12	0	0.64	0.11	0	0.70	0.04
50.7	0	0	-1	0	0	0	0	0
50.7	0	0	0	0	0	-1	0	0
55.2	-0.54	0.01	0	0.71	-0.02	0	0.44	-0.02
55.2	0.02	0.44	0	-0.02	-0.71	0	-0.01	-0.54

Table 5.5: Compositions of the CEF levels in the $|m_j\rangle$ basis for Yb^{3+} moments (J=7/2) for Yb^{3+}) $K_2CsYbP_2O_8$ and $K_3YbV_2O_8$, as determined from our CEF analysis.

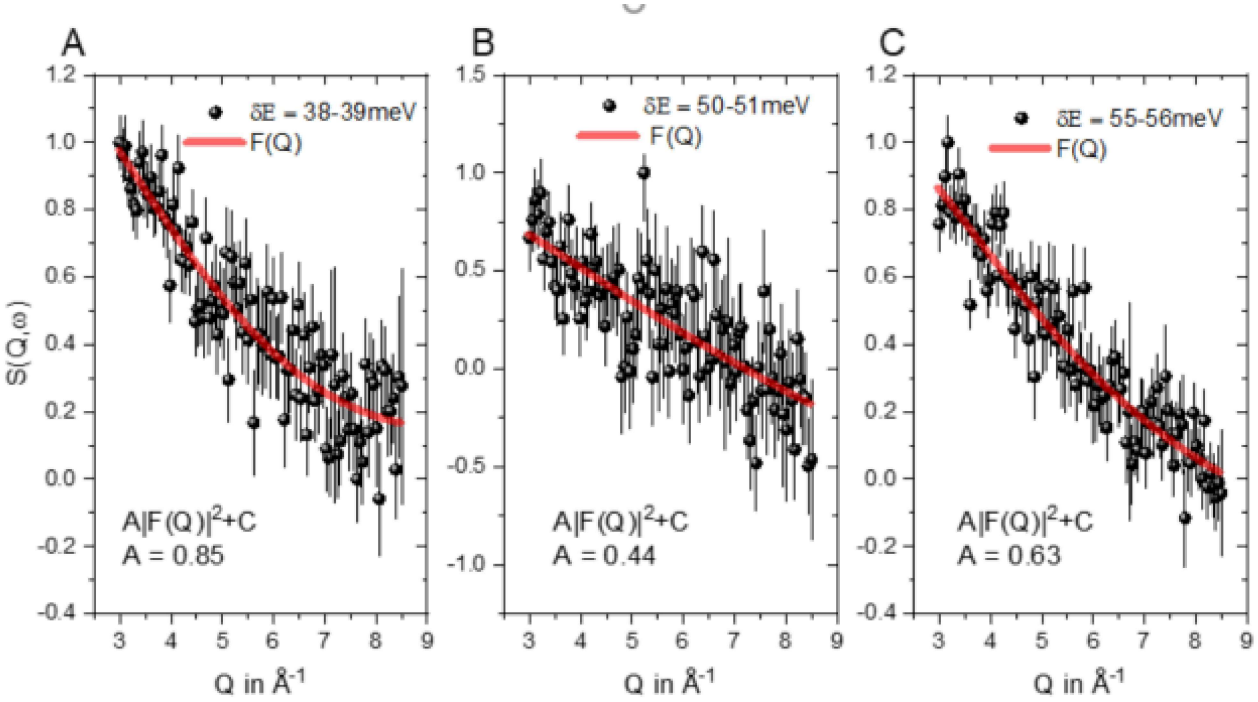

Figure 5.8: E-integrated Q cuts of S(Q, ω) at 7K with 310K data as the background, centered around CEF positions. $K_3YbV_2O_8$ structure factor for different energy positions.

5.4 Persistent spin dynamics probed by μSR

This section describes our results of muon spin relaxation performed at ISIS, STFC, (UK) on $K_3YbV_2O_8$ powder sample using the MUSR instrument. Given the low magnetic exchange of the Yb-based triangular magnets, it is all the more important to investigate their spin dynamics down to mK temperatures.

Two different setups were used: a dilution fridge and a conventional He-flow cryostat which give different backgrounds.

In Fig.5.9A. we plot the time dependence of the detector asymmetry of the muon disintegration, A(t), at several fields applied in the longitudinal direction (LF mode), at 60mK. First we note the absence of any significant dip in the ZF mode. If the relaxation were of static origin, the corresponding field would not exceed a few Gauss and we would expect a complete decoupling in a LF of 10-20 G, which is not observed. From this measurement, we establish the presence of a fluctuating state of the Yb^{3+} spins down to 60mK.

We then focus on the temperature dependence of the muon relaxation, λ. To do this we analyse A(t) at different temperatures (Fig.5.9B,C.). At high temperatures, above 50K (see Fig.5.9C.) we observe the emergence of a weak oscillation or a dip in A(t) around t = 5μs. If $K_3YbV_2O_8$ is supposedly paramagnetic in this temperature regime, then there is no reason to observe this dip except if there is a second muon site that experiences the static nuclear moments. This is a reasonable physical scenario as in $K_3YbV_2O_8$ there are multiple oxygen sites and the muon can couple to any one of these oxygen anions and so we consider that the first muon site corresponds to the muons close

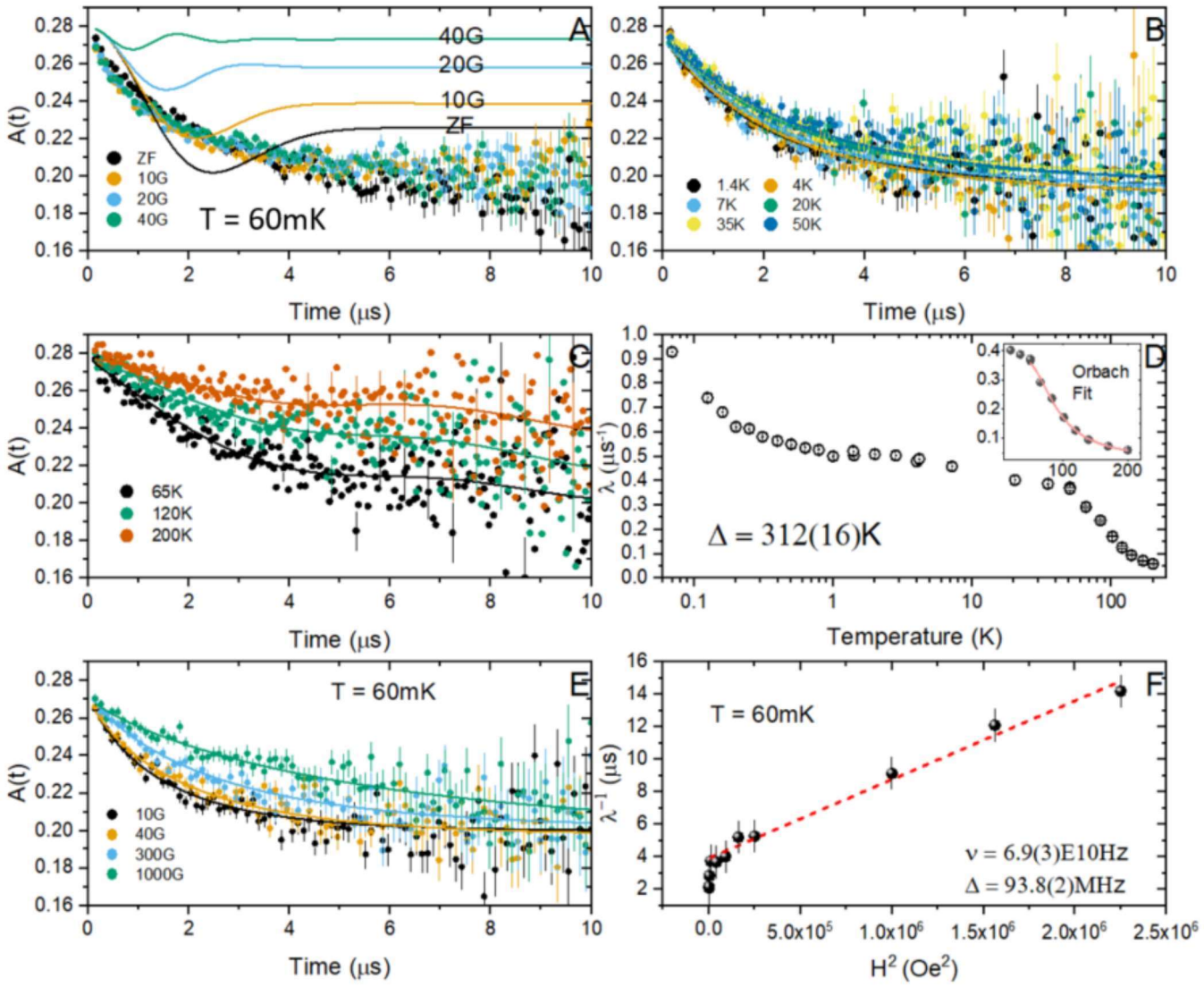

Figure 5.9: **A.** LF decoupling measurement for $K_3YbV_2O_8$ muon spin relaxation at 60mK. The colored lines indicate the corresponding static Kubo-Toyabe functions at different LF values. **B.** Selected plots of temperature dependence at 10G LF, below 50K. **C.** Selected high temperature plots under 10G LF **D.**Spin relaxation as a function of temperature, as estimated from the fits. The inset shows the fit of the Orbach spin-lattice relaxation process **E.** Selected A(t) at 60mK for different values of LF **F.** Linear dependence of the spin relaxation λ with H^{-2}, the dashed line represents the fit with the Redfield equation.

to the Yb^{3+} moments, whereas the second muon site corresponds to muons that have thermalized relatively far from the Yb^{3+} moments. Thus we use a simple model with two muon sites in $K_3YbV_2O_8$ and a constant temperature independent sample background accounting for muons stopping outside the sample. We attempt to model A(t) with this argument where we choose an exponential decay function to model the relaxation at the first muon site and a Kubo Toyabe (KT) function to represent the non-relaxing A(t) of the second muon site, with a constant temperature independent background B:

$$A(t) = A_1 \exp\{-\lambda_1 t\} + A_2 KT(H = 10G, \Delta, t) + B \tag{5.4}$$

KT(H, Δ, t) is the Kubo-Toyabe relaxation function, where H=10G is the longitudinal field, Δ is the width of the field distribution, and B is the background. The fits are constrained by fixing the value of A_1, A_2, B and we have A_2 = 2$\times$ A_1. The fits are shown by the solid lines in Fig.5.9C. and are in good agreement with the observation.

At low temperatures ($<$50K), the situation is different and we observe that the relaxation becomes exponential and does not change significantly with temperature (Fig.5.9B.) . Following the high temperature analysis leading to consider two muon sites, A(t) can be approximated by two exponential decays at low temperatures($\leq$ 50K), where, the first one is with a strong relaxation rate λ_1 and the second one with a weak relaxation rate, and to make our analysis more coherent we fix the ratio A_2/A_1 to be the same as found at high temperature. The low-temperature model can be written as follows:

$$A(t) = A_1 \exp\{-\lambda_1 t\} + A_2 \exp\{-\lambda_2 t\} + B' \tag{5.5}$$

A_1, A_2 is the asymmetry corresponding to the first and second sites, respectively, and B' is the background. From our fits using this model, we find that the spin relaxation λ_1 is an order of magnitude larger than λ_2. λ_2 being weak, it makes the second component significantly flat. This relaxation wipes out any possible dip of static origin.

The spin relaxation λ_1 as a function of temperature obtained from our analysis is shown in Fig.5.9D. Upon cooling from 200K to 50K, we note a bump of λ till it hits a plateau at 50K. This bump[3] is fitted with an Orbach spin-lattice relaxation process. We estimate the energy gap between the ground state doublet and the first excited state to be 26meV or 312K (see Sec.2.3), that is in the same ballpark with the 1st CEF energy level value that we obtained from inelastic neutron scattering analysis (38.2meV). As the temperature is decreased, λ plateaus from 50K till 1K, and we observe a gradual increase of λ below this temperature. The situation is similar as in $YbMgGaO_4$ [44], where a temperature-independent plateau appears till 4K, followed by an increase of lambda till it reaches a low-temperature plateau at 0.4K till the lowest measured temperature of 45mK. The authors attribute the low-temperature-independent plateau to be a signature of the U(1) QSL phase as it shows persistent spin dynamics well below the interaction temperature. Given the fact that the interaction θ_{KYVO} is much weaker than θ_{YMGO} (θ_{KYVO} = θ_{YMGO}/6), it is then reasonable to expect a λ plateau that would occur at lower temperatures ($\leq 60mK$) than investigated here.

We also performed LF measurements to quantify the response of the fluctuations under an applied field. The longitudinal field dependence measurement at the base temperature is reported in Fig.5.9E. We note the change of the A(t) as the field is increased, and we fit this measurement with a stretched exponential model with a background:

$$A(t) = A \exp\big(-(\lambda t)^{\beta}\big) + B \tag{5.6}$$

A is the sample asymmetry, β is the stretch exponent, and B is the background. We manage to constrain A, β,

[3]We observe an inflection in the susceptibility measurement at the same temperature region, see Sec.5.2

and B over all the measurements for this fit. The value of the stretch coefficient $\beta = 0.75$ is inferior to 1 in agreement with the existence of multiple muon sites.

The dependence of λ^{-1} as a function of H^2 is shown Fig.5.9F. This inverse square dependence of the spin relaxation λ with the external field is expected for a Lorentzian fluctuation spectrum within the framework of the Redfield relaxation theory. This exponent is commonly observed across literature from paramagnetic salts [48] to frustrated magnetic systems where the persistent spin dynamics is observed. From the Redfield model we obtain the fluctuation ν = 6.9(3)$\times 10^{10}$ Hz and Δ = 93.8(2)MHz. Using the relation $\Delta \approx \gamma_\mu \sqrt{< B_{loc}^2 >}$, we obtain $\sqrt{< B_{loc}^2 >} \approx$ 1 kG. One possible explanation for the large internal field is because it is dominated by dipolar fields rather than exchange fields.

Comparing our analysis to $YbMgGaO_4$ (see Li et al. [48]) reveals that S(t), the dynamic autocorrelation function, behaves as a power law at low temperatures in $YbMgGaO_4$ and attenuates much more slowly compared to the paramagnetic regime at high temperatures($\geq$ 4K). At low temperatures, this observation was interpreted as the onset of long-time spin correlations. The Yb^3 moments in $YbMgGaO_4$ are highly entangled not only in space but also in time, without exhibiting symmetry violation or spin freezing. In the paramagnetic regime, they found ν = 4$\times 10^{10}$ Hz and Δ = 60 MHz. Here, we have fitted the data with the λ_{avg} in contrast to the analysis presented by the authors. However, we can confirm the fast fluctuation limit of the Yb^{3+} moments in $K_3YbV_2O_8$ since even at 60mK, we observe $\Delta \ll \nu$.

Thus in conclusion, we have established the dynamic character of the moments in $K_3YbV_2O_8$ that we probe further in the next section using INS.

5.5 Dynamic correlations probed by inelastic neutron scattering

We report our results of the low energy neutron scattering experiment performed at ILL, Grenoble, France, on a powder sample of $K_3YbV_2O_8$, on the IN6 spectrometer. The S(Q,ω) plots measured at an incident energy E_i = 3.2meV at different temperatures are depicted in Fig.5.10. From the figures, we note an extremely weak temperature-dependent scattering signal and the presence of spurious features likely arising from incoherent elastic scattering from the monochromator and a nuclear Bragg reflection from the sample. These spurious scattering intensities due to multiple scattering are characterized by a vertical rod-shaped intensity emerging from the elastic line at the nuclear Bragg peak positions (see Fig.5.11).

For investigating the presence of quasielastic scattering we take Q-integrated E-cuts at 0.5Å^{-1} and 1.75Å^{-1}, with δQ = 0.3Å^{-1}. In both cases (see Fig.5.11C,D.) the peak centered at 0meV is broader than the resolution of the instrument (ΔE = 0.07meV, FWHM), suggesting the presence of quasi-elastic scattering extending up to $\sim$ 0.4meV. In Fig.5.11B. we fit the 60mK, E_i = 3.2meV measurement with an elastic and a quasielastic peak, also taking into account the Bose Factor (see Eqn.5.7):

$$S(E) = A_1 \exp\left(-\left[\frac{E}{\sqrt{2}w_1}\right]^2\right) + \left(\frac{2A_2}{\pi} E \frac{w_2^2}{4E^2 + w_2^2}\right) / \left(1 - \exp\left(-\frac{E}{k_B T}\right)\right) \tag{5.7}$$

here, A_1, w_1 is the intensity and the width of the elastic peak. A_2, w_2 is the quasielastic component's intensity and characteristic width, and the dividing factor is the Bose factor at temperature T. We find out from the analysis that if w_1 is constrained to the instrument resolution of 0.07meV, the quasielastic component is necessary to model this measurement correctly. The fit thus confirms the presence of a quasielastic component till the base temperature of 60mK. The presence of the quasielastic component is consistent with liquidlike correlations or fluctuations in $K_3YbV_2O_8$ down to 60mK in agreement with our μSR results.

Furthermore, we note the presence of an inelastic contribution around 0.6meV, appearing below 800mK. However, the signal is weak, and because of the proximity to multiple scattering artifacts, the signal is challenging to isolate. For investigating the nature of this inelastic peak mode, we perform an E-integrated Q cut for E=0.65meV with δE = 0.1meV. The cut shown in 5.12A. shows a clear dispersive signal in Q; however, the low intensity, presence of artifacts, and the broad signal due to the powder averaging make it challenging to fit and interpret this

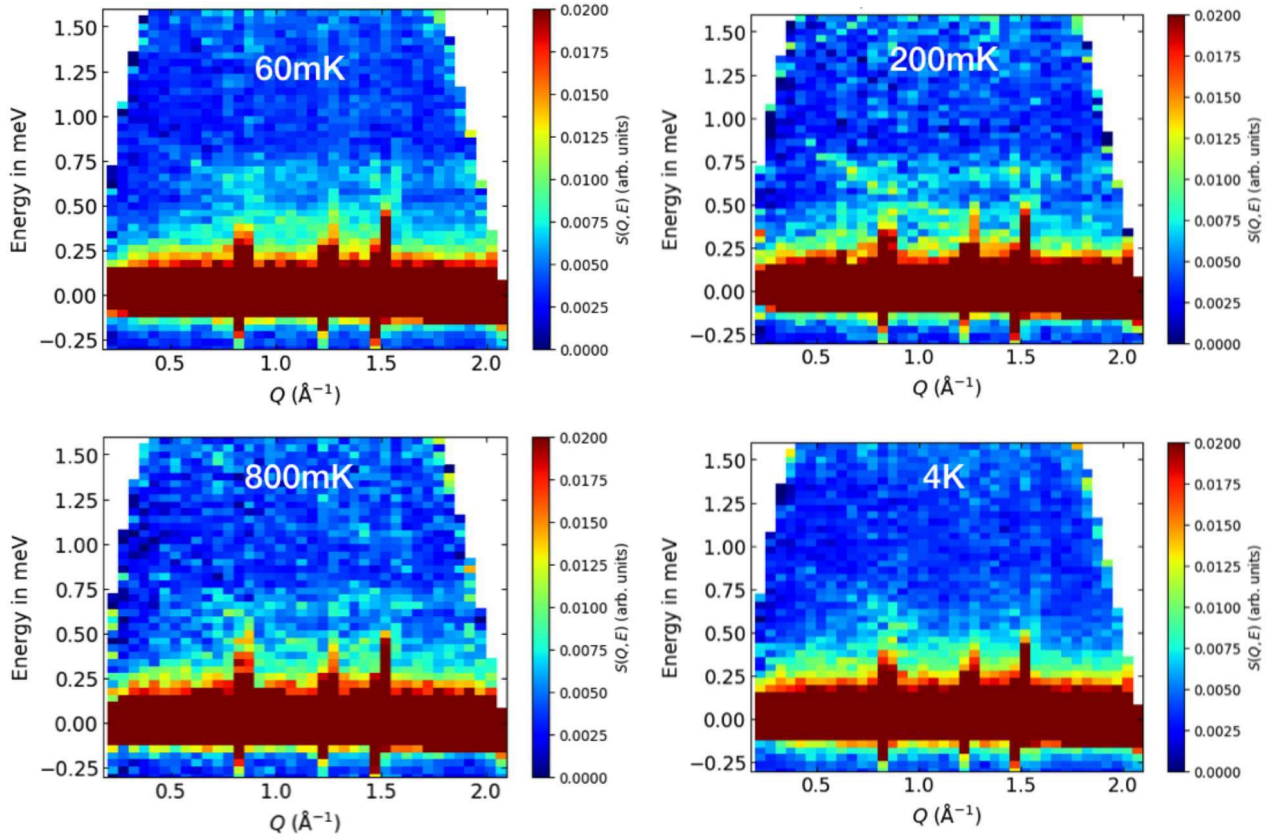

Figure 5.10: S(Q,ω) intensity plots for low energy INS between 60mK and 4K for powder sample of $K_3YbV_2O_8$, with E_i = 3.2meV.

measurement. Still, we believe that this intensity is genuine because for the Q-integrated E cut at 1.75Å^{-1}, around 0.7meV there is a temperature dependence of the inelastic scattering intensity(see Fig.5.11D). We observe that the intensity decreases abruptly from 60mK to 4K in this region.

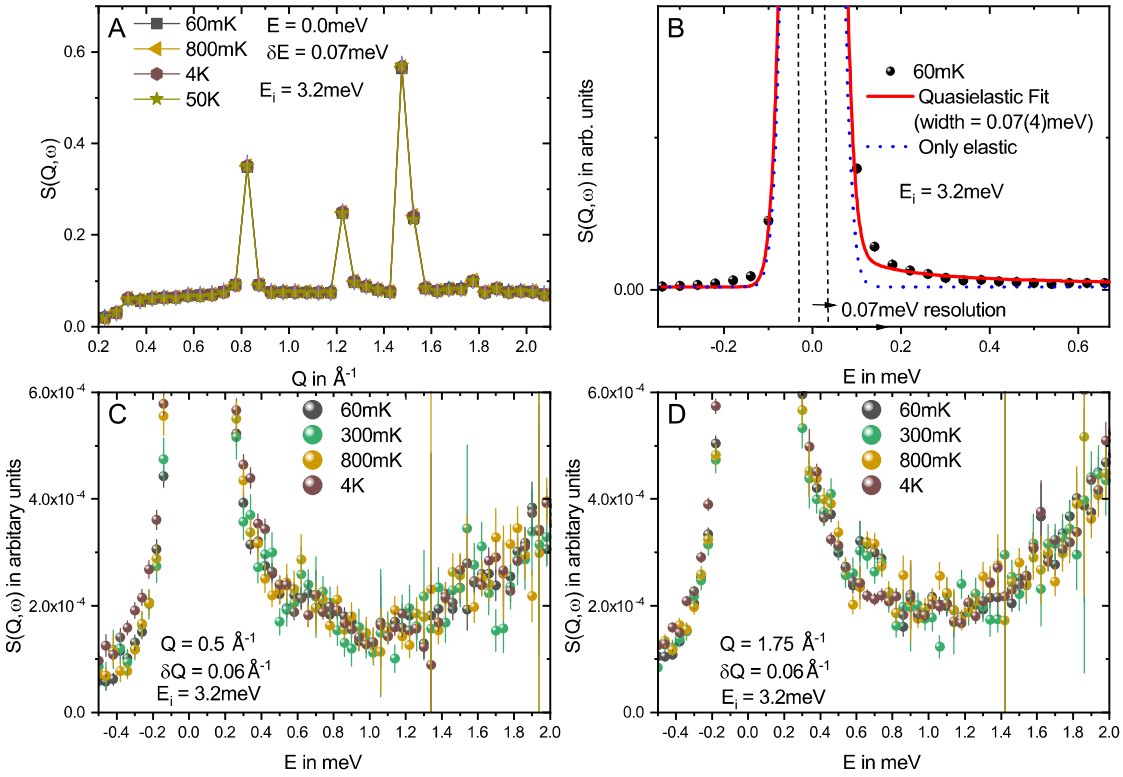

Figure 5.11: **A.** Elastic cut of $K_3YbV_2O_8$ at E_i = 3.2meV. **B.**60mK cut at 0.5Å^{-1}; red line shows fit with a quasielastic peak represented by a Gaussian, as an elastic peak is not sufficient to fit the intensity at E = 0.2meV **C.** and **D.** shows the Q-integrated E-cuts from the low energy INS plots for 0.5Å and 1.75Å for $K_3YbV_2O_8$ powder sample. The temperature evolution around 0.65meV for **D.** is clearly noticeable from this plot.

In Fig.5.12A, we show the cut of the dynamic susceptibility χ'' at 0.65meV within a 0.1meV integrated window. The Fig.5.12B, shows the measurement at 60mK and Fig.5.12C shows the 60mK subtracted by the 4K measurement. We qualitatively observe a slight temperature dependence specifically in the regions free from spurious contributions, as highlighted by the yellow boxes. This temperature dependence can also be observed in Fig.5.11D. and Fig.5.10.

We first try to understand this excitation by considering that a small fraction of Yb^{3+} moments start forming singlet locally with the nearest or the next nearest neighbors in the triangular plane. We model this behavior with a powdered averaged equal time structure factor of valence bonds [62] as given below, where the spins of the nearest neighbor Yb^{3+} ions on the triangle lattice entangle to form valence bonds.

$$\chi(Q)'' = |F(Q)|^2\left(1 - \alpha\frac{\sin(Qd)}{Qd}\right) \tag{5.8}$$

where F(Q) is the analytical estimation of the Yb^{3+} form factor and d is the distance between antiferromagnetically interacting spins, and α is the effective contribution of the moment.

The signal to noise ratio is poor and we observe an increase in intensity around 1.1$Å^{-1}$ and 1.8$Å^{-1}$ upon cooling (see Fig.5.12A.). The fit gives a reasonable agreement with the 60mK data, for both the nearest neighbor and the

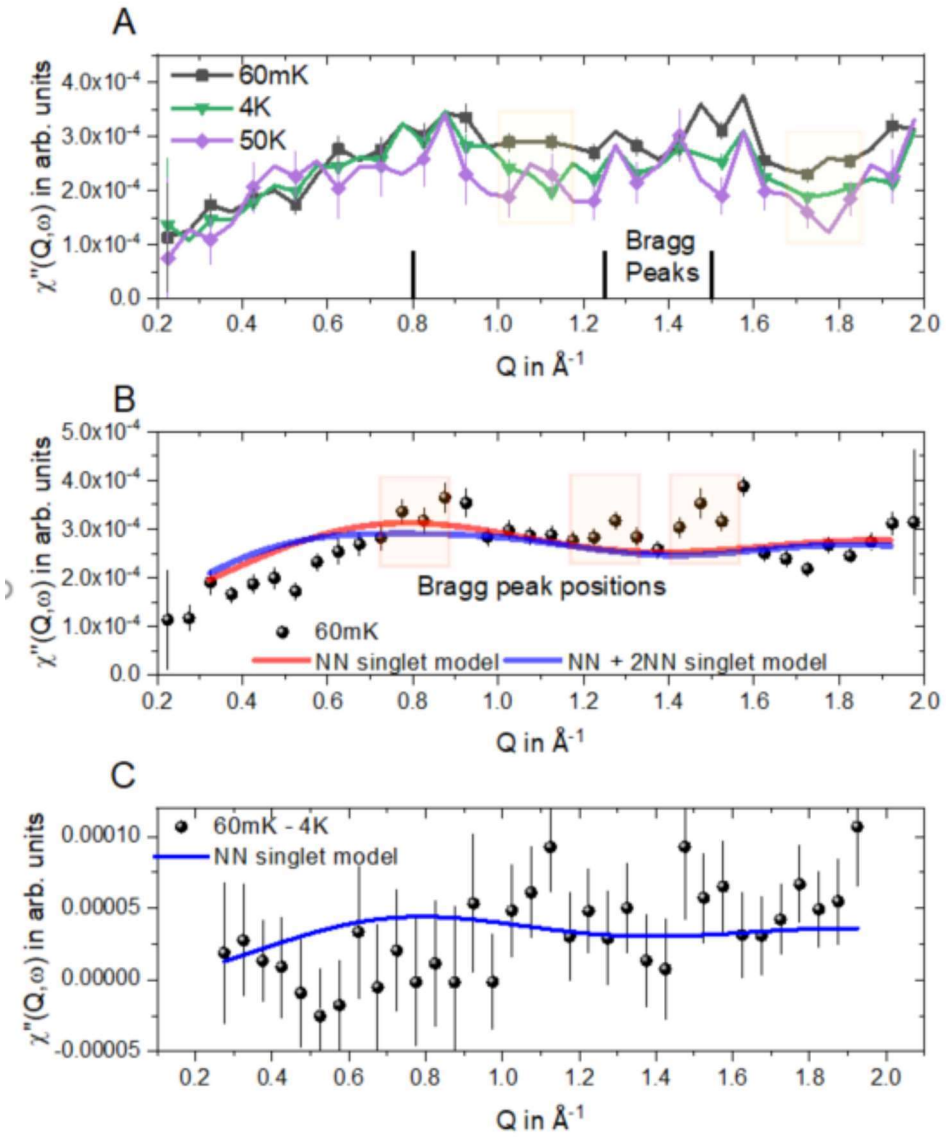

Figure 5.12: **A.** E-integrated Q-cut at 0.65meV, with dE = 0.1meV at 60mK, 4K and 50K showing intensity of inelastic excitation signal. **B.** 60mK measurement and fit with nearest neighbor and 2nd nearest neighbor model. The shaded areas depict the zones contaminated by multiple reflections from the Bragg peak positions. **C.** 60mK measurement subtracted by 4K measurement and the corresponding fit with a nearest neighbor correlation model.

next nearest neighbor correlation, given that we do not consider the zones contaminated by the spurions. We then fit the subtracted data set (60mK-4K) to qualitatively understand if the nearest neighbor singlet model (d_{nn} = 5.84Å) also satisfies the observed intensities. However, from the fit shown in Fig.5.12C, it becomes clear from the absence of intensity at Q = 0.8$Å^{-1}$, that the peak corresponding to the nearest neighbor distance is absent. Furthermore, the relatively high intensity at Q = 1.1$Å^{-1}$ and 1.8$Å^{-1}$ can not be accounted for by the valence bond model involving singlet formation between the Yb^{3+} spins and would be reminiscence of $Yb_2Ti_2O_7$. Another possible explanation is that below 1K, a correlated regime forms and persists to at least 100mK. In this picture, it remains unclear if a transition temperature exists below 1K. In this correlated regime, vestiges of spin-wave-like excitation would still be present, but with a short lifetime resulting in a broad signal up to 0.6meV, that would resemble paramagnon excitation [63]. Interestingly, $K_3YbV_2O_8$ shares some similarities with the pyrochlore $Yb_2Ti_2O_7$ (see Sec.7.2). The inelastic magnetic spectrum in $Yb_2Ti_2O_7$ shows no temperature dependence up to temperatures greater than 2.5 K (800mK for $K_3YbV_2O_8$). The scattering continuum also has a structure in Q, with vestiges of overdamped ferromagnetic spin waves present at small Q. To confirm the presence of spin waves in $K_3YbV_2O_8$, a high flux INS experiment in a single crystal should be performed. Alternatively under applied fields, it will be possible to observe the inelastic signal's evolution of polarised spin waves and quantify the spin Hamiltonian. We expect the INS signal to be weak, and we should also consider complementary ESR measurements [44] and detailed single-crystal magnetic characterization to estimate the spin Hamiltonian. This would be the next step to locate $K_3YbV_2O_8$, which has a different anisotropy than $YbMgGaO_4$, in the 2D THAF phase diagram and understand the exotic physics at play.

5.6 Conclusion

In conclusion, we have studied the magnetic properties of the newly synthesized compounds $K_3YbV_2O_8$ and $K_2CsYbP_2O_8$. Both these compounds are an example of disorder-free, 2D triangular magnetic lattices.

In this new family of compounds, we report from the M(H) and susceptibility measurements that the inter-ionic interactions between the Yb^{3+} ions are antiferromagnetic for both the compounds. However, the interaction strength of $K_2CsYbP_2O_8$ is an order of magnitude weaker than $K_3YbV_2O_8$. From our fit of the magnetic susceptibility, we estimate this to be of the order of 0.5K in $K_3YbV_2O_8$.

From our CEF analysis of both compounds, we do not notice CEF broadening due to disorder effects as seen in $YbMgGaO_4$, and we confirm that the ground state doublet is well separated ($\geq$ 30meV) from the CEF levels for both compounds. These findings are compatible with the $S_{eff} = 1/2$ picture. Furthermore, we report a similar anisotropy $\frac{g_\perp}{g_\parallel}$ of 0.6 in $K_3YbV_2O_8$ and $K_2CsYbP_2O_8$ indicating an intermediate character between Heisenberg and Ising.

Fluctuations of the spins is confirmed by our muon relaxation and INS experiment for $K_3YbV_2O_8$ down to 60mK. The μSR also suggests that the spins enter into a correlated regime at low temperatures ($\leq 1K$). Interestingly, we observe a weak, temperature-dependent intensity in the ZF spectrum of the INS experiment below 800mK. From

our analysis, the most likely explanation for the inelastic signal are paramagnet like excitations that appear in a correlated regime above a transition temperature that is likely below 100mK.

Our findings may offer the opportunity to observe other exotic properties of this new disorder-free triangular family of compounds. Furthermore, Yb^{3+} can be substituted by other rare-earth elements, and recent efforts [64] have been made in this direction.

Chapter 6

$Ba_6Yb_2Ti_4O_{17}$

We continue the investigation of disorder free 2D triangular antiferromagnets with the study of the novel family of compounds with the chemical formula $Ba_6Re_2Ti_4O_{17}$ (Re = Yb). The Yb^{3+} ions form perfect equilateral triangular planes separated by non-magnetic Ba^{2+} and Ti^{4+} ions. Here the possibility of inter-site disorder (see Sec.3) between Ba^{2+} and Ti^{4+} is eliminated as they occupy very different crystallographic sites. We establish that this family satisfies the S_{eff} =1/2 2D anisotropic THAF picture, and owing to this similarity, it can be closely compared to the well-investigated $YbMgGaO_4$. In this chapter we present the magnetic characterization (Sec.6.2) and the investigation of the low temperature magnetism of $Ba_6Yb_2Ti_4O_{17}$ using neutron scattering (Sec.6.3,6.4) and muon spin relaxation techniques (Sec.6.5).

6.1 Structure and synthesis

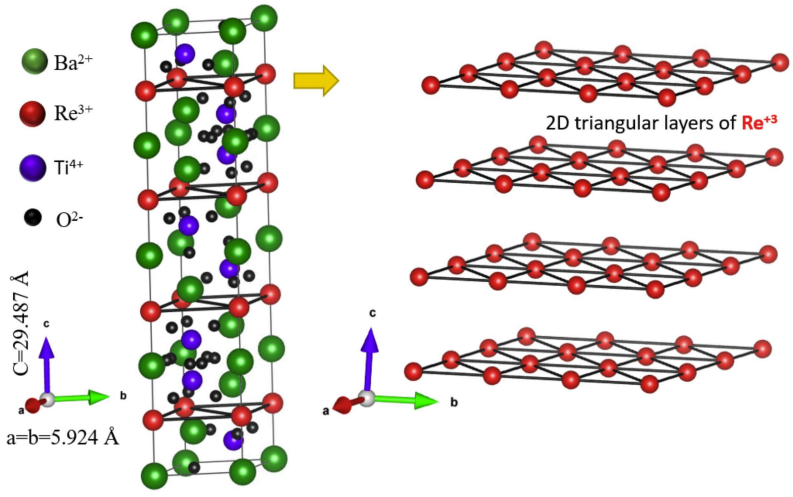

Figure 6.1: Structure of $Ba_6Yb_2Ti_4O_{17}$ of stacked triangular layers separated by non-magnetic Ba and Ti ions. The Yb^{3+} ions occupy the vertices of the triangle in the planes.

Large quantities of powdered sample (5g) were prepared by our collaborators[1] using conventional solid-state synthesis method. To confirm the single-phase purity and structurally characterize the family of $Ba_6Yb_2Ti_4O_{17}$, X-ray diffraction (XRD) measurements were carried out at room temperature to determine the lattice parameters, a = b = 5.907Å and c = 29.426Å and $\alpha = \beta = 90°$ and $\gamma = 120°$. $Ba_6Yb_2Ti_4O_{17}$ crystallizes in space group $P6_3/mmc$ and the point group symmetry of the Yb^{3+} site is D_{3d}. Ba^{2+} and Ti^{4+} have ionic radius 135pm and 56pm, respectively. Additionally, X-ray refinement confirms that the non-magnetic ions, Ba^{2+} and Ti^{4+} occupy distinct crystallographic sites in $Ba_6Yb_2Ti_4O_{17}$ eliminating the disorder due to inter-ion mixing (see Sec.3).

6.2 Magnetism

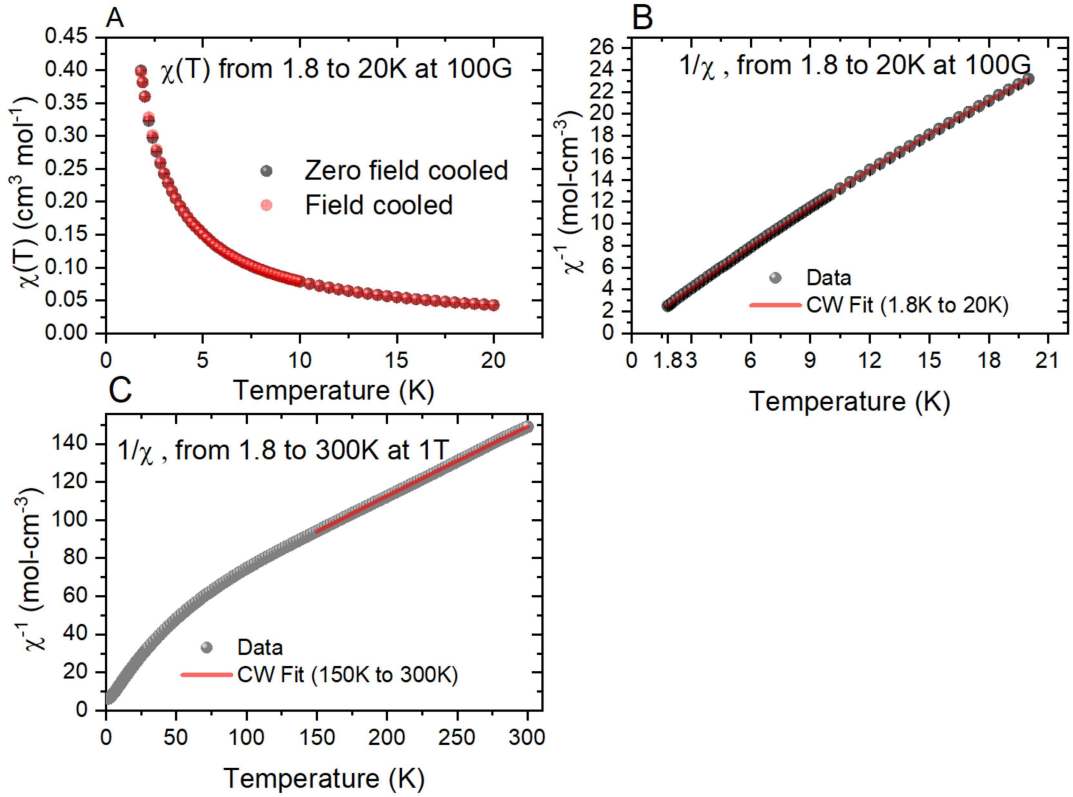

Figure 6.2: **A.** ZFC-FC measurement on powder sample of $Ba_6Yb_2Ti_4O_{17}$ shows no signs of splitting till 1.8K. **B-C** Inverse susceptibility χ^{-1} as a function of temperature in an applied field of 100G and 1T.

In this section we discuss the results of magnetic characterization measurement using a SQUID magnetometer, on a powder sample of $Ba_6Yb_2Ti_4O_{17}$. We first report ZFC-FC susceptibility measurements (Fig.6.2A.) under an applied field of 100G from 20K down to 1.8K. No bifurcation or anomaly is observed and this implies an absence of long range order or spin freezing.

To analyze the low-temperature susceptibility, we plot the inverse susceptibility (Fig6.2) curve that shows a

[1] U.K. Voma, B. Koteswararao Department of Physics, Indian Institute of Technology Tirupati, India

linear dependence in the low-temperature range under an external field of 100G. We fit with the Curie-Weiss model to obtain C_{LT}=0.724(1)cm^3-K/mol with Lande-g factor, g_J = 0.60. The temperature independent susceptibility is around $\chi_0 = 7.03(0.01) \times 10^{-3}$cm^3/mol and we report a very weak antiferromagnetic interaction θ = -0.06(1)K. The diamagnetic susceptibility [61] (χ_D) of $Ba_6Yb_2Ti_4O_{17}$ is $\chi_D = -4.19(1.12) \times 10^{-4}$cm^3/mol and using the relation, χ_0 = χ_{VV} + χ_D, the Van-Vleck susceptibility is then estimated to be, $\chi_{VV} = 7.44 \times 10^{-3}$cm^3/mol.

We also perform a high field (1T) susceptibility measurement between 1.8K to 300K (Fig.6.2B.). The high-field inverse susceptibility curve exhibit a linear or paramagnetic behavior above 150K and display an inflection point around 100K. We fit the susceptibility between 150K to 300K with a Curie-Weiss model, and we report the Curie-Weiss constant C_{HT} = 2.40(6) cm^3-K/mol and g_J=1.1(1). Under the approximation of the Curie-Weiss model, we find that at higher temperatures, the Lande-g factor is close to the Yb^{3+} free ion value, $g_J = 1.2$. The difference between the low temperature and high-temperature g_J is due to the crystal field, where the higher CEF energy levels are populated at higher temperatures. In other words, this difference in the low temperature and high-temperature measurement is justifiable within the S_{eff} = 1/2 picture.

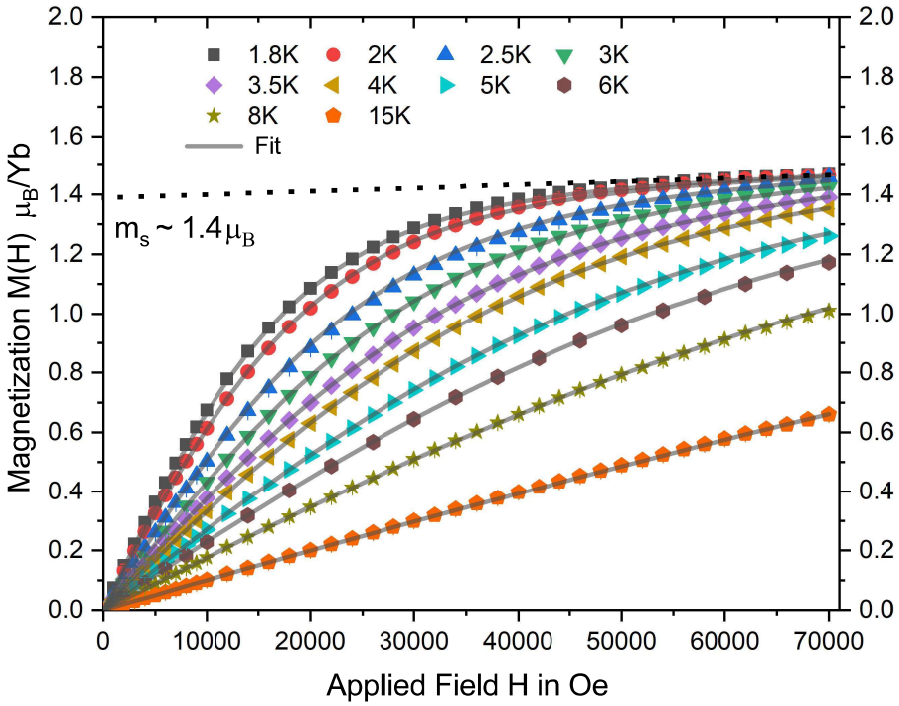

Figure 6.3: M v/s H measurement at multiple temperatures of $Ba_6Yb_2Ti_4O_{17}$ powder. The dashed line is the extrapolation of the low temperature (1.8K) high field (6T to 7T) linear fit for estimating m_s. The solid lines are the global fit with the Brillouin function including interactions θ_{CW}.

Next, we present a series of M(H) measurements in the low-temperature regime($<$20K). From the magnetization measurement (see Fig.6.3), we observe that at low temperatures, a field of 7T almost saturates Yb^{3+} ion, with a

saturation value of 1.4μ_B/Yb^{3+} is obtained. In the paramagnetic regime ($\geq$ 1.8K), we fit the data with a Brillouin function (see Sec.2.4), taking into account the interaction θ_{CW} and the single-ion anisotropy. From the simultaneous fits of the magnetization isotherms at different temperatures, we obtain g_{avg} = 2.80(5) with $g_{\perp}$ = 3.3(2), $g_{\parallel}$ = 1.3(2), and an extremely weak anti-ferromagnetic exchange θ = -0.05(2)K, of the same order of magnitude than the one found in susceptibility measurement. From the estimated g-tensor, we calculate an anisotropy, $\frac{g_{\perp}}{g_{\parallel}}$=2.4(1), which implies that the Yb^{3+} spins have an intermediate character between XY and Heisenberg limit, unlike to $YbMgGaO_4$ (see Sec.3.1). From the fit, the total susceptibility is $\chi_0 = 6.8(5) \times 10^{-3}$ cm^3/mol and $\chi_{VV} = 7.18(6) \times 10^{-3} cm^3/mol$, thus consistent with the susceptibility measurement.

The value of χ_{VV} is inversely proportional to the difference in energy between the ground state doublet and the first excited levels. Thus the weak Van-Vleck term thus obtained indicates that the CEF excitation levels are much larger than 1.8K. Furthermore, the interaction strength we obtain from the low-temperature field cooled measurement hints at a very weak antiferromagnetic behavior in comparison to $YbMgGaO_4$ ($\theta_{YMGO}/\theta_{BYTO} \approx 40$), which is likely due to the significantly larger Yb-Yb inter-ion length even though the interaction depends non-trivially on the nearest neighbor distance (see Sec.5.6).

6.3 Single ion anisotropy

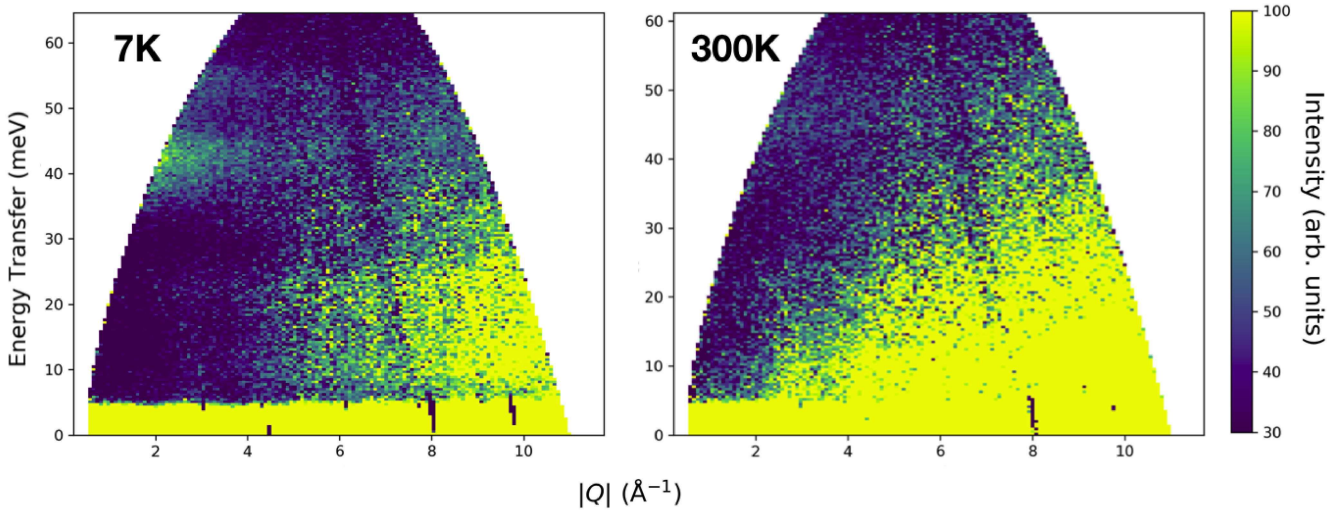

Figure 6.4: Empty can background subtracted S(Q,ω) scans of $Ba_6Yb_2Ti_4O_{17}$; S(Q,ω) scan at 7K(left) and 300K(right) with E_i=72meV and empty Al can as background.

We have performed INS experiment on $Ba_6Yb_2Ti_4O_{17}$ at the Merlin instrument, ISIS, STFC (UK) to investigate the CEF excitation that imposes the single-ion anisotropy of the Yb^{3+} ion. In $Ba_6Yb_2Ti_4O_{17}$ the Yb^{3+} ions have the electronic configurations: [Xe]$4f^{13}$; where the Yb^{3+} ions have localized unpaired electrons in their f-subshell. Similar to $YbMgGaO_4$, the moments of the Yb^{3+} ion have L = 3, S = 1/2 and J = 7/2 and thus four doubly degenerate energy

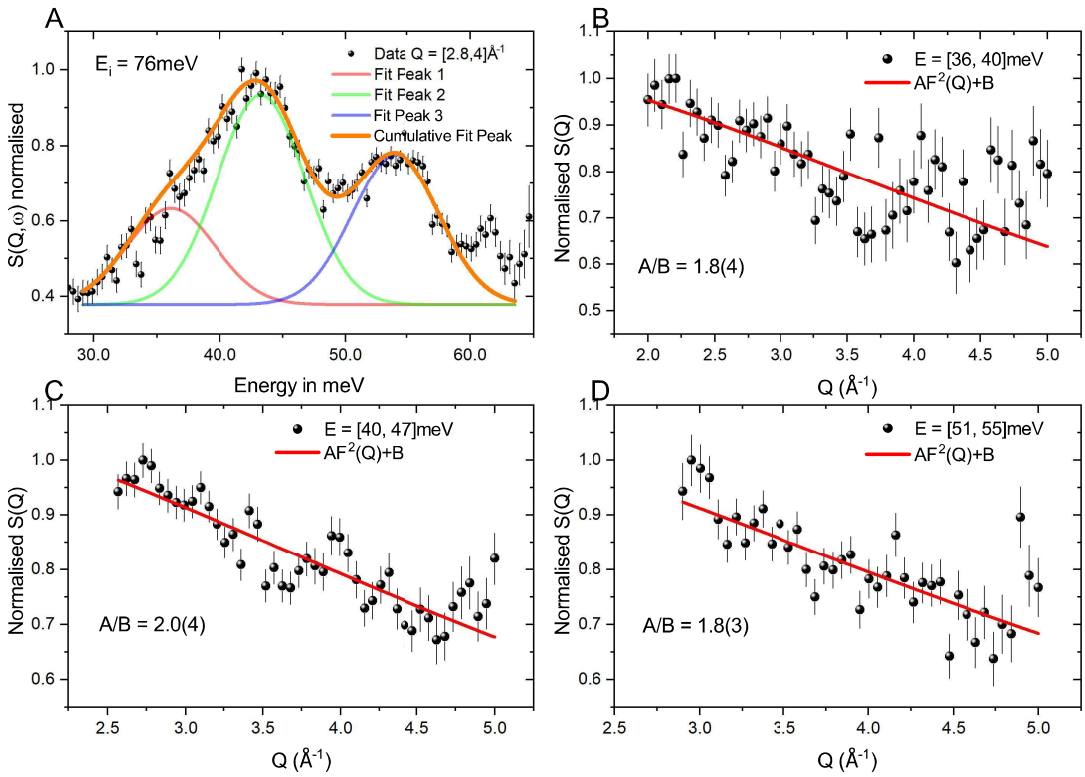

Figure 6.5: **A.** E-cuts for the 7K measurement depicting the CEF peaks and corresponding fit. **B-D.**Q-cuts at the peak positions and corresponding fit with the Yb^{3+} structure factor.

	B_0^2	B_0^4	B_0^6	B_6^6	B_3^4	B_3^6
PC :	1.072	0.033	0.0001	0.0017	0.88	-0.0037
Fit :	-0.44279	-0.00076	0.00146	0.0177	-0.34	-0.0013

Table 6.1: Comparison of Steven's operator coefficients in meV of initial point charge(PC) calculation and fit result

levels that split in the crystal field environment (see Sec.2.3.1).

A large portion of the S(Q,ω) scans for incident energy E_i= 72 meV at 7K, and 300K (Fig.6.4) reveal an intensity in the neutron scattering at high Q ($\geq$ 5Å) and low E values ($\leq$ 30meV), that are due to the phonon modes. At low Q, weak intensities around 40meV in the 7K measurement signals the presence of CEF levels of $Ba_6Yb_2Ti_4O_{17}$. We perform a Q−integrated E cut of S(Q,ω) (in the range [2.8,4]$Å^{-1}$) obtaining S(E) as a function of the energy for this Q range (Fig.6.5A.). From the plot, we discern that the two peak intensities are between 30meV and 60meV. However, three peaks are expected, whereas only two are observed. On a closer inspection, the first peak is asymmetric and much broader than the instrument resolution and therefore is anticipated to be comprised of two peaks in close proximity. The E-integrated Q-cut shows S($|Q|$) that monotonically decreases with increasing $|Q|$ near the peak positions (Fig.6.5B-D.); we fit the Q dependence with the Yb^{3+} magnetic form factor and establish these excitations

as the CEF excitations levels.

To determine the peak position and the relative intensities of the CEF levels, a Q-integrated E-cut (see Fig.6.5A.) is fitted with three Gaussian peaks of constant width (FWHM). The peak positions of the CEF levels for $Ba_6Yb_2Ti_4O_{17}$. are found to be at 36.1(8)meV, 43.2(2)meV and 54.0(1)meV. In the formalism of Steven's operator equivalent coefficients (see Sec.2.3.2) we observe that the model is under constrained. And for this reason, the magnetic saturation value, m_s = 1.41(4)μ_B/Yb^{3+}, that we obtain from the M(H) fit, is used as an additional constraint. Using a single ion point charge calculation for Yb^{3+} in $Ba_6Yb_2Ti_4O_{17}$ as the initial guess of Steven's operator coefficients, we estimate the CEF energy levels and their relative intensities and m_s. We determine the final operator coefficients (see Tab.6.1) corresponding to the minimum of this error between the estimation of the relative intensities, the energy positions, and m_{sat} and the experimental observations. The fit results are consistent with the M(H) measurements, and the CEF fit from this calculation is presented in Fig.6.5 by the solid lines. From the best-fit parameter set, we obtain the CEF Hamiltonian in the $|m_J\rangle$ basis as follows :

Energy (meV)	$\|-7/2\rangle$	$\|-5/2\rangle$	$\|-3/2\rangle$	$\|-1/2\rangle$	$\|1/2\rangle$	$\|3/2\rangle$	$\|5/2\rangle$	$\|7/2\rangle$
$Ba_6Yb_2Ti_4O_{17}$								
0	0	0.63	0	0	-0.45	0	0	-0.64
0	-0.64	0	0	0.45	0	0	0.63	0
36.10	-0.09	0	0	0.76	0	0	-0.64	0
36.10	0	-0.64	0	0	-0.76	0	0	-0.09
43.25	0.07	0.45	0	0.04	-0.46	0	0.04	0.76
43.25	0.76	-0.04	0	0.46	0.04	0	0.45	-0.07
54.02	0	0	0	0	0.	1	0	0
54.02	0	0	1	0	0	0	0	0

Table 6.2: Compositions of the CEF levels in the $|m_j\rangle$ basis for Yb^{3+} moments (J=7/2) for Yb^{3+}) as determined from our CEF analysis.

From Tab.6.2 the GS doublet is extracted for clarity:

$$|\pm\rangle = -0.64\,|\pm 7/2\rangle + 0.63\,|\mp 5/2\rangle \mp 0.45\,|\pm 1/2\rangle \tag{6.1}$$

the ground state is a mixture of the different $|m_j\rangle$ and this is not suprising for Yb^{3+} moments as it was found in previous analyses for example, in $YbMgGaO_4$ [44]. We note that the largest contributions from $|\pm 7/2\rangle$ and $|\pm 5/2\rangle$ states and we obtain g_{avg} = 2.8(1) with $g_{\parallel}$ = 1.2(1) and $g_{\perp}$ = 3.3(1). The g-tensor is cross-checked with our magnetic characterization measurements (Sec.6.2) and is consistent across all our experimental findings. It is interesting here to note that there is no anomalous shoulder observed in the CEF experiment as was observed in $YbMgGaO_4$ [44] (see Sec.3), and this establishes $Ba_6Yb_2Ti_4O_{17}$ as a disorder free 2D triangular candidate for exploring the QSL phase. In the following section, we investigate the dynamics and correlation of the Yb^{3+} moments at low temperatures using INS and muon spin relaxation experiments.

6.4 Low energy inelastic neutron scattering

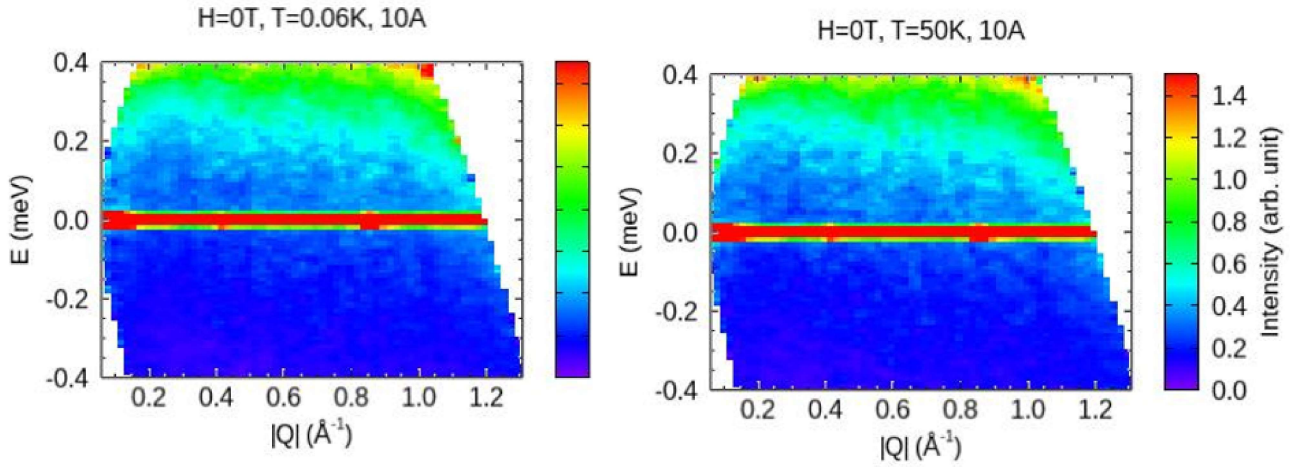

Figure 6.6: S(Q,ω) scans under zero applied field at 60mK and 50K.

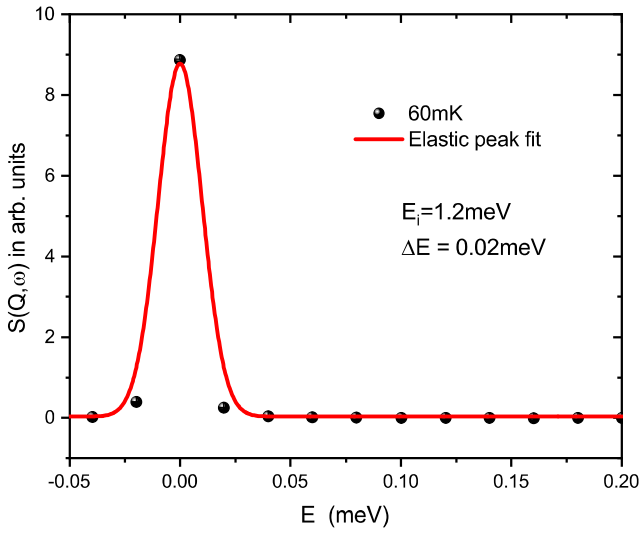

Figure 6.7: E-cut integrated over the whole Q range to investigate the presence of any inelastic or quasielastic excitation. The solid line shows the fit of the observed intensity with a Gaussian having the FWHM of the instrument resolution of 0.02meV.

To probe the nature of the magnetic ground state, we performed a time-of-flight INS experiment on $Ba_6Yb_2Ti_4O_{17}$ powder using the DCS instrument at NIST (USA).

The dynamic structure factor, S(Q,ω) maps in Fig.6.8 are background subtracted INS measurements performed with the highest energy resolution ($\lambda = 10$Å) where the width of the elastic line is 0.02meV. In Fig.6.7, we investigate

the presence of any quasielastic or inelastic signal. At 0.06K, in zero applied field, the observation fits well with just an elastic line of instrumental resolution. Given that the exchange interaction is weak, the width of the quasielastic component is expected to be weak as well. The absence of diffusive scattering at zero field is also remarkable, possibly due to weak exchange interactions. In contrast to $YbMgGaO_4$, where a continuum is observed in the neutron scattering experiments even at higher temperatures (14K), $Ba_6Yb_2Ti_4O_17$ displays no inelastic signal. It is then natural to think that the continuum in $YbMgGaO_4$ is at least partially due to disorder effect as CEF measurements characterize $Ba_6Yb_2Ti_4O_{17}$ as a disorder free compound. However, **(i)** The interaction scale (θ_{CW}) of $YbMgGaO_4$ and $Ba_6Yb_2Ti_4O_{17}$ are very different and **(ii)** We estimated θ_{CW} for $Ba_6Yb_2Ti_4O_{17}$ only above 1.8K. This indicates that future characterization experiments should be performed down to milli-Kelvin temperatures to accurately estimate θ_{CW} for comparing the neutron scattering experimental observations with $YbMgGaO_4$ for instance.

Under an external magnetic field at 0.06K (Fig.6.8), we observe a spectral weight in the inelastic channel. With increasing field, the S(Q,ω) intensity peak shifts linearly in energy while becoming broader and weaker (see Fig.6.9). Gaussian peaks are used to model the magnetic peaks, and (Fig.6.9A.) shows the peak position and FWHM as a function of the applied field. The variation of the peak position with the applied field comes out to be linear with a slope m, from which we obtain g = 2.45(5). From our analysis, we infer that an external field breaks the time-reversal symmetry of the ground state Krammer's doublet and results in a Zeeman splitting. The observed excitation peak is then due to intra-doublet transition of the spins as they are no longer degenerate in energy, and with an increase in the applied field, the Zeeman gap increases, and the peak shifts linearly in E, the slope is then in the first approximation the powder averaged g-tensor value (g_{avg} = 2.45(5)). Secondly, the broadening of the peaks indicates the anisotropy of the g-tensor. This is likely due to the non-isotropic g-tensor ($\frac{g_\perp}{g_\parallel} = 2.4(1)$) that has different parallel and perpendicular components (for the triangular plane).

6.5 μSR

Muon spin relaxation is used as a local probe to study the magnetic properties at low temperatures, complementing our neutron scattering spectroscopy. The following experiment is performed with the MuSR instrument at ISIS, STFC (UK).

At 60mK, muon spin relaxation in the ZF mode (Fig.6.10) does not show any dip in the relaxation curve, which is exponential. We apply an LF field with an increasing magnitude to observe the field dependence of the muon spin relaxation and report the absence of the static '1/3 tail' at long relaxation time T, plus that it does not decouple with the field. The LF decoupling measurements thus establish the absence of a significant static component due to Yb^{3+} moments.

To study the temperature dependence of the muon relaxation, we performed scans in the temperature range 60mK to 300K. In Fig.6.10B. we remark that in the low-temperature range of 4K to 60mK, no noticeable relaxation

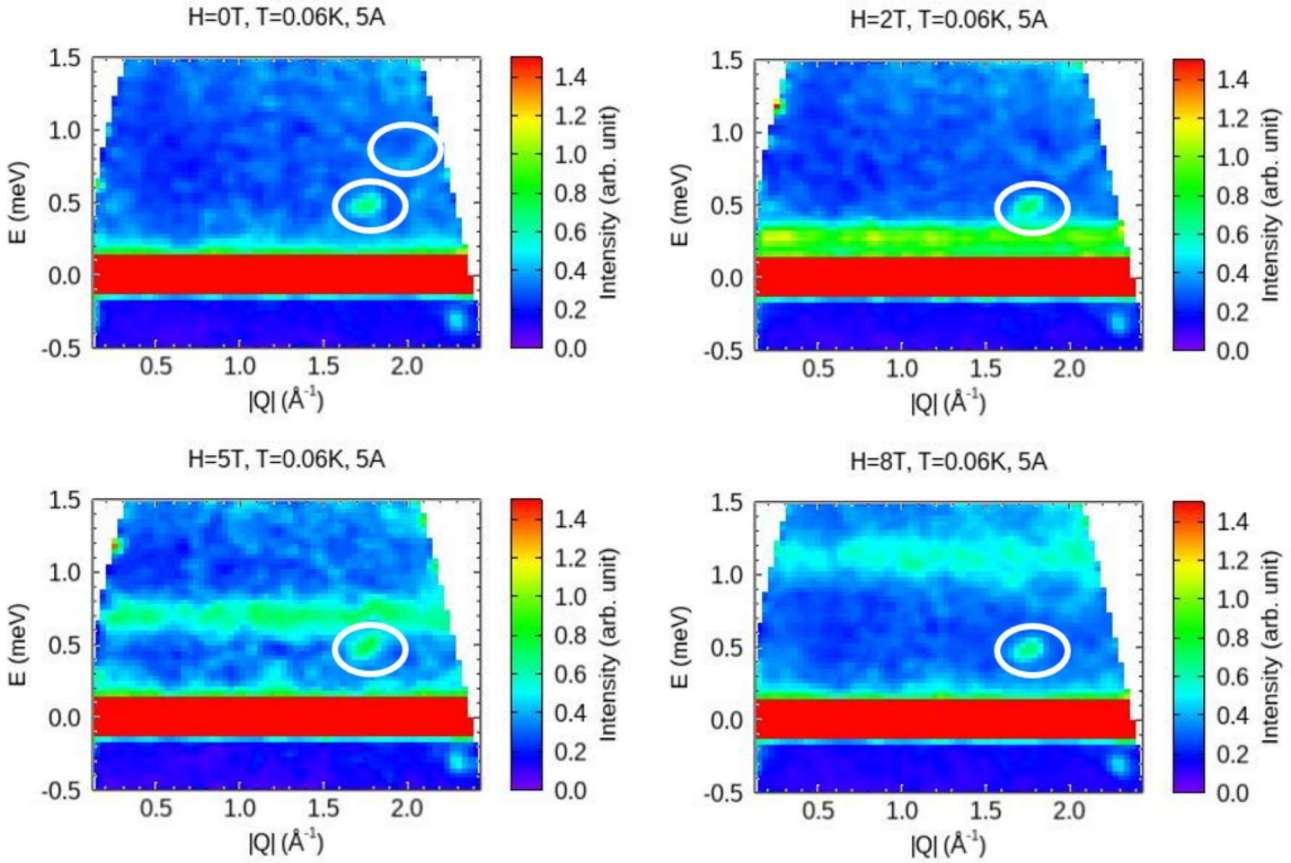

Figure 6.8: S(Q,ω) scans at different applied field: at $0T$, $2T$, $5T$, $8T$; The white circles mark the temperature and field independent spurions from the instrument.

change occurs. Additionally, the relaxation has a high resemblance to an exponential form, so we model it with the stretched exponential function that can take into account multiple muon sites with different relaxation:

$$A(t) = A_s \exp^{-(\lambda t)^{\beta}} + B \tag{6.2}$$

Where A_s, β, and B are the sample asymmetry, stretching parameter, and the background, respectively. We fix A_s and the background, as we do not expect the total asymmetry or the background to vary significantly with temperature.

We find that throughout the temperature range, the value of β can be fixed to 0.63 without compromising the fit quality. In the existing muon literature, it has been noted that a value of β lower than 1 may indicate the presence of multiple muon relaxation sites or a disordered system. As it is less likely to have disorder in $Ba_6Yb_2Ti_4O_{17}$, we speculate that this value of β corresponds to multiple muon sites.

Fig.6.11 shows the corresponding spin relaxation increases as the temperature is decreased to an inflection

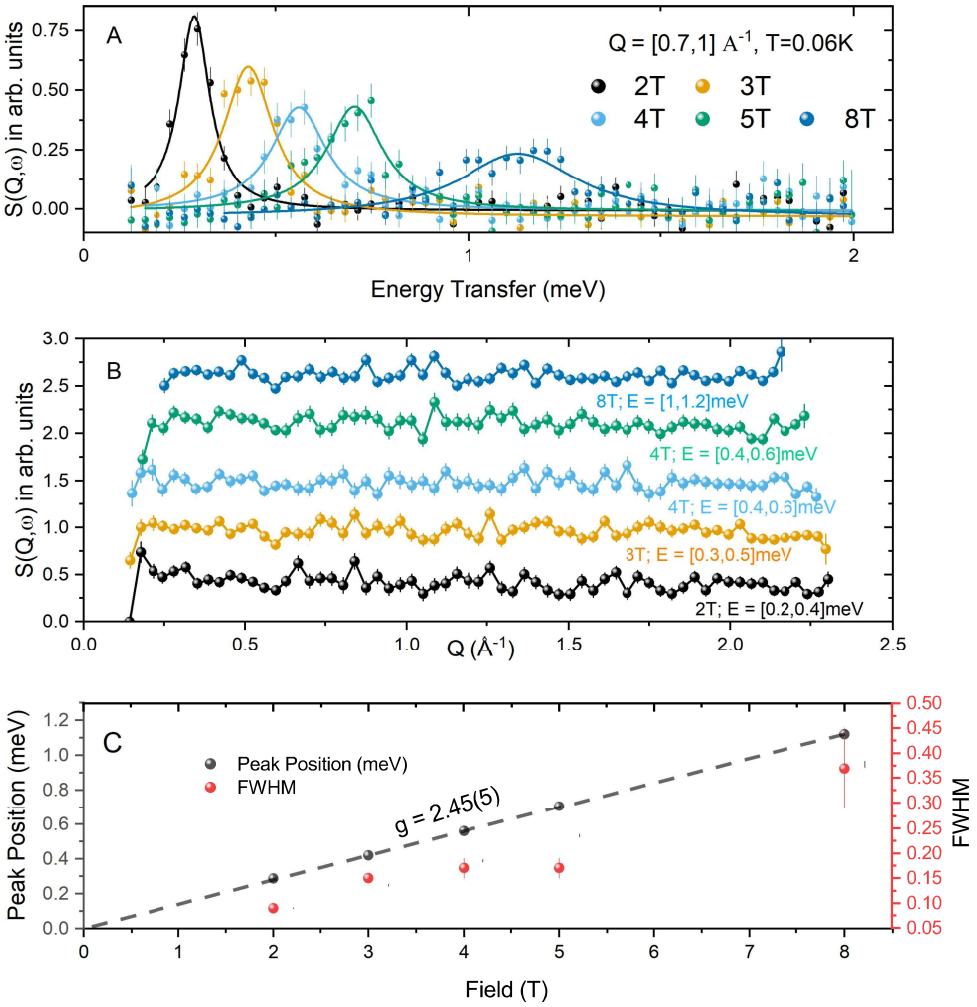

Figure 6.9: **A.** Q-integrated E-cuts of S(Q,ω) depicting the Zeeman splitting of the ground state doublet under applied field. **B.** E-integrated Q-cuts at the peak positions **C.** Linear fit of the peak position (in meV) in black and the FWHM of the peaks as a function of field.

point at around 40K. We explain this slowing down of the spins ($1/T_1$) with an Orbach process (see Sec.2.1.4):

$$\lambda_{muon} = \frac{1}{A \exp^{-\frac{\Delta}{k_B T}} + B} \tag{6.3}$$

Here, Δ is the gap between the ground state and the first excited CEF energy level (Δ = 36meV $\approx$ 418K), and A is the amplitude of interaction while B is the inverse of the saturation value of the spin relaxation λ_s at the plateau between 60mK and 40K, $\lambda_s = 0.58(3)\mu s^{-1}$. We estimate the energy of the 1^{st} excitation level at Δ = 418(20)K, which is in agreement with the CEF experiment. A plateau at 40K appears as temperature decreases,

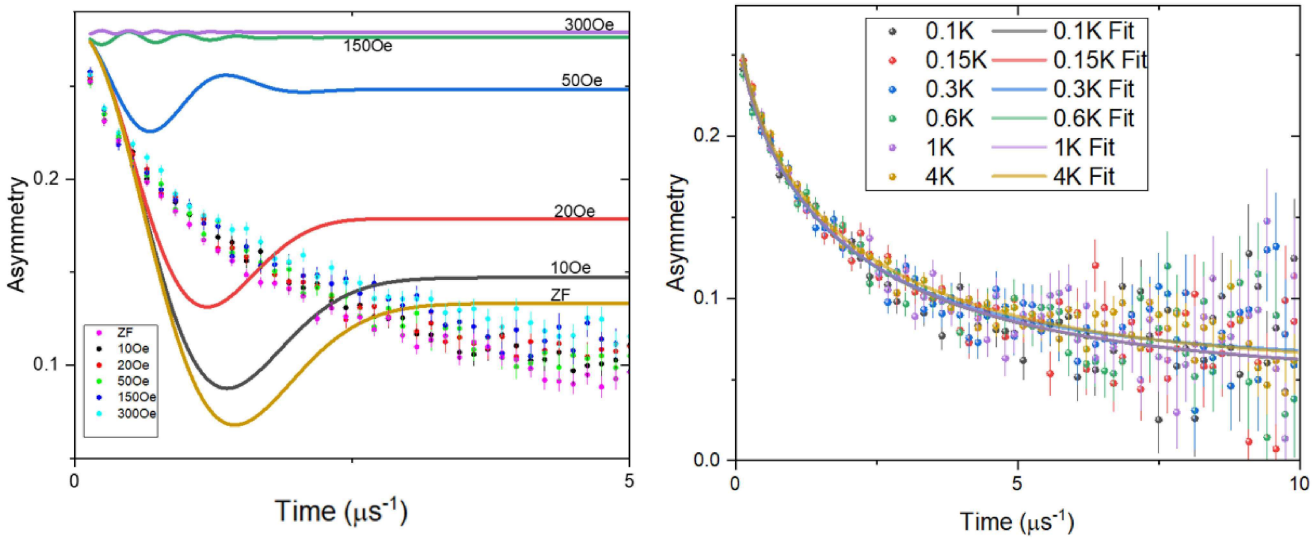

Figure 6.10: [Left] Solid lines show the static Kubo-Toyabe compared with the raw data (shown by scattered points) as a function of field. [Right] Low temperature relaxation and the corresponding fits with a stretched exponential model.

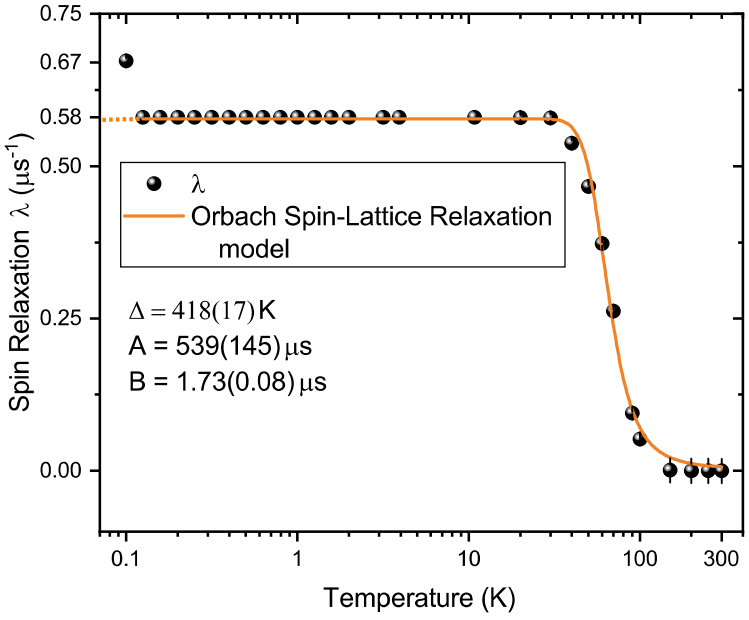

Figure 6.11: Spin relaxation, λ as a function of temperature. The data is fit with the Orbach Model.

which persists until the lowest measured temperature of around 60mK. In contrast, the spin relaxation in $YbMgGaO_4$ (see Sec.3) displays the first plateau starting at around 20K followed by a crossover regime between 4K and 0.4K and then subsequently followed by a second plateau at 0.4K, that persists till 45mK. It is likely that the interaction strength is weaker in $Ba_6Yb_2Ti_4O_{17}$ (0.06(1)K v/s 4K); this crossover regime would be at a temperature lower than 60mK, if it exists.

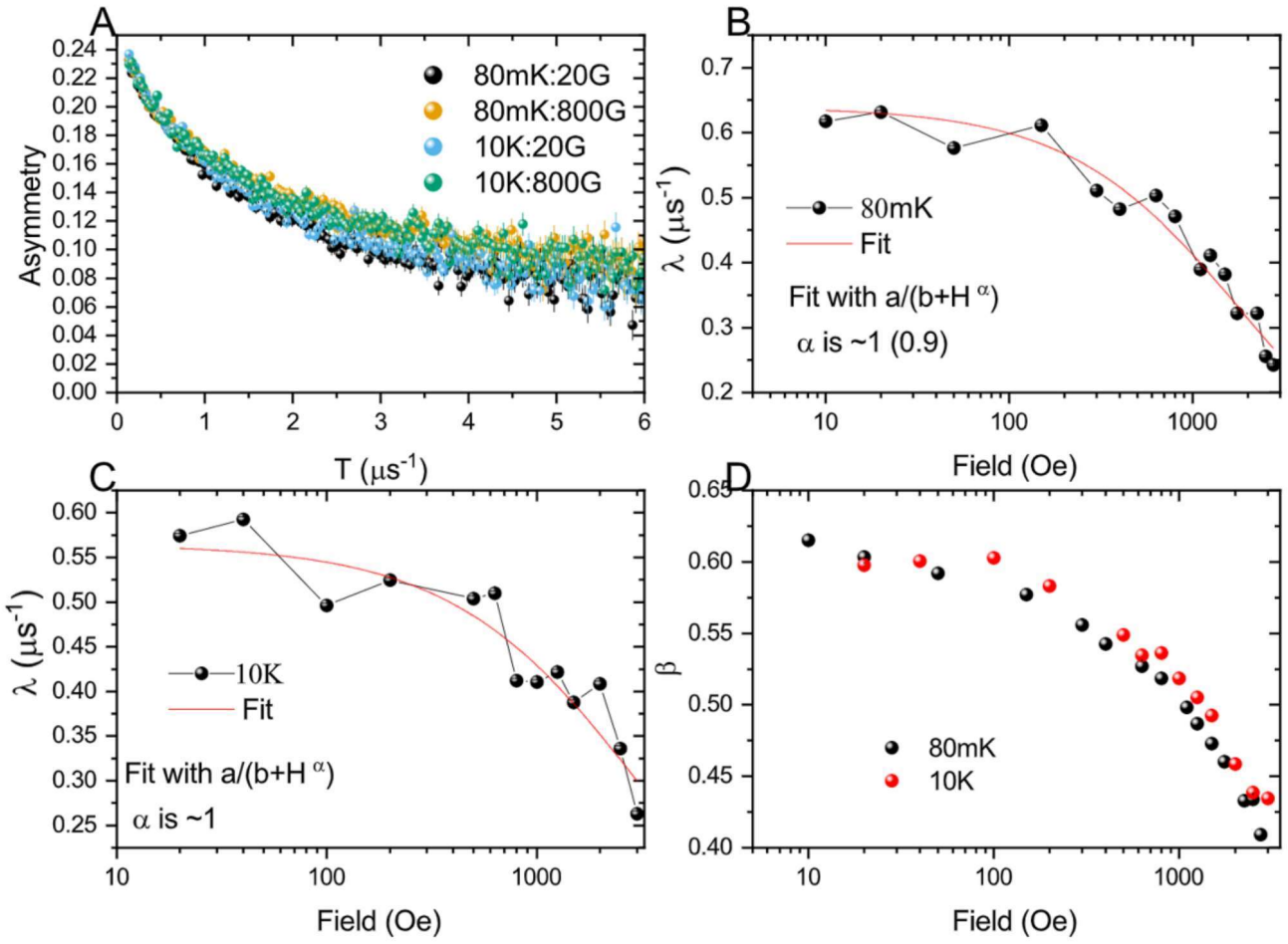

Figure 6.12: **A.**LF dependence of the spin relaxation at 80mK and 10K for LF 20G and 800G. **B,C.**Spin relaxation as a function of the applied field and solid lines shows the fit of the λ with an inverse power law. **D.** Variation of the stretch coefficient β.

Thus the temperature dependence confirms the paramagnetic nature till 60mK, and we perform a field dependence measurement of the muon relaxation to characterize this phase. In Fig.6.12, the LF variation of the spin relaxation λ at T= 80mK and 10K shows that an external field does not easily decouple the muon relaxation and leaves a similar exponential character. We assume multiple muon sites present in the sample similar to the temperature dependence study and we model the muon relaxation under an applied field in the LF mode with a stretched exponential. The relaxations are fitted with β and λ unconstrained, while the A_s and the background is fixed for all field values and we keep β as a free parameter. Inorder to understand the field dependence of λ, we use the empirical formula:

$$\lambda = \frac{A}{B + H^{\alpha}} \tag{6.4}$$

At both 80mK and 10K, we report $\alpha \approx 1$, and thus an inverse dependence of the spin relaxation, λ, on the external

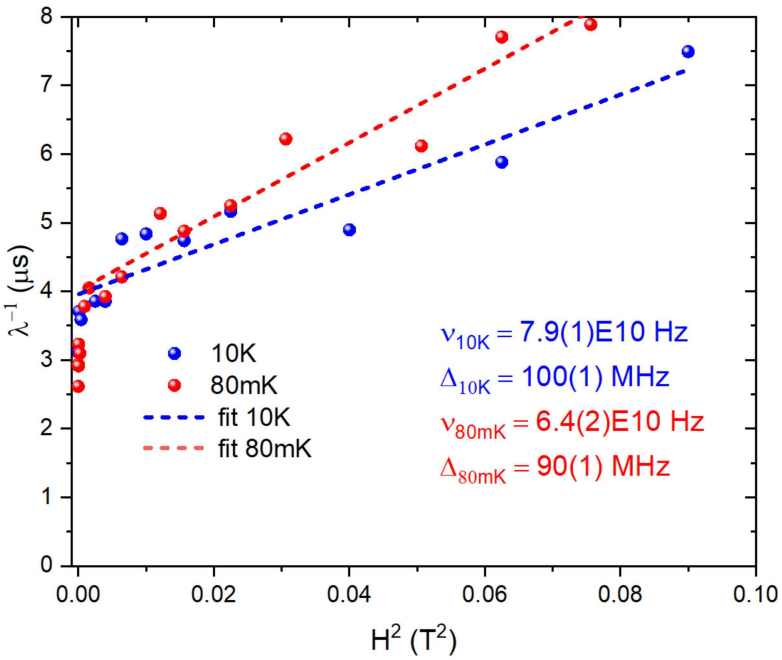

Figure 6.13: Inverse squared dependence of λ_{avg} with field at 80mK and 10K for $Ba_6Yb_2Ti_4O_{17}$. We observe that for low fields there is a strong decoupling effect likely originating from a fraction of static moments.

field.

In order to decouple λ from β, we compute the average spin relaxation λ_{avg} using the following relationship [65] (see Sec.2.1.4),

$$\frac{1}{\lambda_{avg}} = \frac{1}{\lambda\beta}\Gamma(1/\beta) \tag{6.5}$$

We compare λ measured at 80mK and 10K and fit with the Redfield equation. From the fits we obtain the fluctuation ν and the root-mean-squared value of the field distribution, $\Delta \approx \gamma_\mu \sqrt{< B_{loc}^2 >}$ (see Fig.6.13). We report ν_{10K} = 7.9(1)$\times 10^{10}$ Hz, Δ_{10K} = 100(1) MHz, and ν_{80mK} = 6.4 $\times$ 10^{10}, Δ_{80mK}=90(1) MHz. Furthermore, we obtained a similar values for $K_3YbV_2O_8$ in the paramagnetic regime (see Sec.5.4).

The analysis of the LF and ZF-temperature dependence thus confirms the paramagnetic nature of $Ba_6Yb_2Ti_4O_{17}$ down to 100mK and we note that due to the weak Weiss temperature of 0.06(1)K, it is possible that a correlation regime emerges below this temperature. Further experiments in such temperature range need to be performed to characterize the low temperature physics of $Ba_6Yb_2Ti_4O_{17}$.

6.6 Conclusion

In summary, we performed detailed characterization measurements on $Ba_6Yb_2Ti_4O_{17}$ to explore the possibilities of magnetic frustration in the context of disorder free systems. We are confident about the absence of intersite mixing

as our CEF analysis finds no broadening of the CEF levels that would be consistent with the absence of bond randomness or intrinsic structural disorder.

As it turns out, $Ba_6Yb_2Ti_4O_{17}$ satisfies all the initial requirements for a frustrated triangular lattice that can potentially prevent order and remain in the paramagnetic phase till 100mK (Sec.6.5). In this study, we also faced the experimental limitations of rare-earth magnets with weak exchanges. Recent efforts are made to discover disorder free compounds [66], and from our current investigation, it becomes clear that a stronger interaction (θ_{CW}) is needed, likely in the same order as $YbMgGaO_4$, to experimentally identify the absence of order due to frustration effects.

Part IV

Disorder effects in the quantum pyrochlore family $\mathbf{Yb_2(Ti_{(1-x)}Zr}_x\mathbf{)_2O_7}$

Chapter 7

The quantum pyrochlore magnet $Yb_2Ti_2O_7$: a brief survey

7.1 Frustrated magnetism on the pyrochlore lattice

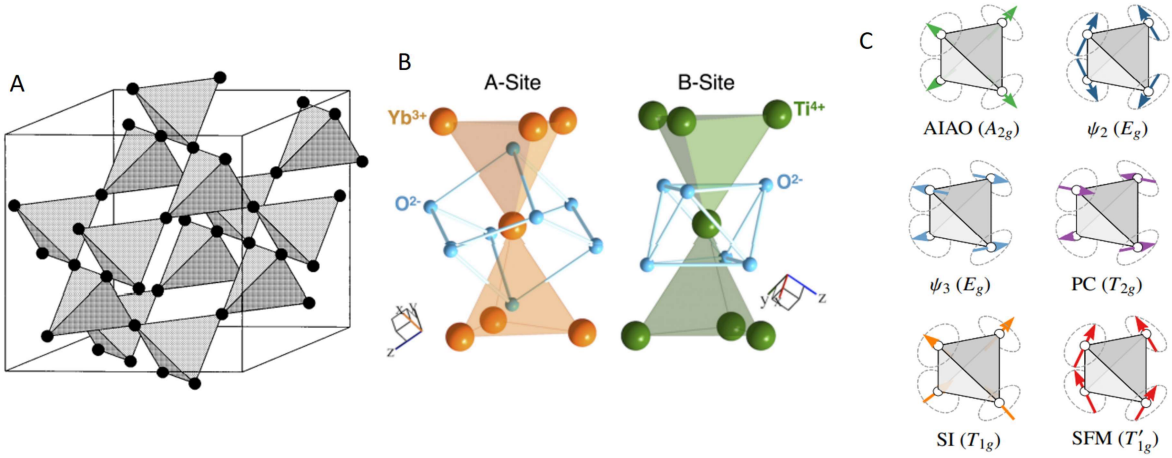

Figure 7.1: **A.** Corner sharing tetrahedra forming the pyrochlore lattice. **B.** The A and the B sites of $Re_2M_2O_7$ with different local oxygen environment. **C.** 6 distinct types of possible spin configurations on a tetrahedron. The two-in two-out configuration is the spin ice case (SI) and the canted ferromagnetic situation is also referred to as a splayed ferromagnet (SFM) **A. B.** and **C.** are extracted from [67, 68, 69] respectively.

7.1.1 The frustrated pyrochlore structure

The rare-earth pyrochlore oxides of the form $Re_2M_2O_7$, where Re^{3+} is a rare-earth element and M^{4+} is a transition metal, of which $Yb_2Ti_2O_7$ is a part of, is of particular interest to physicists as a playground to study magnetic

frustration. In such compounds, the Re^{3+} and the M^{4+} atoms form two different sublattices A and B. These sublattices independently form networks of corner-sharing tetrahedra, one of the canonical crystalline architectures supporting geometrical frustration in three dimensions. The cubic rare-earth titanates of the form $Re_2M_2O_7$ have been especially relevant as many magnetic Re^{3+} ions can occupy the A site while preserving the cubic pyrochlore structure.

In pyrochlores with ferromagnetic interactions, the frustration arises due to the spatial arrangement of the moments on the corners of the tetrahedra. To understand how frustration arises, consider the situations where the spins are of classical Ising anisotropy pointing in or out of the tetrahedron along the local [111] direction. Under such constraints, six configurations simultaneously minimize the energy with two spins pointing out in the local [111] direction and two spins pointing in. The orientation of the magnetic moments in this situation is analogous to the positional organization of protons in water ice and therefore is referred to as spin ice. Additionally, these exhibits a residual magnetic entropy equal to the residual Pauling entropy found in water ice [2]. The first materials identified [70] as spin ices were the pyrochlores $Dy_2Ti_2O_7$ and $Ho_2Ti_2O_7$. Identifying the main issues with $Yb_2Ti_2O_7$ requires first a brief introduction to one of the landmark discoveries in condensed matter physics, spin ices. We briefly discuss then the difference between classical and quantum spin ice and how to model it theoretically. Following this is our brief survey on $Yb_2Ti_2O_7$, where we only focus on the central puzzle. For a detailed review on spin ice physics, the interested reader can consult [71, 72].

7.1.2 Classical spin ice

In classical spin ice compounds such as $Dy_2Ti_2O_7$ and $Ho_2Ti_2O_7$, magnetization measurements reveal a positive (ferromagnetic) Curie-Weiss temperature [70] of θ_{CW} = 1.9K and 0.5K, respectively. To understand the origin of the ferromagnetic interaction, we consider the nearest neighbor dipolar spin ice Hamiltonian, H_{DSIM}, that was introduced in order to describe the low-temperature properties of the spin ice [74] :

$$H_{DSIM} = -J\sum_{i,j}\vec{S}_i\cdot\vec{S}_j + Dr_{NN}^3\sum_{i,j}\left(\frac{\vec{S}_i\cdot\vec{S}_j}{r_{i,j}^3} - \frac{3\vec{S}_i\cdot\vec{S}_j}{r_{i,j}^5}\right) \tag{7.1}$$

The dipolar spin-ice Hamiltonian has contributions from the nearest neighbor exchange term and the classical dipolar interaction term. J is the nearest neighbor exchange, r_{ij} is the distance between the rare-earth ions i and j, D is the dipolar interaction strength, and r_{NN} the nearest-neighbor distance. The spins are vectors in the local frame of reference. The magnetic moments are effectively described by classical spins and not quantum mechanical operators, distinguishing this scenario from the quantum spin ice phase described below.

In the example of $Dy_2Ti_2O_7$ and $Ho_2Ti_2O_7$, the net moment is of the order of $10\mu_B$, which results in a dipolar contribution that is significantly greater than the exchange interaction (J $\simeq$ 1K). An estimation of the dipolar energy scale between two nearest neighbors is of the order of D = 2.4K for both compounds, which, as we will see in the

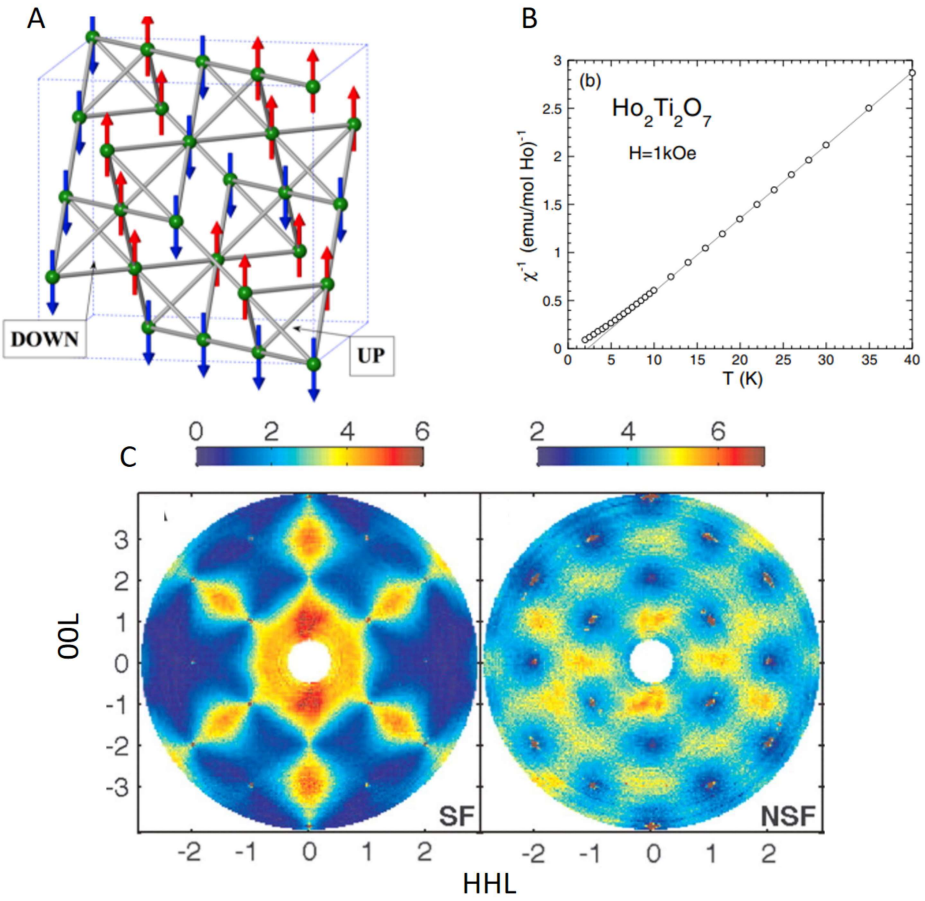

Figure 7.2: **A.** The pyrochlore lattice with 2-up, 2-down Ising magnetic moments in the presence of a z axis anisotropy. **B.** Inverse susceptibility as a function of temperature in $Ho_2Ti_2O_7$ shows a linear behavior under a field of 1 kOe.**C.** Polarised neutron scattering maps of $Ho_2Ti_2O_7$ at T = 1.7 K, the spin flip channel [left] shows pinch points at (0, 0, 2), (1, 1, 1), (2, 2, 2), while the NSF channel is qualitatively more diffusive. **B.** and **C.** extracted from [72], [73] and [70] respectively.

next section, corresponds to the position of the broad specific heat bump.

The validity of the DSIM model is restricted to a 2 level system, and in the case of rare-earths, this is valid only in the low-temperature regime where the spins are compatible with an S_{eff} = 1/2 picture. Under the CEF effects, Ho^{3+} and Dy^{3+} show a high anisotropy ($g_\perp/g_\parallel$ = 1/20) in the g-tensor that further defines the Ising nature of the spins.

The experimental confirmation of the spin ice phase highlights the importance of neutron scattering as an invaluable experimental technique to probe magnetic correlations. Polarized neutron scattering data, taken on a single crystal of $Ho_2Ti_2O_7$ using the D7 spectrometer at ILL, Grenoble, France [70], revealed the pinch points at zone centers in the polarized spin-flip data. Pinch points in the S(Q,ω) maps correspond to the power-law correlations due to the long-range dipolar correlations and justify the DSIM model. Monte Carlo simulations reproduce the observations accurately and confirm $Ho_2Ti_2O_7$ as spin ice. Moreover, neutron scattering experiments have found evidence for fractionalized quasiparticle excitations, interacting through a magnetic Coloumb potential and called magnetic

monopoles.

7.1.3 Quantum spin ice

Quantum spin ice was first coined for explaining the fluctuating phase of $Tb_2Ti_2O_7$ and later used to explain neutron scattering results on $Yb_2Ti_2O_7$. A quantum spin ice is a type of quantum spin liquid, where quantum effects play an essential role in increasing the fluctuation of the moments. In $Yb_2Ti_2O_7$, unlike $Ho_2Ti_2O_7$ and $Dy_2Ti_2O_7$, in which the relatively large moments ($10\mu_B$) can be considered as classical spins with an Ising anisotropy, Yb^{3+} moments are weaker and prone to quantum fluctuations; additionally, the presence of XY components in the g tensor and anisotropic exchanges with transverse terms can induce quantum fluctuations sufficient to destabilize the more conventional ordered states. The primary difference between the classical description and the quantum version of the DSIM model is that the spin Hamiltonian incorporates all the symmetry allowed off-diagonal terms (as in the case of frustrated triangular lattices Sec.1.3.2). The quantum spin ice Hamiltonian then can be expressed as:

$$H = J_{\parallel}\sum_{i,j} S_i^z S_j^z - J_{\pm}\sum_{i,j}(S_i^+ S_j^- + S_i^- S_j^+) + J_{\pm\pm}\sum_{i,j}(\gamma_{i,j} S_i^- S_j^- + \gamma_{i,j}^* S_i^+ S_j^+) + J_{z\pm}\sum_{i,j}\Big(S_i^z(-\gamma_{i,j}^* S_j^+ - \gamma_{i,j} S_j^-) + [i \leftrightarrow j]\Big) \tag{7.2}$$

Here, the effective spins are expressed in the local coordinate along the local "Ising" [111] direction, with $\pm$ referring to the two orthogonal complex directions, γ is a four-dimensional complex unimodular matrix that simplifies the representation of the Hamiltonian and has a purely geometric origin. $J_{\parallel}$ (also sometimes referred to as J_z) is the exchange interaction that corresponds to the Ising case, and the rest of the terms are the transverse and off-diagonal components of the Hamiltonian. The Hamiltonian can also be expressed in the global coordinates. The advantage of writing the Hamiltonian in the local tetrahedron coordinate is to show directly the resemblance and difference with the classical ice model.

This Hamiltonian is the general nearest-neighbors, symmetry-allowed, exchange Hamiltonian for the pyrochlore lattice, and it supports multiple types of ground-state configurations, as shown in Fig.7.1C. for example. In the following section, we focus more specifically on $Yb_2Ti_2O_7$ and discuss some of the crucial results published in the last decade.

7.2 The quantum pyrochlore magnet $Yb_2Ti_2O_7$

7.2.1 Low temperature magnetic properties

In $Yb_2Ti_2O_7$, the site point symmetry is D_{3d} with the main symmetry axis along the [111] directions. The local electrostatic environment of Yb^{3+} in the pyrochlore lattice directly influences the ground state properties of $Yb_2Ti_2O_7$

CEF level	1^{st}	2^{nd}	3^{rd}
E in meV	76(1)	81(1)	116(1)

Table 7.1: Crystal field excitation levels for $Yb_2Ti_2O_7$ [68]

due to the CEF splitting of the J = 7/2 manifold. The single ion anisotropy of Yb^{3+} moments is established by M(H) and CEF measurements [68, 75] and the reported value of the g-tensor in the local coordinate are $g_\perp$ = 3.6(1) and $g_\parallel$ = 1.9(2) and thus giving an XY anisotropy character with $g_\perp/g_\parallel$ = 1.9(1). From the INS-CEF experiment, $Yb_2Ti_2O_7$ shows a single ion ground state that is well separated from the first excited level by 76meV (see Tab.7.1). The authors [68] reports the ground state wavefunction:

$$|\pm\rangle = \pm 0.36(1)\,|\pm 7/2\rangle \pm 0.08(1)\,|\mp 5/2\rangle \mp 0.92(1)\,|\pm 1/2\rangle \tag{7.3}$$

Similar CEF studies [75] report consistent results confirming the S_{eff} = 1/2 nature of the moments in $Yb_2Ti_2O_7$. In contrast to classical spin ice compounds, the ground state wavefunction consists of the superposition of $|m_j\rangle$ states and is very different from the classical Ising case. The superposition also implies a quantum mechanical character of the moments that can not be captured accurately by a classical model and establishes $Yb_2Ti_2O_7$ as an example candidate for studying spin liquid physics.

Magnetization characterization measurements [67, 76] in the paramagnetic regime (above 300mK) identify a ferromagnetic Curie-Weiss temperature of $\approx$ 0.6K for $Yb_2Ti_2O_7$. Specific heat measurements reveal a broad hump at 3K and a sharp $\lambda-$type anomaly around 270mK, indicating a transition [76]. The estimated [76] strength of the Yb^{3+}-Yb^{3+} interactions are 0.3 T/μ_B, and it undergoes a phase transition to an ordered ferromagnetic phase below 300 mK.

Study	J_{zz}	$J_{\pm}$	$J_{\pm\pm}$	$J_{z\pm}$
Ross et al.[71]	0.17(4)	0.05(1)	0.05(1)	-0.14(1)
Thompson et al.[77]	0.026(3)	0.074(2)	0.048(2)	-0.159(2)

Table 7.2: Comparison of different parameters of the exchange Hamiltonian. All values are in meV.

7.2.2 A quantum spin ice Hamiltonian ?

In spin ice physics, it has been found that the long-range dipolar interactions play an essential role in determining the low-temperature magnetic properties. However, in-field neutron studies on $Yb_2Ti_2O_7$ and theoretical considerations found that anisotropic exchange interactions dominate over long-range dipolar interactions. Thus, there needs to

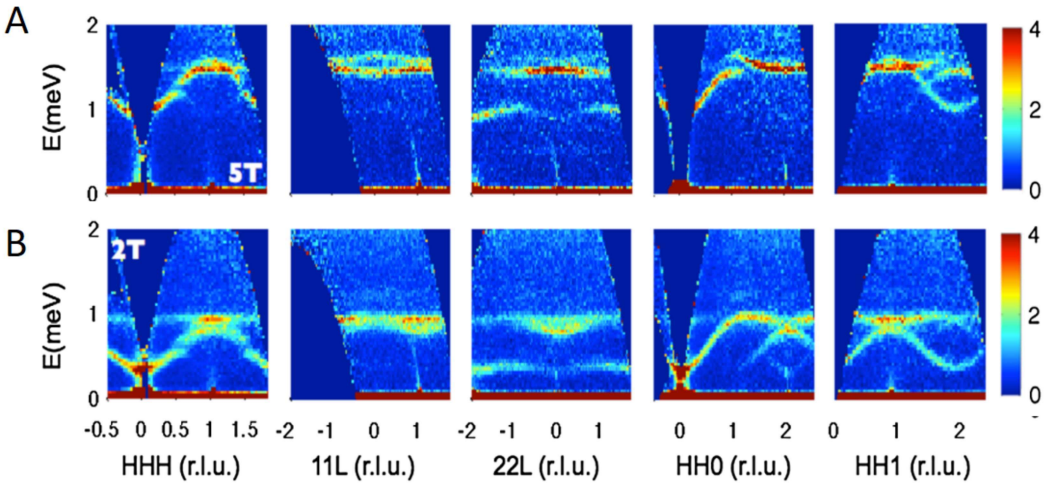

Figure 7.3: S(Q,ω) for T = 30 mK at H = 5T(**A.**) and H = 2 T (**B.**) were measured. The plots show the different slices in the [HHL] plane. The analysis reveals spin wave dispersions in five different directions, from which the parameters of the spin Hamiltonian have been estimated (Tab.7.2). Extracted from [71].

be a total of six parameters (four exchange constants and two g-tensor components, parallel and perpendicular to the local (111) direction) to better describe $Yb_2Ti_2O_7$. At high field values, for example, 2T, the INS spectrum is explained by using a linear spin-wave expansion of this Hamiltonian (Fig.7.3). The parameters estimated by [71] using a spin wave model is shown in Table.7.2. A more recent but similar analysis of the in-field INS spectrum has been done by Thompson et al. [77] and confirmed the strong influence of the anisotropic exchange terms. Moreover, these analyses estimated the parameters of the Hamiltonian that lead to a ferromagnetic ground state. However, these studies could not explain the INS spectrum under a low or zero magnetic field. The following section discusses the controversial and complex problem of understanding the zero-field ground state.

7.2.3 The magnetic ground state of $Yb_2Ti_2O_7$: a controversy

As further experiments tried to confirm the existence of a ferromagnetic type order below 300mK, a controversy began to rise. μSR measurements [78] reveal a fluctuating ground state in both stoichiometric polycrystalline and single-crystal samples, despite the presence of pronounced specific heat peaks at T_c=265 mK and T_c=185 mK, respectively (see Fig.7.4). While other experiments evidenced the presence of a clear dynamical transition with very slow fluctuations [79], some neutron studies suggest that the ferromagnetic transition [80] takes place below 300mK, in agreement with magnetization measurements [81]. In $Yb_2Ti_2O_7$, the presence of a ferromagnetic order strongly depends on the type of sample used and the synthesis methodology [81].

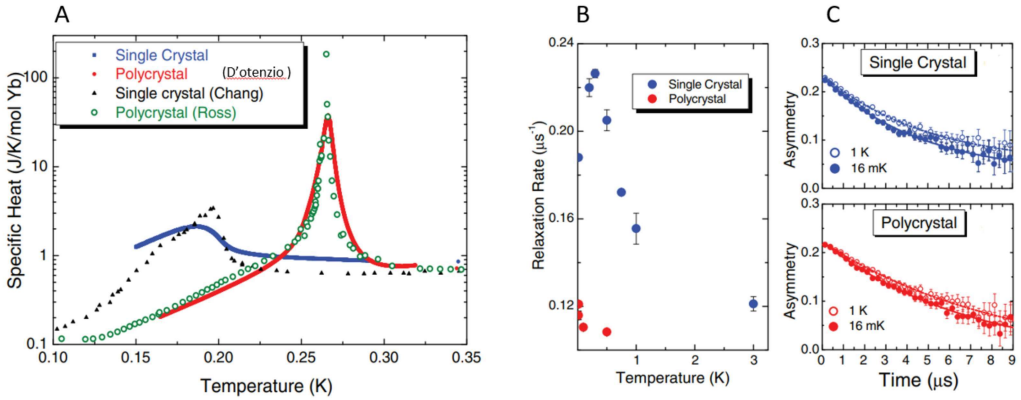

Figure 7.4: **A.** Specific heat from different experiments is shown for comparison and highlight the sample dependency of $Yb_2Ti_2O_7$. **B,C.** LF Muon relaxation under a small field of 0.5mT. Both samples show a fluctuating ground state below T_c. Extracted from [78]

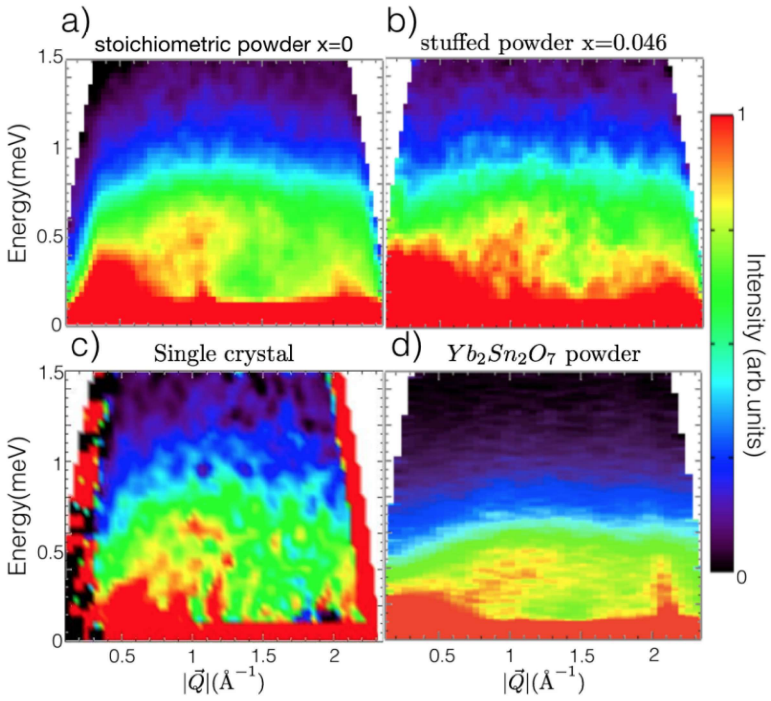

Figure 7.5: Sample dependence of $Yb_2Ti_2O_7$ and comparison of INS observations at 100mK. The high sample sensitivity is evident from the qualitative difference of the S(Q,ω) plots. The stuffed powder has the general form $Yb_{2+x}Ti_{2x}O_{7+y}$ with x=0.046 and $Yb_2Sn_2O_7$ has a similar pyrochlore structure, where Ti is replaced by Sn. Extracted from [63]

7.2.4 Disorder effects: Chemical stress

The nature of the ground state is only a part of the puzzle in the physics of $Yb_2Ti_2O_7$; numerous experiments have revealed [69] a high sample sensitivity. Experiments on the stuffed sample $Yb_{(2+x)}Ti_{(2-x)}O_{7+y}$ highlights this high sensitivity even with minimal defects. Gaudet et al. [68] investigated $Yb_{(2+x)}Ti_{(2-x)}O_{7+y}$ where the excess Yb^{3+} is stuffed in the B sublattice, replacing Ti^{4+}. As the number of neighboring oxygen ions differs for these two sites,

when Yb^{3+} occupies the B sites, the charge neutrality is likely preserved by causing additional oxygen vacancies. CEF analysis reveals that the ground state moment and anisotropy are affected under these additional oxygen vacancies, revealing one of the possible sources of disorder in $Yb_2Ti_2O_7$. Furthermore, comparing INS experiments (see Fig.7.5), the S(Q,ω) plots qualitatively reveal the sample dependency at low temperatures.

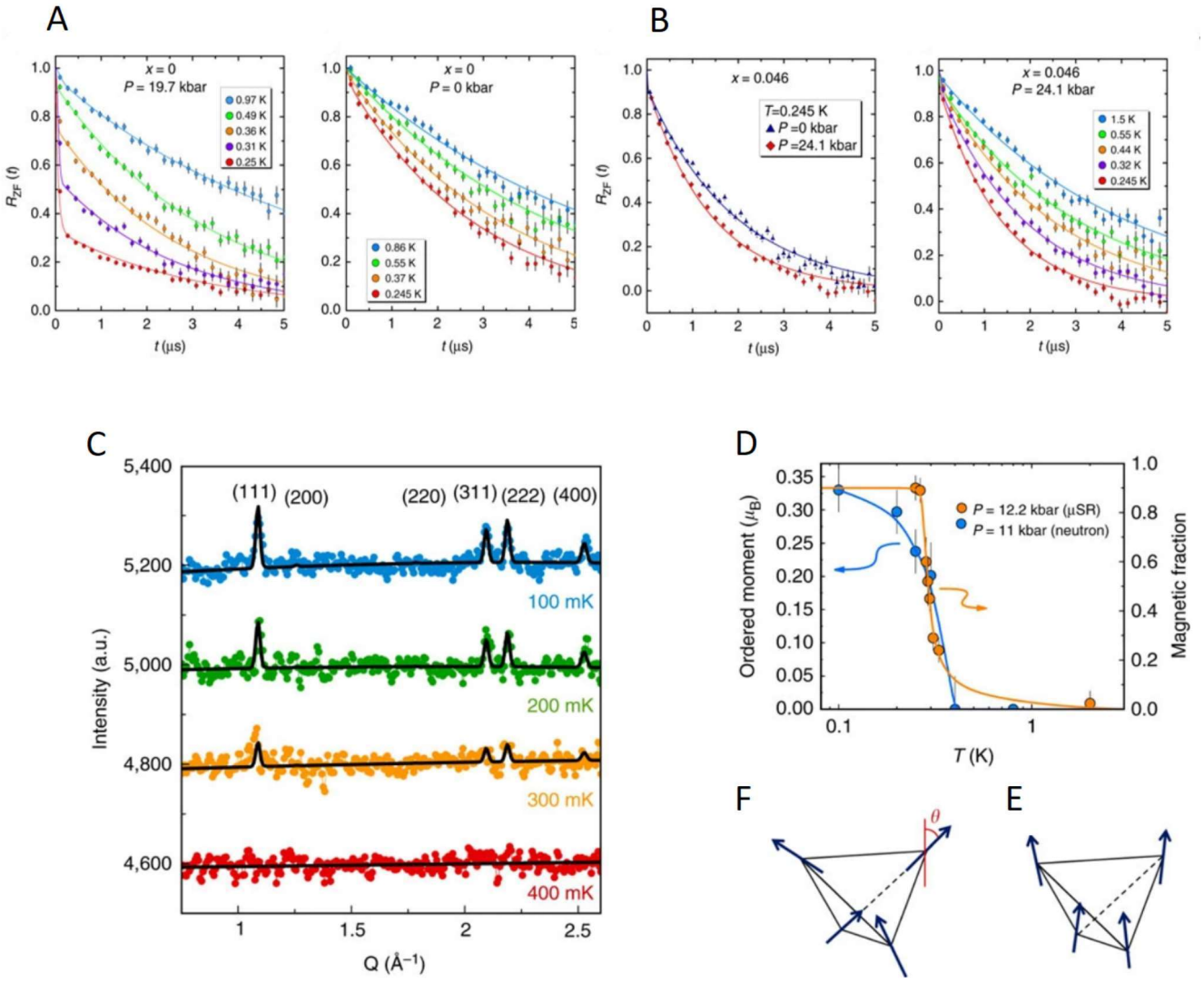

Figure 7.6: **A.** Muon spin resonance spectroscopy of $Yb_2Ti_2O_7$ shows that a spin frozen phase is stabilized under high pressure, which is not the case in the absence of external pressure, or in the case of the stuffed sample, **B.**. **C.** Neutron Diffraction on $Yb_2Ti_2O_7$ between 400 and 100mK, measured under a pressure of 11(2) kbar. **D.** Ordered moment versus temperature determined by neutron diffraction for P=11(2) kbar (blue, left axis) and magnetic fraction determined by μSR for P=12.2 kbar (orange, right axis). **E,F.** θ=14° for P=0 and θ=5° for P=11 kbar, where, θ is the splay angle between the [001] direction and the magnetic moment, tilted towards the local [111] directions of the tetrahedron. Extracted from [82]

Another study [82] combining neutron diffraction and muon spin relaxation confirms a magnetic transition from a disordered, non-magnetic ground state to a splayed ferromagnetic ground state with applied pressure. Neutron studies (Fig.7.6C.) reveal the appearance of magnetic Bragg peaks as the temperature is reduced below 300mK

under pressure. μSR further confirms these findings by revealing that the full fraction of the moments orders under a similar applied pressure. These results were obtained for the stuffed $Yb_{(2+x)}Ti_{(2-x)}O_{7+y}$ sample with x=0.046, which initially shows no ordering without pressure. The remarkable observation from studying the dynamics using μSR is that even relatively low pressure can destroy the disordered spin liquid state and induce magnetic order.

These experiments showed that the origin of sample dependence is mainly due to chemical defects like substitution and highlight that structural strain (chemical or pressure) is an important mechanism that can select the ground state properties of $Yb_2Ti_2O_7$. Very recent progress in chemical synthesis made possible the fabrication of ultra-pure $Yb_2Ti_2O_7$ samples that finally allowed to reach a consensus which is detailed in the following section.

7.2.5 Magnetic properties of the x=0 stoichiometric phase

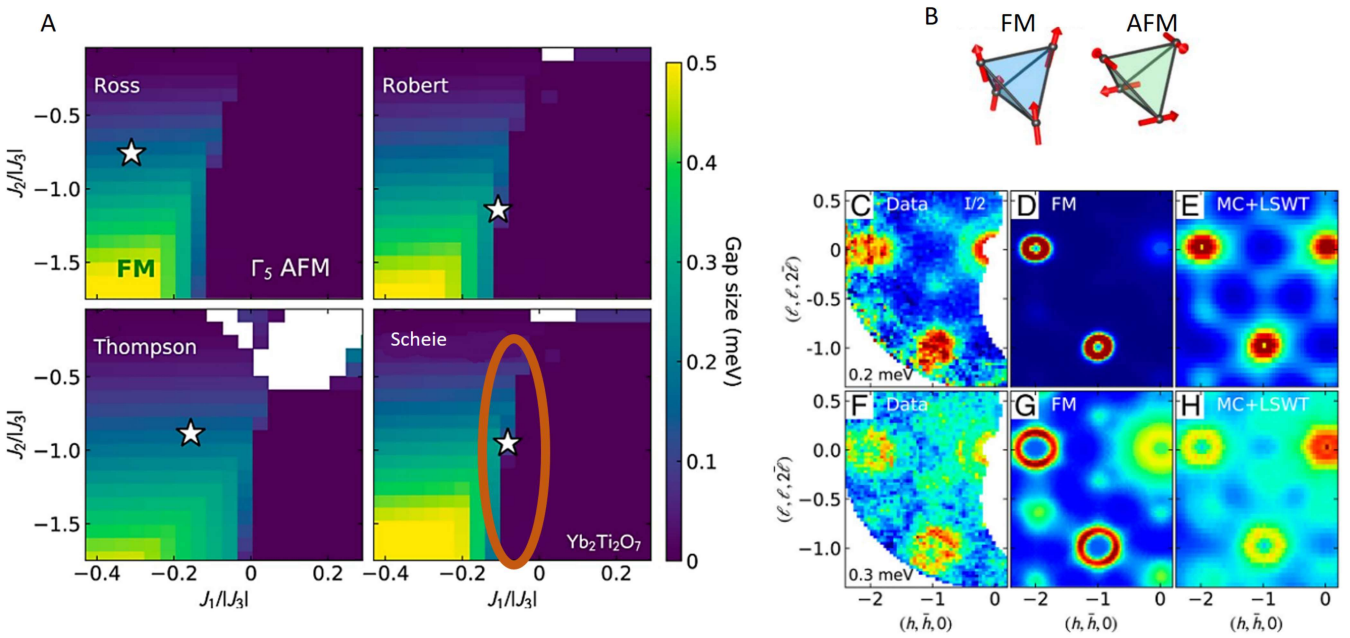

Figure 7.7: **A.** Comparison of calculated zero-field spin wave gap at (220) points estimated by [71, 77, 83, 84]. The orange circle indicate the AFM-FM phase boundary on which $Yb_2Ti_2O_7$ is predicted to lie. J_1, J_2 and J_3 are the exchange parameters of the spin Hamiltonian written in the global reference frame. The color indicates the magnitude of the gap in the INS spectrum. **B.** Schematics for the FM and AFM phase. **C, F.** Shows neutron scattering data integrated at E=0.2meV and 0.3meV at T = 70mK and **D,E,G,H.** shows the simulated S(Q,ω). **D,G.** is the numerical simulation corresponding to a FM ground state, **E,H** Corresponds to numerical simulation using spin wave theory with Monte Carlo technique. Extracted from [84]

Detailed magnetization measurements [81] revealed that the balance of exchange interactions and anisotropy were likely to lead to competing phases. However, the absence of ultra-pure samples led to a difficulty in reaching consensus. Following this investigation, Monte Carlo simulations along with linear spin-wave calculations [85] demonstrate that the ordering and field dependence observed in certain powder and single crystals can arise from the competition between a ferromagnetic and an antiferromagnetic phase, whose boundary is shifted by quantum

fluctuations and mediated by order-by-disorder selection. This scenario was strengthened by the more detailed analysis of the inelastic and diffused neutron scattering data on $Yb_2Ti_2O_7$ that refine its Hamiltonian parameters and conclude to a slightly different location in the phase diagram, very close to the FM/AFM phase boundary [83].

Recent ultrapure single crystals made it possible to reliably investigate the x=0 stoichiometric $Yb_2Ti_2O_7$. Scheie et al. [84] carried out an extensive experimental investigation and numerical analyses taking into account previous ideas and data. Small-angle neutron scattering and INS spectroscopy clarified that $Yb_2Ti_2O_7$ sits at the edge of competing FM and antiferromagnetic-Γ^5 (AFM) phases (see Fig.7.7) and should not be understood as a quantum spin ice candidate [71]. Spin wave calculations and Monte Carlo simulations also reveal that the short-ranged AFM phase is metastable. This AFM phase corresponds to the ψ_2, ψ_3 phase in a tetrahedra's local frame (Fig.7.1C.). Below 300mK, a mixture of these two phases coexists with strong signs of spin dynamics. Furthermore, this phase competition is predicted to exist at higher temperatures and persist in the paramagnetic phase [85, 86].

7.3 Effect of magnetic field on the ground state

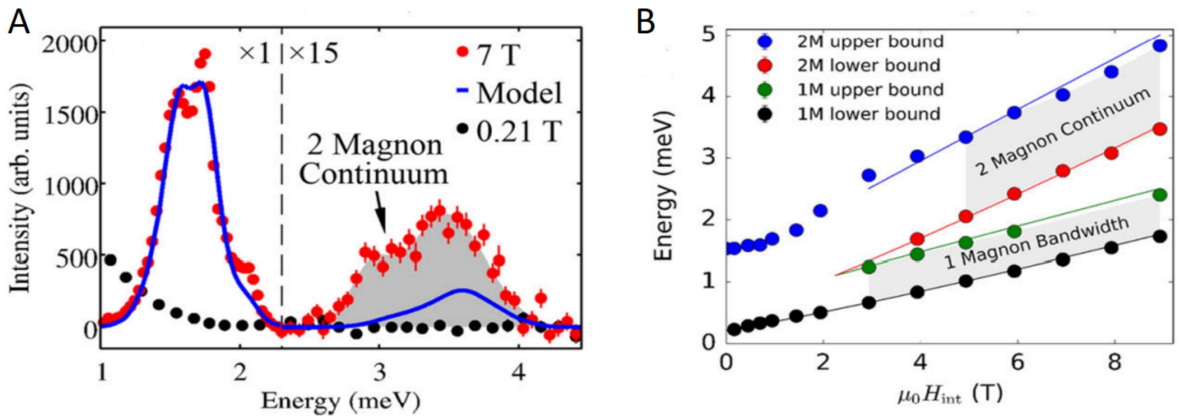

Figure 7.8: **A.** INS experiment with $Yb_2Ti_2O_7$ single crystal, the figure shows the E-cut of the S(Q,ω) intensity and shows the 1^{st} and the 2^{nd} magnon excitations measured at E_i = 6.3meV, and the corresponding fits with a non-interacting spin-wave model. **B.** The linear field dependence of the 1^{st} and the 2^{nd} magnon excitations. Extracted from [77] respectively

INS experiments have been previously performed by Ross et al. [71] and Thompson et al. [77] on $Yb_2Ti_2O_7$ single crystal to understand how the spectrum evolves in a magnetic field. Both studies successfully explain the high field (>2T) spectrum using spin-wave theory (Fig.7.3A,B.). However, there are two issues. First, at lower fields, the semiclassical approach breaks down, and the reason for the fluctuating behavior of the spins is still not clear. Second, Thompson et al. [77] observe a second magnon excitation (see Fig.7.8) that is not compatible with a linear spin wave theory. The authors speculate from the low field measurements that additional quantum effects are necessary to describe the dynamical structure factor of $Yb_2Ti_2O_7$ and they propose a quasiparticle breakdown picture at low fields. Such quasiparticle breakdown affects a considerable portion of the Brillouin zone; however, they

are rare in three-dimensional ordered magnets and reveal unusually high quantum fluctuations. The corresponding predictions of the location of $Yb_2Ti_2O_7$ in the phase diagram are shown in Fig.7.7, and this highlights another puzzling observation in the context of $Yb_2Ti_2O_7$ that we further probe in the next Chapter.

7.4 Outlook

The strong sample dependence of $Yb_2Ti_2O_7$ can be explained because it lies on a critical phase boundary. The effect of disorder in $Yb_2Ti_2O_7$ may thus be a unique situation and offer the opportunity to use chemical substitution as a tuning mechanism to select different ground states. Thus we plan to investigate the low-temperature physics of $Yb_2Ti_2O_7$ under chemical pressure. To do this, one can use Zr, which has a larger ionic radius than Ti^{4+} ($r_{Ti^{4+}} < r_{Zr^{4+}}$), but smaller than Yb^{3+}, which guarantee the possibility of a finer tuning than for previous studies [63] and while keeping the charge balance thus avoiding oxygen defects. Additionally, upon substituting Ti by Zr, the internal chemical stress will indeed be affected, and we know from the literature survey that $Yb_2Ti_2O_7$ is sensitive to such a stress. In the next chapter, we continue our discussion on $Yb_2Ti_2O_7$ by reporting our experimental results on the $Yb_2Ti_{2(1-x)}Zr_{2x}O_7$ series where x = 0 to 0.2.

Chapter 8

The $Yb_2Ti_{2(1-x)}Zr_{2x}O_7$ series

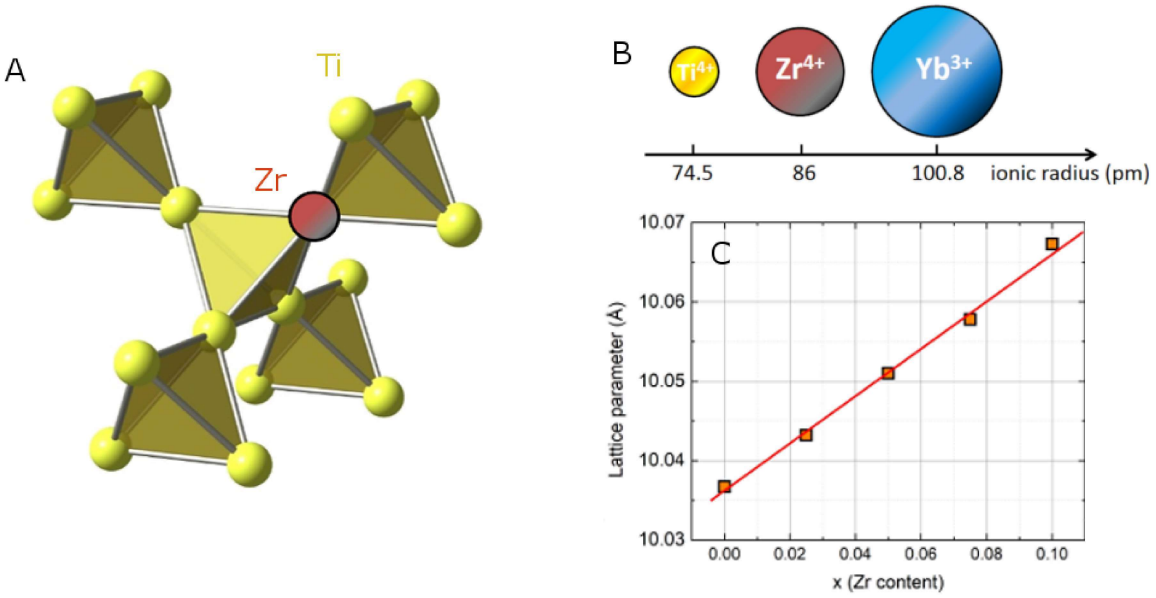

Figure 8.1: (A) Schematic of the corner-sharing lattice of Ti^{4+} substituted by Zr^{4+} ions and (B) evolution of the ionic radius of relevant ions. (C) The lattice parameters of $Yb_2(Ti_{1-x}Zr_x)_2O_7$ powder samples determined by xray diffraction evolve linearly as a function of x. Orange squares represent the data points and the solid red line is a linear fit.

We described the complex ordering processes in frustrated magnets using $Yb_2Ti_2O_7$ as an example in Chapter 7.

We first summarize below the main results. The pyrochlore crystal $Yb_2Ti_2O_7$ contains magnetic Yb^{3+} ions. Its structure and properties were described roughly 50 years ago, but its low temperature magnetic excitations remains to be understood. The critical issue was that some samples produce ferromagnetism below 300 mK, while this ordered phase is highly sensitive to disorder-induced effects. At very low temperatures ($<$300mK), $Yb_2Ti_2O_7$ is ferromagnetic, but its excitation spectrum is comparable to that of a quantum spin liquid. It is now agreed that

$Yb_2Ti_2O_7$ is not in a spin liquid phase but is extremely close to the antiferromagnetic phase. It was discovered that ferromagnetism and antiferromagnetism coexist in the low-temperature state of $Yb_2Ti_2O_7$. Small angle neutron scattering (SANS) experiment provides convincing evidence for metastable antiferromagnetism. This multiphase magnetism likely accounts for the extraordinary sensitivity to disorder of $Yb_2Ti_2O_7$. The low T magnetic excitation spectrum has been attributed to both multimagnon decay as well as fractionalized quasiparticles. The competition between seemingly incompatible magnetic phases is especially significant for frustrated magnetism and requires further theoretical and experimental investigations.

This work on magnetism in pyrochlore lattices is the result of a Franco-Canadian collaboration (M. Gingras, University of Waterloo (Canada) / C. Decorse, ICMMO, Université Paris Saclay (France), E.Lhotel, S.Petit LLB, (France)). We substitute a fraction of the Ti^{4+} ions with Zr^{4+} to characterize the ground state properties of this new related family of compounds $Yb_2Ti_{2(1-x)}Zr_{2x}O_7$. The advantage of substitution with Zr^{4+} over previous approaches [63] is that oxygen vacancies may be avoided since both Zr and Ti have an ionic charge of +4. Secondly, the ionic sizes of Ti^{4+} and Zr^{4+} are close, what allows for a fine tuning by chemical doping. Lastly, this doping can be interpreted as a negative chemical pressure. Given the fact that the P-T phase diagram of $Yb_2Ti_2O_7$ has already been investigated [82] using applied pressure, our findings will complement prior research and pave the way for detailed numerical modelling.

This work is organized into three main sections. In the first section, we present our characterization measurements on the $Yb_2Ti_{2(1-x)}Zr_{2x}O_7$ series of powder samples, with x = 0 to 0.2. This is followed by the neutron scattering experiments on our powder samples of $Yb_2Ti_{2(1-x)}Zr_{2x}O_7$, where we mainly focus on the x=0 stoichiometric sample and the x=0.025 doped sample. We perform zero field and infield measurements to reproduce and validate prior observations for the stoichiometric x=0 sample, followed by a detailed in-field neutron characterization of the x=0.025 sample. We finally qualitatively present our key observations with polarized neutron scattering on the x=0 and the x=0.025 crystal samples.

8.1 Characterization of the $Yb_2Ti_{2(1-x)}Zr_{2x}O_7$ samples

In this section, we present a brief characterization of the polycrystalline samples of $Yb_2Ti_{2(1-x)}Zr_{2x}O_7$ which have been measured or analyzed during the course of this PhD work. These samples have been synthesized and characterized by C. Decorse using x-ray diffraction and by R. Kumar (LPS, postdoctoral fellow in the SQM team). Without presenting the details of the solid-state synthesis, let us just mention that the synthesis protocol requires a long series of annealing and grinding in order to achieve the complete substitution of Zr on the Ti site (Fig.8.1). The increase of the Zr content x is confirmed by the measurement of the lattice parameter using x-ray diffraction that shows a continuous increase as a function of x (Fig.8.1), as expected from the larger ionic radius size of Zr^{4+} ions (86 pm) as compared to Ti^{4+} (74.5 pm) [87].

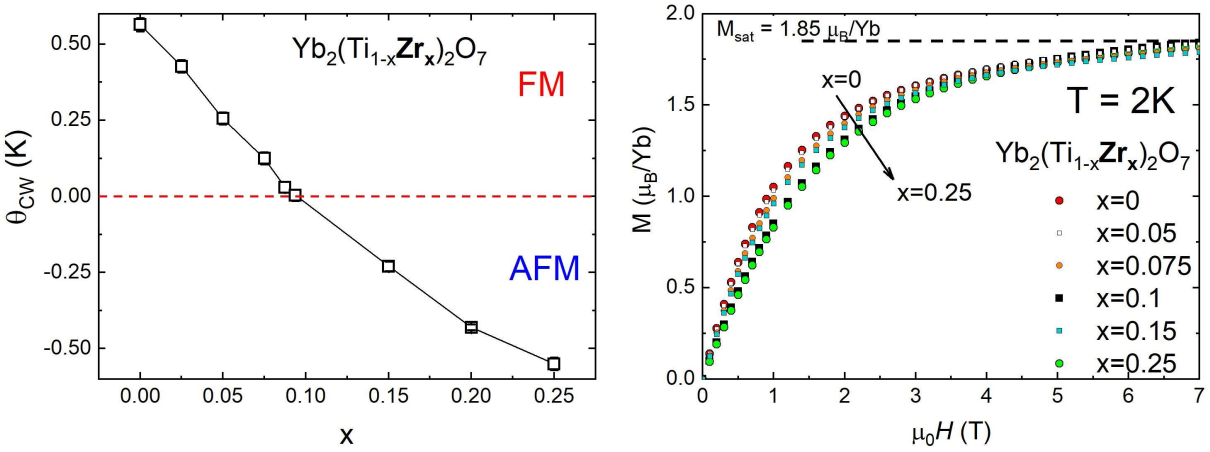

Figure 8.2: (Left) Evolution of the Curie-Weiss temperature as a function of x in $Yb_2Ti_{2(1-x)}Zr_{2x}O_7$ powder samples. (Right) Evolution of the magnetization under applied fields as a function of x at T=2K. For large values of x, reaching the saturation requires a higher applied field due to the presence of antiferromagnetic interaction.

We then turn to the characterization of the magnetic properties of our powder samples using susceptibility and magnetization measurements down to 1.8K. Magnetic susceptibility was measured under an applied field of 1000Oe, and shows a Curie-Weiss paramagnetic behavior in the range 1.8-10 K, which is sufficiently low in temperatures to use satisfactorily the $S_{\rm eff} = 1/2$ model but high enough to prevent any potential signatures of magnetic ordering (occurring around 300mK for the $x = 0$ sample, see Chap.7). We found a continuous evolution of the Curie-Weiss temperature $\theta_{\rm CW}$ as a function of x, very much like the lattice parameter (Fig. 8.2). Interestingly, the sign of the Curie-Weiss temperature changes from positive to negative for a value $x \sim 0.1$, signaling the development of antiferromagnetic correlations at the expense of ferromagnetic ones for large x values. This observation is further confirmed by magnetization measurements performed at 2K for several x contents (Fig.8.2) where the saturation is clearly restraint as x is increased, as it is expected in the presence of an antiferromagnetic interaction.

Due to the typical energy scale of the exchange interaction of $\sim$1 K in this rare-earth pyrochlore family, it is necessary to perform very low temperature measurements to fully characterize the magnetic properties. Given the large number of compounds of the series, we could only conduct measurements on a significant subset of them. Fig.8.3 shows muon spin relaxation and neutron diffraction results down to at least 100mK. The difference of the zero-field muon asymmetry at 20mK between the x=0 and the x=0.1 compound is striking: while the relaxation observed for the $x = 0.1$ remains exponential with a rather slow spin relaxation rate, the muon relaxation for the x=0 sample shows a pronounced non-exponential shape, with a sharp, fast relaxation rate at early times ($t < 0.5$ μs, followed by a slowly decaying relaxation for long times. The later relaxation is similar to what has been found in early measurements of $Yb_2Ti_2O_7$ [88, 89] and was interpreted in the context of very slow spin fluctuations and the presence of short-range order below a critical temperature of $T_c \simeq$ 300mK. This is also the same strong relaxation that was found under applied pressure [82]. Our μSR measurements thus give evidence for a range of ground states occurring for $0 < x < 0.1$.

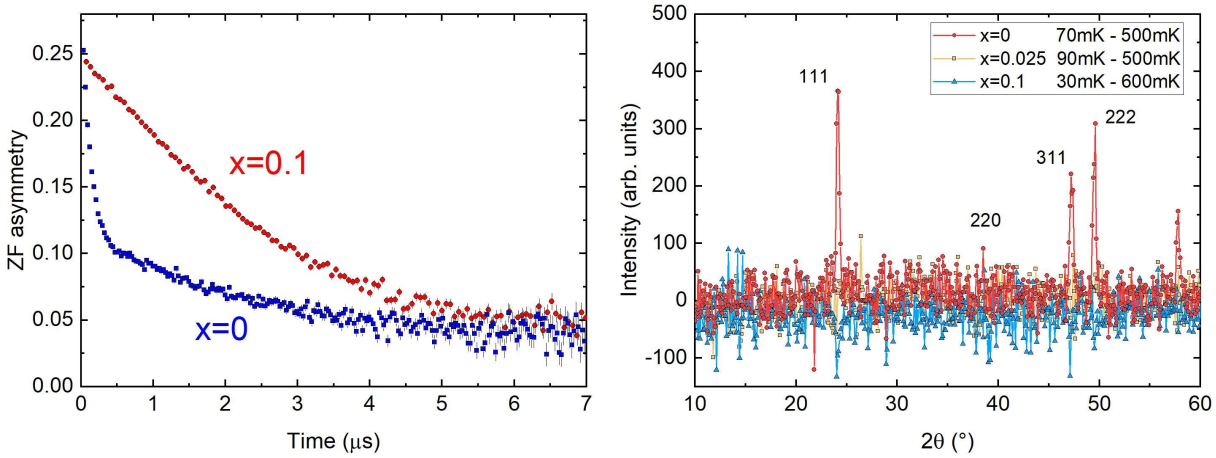

Figure 8.3: (Left) Muon spin relaxation measured at T=20mK under zero applied fields on the LTF spectrometer (PSI) in our x=0 and x=0.1 powder samples. (Right) Neutron diffraction patterns measured below 100mK on the G4.1 instrument (LLB, Saclay) for the x=0, x=0.025 and x=0.1 powder samples. Each pattern has been subtracted from a high temperature dataset of 500 or 600mK. Strong magnetic Bragg peaks at the (111), (311) and (222) positions appears for the x=0 composition only.

We also performed elastic neutron diffraction on our $x = 0$, $x = 0.025$ and $x = 0.1$ powder samples. We report on Fig.8.3 the difference in intensity between the base temperature (< 100mK) and a higher temperature dataset (500 or 600 mK) above the suspected transition for each composition. While the x=0 compound shows strong magnetic Bragg peaks at the (111), (311) and (222) positions, no increase of intensities is detected within our statistics for all the other samples. This is in very good agreement with our μSR results and further highlights the strong sensitivity to pressure of the magnetic properties of the $Yb_2Ti_2O_7$ phase.

8.2 Gapless Continuum of excitation $Yb_2Ti_{2(1-x)}Zr_{2x}O_7$

To begin, we refer to the study by Thompson et al. [77]. The group observed spin dynamics as a function of the applied field using high-resolution INS. The INS spectrum exhibits a scattering continuum in zero field mode (see Chapter 7). A gap is created when an applied magnetic field is present, and the S(Q,ω) maps exhibit broad spin wave-like excitations. At higher fields, dispersive magnons are seen, as well as a two-magnon continuum which emerges. As the field is lowered, the second magnon scattering continuum starts to overlap with the one-magnon bands. The study reveals that the low and high field zones are connected smoothly, without phase transitions, and that the spin gap increases monotonically with the field. Our analysis is along the same spirit, and we perform similar INS experiments under an applied field; however, we use a powder sample, and our experimental setup allowed us to reach only 2K, above the ordering temperature for $Yb_2Ti_2O_7$ ($<$300mK).

The S(Q,ω) intensity maps (see Fig.8.4) reveal the presence of a gapless continuum of scattering intensity for all doping levels. As the doping level is increased from x = 0 to 0.025, for all temperatures, we observe that the intensity at high Q ($>1\text{Å}^{-1}$), low E ($<$1meV) region is suppressed in comparison to the intensity at low Q ($<1\text{Å}^{-1}$),

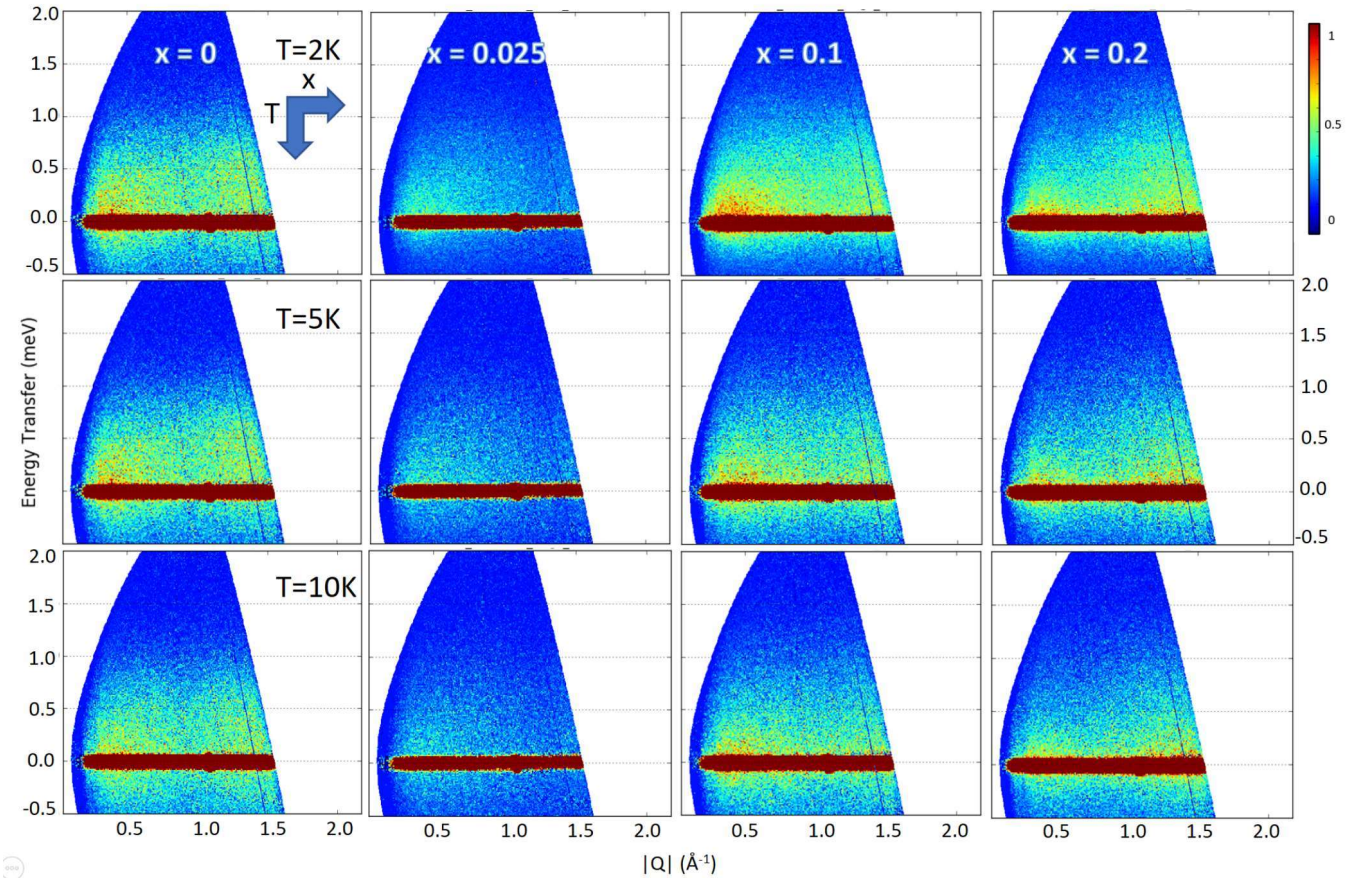

Figure 8.4: S(Q,ω) intensity maps at T = 2K, 5K and 10K with E_i=2.5meV, under zero applied field for $Yb_2Ti_{2(1-x)}Zr_{2x}O_7$, with x = 0, 0.025, 0.1, 0.2. S(Q,ω) intensity is normalized to the number of incident neutrons and a common scale is used for clarity of comparison. Note that the sample mass is not the same for different x, in particular for the x=0.025 and x=0.1 samples. The overall intensity of the x=0.025 measurement is weaker due to the reduced scattering cross section because of a lower mass. (see Tab.8.1)

x	0	0.025	0.05	0.1	0.2
m(g)	4.238(1)	0.991(1)	1.332(1)	4.253(1)	4.268(1)

Table 8.1: Mass of $Yb_2Ti_{2(1-x)}Zr_{2x}O_7$ powder samples measured in INS experiment on LET (ISIS-STFC, UK)

low E region. The redistribution of spectral weight follows in a non-trivial manner as the doping is further increased till x=0.1. The continuum is a signature of the spin dynamics due to the AFM phase in $Yb_2Ti_2O_7$, the fact that INS scattering persists in the presence of doping likely suggest a similar origin of the continuum of scattering. To investigate the evolution of the inelastic signal, we report and analyze the temperature dependence of the dynamical structure factor.

8.2.1 Temperature Dependence

To qualitatively understand the dependence of S(Q, ω), let's consider the Q-dispersion (Fig.8.5) and its evolution with the doping level. Let's consider now the different doping levels, from x=0 to x=0.2. We observe (Fig.8.5A.) that

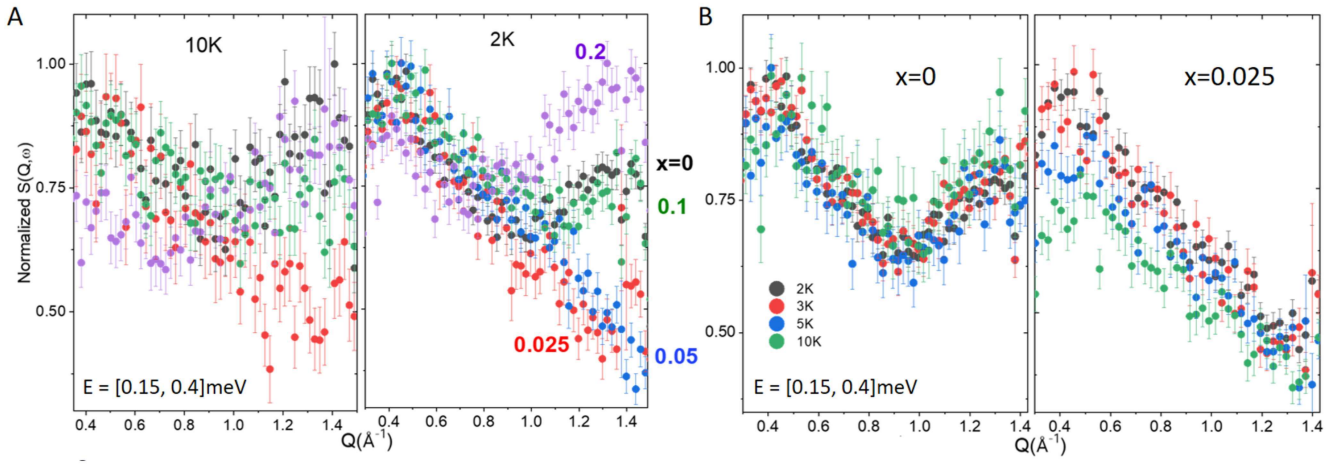

Figure 8.5: **A.** S(Q,ω) cuts at different x for 10K and 2K, normalized by maximum intensity. **B.**Temperature dependence of S(Q,ω) Q-cuts for x=0 and x=0.025.

at 10K and 2K, for x= 0 and 0.1, S(Q,ω) decreases till 1Å^{-1} and recovers intensity at high Q (>1Å^{-1}). However, this is not the same for x= 0.025 and x=0.05 where the intensity is still decreasing at higher Q values. This is interesting as the doping seems to change the Q-dispersion of the low energy modes in a non-trivial manner.

We report the temperature dependence of the Q-dispersion (Fig.8.5B.) between 2K and 10K, for the x=0 and x=0.025 samples only. There is no observable change in the Q-dispersion of the x=0 pure sample. However, the Q-dispersion only evolves slightly in the low Q region for the x=0.025 sample, suggesting a difference between the doped x=0.025 sample and x=0 sample's temperature variation.

In the E-cuts (Fig.8.6A), we qualitatively compare the low energy excitation for the different doping levels. The measurement is normalized with the elastic peak intensity for comparison. We observe that as the doping level is increased from 0 to 0.05, no significant change is observed in the inelastic channel. However above a doping level of x = 0.1, a rise in the S(Q,ω) intensity is noticeable at E = 0.2meV. This is likely due to the increase of the quasielastic contribution that implies an increase of low energy fluctuations in the highly doped samples.

The comparison between the different doping levels is not trivial, and we focus mainly on the pure x=0 sample and the x=0.025 sample in the following to study the temperature dependence of the inelastic scattering at low energy (see Fig.8.6B.).

The situation is similar in both samples, and we observe that as the temperature is lowered, the inelastic intensity increases down to 5K, below which we do not notice any significant temperature variations for both samples. The data is fitted at T=10K and T=5K with Eqn.8.1:

$$S(Q,E) = A_E \exp\{-(E/2w_E)^2\} + (1-\exp\{-E/k_BT\})^{-1}\left[\frac{A_L E w_L}{E^2+w_L^2} + A_{INS}\exp\{-((E-E_c)/2w_{INS})^2\}\right] \quad (8.1)$$

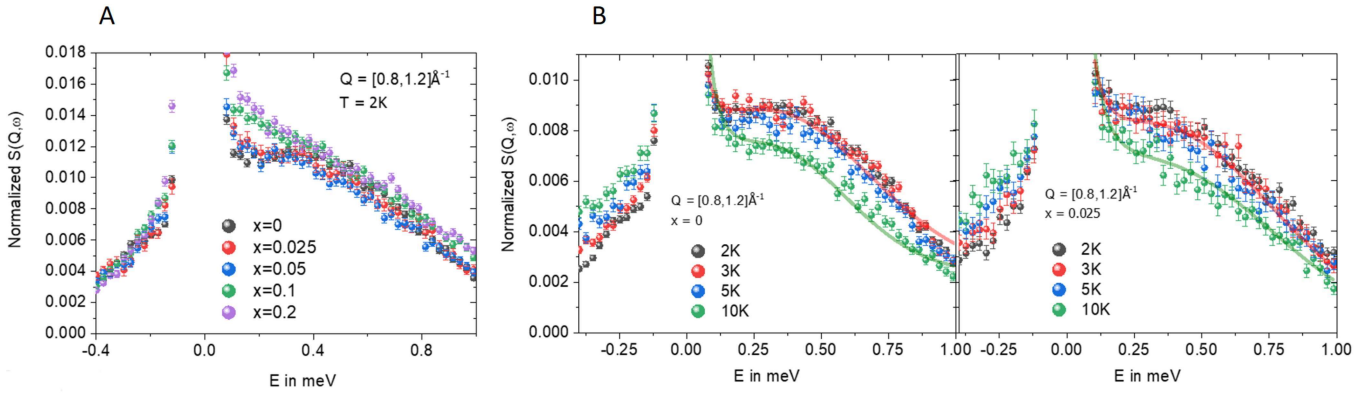

Figure 8.6: **A.** E-cut of S(Q,ω) and its temperature dependence of doping fraction x, normalized by maximum intensity. **B.** Temperature dependence of E-cut for x=0 and x=0.025 fitted with quasielastic and inelastic components, depicted by solid lines.

where the first term is the elastic component and the second term is the quasielastic and inelastic excitation that is modelled by a Gaussian peak. For the fits the inelastic component is constrained at E_c = 0.35 for both x = 0 and x=0.025. From the fits of x=0, the ratio of the peak intensity of the inelastic magnetic excitation at low temperature ($\leq$ 5K) vs 10K is 1.2(1), and we also report a factor of 1.3(1) increase in quasielastic intensity at lower temperatures. For x = 0.025, the 1.3(1) increase of the inelastic component is similar, and we also remark a rise in the quasielastic intensity by a factor 1.8(1). We can confirm from our fits that the low energy temperature dependence is similar in these two samples. The fits also confirm the presence of dynamics as is evidenced by the quasielastic component that we use to model the low energy region.

In summary, we note a similarity between the pure and the doped samples' temperature variation; the only significant difference in observation comes from the low Q ($<1\text{Å}^{-1}$) region of the x=0.025 sample. In contrast to the pure sample, we notice a slight temperature dependence in this region.

8.2.2 Field Dependence

INS previously performed by Thompson et al. [77] on $Yb_2Ti_2O_7$ single crystal has revealed how the spectrum evolves in a magnetic field. In the light of this investigation, we perform similar experiments but at a higher temperature of 2K, where $Yb_2Ti_2O_7$ is not ordered but displays essentially the same features in the inelastic spectrum than at 100mK, first to reproduce the results obtained by Thompson et al. [77] and then to validate our measurements on the pure powder sample. In the x=0 situation (see Fig.8.8, top panel), we observe that the field dependence of S(Q,ω) of the x=0 powder sample is similar to the previous in-field study [77] at T=2K. The magnetic character of this continuum scattering is confirmed by a strong field dependence. In addition, dispersive modes appear and evolve under an applied field from 0.6T to 7T. At low H, we notice a redistribution of spectral intensity, and as the field is increased, the excitations become sharper and increase in energy transfer.

We observe a more diffuse scattering in the x=0.025 sample, additionally with the suppression of intensity at

higher Q ($\geq 1\text{Å}^{-1}$). The most exciting fact is, that doping with Zr does not suppress this dynamical behavior and instead modifies the spectral distribution. To understand the role of the negative chemical pressure on this dynamical phase, we analyze the field dependence of the E-cuts. In the x=0 sample (see Fig.8.8), at low H, we observe the maximum peak intensity shift in energy at a rate of 0.20(1) meV/T with the excitation bandwidth remaining constant. As the field is increased (Fig.8.8B.), a gap is introduced between the elastic peak and the inelastic excitation which increases linearly with H. We also report the sharpening of the excitation band with an increase in intensity at the high field values. It is clear that a single Gaussian is not suitable to model the intensity peaks. Therefore we use multicomponent Gaussians to fit the measured spectrum. This is reasonable as the energy spectrum is powder averaged and may consist of multiple spin-wave modes. Furthermore, even at 2K, we observe the 2^{nd} excitation band (Fig.8.8C.) that is an order of magnitude weaker than the first band. This second excitation band shifts at a rate of 0.37(1) meV/T. Similar to Thompson et al. we also report the simultaneous broadening and weakening of the peak with increasing H. Furthermore, the gap between these two bands also increases linearly with H, as the second excitation shifts twice the first band's rate. We could perform this analysis till 4T, below which it becomes complicated to disentangle these two bands due to a considerable overlap. Our analysis reproduces the previous investigations and confirms the similarity of our pure $Yb_2Ti_2O_7$ sample with the previous experiment.

In the light of the previous study, we investigate the x = 0.025 sample (see Fig.8.9) by performing similar mea-

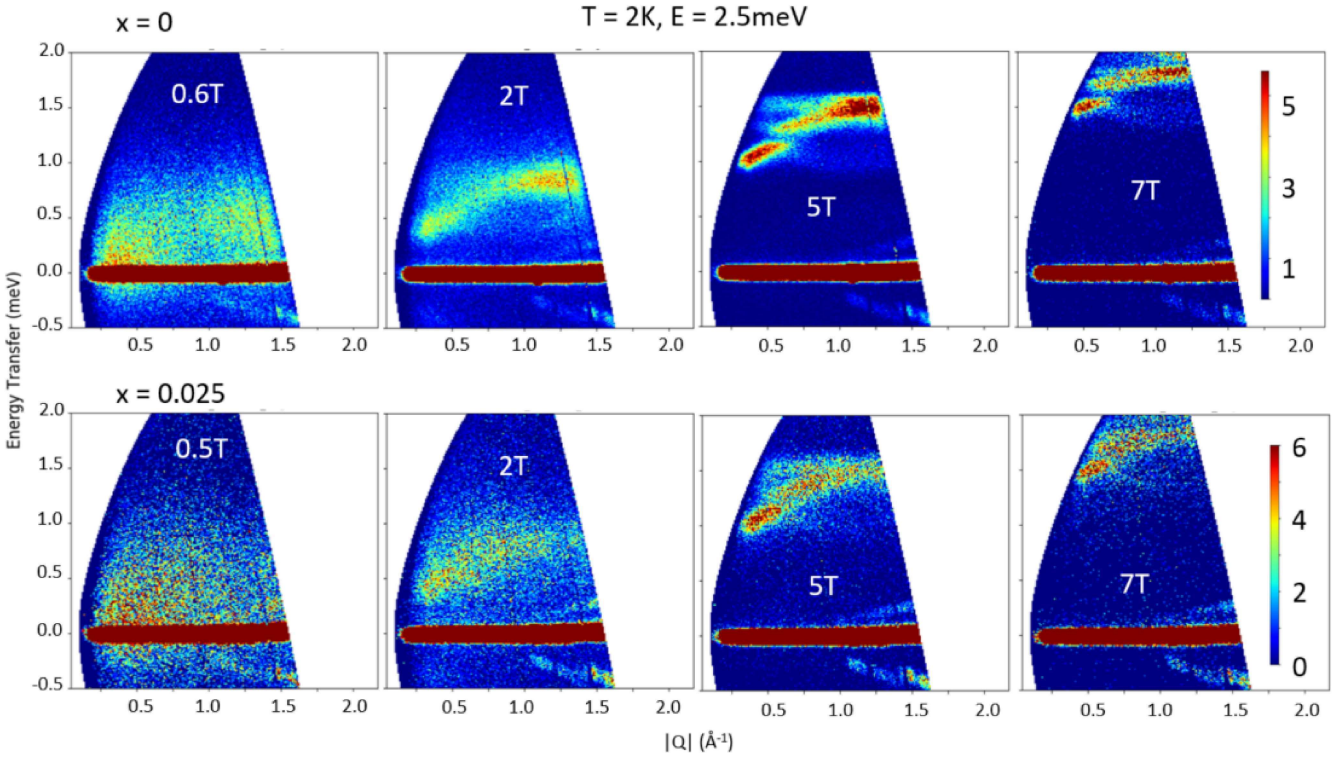

Figure 8.7: Comparison of S(Q,ω) intensity maps for selected values of applied field for x=0 and 0.025 powder samples. Intensity cutoff selected for maximum visual clarity and comparison.

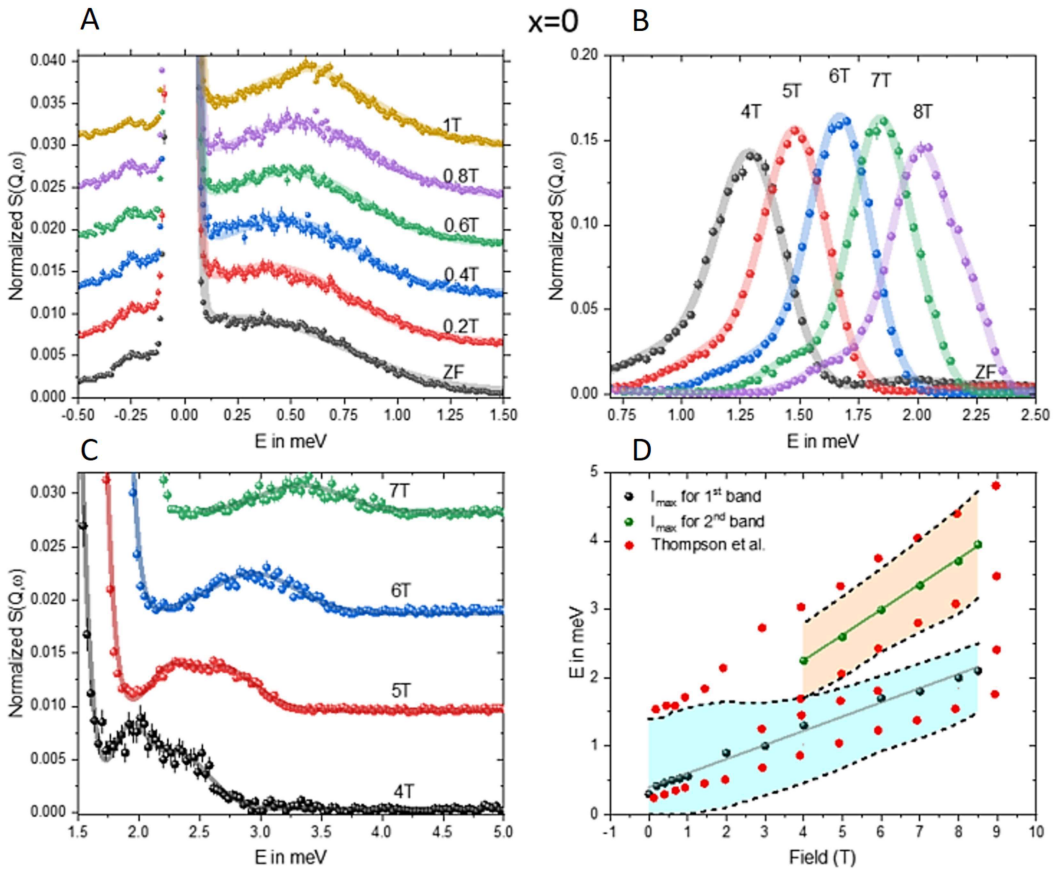

Figure 8.8: Q-integrated E cuts of S(Q,ω) with Q =[0.8,1.2]Å^{-1}. **A,B.** Spectral redistribution and linear evolution with field, solid lines shows the corresponding fits to data using Eqn.8.1. **C.** Evolution of second excitation band measured with E_i = 6.2meV. **D.** Comparison of our results with Thompson et al. [77], the points represent the maximum intensity peaks as obtained from the fits, the colored regions with dotted lines estimates the spread of the excitation bands and is calculated from the Gaussian fits.

surements and analysis for the doped sample. The low field evolution turns out to be similar to the x=0 sample (see Fig.8.9A.). We observe the similar evolution of the inelastic peak and a linear increase of the separation between the elastic and the inelastic excitation as the field is increased at a rate 0.21(1) meV/T. At intermediate and higher field values the inelastic peak rise in intensity, followed by a narrowing of its bandwidth. Strikingly, we also recover a weak second band at higher fields that has a similar field dependence, i.e., it becomes weaker and broader with increasing field. In contrast to the x=0 sample, under the highest applied field (8T), we do not observe a gap between the two bands, and the 2$^{\text{nd}}$ excitation shifts linearly at a rate of 0.24(9)meV/T. The critical distinction in the x=0.025 sample is that the peak of the second band shifts at a similar rate as the peak intensity of the first band.

Furthermore, we identify that the rate of shifting for the x=0.025 case corresponds to the rate of shifting of the 1$^{\text{st}}$ band of the x=0 case. The consequence of this observation is that the 2-magnon interaction picture can be numerically tested with our observations to check the validation of the quasiparticle breakdown hypothesis [77] that is used to explain the field dependence for the x=0 pure sample.

We also realize from the results of the powder INS that to pinpoint the ground state of the x=0.025 sample, polarized neutron scattering experiments will be necessary. Thus in the next section, we complement the current analysis with polarized neutron scattering experiments on crystals with x=0 and x=0.025 to clarify the magnetic ground state properties of this family of compounds.

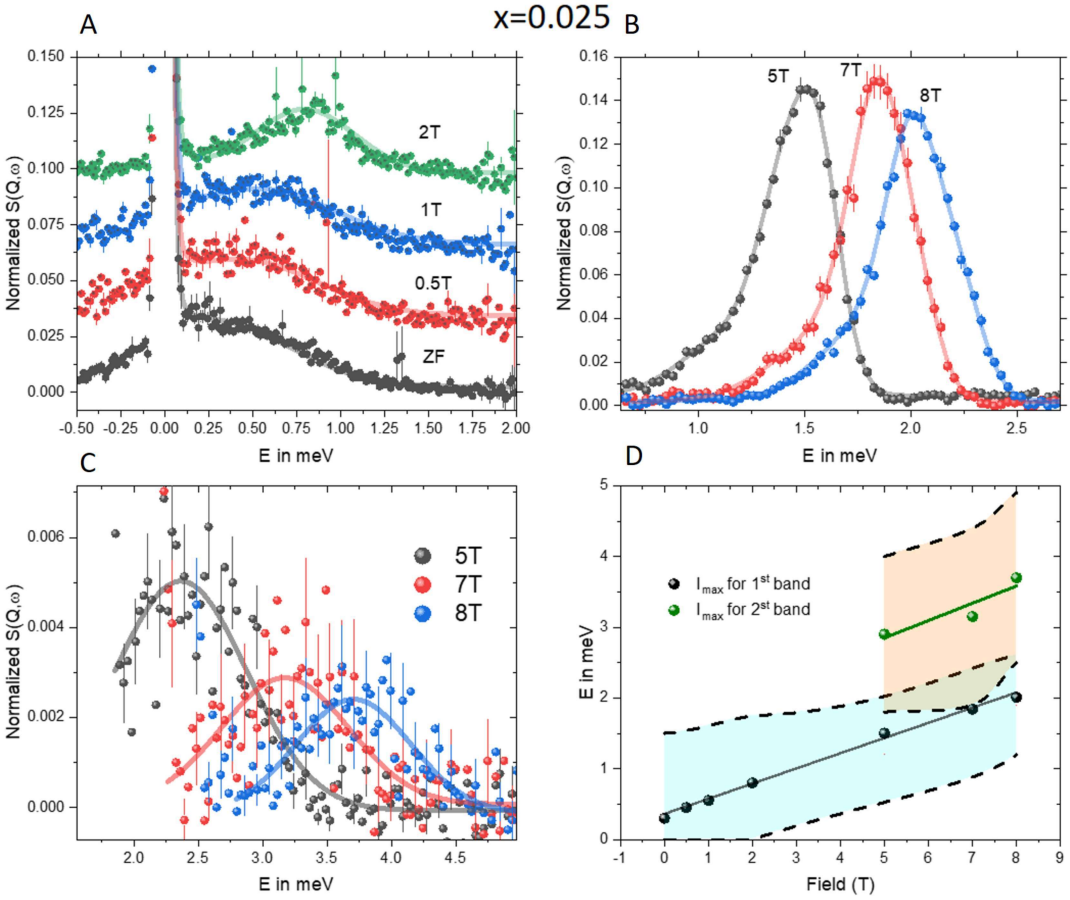

Figure 8.9: **A.** Q-integrated E cuts of S(Q,ω) with Q =[0.8,1.2]Å^{-1} for x=0.025. **A,B.** Spectral redistribution and linear evolution with field, solid lines shows the corresponding fits to data using Eqn.8.1. **C.** Evolution of second excitation band measured with E_i = 6.2meV. **D.** Dependence of intensity peak position as a function of applied The points represent the maximum intensity peaks as obtained from the fits, the colored regions with dotted lines estimates the spread of the excitation bands and is calculated from the Gaussian fits, similarly to Fig.8.8.

8.2.3 Polarized neutron scattering on x=0 and x=0.025 single crystals

We perform polarized neutron scattering on the D7 instrument at ILL, Grenoble, France, to probe the low-temperature magnetic excitation of $Yb_2Ti_{2(1-x)}Zr_{2x}O_7$. In this experiment crystal samples of $Yb_2Ti_{2(1-x)}Zr_{2x}O_7$ (x=0 and 0.025) are used to map diffuse scattering in the (H H L) plane.

We perform scans till 300mK for $Yb_2Ti_2O_7$ (below which it starts to develop ferromagnetic order [63] as we verified with another separate experiment on MACS, NIST, Gaithersburg, USA) and till 55mK for $Yb_2Ti_{2(1-x)}Zr_{2x}O_7$. Our experiment reveals that ferromagnetic order is suppressed till at least 55mK for the x=0.025 sample. This is not

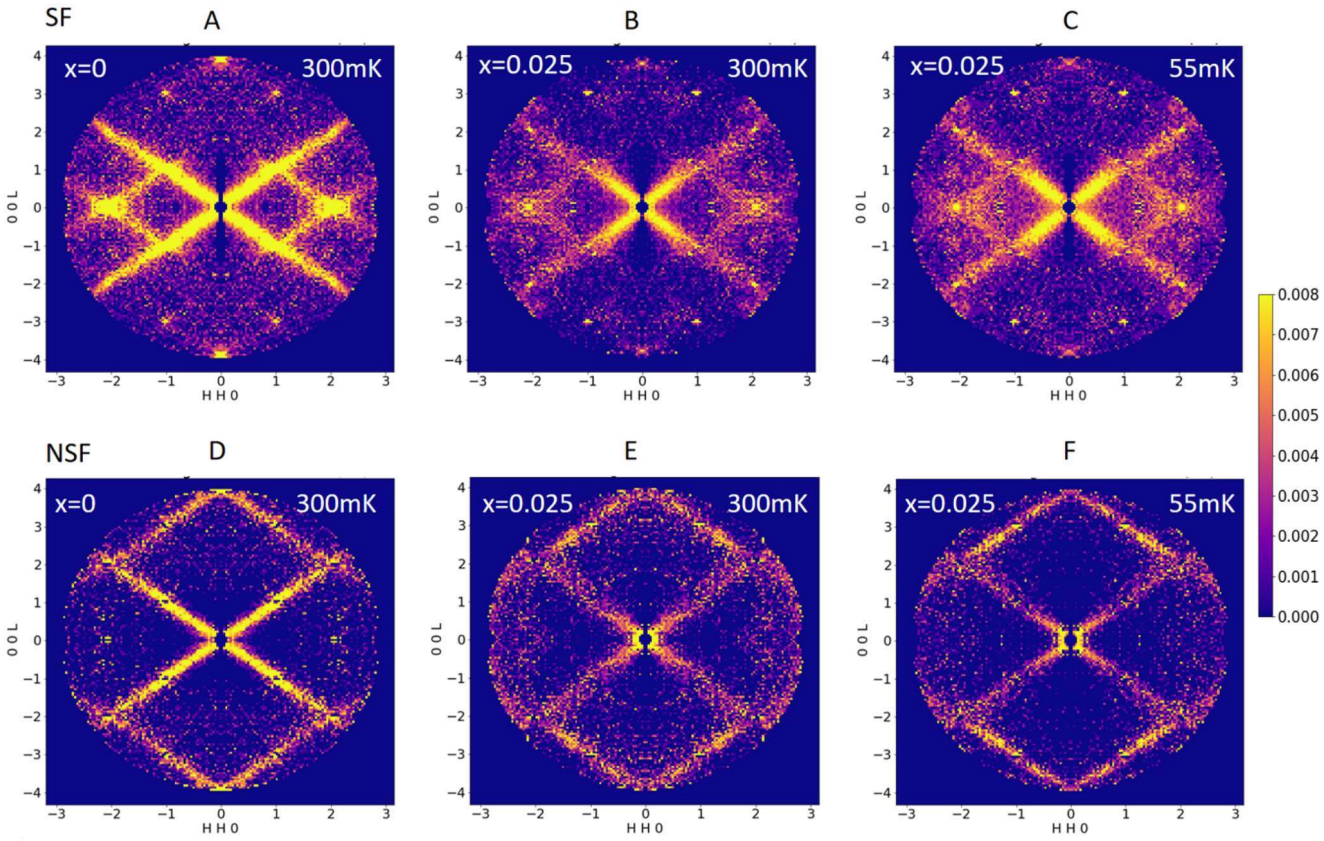

Figure 8.10: Symmetrized 5K background subtracted S(Q) maps in (hhl) plane of polarized neutron scattering experiment **A-C.** Spin flip measurements for x=0 and x=0.025 samples, **D-F.** Non spin flip measurements.

surprising given the high sensitivity of the magnetic ground state of $Yb_2Ti_2O_7$ to internal stress.

In (Fig.8.10) we compare the background subtracted measurement (with the corresponding measurements at 5K as the background) of $Yb_2Ti_{2(1-x)}Zr_{2x}O_7$. First, let's consider the measurements at T = 300mK of our x=0 sample (Fig.8.10A,D.). We observe scattering intensity rods in the (111) direction in both the SF and NSF channel. The coexistence of these three-dimensional longitudinal correlations, or rod features, are also reported by Thompson et al. and others before them [71].

Let's consider now only the SF channel (Fig.8.10A-C.). For the x=0 sample, (Fig.8.10A.) we observe high intensities at Brillouin zone positions (1, 1, 3) (Bragg peak) , (2, 2, 0), and (0, 0, 4). In the context of the $Yb_2Ti_2O_7$, intensity at the (2, 2, 0) point indicates antiferromagnetic correlations. The presence of the (111) rods and the intensity at the (2, 2, 0) point simultaneously correspond to correlations [84] beyond a single tetrahedron that are numerically reproduced by considering a multiphase. For the x=0.025 sample, (Fig.8.10B,C.), in contrast to the x=0 sample, we report a lower intensity at high Q. This is reminiscent of our powder INS experiment (Fig.8.5A at 2K), where we also note the drop in intensity of S(Q,ω) in the x=0.025 powder sample. Secondly, we measure a high intensity at the (2, 2, 0) point, similar to the x=0 sample. From the arguments provided in the context of the x=0 sample [84] we can speculate that $Yb_2Ti_{2(1-x)}Zr_{2x}O_7$ (x=0.025) is also in a mixed phase.

Let us now consider the NSF channel (Fig.8.10D-F.) For the x=0 sample, we observe intensity at the (2, 2, 2) and (0, 0, 4) points with the presence of rods at high Q in the (111) direction. Comparing NSF with the SF channel (Fig.8.10D.), we note the intensity at (2, 2, 0) is suppressed. The NSF measurements, for the x=0.025 sample, is similar to x=0 sample (Fig.8.5E-F.). However the difference is in the intensity distribution of these (111) rods. For x=0, the intensity of the (111) rods at low Q is higher than the intensity at high Q; this is not the case for the x=0.025 sample, where at low Q, we observe a similar intensity in the (111) rods as at high Q.

To conclude, the observations strongly suggest that order/fluctuation can be tuned by chemical doping of Zr in $Yb_2Ti_2O_7$. The qualitative similarities and differences between S(Q,ω) of these two samples can be further modeled by the microscopic Hamiltonian to perform a comparative analysis and is planned as the future step of this work. Using the multiphase formalism similar to $Yb_2Ti_2O_7$, we will be able to estimate how far from the AFM/FM phase boundary $Yb_2Ti_{2(1-x)}Zr_{2x}O_7$ is located. Further experiments using other doping levels are likely to be very useful to understand how $Yb_2Ti_2O_7$ can be tuned in the phase diagram of the pyrochlore and thus offers a new technique to probe the phase diagram experimentally.

8.3 Conclusion and perspective

In conclusion, we have convincingly shown that $Yb_2Ti_2O_7$ can be effectively displaced from the AFM/FM multiphase without suppression of spin dynamics by chemical doping. Furthermore, we demonstrate that doping with Zr, or artificial stress, is a way to tune the ordering temperature of $Yb_2Ti_2O_7$ without affecting the low-temperature dynamics.

From the characterization measurements, we report that the Curie-Weiss temperature can vary from FM to AFM by adjusting the doping level. The ground state of the x=0 parent compound exhibits both ferromagnetic and antiferromagnetic correlations [84]. For the x=0 sample, the pyrochlore settles into an FM/AFM multiphase, and our initial analysis suggests a similar situation for x=0.025 sample where at T=55mK we observe signatures of such competing phases. Inelastic neutron scattering experiments reveal a gapless scattering continuum at ZF with strong signs of spin dynamics and antiferromagnetic correlation. This gapless character suggests that the phase boundary between FM and AFM states in $Yb_2Ti_2O_7$ is extended. It remains an open question for $Yb_2Ti_{2(1-x)}Zr_{2x}O_7$, with x=0.025, to see if a similar continuous phase boundary exists between the AFM phase and some other fluctuating phase.

We have also shown from our INS powder experiments and analysis on $Yb_2Ti_2O_7$ a striking similarity in the field evolution of magnetic excitation between the observations at 2K and 150mK, indicating that spin-spin correlation operator at high T and T = 0 might indeed be proportional as is proposed by the theoretical framework [86].

The research work with the $Yb_2Ti_{2(1-x)}Zr_{2x}O_7$ series will be continued in the future, with plans to reproduce the polarized neutron measurement numerically. The project has already provided us insights into pyrochlore mag-

netism and, in the future, will allow us to better understand the puzzle of sample sensitivity in this category of compounds.

Conclusion

This thesis is dedicated to the experimental study of new rare-earth based frustrated quantum magnets using magnetization measurements, neutron and muon spectroscopies. Motivated by the recent discovery of the new quantum triangular magnet $YbMgGaO_4$ –which shows experimental signatures of spin liquid behavior in the presence of strong chemical disorder –, we first investigated the sister compound $ErMgGaO_4$ of the same chemical family in order to shed new lights on the effect of disorder on their magnetic properties. Alternatively, we focused on new Yb-based quantum triangular magnets, with a perfect triangular lattice and without any detectable disorder effect, to search for other quantum spin liquid candidates. Our work provides three classes of compounds for the investigation of the interplay between correlations, disorder, and frustration in 2D rare-earth based triangular magnets. Finally, we investigated the new pyrochlore series $Yb_2(Ti_{1-x}Zr_x)_2O_7$, where the substitution of Zr on the Ti site is used as chemical pressure to destabilize the magnetic order observed for the pure, x=0, parent compound, and explored the evolution of the spin dynamics in the vicinity of this peculiar x=0 phase in the relevant phase diagram.

Our main results for each part are summarized in the corresponding paragraphs below.

S_{eff} = 1/2 triangular anisotropic antiferromagnets

$ErMgGaO_4$: $ErMgGaO_4$ is, like $YbMgGaO_4$, an example of a 2D triangular antiferromagnet with intrinsic disorder. Er^{3+} as the rare-earth ion, implies a significant difference of the anisotropy of the moments in comparison to Yb^{3+} moments; This was the primary experimental aim, to study the effects of the 'same' disorder but under a modified anisotropy. This work focused on a recently synthesized powder sample with a high purity, obtained from our collaborators at McMaster University. From magnetization measurements, we confirmed the single-ion anisotropy $g_\perp/g_\parallel$ = 1.0(1) already reported on a single-crystal and further detected a signature of magnetic order at T = 2.5K with a zfc-fc splitting in the magnetic susceptibility. This static order is characterized by an asymmetric lineshape of the elastic neutron scattering intensity close to the M point of the Brillouin zone, in agreement with the Warren function expected for two-dimensional order but with a distribution of correlation lengths. Our analysis indicates that such correlations can have a spatial spread up to 70 Å. This elastic scattering clearly appears below T = 2.5K and is consistent with our susceptibility measurements. The position of this elastic intensity (M point) is in agreement with a striped order state, as predicted for the sister compound $YbMgGaO_4$ by DMRG calculations. Furthermore,

neutron and muon spectroscopies both showed the existence of persistent dynamics in the form of a quasi-elastic continuum and a constant muon spin relaxation rate down to 25mK. The emergence of an ordered state in the presence of spin dynamics is a recurrent theme in rare-earth frustrated systems, and here may be interpreted as a ground state made of a superposition of all the possible degenerate stripe-ordered phases, but separated by a small energy barrier, which can be overcome by thermal fluctuations or quantum tunnelling. While this is not the definition of a quantum spin liquid, it gives perhaps a more generic scenario to understand the ubiquitous spin fluctuations in the context of rare-earth frustrated magnets in the presence of strong disorder. Finally, we note that this inelastic continuum observed for $ErMgGaO_4$ is highly similar to the situation encountered in $YbMgGaO_4$. However, our very recent INS experiment (not presented here) on $YbMgGaO_4$ shows no static correlations emerging in the low-temperature regime, in agreement with the reports from literature. If this excitation continuum is mainly due to broadened spin waves originating from an ordered phase, why is such an order absent in $YbMgGaO_4$? The difference in the Hamiltonian parameters between the two compounds may thus be, after all, the key to understand their different ground states. Future experiments with high-quality single crystal of $ErMgGaO_4$ should help to clarify this situation.

$K_3YbV_2O_8$ and $K_2CsYbP_2O_8$: . In this new family of disorder-free triangular compounds, we reported from the M(H) and susceptibility measurements that the inter-ionic interactions between the Yb^{3+} ions are antiferromagnetic for both the compounds but rather weak, an order of magnitude lower, as compared to the $ReMgGaO_4$ family members. The interaction strength of $K_2CsYbP_2O_8$ is even weaker, likely due to the phosphate orbitals on the exchange path, and we thus focused on $K_3YbV_2O_8$. From our fit of the magnetic susceptibility, we estimated the antiferromagnetic interaction to be of the order of 0.5K in $K_3YbV_2O_8$. From our CEF analysis of INS measurements in both compounds, we did not notice signs of CEF broadening due to disorder effects as was seen in $YbMgGaO_4$ and safely validated the S_{eff} = 1/2 picture of Yb^{3+} at low temperature, with an anisotropic character of the moments of $g_\perp/g_\parallel$ = 0.6(1). Fluctuations of the spins is confirmed by μSR spectroscopy for $K_3YbV_2O_8$ down to 60mK, with a rise of the muon spin relaxation rate which suggests that the spins enter into a correlated regime at low temperatures ($\leq 1K$). Interestingly, from INS experiments we observed a weak, temperature-dependent intensity in the inelastic spectrum below 800mK. From our analysis, the most likely explanation for the inelastic signal are paramagnetic-like excitations that appear in a correlated regime above a transition temperature, T_c that is likely below 100mK. Future experiments to search for the low T_c on such compounds will be very interesting.

$Ba_6Yb_2Ti_4O_{17}$: The second disorder-free family that we investigated is the $Ba_6Re_2Ti_4O_{17}$ family, with Re = Yb. Here, our magnetization measurements also evidenced an extremely weak exchange interaction (0.05K), possibly due to the even larger inter-ionic distances. Magnetization and INS measurements both showed that $Ba_6Yb_2Ti_4O_{17}$ satisfies the $S_{\rm eff}$ = 1/2 model. The INS and muon spectroscopic studies gave evidence for a paramagnetic phase down to 100mK in $Ba_6Yb_2Ti_4O_{17}$. It may enter into a correlated regime below this temperature, which would be highly difficult to probe experimentally.

Quantum pyrochlore series $Yb_2(Ti_{1-x}Zr_x)_2O_7$

In this section we reported our measurements on the new series of polycrystalline samples $Yb_2(Ti_{1-x}Zr_x)_2O_7$, and on two single crystals with a level of substitution $x = 0$ and $x = 0.025$, which allow for a comparative analysis between the parent compound (x=0) and the Zr-substituted counterparts. Our results quantitatively reproduced previous findings on the stoichiometric, $x = 0$, $Yb_2Ti_2O_7$ phase and confirmed the extreme sensitivity of the splayed ferromagnetic order, which exists only for the $x = 0$ parent compound. From magnetization and susceptibility measurements, we note that the interaction can possibly be tuned from a net ferromagnetic to antiferromagnetic one by the effect of these substitutions. We then observed the presence of an excitation continuum in the INS spectrum for all the substitution levels and further revealed a non-trivial change in the spectral distribution in zero field as the substitution level increases from $x = 0$ to $x = 0.2$. Indeed, at a level of $x = 0.025$, we found evidence for a change of behavior in the inelastic spectrum, with a noticeable reduction in the spectral weight at high Q values and low energies. Under an applied external field, the continuum becomes sharper and shifts linearly with the field magnitude, resembling broad and damped polarized spin waves. At even higher energies, a second type of broad excitations is observed which was interpreted as a two magnon-like excitations band for the $x = 0$ phase in the literature. While our measurements did reproduce this behavior for the $x = 0$ sample, this explanation does not hold for the $x = 0.025$ which shows a linear shift of the band with a different amplitude than for the first-magnon excitation band, accompanied by a significant broadening. A detailed modelling of our polarized neutron scattering on the two $x = 0$ and $x = 0.025$ single crystal samples may hold the key for understanding the mechanism that turns the splayed ferromagnetic order into a fluctuating spin liquid regime, perhaps because of a strong scattering of magnons by random induced-disorder. In the light of these findings, future experiments to magnetically characterize the x=0.025 crstals under external pressure can be very interesting if we can reproduce similar observations as the x=0 stoichiometric case, this will further allow us to quantify the disorder effects by doping.

Bibliography

[1] Maureen M. Jullan. “The third law of thermodynamics and the residual entropy of ice”. In: *Journal of Chemical Education* 60.1 (1983), pp. 65–66. ISSN: 00219584. DOI: 10.1021/ed060p65.

[2] J. W. Stout W. F. Giauque. *The Entropy of Water and the Third Law of Thermodynamics. The Heat Capacity of Ice from 15 to 273 °K.* Tech. rep. 5. 1936, p. 1145. URL: https://pubs.acs.org/sharingguidelines.

[3] L. Pauling. “The Nature Of Chemical Bond. Application”. In: *Phys. Rev* 455.1927 (1931), p. 1367. URL: https://pubs.acs.org/doi/pdf/10.1021/ja01355a027.

[4] M. J. Harris et al. “Geometrical frustration in the ferromagnetic pyrochlore Ho2Ti2O7”. In: *Physical Review Letters* 79.13 (1997), pp. 2554–2557. ISSN: 10797114. DOI: 10.1103/PhysRevLett.79.2554. URL: https://doi.org/doi:10.1103/PhysRevLett.79.2554.

[5] Stefano Gianni et al. “Fuzziness and Frustration in the Energy Landscape of Protein Folding, Function, and Assembly”. In: *Accounts of Chemical Research* 54.5 (2021), pp. 1251–1259. ISSN: 15204898. DOI: 10.1021/acs.accounts.0c00813. URL: https://dx.doi.org/10.1021/acs.accounts.0c00813.

[6] I. N. Askerzade and A. Aydin. “Frustration effect on escape rate in Josephson junctions between single-band and three-band superconductors in the macroscopic quantum tunneling regime”. In: *Low Temperature Physics* 47.4 (Apr. 2021), pp. 282–286. ISSN: 1063777X. DOI: 10.1063/10.0003738. URL: https://aip.scitation.org/doi/abs/10.1063/10.0003738.

[7] John W Clark. “Variational theory of nuclear matter”. In: *Progress in Particle and Nuclear Physics* 2 (1979), pp. 89–199. ISSN: 0146-6410. DOI: https://doi.org/10.1016/0146-6410(79)90004-8. URL: https://www.sciencedirect.com/science/article/pii/0146641079900048.

[8] G H Wannier. “Antiferromagnetism. The triangular Ising net”. In: *Physical Review* 79.2 (1950), pp. 357–364. ISSN: 0031899X. DOI: 10.1103/PhysRev.79.357.

[9] P. W. Anderson. “Resonating Valance Bonds: A new kind of insulator?” In: (1972). URL: https://reader.elsevier.com/reader/sd/pii/0025540873901670?token=B2002A7D570EA47E7767417D2DB138876C9F4C5129BF80F56C originRegion=eu-west-1&originCreation=20210924120334.

[10] P Fazekas and P W Anderson. “On the ground state properties of the anisotropic triangular antiferromagnet”. In: *The Philosophical Magazine: A Journal of Theoretical Experimental and Applied Physics* 30.2 (Aug. 1974), pp. 423–440. ISSN: 0031-8086. DOI: 10.1080/14786439808206568. URL: https://doi.org/10.1080/14786439808206568.

[11] Yuesheng Li, Philipp Gegenwart, and Alexander A. Tsirlin. “Spin liquids in geometrically perfect triangular antiferromagnets”. In: *Journal of Physics Condensed Matter* 32.22 (2020). ISSN: 1361648X. DOI: 10.1088/1361-648X/ab724e. URL: https://doi.org/10.1088/1361-648X/ab724e.

[12] Leon Balents. “Spin liquids in frustrated magnets”. In: *Nature* 464.7286 (2010), pp. 199–208. DOI: 10.1038/nature08917.

[13] Lucile Savary and Leon Balents. *Quantum spin liquids: A review*. Jan. 2017. DOI: 10.1088/0034-4885/80/1/016502.

[14] Pontus Laurell et al. “Quantifying and Controlling Entanglement in the Quantum Magnet”. In: *Physical Review Letters* 127.3 (2021). ISSN: 10797114. DOI: 10.1103/PhysRevLett.127.037201.

[15] Pietro Carretta and Amit Keren. “NMR and muSR in Highly Frustrated Magnets”. In: *Introduction to Frustrated Magnetism: Materials, Experiments, Theory*. Ed. by Claudine Lacroix, Philippe Mendels, and Frédéric Mila. Berlin, Heidelberg: Springer Berlin Heidelberg, 2011, pp. 79–105. ISBN: 978-3-642-10589-0. DOI: 10.1007/978-3-642-10589-0{_}4. URL: https://doi.org/10.1007/978-3-642-10589-0_4.

[16] Fabrice Bert. “Local probes of magnetism, NMR and μ SR: A short introduction”. In: *École thématique de la Société Française de la Neutronique* 13 (2014), p. 03001. ISSN: 2107-7223. DOI: 10.1051/sfn/20141303001.

[17] C. Broholm et al. “Quantum spin liquids”. In: *Science* 367.6475 (Jan. 2020). ISSN: 10959203. DOI: 10.1126/science.aay0668.

[18] M. R. Norman. “Colloquium: Herbertsmithite and the search for the quantum spin liquid”. In: *Reviews of Modern Physics* 88.4 (Dec. 2016), p. 041002. ISSN: 15390756. DOI: 10.1103/REVMODPHYS.88.041002/FIGURES/14/MEDIUM. URL: https://journals.aps.org/rmp/abstract/10.1103/RevModPhys.88.041002.

[19] David A. Huse and Veit Elser. “Simple Variational Wave Functions for Two-Dimensional Heisenberg Spin-½ Antiferromagnets”. In: *Physical Review Letters* 60.24 (June 1988), p. 2531. ISSN: 00319007. DOI: 10.1103/PhysRevLett.60.2531. URL: https://journals.aps.org/prl/abstract/10.1103/PhysRevLett.60.2531.

[20] Zhenyue Zhu et al. “Topography of Spin Liquids on a Triangular Lattice”. In: *Physical Review Letters* 120 (May 2018), p. 207203. ISSN: 10797114. DOI: 10.1103/PhysRevLett.120.207203.

[21] Olexei I Motrunich. “Variational study of triangular lattice spin-1 2 model with ring exchanges and spin liquid state in κ-(ET)2Cu2(CN)3”. In: *Physical Review B - Condensed Matter and Materials Physics* 72.4 (2005). ISSN: 10980121. DOI: 10.1103/PhysRevB.72.045105.

[22] G Misguich et al. “Spin-liquid phase of the multiple-spin exchange Hamiltonian on the triangular lattice”. In: *Physical Review B - Condensed Matter and Materials Physics* 60.2 (1999), pp. 1064–1074. ISSN: 1550235X. DOI: 10.1103/PhysRevB.60.1064.

[23] A. (Alain) Le Yaouanc and Pierre Dalmas de. Réotier. *Muon spin rotation, relaxation, and resonance : applications to condensed matter*. Oxford University Press, 2011, p. 486. ISBN: 978-0-19-959647-8.

[24] G. Squires. *Introduction to the theory of thermal neutron scattering*. Dover Publication, 1996.

[25] Carl D. Anderson. “Unraveling the Particle Content of the Cosmic Rays”. In: *EnSci*. Vol. 46. 2. 1985, pp. 117–132. DOI: 10.1007/978-94-009-5434-2{_}11. URL: https://ui.adsabs.harvard.edu/abs/1982EnSci..46...13A/abstract.

[26] Dario Buttazzo and Paride Paradisi. “Probing the muon g-2 anomaly at a Muon Collider.” In: *arXiv: 2012.02769* (2020).

[27] L Nuccio, L Schulz, and A J Drew. “Muon spin spectroscopy: magnetism, soft matter and the bridge between the two”. In: *Journal of Physics D: Applied Physics* 47.47 (Nov. 2014), p. 473001. ISSN: 0022-3727. DOI: 10.1088/0022-3727/47/47/473001. URL: https://iopscience.iop.org/article/10.1088/0022-3727/47/47/473001%20https://iopscience.iop.org/article/10.1088/0022-3727/47/47/473001/meta.

[28] E. Kermarrec. *Nouveaux états quantiques de spin induits par frustration magnétique sur le réseau kagome*. 2012. URL: https://tel.archives-ouvertes.fr/tel-00783605.

[29] Toshimitsu Yamazaki. “Kubo-Toyabe Theory revisited by muons and study of dynamics of spin glasses”. In: *Physical property research (Japan)* (1981).

[30] S. Blundell. “Magnetism in Condensed Matter (Oxford Master Series in Physics)”. In: (2001), p. 256.

[31] F. Brouers and O. Sotolongo-Costa. “Relaxation in heterogeneous systems: A rare events dominated phenomenon”. In: *Physica A: Statistical Mechanics and its Applications* 356.2-4 (Oct. 2005), pp. 359–374. ISSN: 03784371. DOI: 10.1016/j.physa.2005.03.029.

[32] R Orbach. “On the theory of spin-lattice relaxation in paramagnetic salts”. In: *Proceedings of the Physical Society* 77.4 (1961), pp. 821–826. ISSN: 03701328. DOI: 10.1088/0370-1328/77/4/301.

[33] Matthew Blakeley. “Macromolecular crystallography using neutrons”. In: *The Biochemist* 36.3 (June 2014), pp. 40–42. ISSN: 0954-982X. DOI: 10.1042/BIO03603040. URL: /biochemist/article/36/3/40/653/Macromolecular-crystallography-using-neutrons.

[34] S M Yusuf et al. “Two- and three-dimensional magnetic correlations in the spin- 1/2 square-lattice system Zn2VO(PO4)2”. In: *Physical Review B - Condensed Matter and Materials Physics* 82.9 (2010). ISSN: 10980121. DOI: 10.1103/PhysRevB.82.094412.

[35] BE Warren. “X-ray diffraction in random layer lattices”. In: *Physical Review* 59 (1941), p. 693.

[36] Masatoshi Arai. “Experimental Techniques”. In: *Experimental Methods in the Physical Sciences*. Vol. 44. Academic Press, 2013, pp. 245–320. DOI: 10.1016/B978-0-12-398374-9.00003-6.

[37] John Hasbrouck. Van Vleck. *The theory of electric and magnetic susceptibilities.* Oxford University Press, 1965, p. 384. ISBN: 0198512430.

[38] K. W.H. Stevens. “Matrix elements and operator equivalents connected with the magnetic properties of rare earth ions”. In: *Proceedings of the Physical Society. Section A* 65.3 (1952), pp. 209–215. ISSN: 03701298. DOI: 10.1088/0370-1298/65/3/308. URL: https://ui.adsabs.harvard.edu/abs/1952PPSA...65..209S/abstract.

[39] David J. Wales and Jonathan P.K. Doye. “Global optimization by basin-hopping and the lowest energy structures of Lennard-Jones clusters containing up to 110 atoms”. In: *Journal of Physical Chemistry A* 101.28 (July 1997), pp. 5111–5116. ISSN: 10895639. DOI: 10.1021/jp970984n. URL: https://pubs.acs.org/doi/full/10.1021/jp970984n.

[40] M. J. D. Powell. “An efficient method for finding the minimum of a function of several variables without calculating derivatives”. In: *The Computer Journal* 7.2 (Jan. 1964), pp. 155–162. ISSN: 0010-4620. DOI: 10.1093/comjnl/7.2.155. URL: https://academic.oup.com/comjnl/article/7/2/155/335330.

[41] Noboru Kimizuka and Eiji Takayama. “Ln(GaM2+)O4 and Ln(AlMn2+)O4 compounds having a layer structure [Ln = Lu, Yb, Tm, Er, Ho, and Y, and M = Mg, Mn, Co, Cu, and Zn]”. In: *Journal of Solid State Chemistry* 41.2 (Feb. 1982), pp. 166–173. ISSN: 1095726X. DOI: 10.1016/0022-4596(82)90199-2.

[42] Yuesheng Li et al. “Gapless quantum spin liquid ground state in the two-dimensional spin-1/2 triangular antiferromagnet YbMgGaO4”. In: *Scientific Reports* (2015). DOI: 10.1038/srep16419. URL: https://www.nature.com/articles/srep16419.

[43] Yuesheng Li et al. “Rare-Earth Triangular Lattice Spin Liquid: A Single-Crystal Study of YbMgGaO 4”. In: *Physical Review Letters* (2015). DOI: 10.1103/PhysRevLett.115.167203.

[44] Yuesheng Li et al. “Crystalline Electric-Field Randomness in the Triangular Lattice Spin-Liquid YbMgGaO 4”. In: *Physical Review Letters* (2017). DOI: 10.1103/PhysRevLett.118.107202.

[45] Jens Jensen and A.R. Mackintosh. “Rare earth magnetism: structures and excitations”. In: *Physics* (1991), p. 403. URL: http://www.fys.ku.dk/~jjensen/Book/Ebook.pdf.

[46] Zhaofeng Ding et al. “Persistent spin dynamics and absence of spin freezing in the H-T phase diagram of the two-dimensional triangular antiferromagnet YbMgGaO4”. In: *Physical Review B* 102.1 (2020), p. 14428. ISSN: 24699969. DOI: 10.1103/PhysRevB.102.014428.

[47] Zhenyue Zhu et al. “Disorder-Induced Mimicry of a Spin Liquid in YbMgGaO 4”. In: (2017). DOI: 10.1103/PhysRevLett.119.157201.

[48] Yuesheng Li et al. “Muon Spin Relaxation Evidence for the U(1) Quantum Spin-Liquid Ground State in the Triangular Antiferromagnet YbMgGaO4”. In: *Physical Review Letters* 117.9 (2016). ISSN: 10797114. DOI: 10.1103/PhysRevLett.117.097201.

[49] Zhen Ma et al. “Spin-Glass Ground State in a Triangular-Lattice Compound YbZnGaO4”. In: *Physical Review Letters* 120 (2018). ISSN: 10797114. DOI: 10.1103/PhysRevLett.120.087201.

[50] Giorgio Parisi. *Spin glasses and fragile glasses: Statics, dynamics, and complexity*. 2006. DOI: 10.1073/pnas.0601120103. URL: www.pnas.orgcgidoi10.1073pnas.0601120103.

[51] Christian Balz et al. “Physical realization of a quantum spin liquid based on a complex frustration mechanism”. In: *Nature Physics* 12 (2016), pp. 942–949. ISSN: 17452481. DOI: 10.1038/nphys3826. URL: www.nature.com/naturephysics.

[52] Yao Shen et al. “Fractionalized excitations in the partially magnetized spin liquid candidate YbMgGaO4”. In: *Nature Communications* 9 (2018). ISSN: 20411723. DOI: 10.1038/s41467-018-06588-1. URL: www.nature.com/naturecommunications.

[53] Yao Shen et al. “Evidence for a spinon Fermi surface in a triangular-lattice quantum-spin-liquid candidate”. In: *Nature* 540 (2016), pp. 559–562. DOI: 10.1038/nature20614.

[54] Yao Dong Li and Gang Chen. “Detecting spin fractionalization in a spinon Fermi surface spin liquid”. In: *Physical Review B* 96.7 (2017), p. 75105. ISSN: 24699969. DOI: 10.1103/PhysRevB.96.075105.

[55] Joseph A M Paddison et al. “Continuous excitations of the triangular-lattice quantum spin liquid YbMgGaO4”. In: *Nature Physics* 13 (2017). DOI: 10.1038/NPHYS3971. URL: www.nature.com/naturephysics.

[56] Yuesheng Li et al. “Rearrangement of Uncorrelated Valence Bonds Evidenced by Low-Energy Spin Excitations in YbMgGaO4”. In: *Physical Review Letters* 122.13 (2019). ISSN: 10797114. DOI: 10.1103/PhysRevLett.122.137201.

[57] J. Knolle and R. Moessner. *A field guide to spin liquids*. 2019. DOI: 10.1146/annurev-conmatphys-031218-013401.

[58] F. Alex Cevallos, Karoline Stolze, and Robert J. Cava. “Structural disorder and elementary magnetic properties of triangular lattice ErMgGaO4 single crystals”. In: *Solid State Communications* 276 (2018), pp. 5–8. ISSN: 00381098. DOI: 10.1016/j.ssc.2018.03.015. URL: https://reader.elsevier.com/reader/sd/pii/S0038109818300991?token=C31448A8E224E7A8F578DEA2F913116224A127403DBB0C188130BDF03FADAB9C15C13BA0B62EoriginRegion=eu-west-1&originCreation=20210531133133.

[59] Y. Cai et al. “μ SR study of the triangular Ising antiferromagnet ErMgGaO4”. In: *Physical Review B* 101.9 (Mar. 2020), p. 094432. ISSN: 24699969. DOI: 10.1103/PhysRevB.101.094432. URL: https://journals.aps.org/prb/abstract/10.1103/PhysRevB.101.094432.

[60] U K Voma et al. “Electronic structure and magnetic properties of the effective spin J eff = 1 2 two-dimensional triangular lattice K 3 Yb (VO4)2”. In: *Physical Review B* 104.14 (2021), p. 144411. ISSN: 24699969. DOI: 10.1103/PhysRevB.104.144411.

[61] Gordon A. Bain and John F. Berry. “Diamagnetic corrections and Pascal’s constants”. In: *Journal of Chemical Education* 85.4 (2008), pp. 532–536. ISSN: 00219584. DOI: 10.1021/ed085p532. URL: http://fizika.si/magnetism/DiamagneticCorrectionsandPascalsConstants.pdf.

[62] M Mourigal et al. “Molecular quantum magnetism in LiZn2Mo3O8”. In: *Physical Review Letters* 112.2 (2014). ISSN: 00319007. DOI: 10.1103/PhysRevLett.112.027202.

[63] J Gaudet et al. “Gapless quantum excitations from an icelike splayed ferromagnetic ground state in stoichiometric Yb 2 Ti 2 O 7”. In: (). DOI: 10.1103/PhysRevB.93.064406.

[64] Danielle R Yahne et al. “Pseudospin versus magnetic dipole moment ordering in the isosceles triangular lattice material K3Er(VO4)2”. In: *Physical Review B* 102.10 (2020), p. 104423. ISSN: 24699969. DOI: 10.1103/PhysRevB.102.104423.

[65] C P Lindsey and G D Patterson. “Detailed comparison of the Williams-Watts and Cole-Davidson functions”. In: *The Journal of Chemical Physics* 73.7 (1980), pp. 3348–3357. ISSN: 00219606. DOI: 10.1063/1.440530. URL: https://doi.org/10.1063/1.44053073,3348https://doi.org/10.1063/1.4985839https://doi.org/10.1063/1.466117.

[66] Hwanbeom Cho et al. “Studies on Novel Yb-based Candidate Triangular Quantum Antiferromagnets: Ba3YbB3O9 and Ba3YbB9O18”. In: *arXiv : 2104.01005* (2021). URL: https://arxiv.org/pdf/2104.01005.pdf.

[67] S T Bramwell et al. “Bulk magnetization of the heavy rare earth titanate pyrochlores - A series of model frustrated magnets”. In: *Journal of Physics Condensed Matter* 12.4 (Jan. 2000), pp. 483–495. ISSN: 09538984. DOI: 10.1088/0953-8984/12/4/308. URL: https://iopscience.iop.org/article/10.1088/0953-8984/12/4/308%20https://iopscience.iop.org/article/10.1088/0953-8984/12/4/308/meta.

[68] J. Gaudet et al. “Neutron spectroscopic study of crystalline electric field excitations in stoichiometric and lightly stuffed Yb2Ti2 O7”. In: *Physical Review B - Condensed Matter and Materials Physics* 92 (2015). ISSN: 1550235X. DOI: 10.1103/PhysRevB.92.134420.

[69] Jeffrey G Rau and Michel J P Gingras. “Frustrated quantum rare-earth pyrochlores”. In: *Annual Review of Condensed Matter Physics* 10.1 (2019), pp. 357–386. DOI: 10.1146/annurev-conmatphys-022317-110520. URL: https://doi.org/10.1146/annurev-conmatphys-022317-110520.

[70] T. Fennell et al. “Magnetic Coulomb Phase in the Spin Ice Ho2Ti2O 7”. In: *Science* 326 (2009), pp. 415–417. ISSN: 00368075. DOI: 10.1126/science.1177582. URL: https://www.science.org/doi/abs/10.1126/science.1177582.

[71] Kate A Ross et al. “Quantum Excitations in Quantum Spin Ice”. In: *Physical Review X* 1.2 (2011), pp. 1–10. ISSN: 21603308. DOI: 10.1103/PhysRevX.1.021002.

[72] M. J.P. Gingras and P. A. McClarty. “Quantum spin ice: A search for gapless quantum spin liquids in pyrochlore magnets”. In: *Reports on Progress in Physics* 77.5 (2014), p. 056501. ISSN: 00344885. DOI: 10.1088/0034-4885/77/5/056501.

[73] K. Matsuhira et al. “Low temperature magnetic properties of frustrated pyrochlore ferromagnets Ho2Sn2O7 and Ho2Ti2O7”. In: *Journal of Physics Condensed Matter* 12.40 (Oct. 2000), p. L649. ISSN: 09538984. DOI: 10.1088/0953-8984/12/40/103. URL: https://iopscience.iop.org/article/10.1088/0953-8984/12/40/103%20https://iopscience.iop.org/article/10.1088/0953-8984/12/40/103/meta.

[74] Byron C. Dem Hertog and Michel J.P. Gingras. “Dipolar Interactions and Origin of Spin Ice in Ising Pyrochlore Magnets”. In: *Physical Review Letters* 84.15 (Apr. 2000), p. 3430. ISSN: 10797114. DOI: 10.1103/PhysRevLett.84.3430. URL: https://journals.aps.org/prl/abstract/10.1103/PhysRevLett.84.3430.

[75] J A Hodges et al. “The crystal field and exchange interactions in Yb2Ti2O7”. In: *Journal of Physics Condensed Matter* 13.41 (Sept. 2001), pp. 9301–9310. ISSN: 09538984. DOI: 10.1088/0953-8984/13/41/318. URL: https://iopscience.iop.org/article/10.1088/0953-8984/13/41/318%20https://iopscience.iop.org/article/10.1088/0953-8984/13/41/318/meta.

[76] P. Bonville et al. “Transitions and spin dynamics at very low temperature in the pyrochlores yb2Ti2O7 and Gd2Sn2O7”. In: *Hyperfine Interactions* 156-157.1-4 (2004), pp. 103–111. ISSN: 03043843. DOI: 10.1023/b:hype.0000043235.21257.13. URL: https://link.springer.com/article/10.1023/B:HYPE.0000043235.21257.13.

[77] J. D. Thompson et al. “Quasiparticle Breakdown and Spin Hamiltonian of the Frustrated Quantum Pyrochlore Yb2Ti2 O7 in a Magnetic Field”. In: *Physical Review Letters* 119.5 (Mar. 2017). ISSN: 10797114. DOI: 10.1103/PhysRevLett.119.057203. URL: https://arxiv.org/abs/1703.04506v1.

[78] R M D’ortenzio et al. “Unconventional magnetic ground state in Yb 2 Ti 2 O 7”. In: *PHYSICAL REVIEW B* 88 (2013), p. 134428. DOI: 10.1103/PhysRevB.88.134428.

[79] P. Bonville et al. “Transitions and spin dynamics at very low temperature in the pyrochlores yb2Ti2O7 and Gd2Sn2O7”. In: *Hyperfine Interactions* 156-157.1-4 (2004), pp. 103–111. ISSN: 03043843. DOI: 10.1023/b:hype.0000043235.21257.13. URL: https://link.springer.com/article/10.1023/B:HYPE.0000043235.21257.13.

[80] Yukio Yasui et al. “Ferromagnetic transition of pyrochlore compound Yb2Ti 2O7”. In: *Journal of the Physical Society of Japan* 72.11 (Nov. 2003), pp. 3014–3015. ISSN: 00319015. DOI: 10.1143/JPSJ.72.3014.

[81] E. Lhotel et al. “First-order magnetic transition in Yb2 Ti2 O7”. In: *Physical Review B - Condensed Matter and Materials Physics* 89.22 (June 2014). ISSN: 1550235X. DOI: 10.1103/PhysRevB.89.224419.

[82] E Kermarrec et al. “Ground state selection under pressure in the quantum pyrochlore magnet Yb2Ti2O7”. In: *Nature Publishing Group* 8 (2017), pp. 1–5. DOI: 10.1038/ncomms14810. URL: http://dx.doi.org/10.1038/ncomms14810.

[83] J. Robert et al. “Spin dynamics in the presence of competing ferromagnetic and antiferromagnetic correlations in Yb2Ti2 O7”. In: *Physical Review B - Condensed Matter and Materials Physics* 92.6 (Aug. 2015), p. 064425. ISSN: 1550235X. DOI: 10.1103/PHYSREVB.92.064425/FIGURES/15/MEDIUM. URL: https://journals.aps.org/prb/abstract/10.1103/PhysRevB.92.064425.

[84] Allen Scheie et al. “Multiphase magnetism in Yb2Ti2O7”. In: *Proceedings of the National Academy of Sciences of the United States of America* 117.44 (Nov. 2020), pp. 27245–27254. ISSN: 10916490. DOI: 10.1073/pnas.2008791117. URL: https://www.pnas.org/content/117/44/27245%20https://www.pnas.org/content/117/44/27245.abstract.

[85] L. D.C. Jaubert et al. “Are Multiphase Competition and Order by Disorder the Keys to Understanding Yb2Ti2 O7 ?” In: *Physical Review Letters* 115.26 (Dec. 2015), p. 267208. ISSN: 10797114. DOI: 10.1103/PhysRevLett.115.267208. URL: https://journals.aps.org/prl/abstract/10.1103/PhysRevLett.115.267208.

[86] Akshat Pandey, Roderich Moessner, and Claudio Castelnovo. “Analytical theory of pyrochlore cooperative paramagnets”. In: *Physical Review B* 101.11 (Mar. 2020), p. 115107. ISSN: 24699969. DOI: 10.1103/PhysRevB.101.115107. URL: https://journals.aps.org/prb/abstract/10.1103/PhysRevB.101.115107.

[87] R. D. Shannon. “Revised effective ionic radii and systematic studies of interatomic distances in halides and chalcogenides”. In: *Acta Crystallographica Section A* 32.5 (Sept. 1976), pp. 751–767. ISSN: 16005724. DOI: 10.1107/S0567739476001551. URL: https://onlinelibrary.wiley.com/doi/full/10.1107/S0567739476001551%20https://onlinelibrary.wiley.com/doi/abs/10.1107/S0567739476001551%20https://onlinelibrary.wiley.com/doi/10.1107/S0567739476001551.

[88] J. A. Hodges et al. “First-Order Transition in the Spin Dynamics of Geometrically Frustrated Yb2Ti2O7”. In: *Physical Review Letters* 88.7 (Feb. 2002), p. 4. ISSN: 10797114. DOI: 10.1103/PhysRevLett.88.077204. URL: https://journals.aps.org/prl/abstract/10.1103/PhysRevLett.88.077204.

[89] A. Yaouanc, A. Maisuradze, and P. Dalmas De Réotier. “Influence of short-range spin correlations on the μsR polarization functions in the slow dynamic limit: Application to the quantum spin-liquid system Yb2Ti2O7”. In: *Physical Review B - Condensed Matter and Materials Physics* 87.13 (Apr. 2013), p. 134405. ISSN: 10980121. DOI: 10.1103/PhysRevB.87.134405. URL: https://journals.aps.org/prb/abstract/10.1103/PhysRevB.87.134405.